Simulating real molecules with tensor network techniques

Sam Mardazad

SIGILL. UNIVERSITAT. LUDOVIC. MAXIM.

München 2022

Simulating real molecules with tensor network techniques

Sam Mardazad

Dissertation
an der Fakultät für Physik
der Ludwig-Maximilians-Universität
München

vorgelegt von
Sam Mardazad
aus München

München, den 7.April 2022

Erstgutacher/in: Prof. Dr. Ulrich Schollwöck
Zweitgutachter/in: Prof. Dr. Christian Ochsenfeld
Tag der mündlichen Prüfung: 24.Juni 2022

Zusammenfassung

Die Beschreibung quantenmechanischer Systeme, wie großer Moleküle, aus der Grundlagenperspektive ist, dank des Fortschritts numerischer Verfahren und der enormen Rechenleistung moderner Computer, in greifbare Nähe gerückt. In dieser Arbeit implementieren wir einen Rahmen zur Erweiterung des Matrix-Produkt-Zustand-Ansatzes zu höheren Topologien und zeigen, wie mit diesen Zuständen physikalische Eigenschaften großer Systeme berechnet werden können. Wir diskutieren diverse mögliche Anwendungen, die zumeist über den ursprüglichen, eindimensionalen Einsatzbereich von MPS hinaus gehen. Dies führt zu neuen Fragestellungen, wie der Notwendigkeit, sich mit Systemen ohne konkreten Dimensionlitätsbegriff zu befassen, sowie der Implementierung neuer Algorithmen zur Berechnung von Observablen. Wir besprechen sowohl statische, als auch dynamische Tensornetzwerkanwendungen und beschäftigen uns ausgiebig mit der Frage der dynamischen Adaptierung der Einteilchenorbitale. Anschließend verwenden wir eine neue Methodik zur Behandlung großer, lokaler Hilberträume mit gebrochener $U(1)$ Teilchenzahlerhaltung, um Fermi-Bose-Gemische effizient zu beschreiben. Dies ermächtigt uns, im Folgenden, zu zweierlei Untersuchungen.

Zuerst behandeln wir das statische, eindimensionale Hubbard-Holstein-Modell erneut und berechnen ein Phasendiagramm mit hoher numerischer Güte. Auch wenn es sich hierbei nicht um eine Grundlagenrechnung handelt, so ist sie doch von hohem Interesse für die theoretische Deutung realistischer Systeme, wie wir im entsprechenden Teil argumentieren werden. Zusätzlich zu der antiferromagnetischen und der Peierls Phase, die bereits in früheren Untersuchungen gefunden worden sind, können wir auch die Existenz einer metallischen Phase dazwischen bestätigen. Des Weiteren finden wir ein zuvor nicht beschriebenes Signal in der metallischen Phase. Dieses wird gekennzeichnet durch eine breitere Phononenverteilung und das Erscheinen von nur einer Anregung ohne Energiedifferenz, welche höchst wahrscheinlich ein Spin-Gap hat, jedoch kein Charge-Gap.

Im Folgenden wenden wir uns der ab-initio Behandlung großer organischer Moleküle außerhalb des Gleichgewichts, in Abwesenheit der Gültigkeit der Born-Oppenheimer Näherung, zu. Wir nutzen unsere Methoden zur Simulation der Dynamik der zwei niedrig-liegenden Anregungen des Pyrazin-Moleküls S_1 und S_2 und stellen eine Übereinstimmung mit vorherigen Arbeiten fest. Des Weiteren erkennen wir, dass die Dynamik größtenteils durch die klassische, reduzierte Dichtematrix korrekt wiedergegeben wird. Dann wenden wir uns dem Thema unseres Hauptinteresses zu, der Singulett-Spaltung in großen, organischen Molekülen. Singulett-Spaltung ist ein spinerlaubter, photo-physikalischer Prozess, bei dem ein Singulett Exciton in zwei Triplett Excitone zerfällt. Es wird angenommen, dass dadurch ein Verschieben der theoretischen Grenze für die Effizienz von Solarzellen erreicht werden kann, und daher wird diesem Prozess eine Schlüsselrolle bei der Entwicklung neuer Photovoltaikgeräte zugesprochen. Wir finden eine hervorragende Übereinstimmung mit experimentellen Messungen in dem von uns untersuchten 1,4-bis(11-phenyltetracen-5-yl)Benzol Molekül und können des Weiteren diejenigen Moden feststellen, die für den Energietransfer zwischen den Systemen verantwortlich sind. Weiterhin berechnen wir den Ertrag an Triplett Elektronen für verschiedene, im Experiment einstellbare, Parameter und finden auch hier eine Übereinstimmung mit den Messungen. Eine charakteristische Zeitskala gibt sich zu erkennen, die unabhängig von den elektronischen Parametern ist. Daher untersuchen wir deren Ursprung, im Zuge dessen unsere Analyse zeigt, dass es sich hierbei um einen durch Kohärenzen getriebenen Prozess handelt. Des Weiteren wird der Ursprung des Zusammenbruchs der Kohärenzen, durch ein Kombinationsvorgehen aus Analytik und Numerik, untersucht. Dies ermöglicht uns nicht nur, den exakten Wert dieser Zeitskala anzugeben, sondern verbindet auch den Grund für den Zeitpunkt des Zusammenbruchs der Kohärenzen mit dem Ausbilden von Quasiteilchen und der Renormierung derer effektiver Tunnelamplituden.

Abstract

Describing quantum mechanical systems, like large molecules, from first principles has come within reach of numerical techniques due to the progress in method development and the enormous computational power of modern day computers. In this thesis we establish a framework in order to extend the matrix product state ansatz to higher topologies and demonstrate how to compute physical properties of large systems with these states. We discuss various possible applications mostly going further than the original domain of applicability for one-dimensional systems. This introduces additional issues like the necessity to deal with systems without a notion of dimensionality, as well as implementing new algorithms in order to be able to compute observables. We discuss static and dynamic applications of tensor networks and deal extensively with the question of single particle orbitals and their optimization on the fly. We then use a new method for the treatment of large local Hilbert spaces with broken $U(1)$ particle number symmetry in order to describe efficiently Fermi-Bose mixtures. This enables us to do investigations of two systems.

First, we revisit the static one-dimensional Hubbard-Holstein model and map out its phase diagram faithfully. Even though not a first principles model, it is still of high interest in the theoretical clarification of realistic systems, as we shall argue. In addition to the antiferromagnetic phase and the Peierls phase known from previous investigations, we can also confirm the existence of an intermediate metallic phase. Furthermore, we find new features within the metallic phase which were not described before. These include the existence of a broader phonon distribution and the emergence of a single gapless mode which is most likely spin gapped but does not have a charge gap.

Second, we turn to the ab-initio out-of-equilibrium investigation of the dynamics of large organic molecules in the vicinity of a breakdown of the Born-Oppenheimer approximation. We benchmark our methods with the pyrazine molecule and its two low lying excitations S_1 and S_2 and find agreement to previous works. Furthermore, we find the main part of the dynamics to be captured by the classical reduced density matrix. Then we turn to our main topic of interest, the singlet fission in large organic molecules. Singlet fission is a spin-allowed photo physical process in which a singlet exciton decays into two triplets excitons. It is widely believed to be able to shift the theoretical bounds of solar cells and therefore might be key to the development of new photo voltaic devices. In addition to an excellent agreement to experimental data, we investigate the modes which dominate the energy transfer in 1,4-bis(11-phenyltetracen-5-yl)benzene and compute the triplet electron yield for various experimentally tuneable parameters. This, as well, is in good agreement with experimental measurements. A characteristic time-scale arises, which is independent of the chosen electronic parameters. Therefore, we investigate its origin where our analysis shows that it is a coherence-driven process. Furthermore, the origin of the breakdown of coherence is investigated with a hybrid approach between analytics and numerics. This not only enables us to give an exact numerical value for this time-scale, but also attaches the reason for the particular value to quasi particle formation and the renormalization of their effective hopping elements.

List of publications

This work is based on the following publications and preprints which are partially reprinted.

[DMD+21] Lexin Ding, Sam Mardazad, Sreetama Das, Szilárd Szalay, Ulrich Schollwöck, Zoltán Zimborás, and Christian Schilling. Concept of Orbital Entanglement and Correlation in Quantum Chemistry. *Journal of Chemical Theory and Computation*, 17(1):79–95, 2021. PMID: 33430597

[MXY+21] Sam Mardazad, Yihe Xu, Xuexiao Yang, Martin Grundner, Ulrich Schollwöck, Haibo Ma, and Sebastian Paeckel. Quantum dynamics simulation of intramolecular singlet fission in covalently linked tetracene dimer. *The Journal of Chemical Physics*, 155(19):194101, 2021

The following manuscript is currently in preparation and is also partially reprinted in this thesis.

[MGS+22] Sam Mardazad, Martin Grundner, Ulrich Schollwöck, Adrian Kantian, Thomas Köhler, and Sebastian Paeckel. Emergence of bond-order wave phase in the half filled Hubbard-Holstein chain. Preliminary title, 2022

Additionally, while working on this thesis the author contributed to the publications listed below.

[PMB+21] Felix A. Palm, Sam Mardazad, Annabelle Bohrdt, Ulrich Schollwöck, and Fabian Grusdt. Snapshot-based detection of $\frac{1}{2}$-Laughlin states: coupled chains and central charge, 2021

Table of contents

II Applications

Introduction

1

> The underlying physical laws necessary for the mathematical theory of a large part of physics and the whole of chemistry are thus completely known, and the difficulty is only that the exact application of these laws leads to equations much too complicated to be soluble.
>
> (Paul Adrien Maurice Dirac. Quantum mechanics of many-electron systems. *Proceedings of the Royal Society of London. Series A*, 123(792), 1929)

Many physicists might have encountered this statement in one or the other form. I personally remember hearing something similar, i.e. that “the rest is chemistry”, after deriving the hydrogen spectrum from the Schrödinger equation in my undergraduate studies. It might seem tempting to believe that the solution of the fundamental equations is just a formality and the efforts of science should be focussed toward deriving new laws instead of dealing with known ones. However, we believe that this is not the case and that we need to be able to solve quantum systems in order to learn interesting occurrences of nature.[1] After all we would not be dealing with it in this thesis otherwise. Most likely, the reductionist approach of the last century and its enormous success in explaining a variety of phenomena might have led to a misinterpretation of Dirac’s statement. He was quite certainly aware of the necessity for solving the complicated equations that describe matter.

As a matter of fact, the fundamental quantum equations governing most of the every-day experience are known [LP00]. But reductionism can not explain the plethora of materials around us. Quite in contrast their properties are emergent due to the large number of particles [And72].[2] Unfortunately, a large number of particles can make exact solutions next to impossible, which is by no means a problem restricted to physics and commonly referred to as the curse of dimensionality. We certainly do not claim to have fully grasped the interplay of nature and emergence, in fact our scientific goals are much more modest. In the course of this thesis, however, we set our goal to solving (numerically) the equations Dirac referred to for some many particle systems, where this is possible, and explore the rich amount of physics they can show.

There is an informal separation between those who describe the outcome of experiments on a phenomenological level and the ones who try to extrapolate the reduced constituents back to macroscopic systems. As we belong to the latter one, our aim is, in the best case, to take the many-body generalization of the Schrödinger equation for N particles

$$\dot{\psi}(t, x_1, \ldots, x_N) = -\mathrm{i}\hat{H}(t, x_1, \ldots, x_N)\psi(t, x_1, \ldots, x_N) \ , \tag{1.1}$$

where the dot-notation means time derivative, and find solutions. If the Hamiltonian $\hat{H}$ is not explicitly time dependent, we can split off the time evolution and look at the static eigenvalue problem

$$\hat{H}(x_1, \ldots, x_N)\psi(x_1, \ldots, x_N) = E\psi(x_1, \ldots, x_N) \ , \tag{1.2}$$

with E being the energies of our system. Even the static part is far from being trivial. If we, for instance, have a look at the Hamiltonian describing a generic molecule, neglecting relativistic effects, we need to take into account the motion of all nuclei I and all electrons i and their pairwise electrostatic interaction, i.e. the five terms

$$\hat{H} = -\sum_{i=1}^{N} \frac{\Delta_i}{2m_i} - \sum_{iI} \frac{Z_I e^2}{|x_i - x_I|} + \sum_{i<j} \frac{e^2}{\left|x_i - x_j\right|} - \sum_{I=1}^{M} \frac{\Delta_I}{2m_I} + \sum_{I<J} \frac{Z_I Z_J e^2}{|x_I - x_J|} \ . \tag{1.3}$$

For the sake of completeness we would like to mention that also relativistic effects can be accounted for [BKK18, SBG+20, BVV+20].

---

[1] From here on I will refer to the reader and myself as “we”.

[2] Even tough I am not a big fan of Goethe, I have to agree with Mephisto here [vG01]: “Dann hat er die Teile in seiner Hand, Fehlt leider! nur das geistige Band.”

Since eq. (1.3) seems impossible to solve – where should we even start? For the moment, let us state that the motion of the nuclei can be separated from the motion of the electrons via the well known Born-Oppenheimer approximation (BO approximation) with which we are going to deal in more detail in chapter 7. This makes the last two terms in eq. (1.3) vanish or constant, respectively, leaving us behind with a constant dependence on the nuclear position in the second term. As any other quantum mechanical wavefunction, $\psi(x_1, \dots, x_N)$ might be expanded in terms of a basis in order to find a meaningful representation [Gau28, Sla28]. Typically, one chooses a single particle basis of the individual constituents $\{\varphi_i(x)\}_i$ to do so. These do not necessarily have to be eigenfunctions of the single particle Hamiltonian, it is sufficient if they are complete, i.e. every state in the Hilbert space can be formed by their linear combination. However, in the original approach by Hartree [Har28a, Har28b, Har28c, S47] it was argued that the product of the individual single particle wavefunctions should be a good approximation to the true many-body wavefunction

$$\psi(x_1, \dots, x_N) = \phi_{i_1}(x_1) \dots \phi_{i_N}(x_N) \,, \tag{1.4}$$

where we choose a suitable level i_j for each particle j. Since this wavefunction actually sees the exchange of two particles, but real quantum particles are indistinguishable (up to a phase upon exchange), we can introduce the totally anti-symmetric superposition of all wavefunctions [Hei26, Sla29],

$$\psi(x_1, \dots, x_N) = \det \begin{bmatrix} \phi_1(x_1) & \dots & \phi_1(x_N) \\ \vdots & \ddots & \vdots \\ \phi_L(x_1) & \dots & \phi_L(x_N) \end{bmatrix} / \sqrt{N!} \,, \tag{1.5}$$

also known as Slater determinant. This is a valid wavefunction for fermions and in the case of bosons one just replaces det $\longrightarrow$ perm. Working with this wavefunction representation made the first description of atomic and molecular properties by means of quantum mechanics possible through the well known Hartree Fock (HF) method [Foc30, Sla30]. Actually, these Slater determinants form a basis of the complete many-body Hilbert space $\mathcal{H}$, i.e. any state within it can be written as superposition

$$\psi(x_1, \dots, x_N) = \sum_{i_1 \dots i_L} c_{i_1 \dots i_L} \det \begin{bmatrix} \phi_{i_1}(x_1) & \dots & \phi_{i_1}(x_N) \\ \vdots & \ddots & \vdots \\ \phi_{i_L}(x_1) & \dots & \phi_{i_L}(x_N) \end{bmatrix} \,, \tag{1.6}$$

where the c coefficients are to be determined for the individual state. Unfortunately, this also has a few downsides which are quite peculiar to work with. The main obstacle is the high degree of inefficiency as we are "counting" all particles and keeping track of their state. But this is quite unnecessary, as quantum particles obey the aforementioned indistinguishability, therefore, we do not care about the individual particles. This is more an artefact of our non-quantum information storage system.

Inefficiency is eased by the introduction of the second quantization [Foc32] which turns to a much more efficient way of accounting. Instead of keeping track of each individual particle we just note down how many particles are in a certain orbital, i.e.

$$\det \begin{bmatrix} \phi_1(x_1) & \dots & \phi_1(x_N) \\ \vdots & \ddots & \vdots \\ \phi_L(x_1) & \dots & \phi_L(x_N) \end{bmatrix} \longrightarrow |n_1\rangle_1 \, |n_2\rangle_2 \dots |n_L\rangle_L = |n_1 \dots n_L\rangle \tag{1.7}$$

for n_i excitations in the orbitals ϕ_i, created by means of the creation and annihilation algebra

$$|1\rangle_i = \hat{c}_i^\dagger \, |0\rangle_i \qquad |0\rangle_i = \hat{c}_i \, |1\rangle_i \;. \tag{1.8}$$

Note that the (anti-) commutation algebra of the particles is now shifted into the operators which span these Hilbert spaces $|n_1 \dots n_L\rangle = (\hat{c}_1^\dagger)^{n_1} \dots (\hat{c}_L^\dagger)^{n_L} \, |0\rangle$, which is also a nice property of this framework. This leaves us with the task of determining the coefficients c for the wavefunction

$$|\psi\rangle = \sum_{n_1 \dots n_L} c_{n_1 \dots n_L} \, |n_1 \dots n_L\rangle \;, \tag{1.9}$$

which is quite easily said and close to impossible for realistically large systems. If we call the number of particles which can be in a single particle state d and have a total of L of such orbitals the size of this coefficient vector is $d^L = \dim \mathcal{H}$, i.e. we still have to struggle with the exponentially large state space of many particles. Therefore, this procedure of exact diagonalization (ED) can only be done for small systems. Even upon exploitation of symmetries it can only be pushed to e.g. 30 to 50 spins [WL18, WL20].

Fortunately, nature is not that crude to us. Methods do exist which all have their custom domain, thus enabling us to compute quantum many-body properties of large systems efficiently, at least from a numerical perspective. One of the more prominent ones is the density functional theory (DFT) [HK64, KS65, Ull12] which maps the many-body Schrödinger equation to a single particle equation, allowing one to solve it efficiently. However, DFT introduces a so called exchange correlation functional where it stores all the system's specific information and which is a highly unpleasant quantity. For weakly correlated cases one can approximate this functional quite well, however, in the strong correlation limits the results start deviating [SG88, SGN95]. Furthermore, there are Monte Carlo methods [MRR+53] which focus on deriving the partition sum of the system, instead of the wavefunction. As the partition sum is an integral and the convergence of typical Monte-Carlo methods goes as $\sim m^{-1/2}$, where m is the number of random samples, the convergence seems guaranteed. Yet, this is only possible as long as the particles do not suffer from a sign problem [TW05], i.e. the NP-hard reconstruction of the sign of the probability distribution. Unfortunately, this is not the case for fermions and frustrated problems. Furthermore, one often struggles with the zero temperature limit.

In the course of this thesis we shall focus on treating molecules with large Hilbert spaces by means of tensor network methods. These methods, which we shall introduce in the next chapter, were originally designed for zero temperature (but can also go beyond) and are able to capture a significant part of the entangled many-body Hilbert space [Whi92, Whi93, VGRC04, Sch05, Sch11]. We will focus on using as little approximation as necessary and try to link system properties to microscopic causes. As it turns out, it is possible to treat many systems with a reasonable amount of resources [CKG04, VAL+18, FML+19, MXY+21, FGL21, CHH+22]. We will start off by explaining how to generalize the tensor network ansatz for loop free networks [NC13, MVS+15, GVW+18] in chapter 3 and describe all the necessary components to set up an extremely powerful toolbox in the treatment of strongly correlated systems [LS03, RNW06, Sch11, BLMR11]. Furthermore, we will continue explaining how to extend static quantum wavefunctions [HCO+11, HLO+16, PKS+19, BA20] and look at dynamic properties of systems in a well controlled fashion in chapter 5. We will deal intensively with the question of the choice of single particle orbitals [KVLE16] in chapter 6 and finish the technical discussion with an extension beyond BO approximation quantum dynamics [KSP21, SKM+21, MXY+21].

The second part of this work is divided into two chapters. First, we will execute very careful investigation of static electronic systems going beyond the BO approximation by means of an idealized electron-phonon model [HF83, Nas87, Tak96, Tak96, Hir85, HF83, MSJ04, TAA07]. Here, we discuss the previous findings of the employed model and why we believe there are new unknown so far features which we tried to map out faithfully [MGS+22]. Second, we are going to discuss the exact out-of-equilibrium quantum dynamics of molecules [WLX+21, THRB+15a, ZXJL16, RCT18, CBP+13, Tao19, ZZL17, XSBF+19, THRB+15a, MST+17, BG, GB21, SXC+20, SLH+21, STM+19] and present results obtained by our framework for two molecules of our choice. One of them [MXY+21] is of particular interest for the field of organic semiconductors in that it might be able to improve the efficiency of light harvesting significantly. We compare our calculated results to experiment to check the reliability of our methods and are going to see that our model is in excellent agreement. Furthermore, we deal with the question of how to increase the light harvest by tuneable parameters in experiment. Lastly, we shall combine analytical and numerical results in order to figure out the microscopic origin for the photo-absorption properties.

Tensor networks

Genesis | 2

Originally invented for local one-dimensional (1d) systems, the density matrix renormalization group (DMRG) [Whi92, Whi93] and its formulation in terms of matrix product states (MPS) [Sch11] soon became a de facto standard for the treatment of strongly correlated quantum condensed matter systems.

Basically, DMRG extends Wilson's ideas, targeting the Kondo problem nowadays known as numerical renormalization group (NRG) [Wil75]. The combination of the renormalization group (RG) approach, i.e. trying to isolate relevant degrees of freedom and getting rid of the irrelevant ones, combined with the enormous potential of the rising computational power of modern day computers [Moo65] provided a powerful way to study systems with a macroscopic number of degrees of freedom. By isolating high energy contributions to the system, Wilson was able to derive an effective Hamiltonian and solve the system exactly. Unfortunately, NRG has strong limitations regarding the models it can be efficiently deployed for [Wil75, Sch05, Whi92, Sch11]. This motivated White (who was a former student of Wilson) to search for other means to locate irrelevant degrees of freedom. In his ground-breaking work [Whi92] from 1992 he provided the calculation which is the basis for modern-day DMRG and tensor network approaches. Essentially, the idea is to decimate basis states with low density matrix spectral weight instead of those with high energies. Given this procedure, an optimal representation is found for a chosen truncation threshold [Whi92].

Let us elaborate a bit on this, following the argumentation from [Sch05]. Consider a 1d bipartite system $AB = A \otimes B$, i.e. its wave function reads

$$|\psi\rangle = \sum_{a=1}^{m_A} \sum_{b=1}^{m_B} \Psi_{ab} \, |a\rangle \, |b\rangle \ . \tag{2.1}$$

Here, $\Psi_{ab} \in \mathbb{C}$ are coefficients and the basis states $|a\rangle \in A$ and $|b\rangle \in B$ are elements of the respective subspaces. Now we want to approximate this wave function by using a smaller number of basis states, e.g. in A, therefore defining the expansion (with unknown coefficients)

$$|\tilde{\psi}\rangle = \sum_{a'=1}^{m'_A} \sum_{b=1}^{m_B} \tilde{\Psi}_{a'b} \, |a'\rangle \, |b\rangle \qquad m'_A \leq m_A \ . \tag{2.2}$$

The question arises, how to choose the coefficients $\tilde{\Psi}_{a'b}$ and the new basis $\{|a'\rangle\}$ in such a way that $|\tilde{\psi}\rangle$ is as close as possible to the original state $|\psi\rangle$, given a fixed value of m'_A. Expanding the new basis in terms of the old one, i.e. $|a'\rangle = \sum_a c_{a'a} \, |a\rangle$, yields

$$|\tilde{\psi}\rangle = \sum_{a'ba} \tilde{\Psi}_{a'b} c_{a'a} \, |a\rangle \, |b\rangle \ . \tag{2.3}$$

This reduces the problem to an optimization, namely minimize the distance

$$\big\| |\psi\rangle - |\tilde{\psi}\rangle \big\|_2^2 = 1 - 2\,\mathrm{Re}\left(\sum_{aba'} \Psi^*_{ab} \tilde{\Psi}_{a'b} c_{a'a} \right) + \sum_{a'b} \big|\tilde{\Psi}_{a'b}\big|^2 \tag{2.4}$$

by varying c and $\tilde{\Psi}$. By first minimizing with respect to $\tilde{\Psi}$ we obtain

$$1 - \sum_{aa'b} c^*_{a'a} \rho_{ab} c_{a'b} = 1 - \sum_{a'} \langle a' | \rho | a' \rangle \ . \tag{2.5}$$

We recognize this as the Rayleigh quotient, being minimal for $|a'\rangle$ an eigenvector of the density matrix $\rho = |\psi\rangle \langle\psi|$ of the wave function. Therefore, the eigenbasis of ρ is our ideal expansion basis and the accuracy of the approximation is controlled by the number of eigenvectors taken into account (ordered by increasing eigenvalues $\langle a' | \rho | a' \rangle = \lambda_{a'}$).

As already mentioned in eq. (1.6), the Hilbert spaces of many-body wave functions are usually too large to solve exactly with an arbitrary number of determinants. However, a subsystem consisting of a small number of orbitals can usually be treated exactly. Therefore, the optimal compression scheme leads to the definition of the (a bit general) DMRG sweeping pattern: Firstly, we solve a subsystem of AB. Secondly, we compress via the reduced density matrix (RDM) criterion, and finally, we iterate until the desired convergence sets in. Typically, one chooses the subspace small such that the computational cost remains controllable, i.e. one or two orbitals. Even though this seems slightly basic and modern day tensor network algorithms have come a long way, becoming quite sophisticated, this procedure is at the heart of any DMRG approach.

The existence of two different classes of DMRG should be mentioned, the infinite and the finite system approach. The main difference is in the partitioning of the system during the sweeping procedure, both illustrated in fig. 2.1. The infinite system DMRG actually operates in the thermodynamic limit[1], i.e. increasing the sizes (of both parts of the bipartite system) and particle number from a finite initial value, while keeping the density constant. This way, a recursive procedure is defined. What may sound like a shenanigan at first – after all, how do we simulate an infinite system on a finite computer? – turns out to be possible by reaching a fixed point within the space of density matrices [Sch11]. Therefore, one does not have to continue calculations ad infinitum.

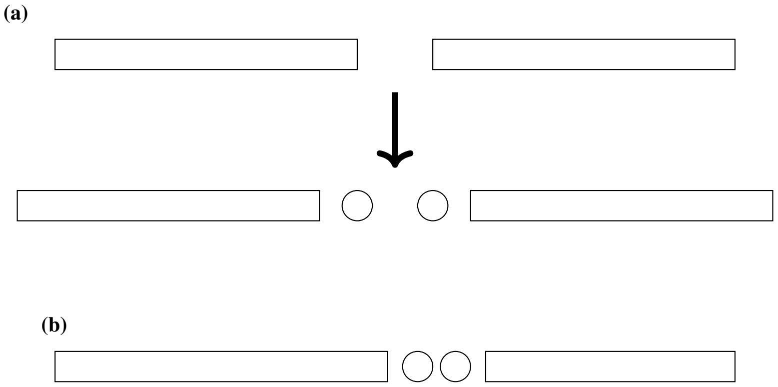

Figure 2.1: Illustration of the different block growing procedures. Figure 2.1a shows the block growing by adding another site to both subsystems. Figure 2.1b shows the system block growing at cost of the environment block.

As is illustrated in fig. 2.1a, we take a given finite bipartite system and add two orbitals to each part. Then we solve for the exact ground state of this composition. With this solution we can obtain the RDM and compress, such that the needed resources do not become unmanageable. When reaching a fixed point, we know that the solution will not change upon reiteration and is the same as in the thermodynamic limit. Unfortunately, the infinite size algorithm has severe shortcomings in regards to convergence, especially regarding observables computed from the wave functions [Sch05]. This, and the fact that it only works on translationally invariant systems, explains why nowadays it is not as extensively used as the finite size algorithm, as molecules or impurity models are not translationally invariant.

The finite system size DMRG does not have such shortcomings. It has a very well controlled error measure, given by the so called truncated weight of the truncation, i.e. the sum of the squares of RDM eigenvalues corresponding to discarded eigenvectors. The main difference is that the growing/shrinking of one system part is accompanied by matching shrinking/growing of the other one. By this procedure the system size is always constant and, as we usually operate in a canonical ensemble, the density is therefore kept constant as well. This way, the entire system is present at every step of the algorithm in the Hamiltonian, providing for a stable solution [Sch05]. This comes at the price of having to operate on large systems and usually at the need of extrapolating results to the thermodynamic limit. For some applications, however, this is not even necessary, e.g. in cold atom experiments [BDZ08, CDS19] with fixed number of atoms or for molecular calculations cutting off the (discrete) orbital space at some point. The latter were extensively studied in the course of this thesis.

The attentive reader might have asked themselves the following question: Given we don't have convergence issues for our system, who can guarantee that there is a reduced Hilbert space in which the problem is representable while still feasible? Or to phrase it differently: Why should m'_A be actually in a regime where we can simulate the system in polynomial time, given that m_A grows exponentially? Of course, as one would expect, this depends on

---

[1] Of at least one dimension.

the considered system. For the systems originally targeted, i.e. gapped local 1d Hamiltonians, it turns out that there is always a finite dimensional reduced Hilbert space to represent the ground state [VC06, Sch11]. This is explained through the connection between the entanglement entropy $S_{A|B}$ of the partitions

$$S_{A|B} = -\operatorname{tr}\left(\hat{\rho}\ln\hat{\rho}\right) = -\sum_{a}\lambda_a \ln\lambda_a \tag{2.6}$$

and the decay of the eigenvalues of the RDM $\hat{\rho}$. If one would seek arbitrary states, the situation would be hopeless. However, ground states (and other low energy states) usually obey an area law. This means that instead of scaling extensively (as the entropy usually does), their entanglement entropy scales with the surface area involved in the bipartition. Since 1d systems have areas of constant size, this explains the success of the approach. This restricts the Hilbert space under consideration to a "corner" of the full one (strictly speaking a subspace), giving a physical reason for the feasibility of the algorithm. After all we are not probing the entire space, we merely ask questions which can be answered.

However, for generic two-dimensional systems, as well as systems with no notion of dimensionality, e.g. molecules in orbital space, no such guarantee exists. Even though there are occasional higher dimensional systems which obey area law-like rules [PEDC05, CEP07] and also cases in which one is able to find a satisfying solution by making use of brute force allocation of computational resources [HSML21, SW12], often the approaches are not fruitful and additional efforts are necessary in order to capture the correct physics of these systems [LS03, BLMR11]. It must be mentioned that some natural extensions of the 1d ansatz do exist, which seem quite promising at the moment, particularly the adaption of the tensor network topology, one of which is going to be the subject of the upcoming chapter 3. Ultimately, much of the efforts in this thesis were directed toward such questions. Given there is no strict limit on the representability of the quantum system, can we still find an approximate representation that will do the job? In the course of this work, we shall explore in which cases it was possible and in which it was not, and if so why.

We are returning to our original algorithm for a second, as in recent years a more clear representation of the DMRG procedure has emerged. Basically, the argument dates back to [OR95], albeit in this work the approach is in the infinite system DMRG framework. Upon noticing that the block growing procedure, i.e. its action on the basis states

$$|a'\rangle_{A\bullet} = \sum_{an_i} M^{n_i}_{a'a}\,|a\rangle_A\,|n_i\rangle_\bullet \tag{2.7}$$

during DMRG could be exploited, they proposed to use this as a variational ansatz, the so called MPS. To phrase it differently, one can look at the coefficients $M^{n_i}_{a'a}$ as maps taking the individual Hilbert spaces to a joint one and in this context DMRG is the way to find the optimal projector, given fixed accuracy [OR95]. When reaching the fixed point of a homogenous system, the M matrices could be used to construct the entire state. This motivated to propose the same ansatz as a framework for a variational optimization of the (rank 3) tensors M in finite system size DMRG [DMDNS98]. Starting from a block consisting of a single site, one can obtain the full MPS

$$|\psi\rangle = \sum_{n_1\ldots n_L} M^{n_1}\cdot\ldots\cdot M^{n_L}\,|n_1\ldots n_L\rangle \tag{2.8}$$

by recursive construction. The dimensionality of this matrices is a central control parameter called the bond dimension m. This makes an MPS basically just an ansatz class for many-body wave functions involving a large number of free parameters. By variational optimization of these parameters, in order to minimize the energy expectation value, one can find a low energy eigenstate which usually turns out to be the ground state. In this process the compression according to the RDM criterion gets replaced by a truncation making use of the singular value decomposition (SVD), a numerical procedure scaling cubic and being equivalent to the former [Sch05]. The central connection here can be made between the eigenvalues of the RDM and the singular values of the decomposition

$$M^{n_i} = U\cdot\begin{bmatrix} s_1 & & & \\ & s_2 & & \\ & & \ddots & \\ & & & s_r \end{bmatrix}\cdot V^\dagger\,, \qquad \lambda_a = s_a^2\,, \tag{2.9}$$

where U and V are unitary. There are a few subtle differences regarding the equivalence of DMRG and MPS variational optimization which the interested reader can find in [Sch11].

It should be mentioned that MPS were not originally developed in the DMRG context but were known to different mathematical and physical communities beforehand. A particularly clean overview of the historic (re-)discoveries of the MPS ansatz class in different contexts can be found in [Pae20].

Another decent nice way to interpret the MPS ansatz is as a controlled tuning between the HF method and ED which we both described in chapter 1. The ED wave function corresponds to exponentially many Slater determinants, summend up with the correct coefficients. However, in the HF method one usually stays with one determinant/permanent and optimizes within the space of single particle orbitals to obtain a good result. Translating this to the MPS language a state with bond dimension $m = 1$ corresponds to a single determinant state

$$|\psi\rangle = \sum_{n_1 \ldots n_L} c_{n_1} \ldots c_{n_L} |n_1 \ldots n_L\rangle \qquad c_{n_i} \in \mathbb{C} \,, \tag{2.10}$$

while the bond dimension of $m \leq d^L$ is the ED solution in eq. (1.9). Note that one usually choses the orbitals on which is operated beforehand in the DMRG procedure.

Coming originally from quantum information theory, a particularly useful notation found its entry to the tensor networks community [Pen71]. As can be seen in fig. 2.2 one represents each tensor with a node having as many legs as its rank. Connected lines indicate tensor-tensor contraction. By doing so, one can write down complicated contractions and tensor operations by drawing nodes and connecting them with lines. As we shall see, this is going to prove useful and even gives us intuition when extending to more general tensor networks. A few comments are needed about the representation of operators in terms of tensor networks. It seems evident that without a feasible way to construct operators, a good representation of the state is almost worthless. We postpone the way to find the representation of an arbitrary operator $\hat{H}$ to a later point in time, and for now simply observe the fact that any operator can be written as

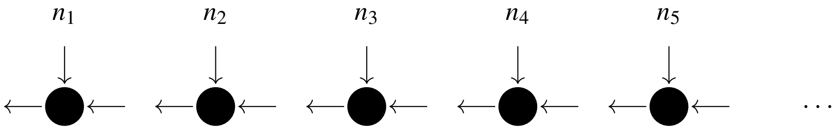

Figure 2.2: Diagrammatic representation of an MPS. The arrows indicate the flow of quantum numbers, therefore guaranteeing their conservation.

$$\hat{H} = \sum_{\substack{n_1 \ldots n_L \\ n'_1 \ldots n'_L}} w_{n'_1 n_1, \ldots, n'_L n_L} |n'_1 \ldots n'_L\rangle \langle n_1 \ldots n_L| \ . \tag{2.11}$$

Now we make use of the fact that the joint local Hilbert spaces can form a d^2 dimensional Hilbert space by tensoring $n'_i \otimes n_i = k_i$. This is a manifestation of the fact that there exists an isomorphism between the operators on a Hilbert space and the states of a twice as large Hilbert space. The corresponding mapping of the bijection yields

$$\hat{H} = \sum_{k_1 \ldots k_L} w_{k_1 \ldots k_L} |k_1 \ldots k_L\rangle = \sum_{k_1 \ldots k_L} W^{k_1} \cdot \ldots \cdot W^{k_L} |k_1 \ldots k_L\rangle \ , \tag{2.12}$$

where we used the MPS representation of an arbitrary state. Now we can just return to the operator in the original space by writing

$$\hat{H} = \sum_{\substack{n_1 \ldots n_L \\ n'_1 \ldots n'_L}} W^{k_1} \cdot \ldots \cdot W^{k_L} |n'_1 \ldots n'_L\rangle \langle n_1 \ldots n_L| \ . \tag{2.13}$$

This is the so called matrix product operator (MPO) form of the operator $\hat{H}$ and is displayed in fig. 2.3.

Albeit all the interesting physical phenomena 1d systems might exhibit, strongly correlated physics barely restricts to these types of systems. For higher dimensions one can usually count on mean-field-like approaches, since quantum fluctuations are typically weaker compared to 1d [SW12]. However, a current frontier of condensed matter physics involves two-dimensional (2d) systems for instance. Here, correlation effects can get into play while

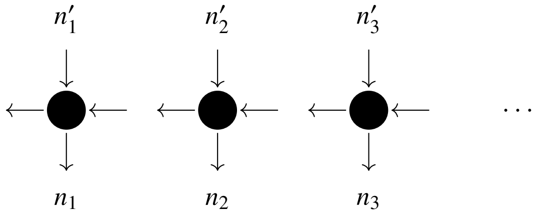

Figure 2.3: Diagrammatic representation of an MPO.

also a richer geometry is present. Strongly correlated molecules where the orbital structure obeys no notion of dimensionality at all are also of much interest as well. Last but not least, multi-orbital impurity models with non-local interactions should be mentioned, albeit living on 1d geometry not being necessarily optimally represented. All these models share the problem that the scaling of the entanglement entropy bounding our bond dimension m is not well controlled. For 2d systems, the necessary bond dimension to capture the correct physics typically scales exponentially in one of the dimensions, whereas it is well controlled in the other [Sch11]. For the other examples, it depends strongly on the choice of orbitals and their ordering on the 1d chain.

Even though a lot of progress was made mapping these types of systems to MPSes [Whi96, WM99, DMS12, QCS$^+$20] the question arises if one can change the topology of the tensor network in such a way that it resembles the physical nature of the system. There are a variety of topologies present, each tailored to a special class of system. To be mentioned are, e.g., the projected entangled pair state (PEPS) structures which resemble the actual geometry of a 2d system by introducing rank 5 tensors out of which the state consists [VC04, VWPGC06]. Unfortunately, operations on PEPS networks are not as well behaved as on the MPS structure and many operations become exponential or even worse when performed exactly [SWVC07]. Additionally complicating is the fact that PEPS networks contain so called loops, i.e. there is more than one way to connect two nodes. As we shall see, loop-free networks obey highly important properties, making calculations more stable and efficient. Nevertheless, there are strong schemes to target these difficulties in PEPS and this direction in tensor networks, more precisely their generalization to infinite PEPS is a very promising area of open research.

Another topology extending the MPS ansatz but remaining loop free is the so called tree tensor network state (TTNS), whose special case – the binary tensor tree (BTT) – is displayed in fig. 2.4. The fundamental idea of a TTNS is to drop the strictly planar geometry of MPS while still insisting on the loop freeness of the network [SDV06, MVLN10]. This is achieved by opening the number of virtual bonds (meaning all bonds which

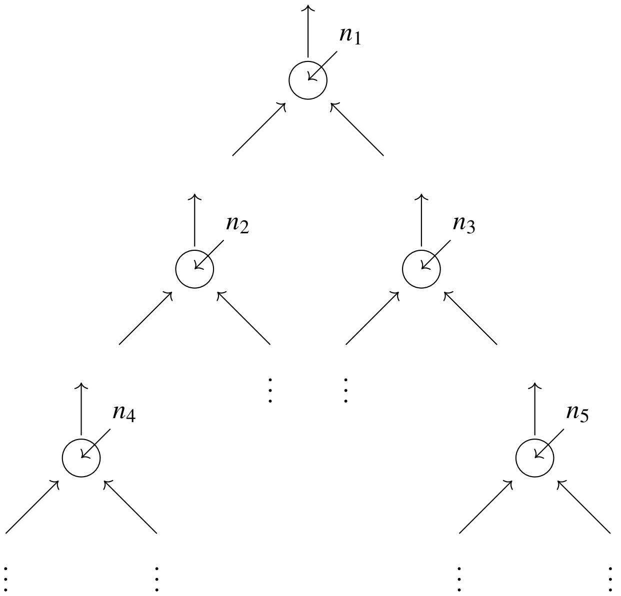

Figure 2.4: Structure of BTT, i.e. a special TTNS with coordination number three.

do not belong to a physical quantum number n_i) to be more than one in one direction. The other direction strictly keeps one virtual bond, i.e. every tensor in the network has exactly one root leg but may have arbitrary virtual descendant legs. Therefore, the BTT is a TTNS with two descendant legs. The pictographical representation in fig. 2.4 formalizes to

$$|\psi\rangle = \sum_{\substack{n_1 \dots n_L \\ \{a_i b_i\}}} M^{n_1}_{a_0 a_1 b_1} M^{n_2}_{a_1 a_2 b_2} M^{n_3}_{b_1 a_3 b_3} \cdots |n_1 \dots n_L\rangle = \sum_{n_1 \dots n_L} M^{n_1} \odot M^{n_2} \odot \cdots \odot M^{n_L} |n_1 \dots n_L\rangle \ . \tag{2.14}$$

It should be noted that we denoted matrix multiplication in the MPS case by $\cdot$ while in the TTNS case we write $\odot$ which means contraction over all common indices. The total number of virtual bonds is called the coordination number. As one easily observes, this leaves only one path to connect any two nodes, namely by determining the last site both nodes have as a common ancestor. Since each node in the tree has only one root, there is only one path to get to this common ancestor. Connecting these two paths leaves us with the path connecting any two nodes. If one of the nodes happens to be an ancestor of the other the situation is even easier.

One of the main advantages of this topology strikes immediately, namely that the construction resembles a higher dimensionality than a 1d system, even though it is itself not 2d. This can be used to shape the cluster of lattice sites in multiple ways. Usually, one tries to create subtrees of strongly correlated sites and stack these orbitals near to each other. These subtrees are then placed somewhere low in the tree (compare fig. 2.4 for up and down areas of the tree) connected by tensors above which need to be in contact with all sites. During the decimation processes of DMRG, a significant advantage can be achieved this way, in that artificial correlation through suboptimal clustering of orbitals can be suppressed. As one would expect this can be exploited excellently in the context of chemical molecules [NC13, MVS+15, WVN14a]. Usually, these applications have a global coupling between the orbitals. However, groups of orbitals may be strongly involved amongst each other while only weakly correlated to other groups of orbitals, for instance due to molecular symmetries or screening effects. Hence, it makes sense to place the orbitals, which are correlated to all other orbitals, on top and cluster the remaining ones in a hand-picked way at the bottom. It should be mentioned that the TTNS geometry is also known in other communities in different contexts, e.g. among the chemists, it is often used in the context of the multi-configurational time-dependent Hartree (MCTDH) method [MMC90, Man08]. However, the fundamental difference between MCTDH and the tensor network methods described here is that MCTDH uses a first quantized wave function. Therefore, a number of subtleties arises between the different methods making them difficult to compare and often more useful or less useful to a certain system of choice.

Of course also condensed matter systems find an application on TTNS [MVLN10, GRS+17]. For instance, one can create long MPS subchains which obey the same advantageous scaling as a pure linear geometry while connecting one of the edges of these via a rank 4 tree tensor to other MPS chains. In cases in which the rows of the system are only weakly entangled this creates a more local connection improving the number of basis states necessary to display the state faithfully. This also works in a dynamical mean-field theory (DMFT)-like context where we need to connect different baths and impurities, however interaction among the baths is usually negligible. It shall be mentioned that many other possible mappings exist which can substantially improve the amount of computational effort needed.

Finally, an important advantage of TTNS lies in the fact that tensor networks with coordination number $z > 2$ are able to capture algebraically decaying correlations, while a pure MPS (with $z = 2$) can only display exponentially decaying ones for finite bond dimensions [MVLN10, WVN14a]. This statement is derived from the fact that overlaps and expectation values of $|\psi\rangle$ (as shall also be discussed in sections 3.3.1 and 3.3.5) can be constructed via recursive contraction of system parts for loop-free networks [Sch11]. This recursive construction is in fact linear and can therefore be displayed via a matrix-multiplication with matrices of dimension m^2. From this, the general statement can be derived that in the thermodynamic limit any correlator $C(i-j) = \langle\psi|O_i O_j|\psi\rangle$, computed from this kind of state, will take the form

$$C(i-j) = c_1 + \sum_{a=2}^{m^2} c_k e^{-|i-j|/\xi_k} \ . \tag{2.15}$$

Here, the coefficients and the decay length ξ_k depend on the linear map for the recursive construction and its eigensystem. The important point is that an MPS is always displaying the correlator as linear sum of exponentially decaying function, since $|i-j|$ just grows linearly in system size. From the TTNS however the situation is quite different, as one can estimate the largest possible distance

$$L = 1 + z \sum_{k}^{Y} (z-1)^{k-1} = \frac{z(z-1)^{Y} - 2}{z-2} \tag{2.16}$$

exponentially growing with the number of layers Y in the hierarchy of fig. 2.4 [SDV06, GVW+18]. This implies a logarithmic scaling of $Y \sim \ln L$ and therefore an algebraic representation in eq. (2.15).

Summarizing this briefly, we found a variational ansatz for quantum many-body wavefunctions optimal for a given amount of resources, originating from the idea of real space decimating quantum systems, in order to obtain the physically relevant degrees of freedom. We did not discuss algorithmic details which shall be presented in the following chapters. Possible extensions of topology were discussed and we became acquainted with the main frameworks of this work, namely the MPS and TTNS. These are going to prove extremely powerful and flexible in the study of low-dimensional quantum systems in the strong correlation regime. However, they tend to come with some caveats which we have to resolve before being able to continue and exploit the full power of these computational methods.

Tree-tensor networks

3

As we have seen, TTNS not only enable us to structure a system on a tensor network more efficiently, they are even able to represent observables correctly with finite bond dimension, where MPS fails. They do so by fundamentally changing the paradigm of planar topology to obtain a structure of clustered sub-trees, while still upholding the loop freeness of the network. However TTNS come, like other tensor network topologies, with a fundamental problem. This is related to the variational optimization (which is at the heart of the most important ground-state and time-evolution schemes, the DMRG and the time-dependent variational principle (TDVP)). For these types of algorithms it is (as we shall see in section 3.3.6) necessary to apply an operator to a state locally, i.e. perform the operation depicted in fig. 3.1. However, variational applications tend to get stuck, when only performed on a single orbital [Sch11, HMSW15, PKS+19]. Usually one avoids this by contracting the tensors corresponding to two orbitals together and performing the algorithms on this joint Hilbert space. This is indicated in fig. 3.1 by the fact, that the physical indices are double arrows, i.e. their dimension can be either d or d^2 and that the number of nodes to the right (also called leaves) is not fixed explicitly. In the course of this work we will fix the topology to be a BTT (i.e. the coordination number being $z = 3$). Therefore single orbital update schemes have an effective $z = 3$, while two site schemes have $z = 4$. As is easily verified [Sch11, PKS+19, GVW+18] the computational cost for this algorithm scales as the $\mathrm{O}\left(m^{z+1} d_{\text{eff}}\right)$. This is problematic since the algorithm gets more and more expensive with increasing number of participating orbitals. For the MPS case, this was not a severe problem, since forming joint Hilbert space between neighbouring orbitals only raised d_{eff} but not the coordination number z. This motivates the three-legged tree tensor network state (T3NS), which we will now discuss.

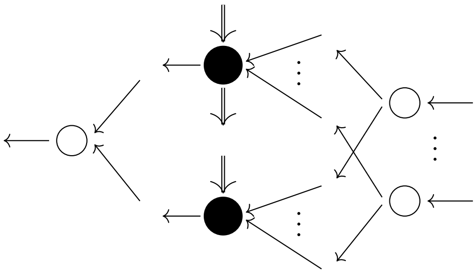

Figure 3.1: Application of an operator to a TTNS. Note that black tensors belong to the tensor network, while white nodes are merging tensors. Note that there is a number of not explicitly defined descendant nodes (also sometimes called leaves).

Three-legged tree tensor network state

3.1

The T3NS [GVW+18] essentially tries to combine the best of both worlds, the pleasant scaling of the MPS during variational optimization and the topological advantages of the BTT. It does so by proposing the following structure:

Rank 3 tensors parametrize the physical degrees of freedom in the single particle orbitals, these we call physical nodes. They are connected with other physical nodes either directly (as in the MPS case) or via so called branching nodes. Branching nodes are rank three BTT-like nodes M_{rab}, which do not carry a physical index. This structure can be seen in fig. 3.2. Here we have MPS subchains, which are connected via branching nodes in the middle of the chain, and do not introduce additional cost, i.e. their optimization scales with $\mathrm{O}\left(m^3 d_{\text{eff}}\right)$. Single site optimization of branching nodes scales with $\mathrm{O}\left(m^4\right)$, i.e. instead of the effective local Hilbert space size we have a factor of m more. For typical applications $d_{\text{eff}} \ll m$, therefore branching nodes are expensive to optimize and need to be placed with care. The two-site optimization scheme's numerical cost is $\mathrm{O}\left(m^4 d_{\text{eff}}\right)$. Note that this scaling is true

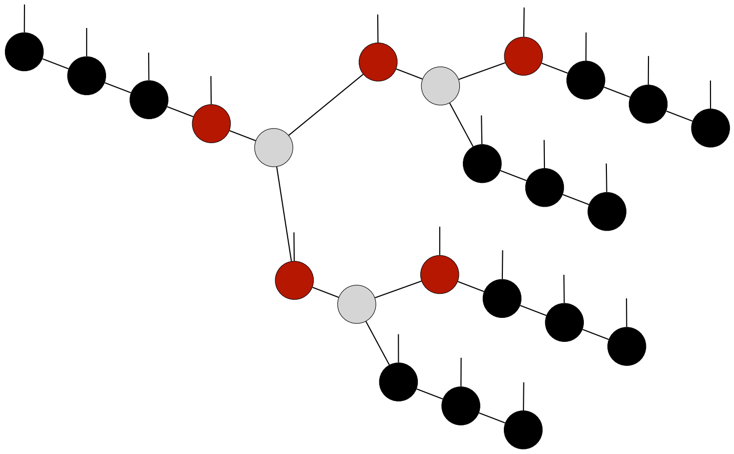

Figure 3.2: Structure of a T3NS. Black and red sites are physical, while grey ones are branching nodes.

for both, two physical orbitals involved, as well as a simple physical-branching construction. The only difference is the increase in the effective local Hilbert space dimension. It should be noted that each additional physical orbital involved into the optimization will increase the effective coordination number by one, thus resulting in a larger scaling with a factor of md, effectively staying one factor of m below the result of the BTT structure. However, usually these many orbital optimizations are very expensive in central processing unit (CPU) time, and given marginal improvements in the accuracy, are not worth the effort [GVW$^+$18].

Having described the new tensor network structure, we would like to demonstrate the most common operations necessary for computations. Before doing such, it is appropriate to introduce a framework in order to deal with fermionic Hilbert spaces.

Fermionic Hilbert spaces 3.2

Up until now we have avoided dealing with the nature of the basis states $|n_1 \dots n_L\rangle$ of the N-particle Hilbert space. Usually, one defines a many body basis set by the number of particles occupying (previously fixed) single particle orbitals. In order to do so, we have to define a vacuum state $|0\rangle$, containing no particles, and some operators $\hat{c}^\dagger$ and $\hat{c}$ which create or annihilate particles in these single particle orbitals [BPE09], respectively. Usually these operators obey some algebra and the annihilator destroys the vacuum, i.e.

$$\left[\hat{c}_i^{(\dagger)}, \hat{c}_j^{(\dagger)}\right]_\mp = 0\,, \tag{3.1}$$

$$\left[\hat{c}_i, \hat{c}_j^\dagger\right]_\mp = \delta_{ij}\,, \tag{3.2}$$

$$\hat{c}_i\,|0\rangle = \hat{c}_i\,|0_1\rangle \dots |0_L\rangle = 0\,. \tag{3.3}$$

We indicate the statistics of the particles involved through the subscript, telling us to use the commutator or the anti-commutator. However, we did suppress through the notation that the bookkeeping counting the number of excitations in single particle orbitals is defined with respect to some reference ordering of the orbitals $\mathfrak{n}$. If we wanted to be completely accurate we should indicate this ordering, e.g. by the subscript

$$|n_1 \dots n_L\rangle_{\mathfrak{n}} = \hat{c}_{\mathfrak{n}_1}^{\dagger n_1} \dots \hat{c}_{\mathfrak{n}_L}^{\dagger n_L}\,|0\rangle\;. \tag{3.4}$$

Of course, this is an issue completely related to bookkeeping and does not influence the physical quantities anyhow. With this definition we can represent any tensor $\hat{T}$ as [BPE09]

$$\bar{T} = \sum_{\vec{n}\vec{m}} {}_{\mathfrak{n}}\langle\vec{n}|\hat{T}|\vec{m}\rangle_{\mathfrak{m}} |\vec{n})(\vec{m}|\,, \tag{3.5}$$

i.e. its numerical representation, indicated by a bar over the symbol. We introduced the fixed numerical bases $|\vec{n}\rangle$, which are defined with respect to some ordering $\mathfrak{n}$ and later on are the basis for the implementation on a computer. Furthermore, we obtain the coefficients of the tensor ${}_{\mathfrak{n}}\langle\vec{n}|T|\vec{m}\rangle_{\mathfrak{m}}$ for this ordering, which is the data stored in memory. If we want to display the same tensor with a different ordering of otherwise equal orbitals we can use the relation between creation operators eq. (3.1) and write

$$|n_1 \dots n_j n_{j+1} \dots n_L\rangle_{\mathfrak{n}} = (\pm 1)^{\hat{n}_j \hat{n}_{j+1}} |n_1 \dots n_{j+1} n_j \dots n_L\rangle_{\mathfrak{n}} = (\pm 1)^{\hat{n}_j \hat{n}_{j+1}} |n_1 \dots n_j n_{j+1} \dots n_L\rangle_{\mathfrak{n}'} \ , \tag{3.6}$$

where again we have different signs for different exchange statistics [BPE09, BWHV17]. Note that Hilbert spaces spanned by the application of bosonic operators do not care about the ordering of orbitals, while fermionic ones do.

Jordan-Wigner transformation 3.2.1

The first strategy in order to handle the fermionic character of a tensor network is to map it to a strictly bosonic basis. This can be done by means of a Jordan-Wigner transformation [JW28]. We are going to demonstrate this for the creation operator, however all calculations for the annihilation operator are analogous. Assuming we have a bosonic Hilbert space consisting of L single particle orbitals. The global operator putting a particle into orbital i can be defined as

$$\hat{c}_i^\dagger = \hat{1}_1 \otimes \dots \otimes \hat{1}_{i-1} \otimes \hat{a}_i^\dagger \otimes \hat{1}_{i+1} \otimes \dots \otimes \hat{1}_L \ , \tag{3.7}$$

where we introduced a local single-site operator (SSO) matrix $\hat{a}^\dagger$. This operator acts solely on the desired orbital and all other ones are transformed under an identity SSO $\hat{1}$. Applying another global creator, it will not differ what is applied first, since the creator SSOs commute among each other and every one commutes with the identity. This is just the behaviour we expect bosonic operators to show. However, for fermions we expect the multiplication to respect the anti-commutation defined in eq. (3.1). Therefore we need to introduce the phase factor

$$\begin{aligned} \hat{c}_i^\dagger \to \exp\left(\mathrm{i}\pi \sum_{j=1}^{i-1} \hat{n}_j\right) \hat{c}_i^\dagger &= \prod_{j=1}^{i-1} \mathrm{e}^{\mathrm{i}\pi\hat{n}_j} \hat{c}_i^\dagger = \prod_{j=1}^{i-1} \left(\hat{1}_j + \hat{n}_j \left(\sum_{k=0}^{\infty} \frac{(\mathrm{i}\pi)^k}{k!} - 1\right)\right) \hat{c}_i^\dagger = \prod_{j=1}^{i-1} \left(\hat{1}_j - 2\hat{n}_j\right) \hat{c}_i^\dagger \\ &= \prod_{j=1}^{i-1} \hat{P}_j \hat{c}_i^\dagger = \hat{P}_1 \otimes \dots \otimes \hat{P}_{i-1} \otimes \hat{a}_i^\dagger \otimes \hat{1}_{i+1} \otimes \dots \otimes \hat{1}_L \ , \end{aligned} \tag{3.8}$$

where we defined the parity operator, which has the entry ±1 when the site is unoccupied/occupied, given by the fermionic occupation number being either zero or one. As one can easily check, by just plugging in the definitions into the anti-commutator and using the known commutation relations of the creators with the occupation number operator, these operators now fulfil the desired algebra eqs. (3.1) and (3.2).

The change in the operator structure is now twofold. First we chose one side of the system which is equipped with parities. This is a resemblance of the fact that we introduced an artificial ordering of modes. For a strictly 1d system this might seem trivial, since the system is planar and therefore each site is either to the left or to the right of another site. However this gets more involved when changing to non-planar topologies like a TTNS. There, this contradicts the locality of the original ansatz, e.g. one has to count from top to bottom left and then to bottom right. Furthermore the operators do not change only one orbital anymore, but all the orbitals to one side of the active site (one should keep in mind that the term site refers to an artificial ordering for any non-MPS-like topology).

For a strictly planar system this is worth the effort. By introducing this transformation, which does not change the Hilbert space but is just a phase factor, we are able to avoid dealing with the exchange statistics. In practice one only has to adjust operators, not the wavefunction which is also an implementation advantage. Since most operators are constructed via usage of these elementary operators, no additional runtime is introduced [HMS17]. The devil is, however, in the detail here, namely in the planar topology of the system. Planar means that any contraction of the tensor network can be performed without two legs having to cross. For an MPS this is always possible (as we shall see in sections 3.2.2 and 3.3) but a tree topology needs further carefulness. There, one needs to introduce so called swap-gates, which multiply two legs with a corresponding phase factor when they cross, e.g. during a contraction [COBV10]. This gets very unhandy and complicated very fast, since each operation has to be checked for its correctness and one missing swap-gate can make an entire chain of results go wrong. Also, this breaks the encapsulation of code, i.e. low level tensor operations have to be implemented at many high level instances of operations. This makes the framework which we will introduce next especially useful for the implementation and bookkeeping of tensor networks going beyond MPS.

Explicit bookkeeping 3.2.2

The basic idea of the explicit bookkeeping is defining a framework which, even though working on the numerical basis $\{|\vec{n})\}$, keeps track of the exchanges in order. It accounts for them by multiplying the coefficients with the corresponding phase factors. The usual operator to swap the ordering of two neighboring modes in the numerical basis is given by matrix multiplication with [BK02, BPE09]

$$|0,0)(0,0| + |0,1)(1,0| + |1,0)(0,1| - |1,1)(1,1| \ . \tag{3.9}$$

Note that a minus sign is only introduced when both orbitals are occupied, which differs from the usual definition of the term swap-gate. Since any permutation of modes can be displayed as successive permutation of neighboring modes until the desired order is reached, a reordering between non-neighboring modes changes the matrix elements of the computational basis as [BPE09]

$$(\vec{u}\vec{x}\vec{v}\vec{z}|\bar{B}'|\vec{m}) = (-1)^{|x||v|}(\vec{u}\vec{v}\vec{x}\vec{z}|\bar{B}|\vec{m}) \ , \tag{3.10}$$

i.e. we need to introduce a phase factor, depending on the number of occupied modes in $\vec{x}$ and $\vec{v}$, which we called $|x|$ and $|v|$. The same logic holds true when contracting two fermionic tensors $\hat{A}$ and $\hat{B}$ in the numerical representation

$$\begin{aligned} \hat{A} &= \sum_{\vec{n}\vec{p}\vec{m}} (\vec{n}\vec{p}|A|\vec{m})\, |\vec{n}\vec{p}\rangle\, \langle\vec{m}| \\ \hat{B} &= \sum_{\vec{k}\vec{q}\vec{n}'} (\vec{k}|B|\vec{n}'\vec{q})\, |\vec{k}\rangle\, \langle\vec{n}'\vec{q}| \ . \end{aligned} \tag{3.11}$$

We desire the contraction in Fock-space $\hat{C} = \hat{B} \circ_n \hat{A}$ given in components by [BPE09]

$$(\vec{k}\vec{p}|C|\vec{m}\vec{p}) = \sum_{\vec{n}} (-1)^{|p||q|}(\vec{k}|B|\vec{n}\vec{q})(\vec{n}\vec{p}|A|\vec{m}) \ . \tag{3.12}$$

The parity prefactor comes from the expansion of eq. (3.11) and permuting according to eq. (3.6). This rule tells us that we can just contract tensors in the numerical basis as if they were bosonic, we just have to pick up the correct parity when contracting legs which are not next to each other. Together with the rule for partial traces [BPE09], i.e.

$$\mathrm{tr}_r\, \hat{A} = \sum_{\vec{n}\vec{m}\vec{r}} (\vec{n}\vec{r}|\hat{A}|\vec{m}\vec{r})\, |\vec{n}\rangle\, \langle\vec{m}| \ , \tag{3.13}$$

we can write the rule for arbitrary contractions in the numerical basis

$$\hat{C} = \mathrm{tr}_r \left(\hat{B} \circ_n \hat{A}\right) = \sum_{\vec{m}\vec{q}\vec{k}\vec{p}\vec{n}\vec{r}} (-1)^{|p||q|+|r|(|p|+|q|)} (\vec{k}\vec{r}|B|\vec{n}\vec{q})(\vec{n}\vec{p}|A|\vec{m}\vec{r})\, |\vec{k}\vec{p}\rangle\, \langle\vec{m}\vec{q}| \ . \tag{3.14}$$

Equipped with this we are now able to define our fermionic tensor network framework, the rules we have to follow are:

1. Any tensor $\hat{T}$ can be expanded in a (somehow ordered) basis with respect to its components

   $$\hat{T} = \sum_{abcd} T^{\mathfrak{abcd}}_{abdc}\, |a\rangle_{\mathfrak{a}}\, |b\rangle_{\mathfrak{b}}\, |c\rangle_{\mathfrak{c}}\, {}_{\mathfrak{d}}\langle d| \ . \tag{3.15}$$

   Here, a, b, c and d are some sets of fermionic modes.

2. Tensor products form joint Hilbert spaces, i.e.

   $$|abc\rangle = |a\rangle\, |b\rangle\, |c\rangle \ , \ \langle abc| = \langle a|\, \langle b|\, \langle c| \ . \tag{3.16}$$

3. Permuting any number of modes gives a definite parity prefactor $P_x = (-1)^{|x|} = \pm 1$, which can be successively computed by permuting single modes. The notation $|x|$ refers to a set of occupied modes of the tensor $\hat{T}$, i.e. an index of the component.

4. Tensors in our framework always preserve quantum numbers due to global symmetries. Taking any product construction from two Hilbert spaces we can expand the new basis in terms of the old one

$$|\vec{m}\rangle_{\mathfrak{m}} = \sum_{\vec{n}\vec{k}} c_{\vec{n}\vec{k}} \, |\vec{n}\vec{k}\rangle_{\mathfrak{n}\oplus\mathfrak{k}} \ . \tag{3.17}$$

By making use of the total particle number $\hat{N}_{\vec{m}} = \hat{N}_{\vec{n}} \oplus \hat{N}_{\vec{k}}$ and its conservation we obtain

$$|m| \, |\vec{m}\rangle_{\mathfrak{m}} = (|n| + |k|) \, |\vec{n}\vec{k}\rangle_{\mathfrak{n}\oplus\mathfrak{k}} \ , \tag{3.18}$$

which implies $P_{|m|} = P_{|n|+|k|}$ or put differently

$$P_{|m|+|n|+|k|} = 1 \ . \tag{3.19}$$

From this rule it also immediately follows that any bipartition of legs has the same parity.

5. We continue working with bosonic tensors in the numerical basis

$$\bar{T} = \sum_{abcd} T_{abcd} |abc)(d| \tag{3.20}$$

with respect to some fixed ordering. Any reordering or contraction needs to be taken into account by the multiplication of the necessary parity into the coefficients. From here on, bosonic states are referred to with regular bra-ket notation. The information about the fermionic character is hidden implicitly in the coefficients. Furthermore, we will often make use of a convenient shorthand notation, when certain information is not necessary. We will introduce an Einstein-summation and suppress the tensor contents T_{abcd} when they are not needed, i.e. we write $T = |a\rangle \, |b\rangle \, |c\rangle \, \langle d|$ but mean what is written in eq. (3.20).

6. Equation (3.14) implies that a contraction between two fermionic tensors is not given by the sole contraction in the numerical basis, but rather by the contraction in the original Fock-space. This can be depicted in the numerical bosonic basis by permuting the respective legs next to each other (by making use of item 3) and then executing

$$\ldots \langle x| \circ_x |x\rangle \ldots \ . \tag{3.21}$$

   (a) We also introduce the sometimes useful definition of the supertrace $\mathrm{str}(\cdot)$. The supertrace is a reduction of legs by contraction, which is in contrast to the regular trace where the reduction takes place by taking overlaps with basis elements and summing over them. This corresponds to doing a second step like in eq. (3.12) instead of eq. (3.13) to obtain eq. (3.14). Therefore, the supertrace is not basis independent, but it differs from the true trace by a parity prefactor, i.e.

$$\mathrm{tr}_r(\cdot) = \mathrm{str}_r(P_r \cdot) \ . \tag{3.22}$$

   However, just like the true trace the super trace is cyclic due to item 4, as is easily verified.

7. Hermitian conjugation † reverses the tensor leg direction and ordering and complex-conjugates the coefficients of the tensor, i.e.

$$\left(T_{abcd} \, |a\rangle \, |b\rangle \, |c\rangle \, \langle d|\right)^\dagger = T^*_{abcd} \, |d\rangle \, \langle c| \, \langle b| \, \langle a| \ . \tag{3.23}$$

8. The overlap between two tensors A and B is defined as

$$\langle A|B\rangle = \mathrm{tr}_{b(B)} \left(A^\dagger \circ_{k(B)} B\right) = P_{b(B)} \, A^\dagger \circ B \ , \tag{3.24}$$

where we introduced the shorthard notation $k(B)$ and $b(B)$ for all kets and bras of B, respectively. Note that switching the contraction and the trace would be possible and will give the same result, because the only difference would be a parity of all kets instead of all bras. This number has to be the same according to items 3 and 4, since it is a bipartition. The norm of a tensor is then just given as $|A| = \sqrt{\langle A|A\rangle}$.

Before we continue to demonstrate common operations on a T3NS we have to fix one last definition, namely how we define our tensors. For practical reasons we defined the MPS and MPO tensors in our toolkit to look like

$$M = |l\rangle\,|p\rangle\,\langle r| \tag{3.25}$$

$$W = |l\rangle\,|p'\rangle\,\langle p|\,\langle r| \ , \tag{3.26}$$

respectively. l is the left or root index, while r is the right or descendant index, and p and p' are physical indices. For the branching nodes we defined the order

$$B = |r\rangle\,\langle b|\,\langle a| \tag{3.27}$$

for both, the state and operator tensors, where we introduced the root leg r and the descendants a and b. By choosing the network constituents like this, contractions between neighboring tensors in the network are possible without introduction of additional signs. Furthermore, the physical legs of the state are kets, which is also desirable since wave functions usually do not live in a dual space. The highest node in the tree (which is uniquely defined due to the absence of loops) will carry the quantum number sector of the total Hilbert space on its left or root leg.

Operations 3.3

Norms and overlaps 3.3.1

The most basic operation is to compute the norm of a T3NS or the overlap between two such states. Given no branching nodes we can define two states

$$\begin{aligned} |\psi\rangle &= a_1\,|0p_1\rangle\,\langle 1| \circ_1 a_2\,|1p_2\rangle\,\langle 2| \ , \\ |\phi\rangle &= a'_1\,|0'p'_1\rangle\,\langle 1'| \circ_{1'} a'_2\,|1'p'_2\rangle\,\langle 2'| \end{aligned} \tag{3.28}$$

where the a_i are the coefficients of the MPS. The overlap is then defined as

$$\begin{aligned} \langle\phi|\psi\rangle &= \mathrm{tr}_2\left(\phi^\dagger \circ_{p_i\leftrightarrow p_i,0\leftrightarrow 0'} \psi\right) \ . \\ &= P_2\, a'^*_1 a'^*_2 a_1 a_2\,|2\rangle\,\langle p_2 1| \circ |1\rangle\,\langle p_1 0| \circ |0p_1\rangle\,\langle 1| \circ |1p_2\rangle\,\langle 2| \\ &= P_2 a'^*_1 a'^*_2 a_1 a_2\,|2\rangle\,\langle p_2 1|\,|1\rangle\,\langle 1| \circ |1p_2\rangle\,\langle 2| \\ &= P_2 a'^*_1 a'^*_2 a_1 a_2\,|2\rangle\,\langle p_2|\,|p_2\rangle\,\langle 2| \\ &= P_2 a'^*_1 a'^*_2 a_1 a_2 (-1)^{|2|} = a'^*_1 a'^*_2 a_1 a_2 \ , \end{aligned} \tag{3.29}$$

just as we expected. Again we can define the norm as $||\,|\psi\rangle\,||_2 = \sqrt{\langle\psi|\psi\rangle}$.

For the T3NS the situation is a bit more complicated. Defining the state as

$$|\psi\rangle = |0p_1\rangle\,\langle 1| \circ |1\rangle\,\langle 32| \circ |2p_2\rangle\,\langle 2'| \circ |3p_3\rangle\,\langle 3'| \tag{3.30}$$

resembles the state in fig. 3.3. Wanting to compute the overlap we obtain

$$\begin{aligned} &\mathrm{tr}_{2'3'}\left[\,|3'\rangle\,\langle p_3 3|\,|2'\rangle\,\langle p_2 2|\,|23\rangle\,\langle 1|\,|1\rangle\,\langle p_1 0| \circ_{p_1 p_2 p_3 0} |0p_1\rangle\,\langle 1|\,|1\rangle\,\langle 32|\,|2p_2\rangle\,\langle 2'|\,|3p_3\rangle\,\langle 3'|\right] \\ &= P_{|2'||3'|}\left(|3'\rangle\,\langle p_3 3|\right)\left(|2'\rangle\,\langle p_2 2|\right)|23\rangle\,\langle 32|\left(|2p_2\rangle\,\langle 2'|\right)\left(|3p_3\rangle\,\langle 3'|\right) \\ &= P_{|2'||3'|}\,|23\rangle\,\langle 32|\,|2'\rangle\,\langle 2'|\,|3'\rangle\,\langle 3'| \\ &= |23\rangle\,\langle 32| = P_{|2||3|} \ . \end{aligned} \tag{3.31}$$

This is again just as we expected, since we can see in fig. 3.3 these two legs cross during the contraction, i.e. they need to be swapped via eq. (3.9). Also note that for the planar part of the diagram crossings now occur, which explains why the MPS does not need a sign introduced. Introducing other contraction orderings which result in different intermediate signs will in the end lead to the same overall sign, both for the MPS and the T3NS topology.

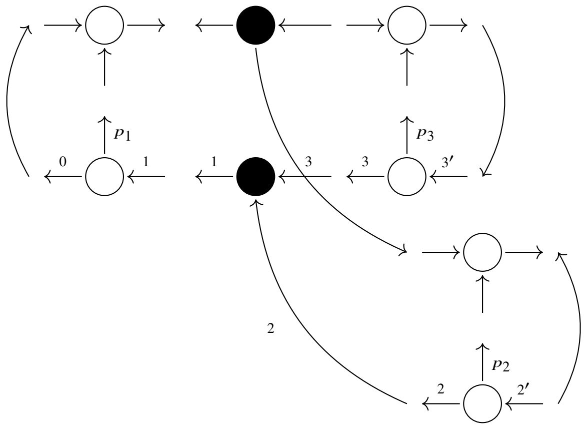

Figure 3.3: Overlap of two T3NSes.

Canonical normalization 3.3.2

The mindful reader might have asked themselves, if the ED- and the MPS representation are equivalent. This is closely related to the question if the MPS representation of a wave function is unique. To get a good understanding of this it is instructive to estimate the number of elements in both wave function representations. The ED tensor $c_{n_1 \ldots n_L}$ has maximally d^L degrees of freedom, while an MPS has

$$2 \sum_{i=1}^{L/2} d^{2i} = 2d^2 \, \frac{d^L - 1}{d^2 - 1} \,, \tag{3.32}$$

which is somewhat larger. It is to mention that the maximal bounds are rarely satisfied, e.g. due to symmetries making tensors sparse but also due to the fact that the MPS usually finds an optimal representation in a small subspace of the full Hilbert space. However, this mere theoretical argument for the worst-case scenario is useful to actually see that the representations can not be equivalent, since the MPS has more degrees of freedom. This is related to the gauge of a tensor network [Sch11], i.e. the fact that we can introduce an identity by means of an arbitrary invertible matrix $\hat{U}$ in between our MPSes, without changing our state

$$\hat{M}^{n_i} \cdot \hat{M}^{n_{i+1}} = \hat{M}^{n_i} \cdot \hat{U}^{-1} \cdot \hat{U} \cdot \hat{M}^{n_{i+1}} \,. \tag{3.33}$$

Note that this operation is planar and does not introduce any fermionic signs.

One usually exploits this fact by using a special one among the gauges, which is called the mixed canonical picture. This can always be employed as long as the tensor network does not have loops, i.e. there is only one way to connect two nodes [Sch11]. The basic principle is given by the observation that all matrices can be decomposed via an SVD

$$\hat{M} = M_{lpr} \left|l\right\rangle \left|p\right\rangle \left\langle r\right| = U_{lpx} \left|l\right\rangle \left|p\right\rangle \left\langle x\right| \circ_{x \leftrightarrow x'} S_{xx'} \left|x\right\rangle \left\langle x'\right| \circ_{x' \leftrightarrow x''} V_{x''r} \left|x''\right\rangle \left\langle r\right| \,, \tag{3.34}$$

where U and V are unitary matrices and S is diagonal in the so called singular values. Note that also here no sign needs to be introduced due to the planarity of the operation which is depicted in fig. 3.4a. Through successive application of the SVD, for the MPS in any direction and for the TTNS in root direction, and multiplication of the transfer tensor $\hat{S} \cdot \hat{V}$ into the direction of application one can obtain a state which consists entirely of normalized tensors, as is depicted in fig. 3.4b. The only remaining not normalized tensor is the one on the root node, where we can not shift the transfer tensor further. The advantage of this particular representation lies in the computation of overlaps with states like this. Since any operator besides the active side (in our case the root node) is an unitary matrix, a partial contraction with its complex conjugate will give

$$\left|l'\right\rangle \left\langle l\right| \circ U^*_{lpx} \left|x'\right\rangle \left\langle p\right| \left\langle l'\right| \circ U_{lpx} \left|l\right\rangle \left|p\right\rangle \left\langle x\right| = \left|x'\right\rangle \left\langle x\right| \tag{3.35}$$

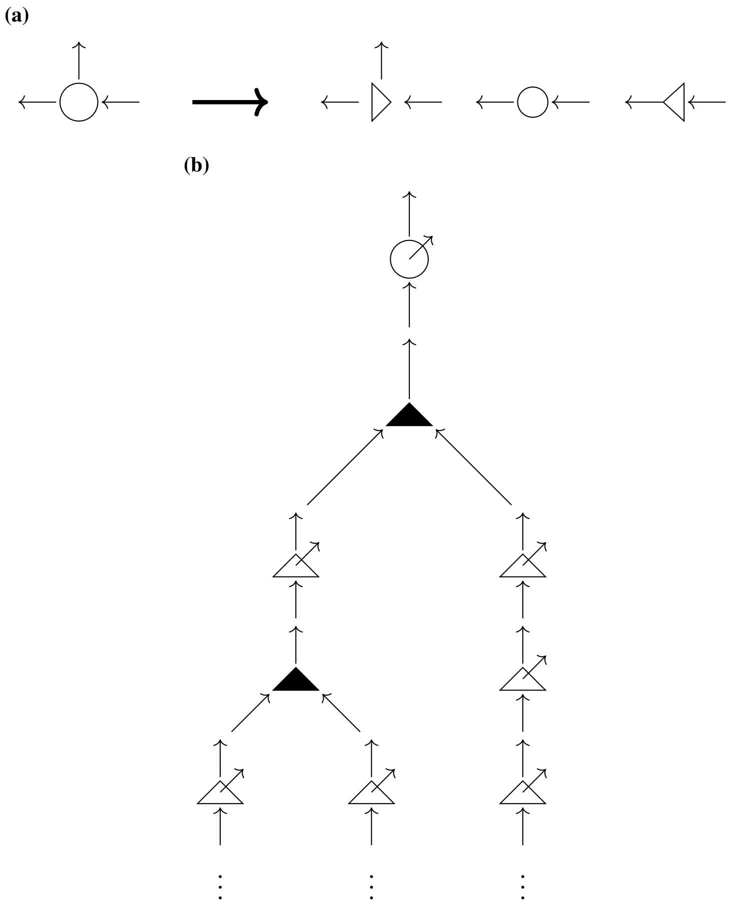

Figure 3.4: Normalization of tensors in order to create a canonical representation. Again black nodes are branching and white nodes are physical.

for a right-/root-normal MPS/TTNS or

$$P_{|r|}V^*_{xpr}\,|r'\rangle\,\langle p|\,\langle x'|\circ V_{xpr}\,|x\rangle\,|p\rangle\,\langle r|\circ|r\rangle\,\langle r'| = P_{|r|}P_{|p|}\,|x\rangle\,\langle x'| = P_{|x|}\,|x\rangle\,\langle x'| \tag{3.36}$$

for a left-normalized MPS or a TTNS normalized towards a certain node in the middle of the tree. Note that the parity P_r in the latter case comes from the definition of the trace in eq. (3.24). This “inheritance” of the parity factor for the index-direction over which is traced is typical for the entire framework and we will encounter it again for other operations. This holds true as long as the respective tensor content is correctly normalized. Therefore, any overlap can be computed by sole involvement of the active site, if both participating states are canonically normalized. We then simply write

$$\begin{aligned}\langle\phi|\psi\rangle &= \mathrm{tr}_r\left(\phi^*\psi\,|l'\rangle\,\langle l|\circ|r'\rangle\,\langle p|\,\langle l'|\circ|l\rangle\,|p\rangle\,\langle r|\circ P_{|r|}\,|r\rangle\,\langle r'|\right)\\ &= \phi^*\psi\ ,\end{aligned} \tag{3.37}$$

and analogously on a branching node, if necessary. This way we are not only able to compute overlaps without having to contract the entire network, sometimes it even helps speeding up expectation values. In particular when computing expectation values with operators which leave parts of the system invariant (i.e. act with identities on these orbitals) we can neglect them safely for the price of several SVDs. The easy computation of tensor network contractions is furthermore crucial at the heart of variational optimizations like the DMRG or the TDVP algorithm. The most time-consuming part of these types of algorithms is the application of the effective Hamiltonian (reduced to just one orbital) on the local MPS/T3NS state tensor. When the state is in a canonical form, the generalized eigenvalue problem of this effective Hamiltonian reduces to a regular eigenvalue problem due to the overlap matrix

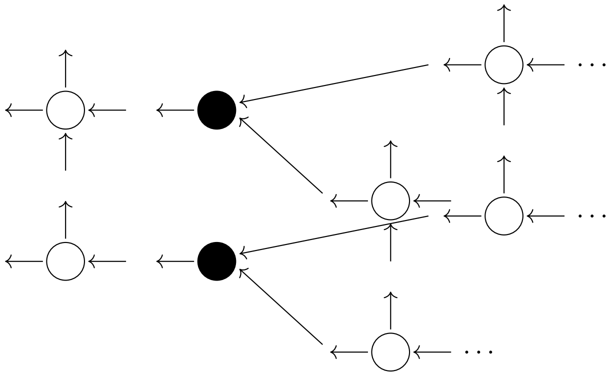

Figure 3.5: T3NO applied to a T3NS.

collapsing to an identity [Sch11]. Therefore, the algorithm does not only get more feasible but also substantially more numerically stable.

Finally, a discussion regarding normalization of a TTNS in analogy to the left-normalization of MPSes up to a certain node is in order. Given a node we can just root-normalize the entire tree and then follow the path from the root to the target node, always normalizing towards the path's direction. Physical nodes will show a similar structure as in a MPS, branching nodes will be pointing either towards the A-or the B-direction.

State-operator application 3.3.3

Another important operation which we often need to perform is the application of a three-legged tree tensor network operator (T3NO) to a T3NS. We define the application of the operator $\hat{H}$ to a state $|\psi\rangle$, resulting in a new state as

$$|H\psi\rangle = \hat{H} \circ_{\vec{n}} |\psi\rangle \ . \tag{3.38}$$

By the notation $\circ_{\vec{n}}$ we once intent to sum over all physical indices. Note however, that there is no trace this time for the ingoing legs at the ends of the network. Furthermore, the T3NO has the special property that its physical and branching nodes have different ranks. Therefore, the multiplication of the physical nodes is going to be regular while the branching nodes would need the involvement of an outer product. To avoid this we make use of the fact that we want the virtual legs to live on a joint Hilbert space and avoid the outer product by clever contraction. Through this we also save some orders in computation complexity. This contraction strategy is also called zip-up [Sch11], because one works on one node only and sweeps through the system. In case of a physical node the tensors have to be contracted like

$$\begin{aligned} |l'\rangle\, |p'\rangle\, \langle p|\, \langle r'| \circ_p |l\rangle\, |p\rangle\, \langle r| &= P_{|r'||p|}\ \ |l'\rangle\, |p'\rangle\, \langle r'|\, \langle p| \circ |l\rangle\, |p\rangle\, \langle r| \\ &= P_{|r'||p|}\ \ |l'l\rangle\, |p'\rangle\, \langle r'r| \ . \end{aligned} \tag{3.39}$$

By making use of the fuse-and split tensors, $|\tilde{l}\rangle\, \langle l'|\, \langle l|$ and $|r\rangle\, |r'\rangle\, \langle\tilde{r}|$, whose application is planar and does not introduce any signs we obtain

$$P_{|r'||p|}\ \ |\tilde{r}\rangle\, |p'\rangle\, \langle\tilde{r}| \ . \tag{3.40}$$

This is the new MPS tensor, however we introduced a parity factor of $P_{|r'||p|}$ which is exactly the Jordan-Wigner parity we would have gotten if we transformed the operators according to eq. (3.8). So the total block is multiplied with a minus sign if the orbital is occupied and an odd number of particles is residing on the right part of the system (remember our artificial ordering and the Einstein summation).

For applying an operator to a state on a branching node we similarly get

$$\begin{aligned} |r\rangle\, \langle b|\, \langle a| \circ |r'\rangle\, \langle b'|\, \langle a'| &= P_{|b||a'|}\, |r\rangle\, |r'\rangle\, \langle b'|\, \langle b|\, \langle a'|\, \langle a| \\ &= P_{|b||a'|}\, |\tilde{r}\rangle\, \langle\tilde{b}|\, \langle\tilde{a}| \ , \end{aligned} \tag{3.41}$$

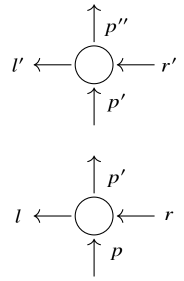

Figure 3.6: Multiplication of two T3NOs. The branching nodes are left away, since their contraction works the same for states and operators.

were the second step is again possible by introducing the respective fuses and splits. Once more, we observe the parity which is necessary for this contraction, however its nature is somewhat different. This is not due to the anti-commutation of physical degrees of freedom, like in the Jordan-Wigner case, it is rather caused by the right leg of the state and the left leg of the operator crossing during the contraction. Therefore, this parity actually would belong to the application of a fermionic swap gate, just as is the case in section 3.3.1.

Operator-operator application 3.3.4

Another largely significant operation, especially when it comes to construction of global Hamiltonians from local SSOs [HMS17], is the multiplication of two operators, i.e. $\hat{H} = \hat{A} \circ \hat{B}$. Since the branching nodes obey the same contraction rule (remember they are rank 3 tensors without physical indices) we shall only discuss details of the physical ones in this section. The contraction rule and parity prefactor is otherwise the same as in section 3.3.3. Following the nomenclature from fig. 3.6 we obtain

$$\begin{aligned} |l'\rangle |p''\rangle \langle p'| \langle r| \circ_{p'} |l\rangle |p'\rangle \langle p| \langle r| &= |l\rangle \Big(|l'\rangle |p''\rangle \langle p'| \langle r'| \Big) |p'\rangle \langle p| \langle r| \\ &= P_{|p'||r'|} |l\rangle \Big(|l'\rangle |p''\rangle \langle r'| \langle p'| \Big) |p'\rangle \langle p| \langle r| \\ &= P_{|p'||r'|} |l\rangle |l'\rangle |p''\rangle \langle r'| \langle p| \langle r| \\ &= P_{(|p'|+|p|)|r'|} |\tilde{l}\rangle |p''\rangle \langle p| \langle \tilde{r}| \ , \end{aligned} \tag{3.42}$$

by again introducing respective merges, i.e. $|\tilde{l}\rangle \langle l'| \langle l|$ and $|r\rangle |r'\rangle \langle \tilde{r}|$. Again, we introduced the same parity factor a Jordan-Wigner transformation would have needed. Therefore, we can safely say the operation does not involve any swap-gates, just as we expected for a planar operation.

Expectation values & block construction 3.3.5

Of course, having a wavefunction and operators is rather unpractical if one is not able to compute observables from it. Often one is interested in expectation values of states with certain operators or, speaking more generally, their overlap elements, i.e. $\langle \phi | \hat{H} | \psi \rangle$. We write our constituents as

$$|\psi\rangle = |0\rangle |p_1\rangle \langle 1| \circ \Big(\dots \Big) \circ |e_1 - 1\rangle |p_{e_1}\rangle \langle e_1| \circ |e_2 - 1\rangle |p_{e_2}\rangle \langle e_2| \circ \dots \tag{3.43}$$

$$\hat{H} = |\tilde{0}\rangle |p'_1\rangle \langle p_1| \langle \tilde{1}| \circ \Big(\dots \Big) \circ |\tilde{e}_1 - 1\rangle |p'_{e_1}\rangle \langle p_{e_1}| \langle \tilde{e}_1| \circ |\tilde{e}_2 - 1\rangle |p'_{e_2}\rangle \langle p_{e_2}| \langle \tilde{e}_2| \circ \dots \tag{3.44}$$

$$|\phi\rangle = |0'\rangle |p'_1\rangle \langle 1'| \circ \Big(\dots \Big) \circ |e'_1 - 1\rangle |p'_{e_1}\rangle \langle e'_1| \circ |e'_2 - 1\rangle |p'_{e_2}\rangle \langle e'_2| \circ \dots \ . \tag{3.45}$$

Here we mention the nodes at the ends of the tree explicitly and hide the bulk inside the first large bracket. Note that, while the tree has only one root node (p_1), it can have an arbitrary number of external vacuum nodes p_{e_i}, which is indicated by the second dots. We can then define the matrix element of the operator H with the two states ψ, ϕ as

$$\langle\phi|\hat{H}|\psi\rangle = \mathrm{tr}_{\{e_i\}}\left[|0'\rangle\langle\tilde{0}|\langle 0| \;\circ_{0\tilde{0}0'}\; \phi^\dagger \circ_{p_i'} \; H \circ_{p_i} \; \psi \circ_{e_i} \; \left(\prod_i |e_i\rangle|\tilde{e}_i\rangle\langle e_i'|\right)\right] \tag{3.46}$$

$$= \left(\prod_i P_{|e_i|}\right)|0'\rangle\langle\tilde{0}|\langle 0| \;\circ\; \phi^\dagger \circ \; H \circ \; \psi \circ \; \left(\prod_i |e_i\rangle|\tilde{e}_i\rangle\langle e_i'|\right) \; . \tag{3.47}$$

Note that we are contracting over the physical indices and the ket (sometimes also called outgoing) dummy indices, but tracing over the bra (incoming) dummy ones. This choice is arbitrary but gets fixed once done and resembles the choice we did in our framework. In eq. (3.47) we went from the fermionic trace to the super trace by introducing the respective parity prefactors. Now everyone is contracted with everyone (after all we want to obtain a scalar). Usually one chooses the ends of the tree e_i in such a way, that they carry the vacuum quantum number, since the root 0 has to carry the Hilbert space sector. Of course the parity of the vacuum (no particles) is always zero, therefore this factor can be set to one. However, it is a good idea to guarantee for an assertion of the vacuum character of the external legs on runtime, since there are applications where outer legs may not carry vacuum quantum numbers.

As usual we would like to have a local recipe which can be applied recursively in order to minimize the computational cost [Sch11]. By virtue of making use of item 4 again, we can shift full tensors to an arbitrary position in eq. (3.47). Therefore, we move all the elements of ψ, H and ϕ which belong to the same orbital together. Starting from the outer vacuum nodes, one is always able to write

$$P_{|e|}\,|e-1\rangle|p_e\rangle\langle e| \circ |\tilde{e}-1\rangle|p_e'\rangle\langle p_e|\langle\tilde{e}| \circ |e'\rangle\langle p_e'|\langle e'-1| \circ |e\rangle|\tilde{e}\rangle\langle e'| \tag{3.48}$$

$$= P_{|e|}P_{|p_e|}\;P_{|\tilde{e}||p_e|}\;\;|e-1\rangle|\tilde{e}-1\rangle\langle e'-1| \tag{3.49}$$

for an arbitrary (physical) node. This object we call a (right-) block and depict it in fig. 3.7a. The $P_{|\tilde{e}||p_e|}$ factor is again the Jordan-Wigner parity, which we need to incorporate the fermionic character of the particles. $P_{|e|}P_{|p_e|}$ is equal to $P_{|e-1|}$, due to item 4, since it is a bipartition of legs. Therefore, we say that right-blocks "inherit" the original parity of the fermionic trace in their construction, which is a point crucial to variational optimization algorithms, as we shall see in section 3.3.6. As already mentioned, the construction of left blocks do not have these parity factors and also inherits this behaviour, i.e.

$$|0'\rangle\langle\tilde{0}|\langle 0| \circ |0\rangle|p_1\rangle\langle 1| \circ |\tilde{0}\rangle|p_1'\rangle\langle p_1|\langle\tilde{1}| \circ |1'\rangle\langle p_1'|\langle 0'| \tag{3.50}$$

$$= P_{|p_1||\tilde{1}|}\,|1'\rangle\langle\tilde{1}|\langle 1| \; . \tag{3.51}$$

The last piece remaining to check is the role of branching nodes for the block construction in expectation values, as is shown in fig. 3.7b exemplary for the construction of a contraction towards the root. First we have

$$P_{|a|}P_{|b|}\;\;|r\rangle\langle b|\langle a| \circ |\tilde{r}\rangle\langle\tilde{b}|\langle\tilde{a}| \circ |a'\rangle|b'\rangle\langle r'| \tag{3.52}$$

$$= P_{|r|}\;P_{|\tilde{a}||b|}\;\;|r\rangle|\tilde{r}\rangle\langle r'| \; , \tag{3.53}$$

which also inherits the parity and furthermore exhibits the swap-gate corresponding to the crossing of $\tilde{a}$ and b. When constructing contractions downwards the tree we first get

$$|r'\rangle\langle\tilde{r}|\langle r| \circ |r\rangle\langle b|\langle a| \circ |\tilde{r}\rangle\langle\tilde{b}|\langle\tilde{a}| \circ |r'\rangle\langle b'|\langle a'| \tag{3.54}$$

$$= |r'\rangle\langle\tilde{b}|\langle b|\langle\tilde{a}|\langle a| \circ |a'\rangle|b'\rangle\langle r'| \tag{3.55}$$

$$|r'\rangle\langle\tilde{b}|\langle b|\langle\tilde{a}|\langle a| \circ |a'\rangle|b'\rangle\langle r'| \circ \begin{cases} |a\rangle|\tilde{a}\rangle\langle a'| \\ |b\rangle|\tilde{b}\rangle\langle b'| \end{cases} \tag{3.56}$$

$$= \begin{cases} P_{|a'|}\,|b'\rangle\langle\tilde{b}|\langle b| \\ P_{|b'|}\,|a'\rangle\langle\tilde{a}|\langle a| \end{cases} \quad . \tag{3.57}$$

Here, it holds true again that the contractions downwards the tree do not introduce any additional parities. The only necessary parity is the one induced by two legs of the binary node crossing.

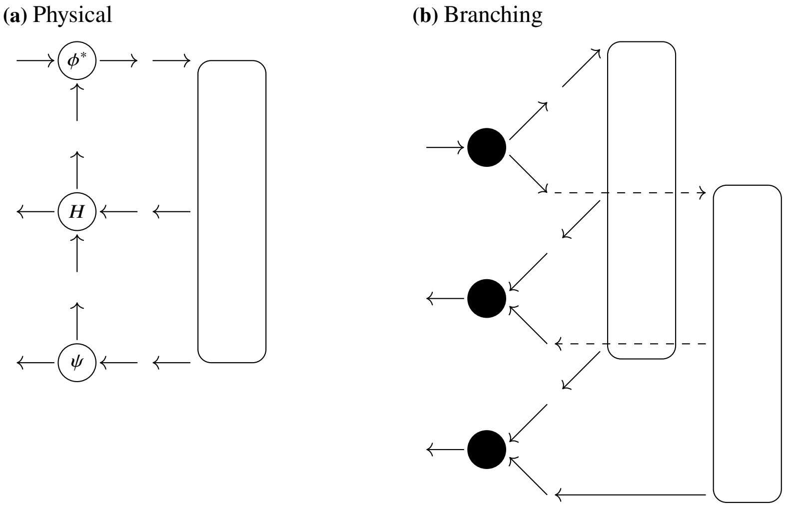
(a) Physical **(b)** Branching

Figure 3.7: Different contraction schemes for the computation of a matrix element from T3NSes and a T3NO.

Optimization 3.3.6

The last basic operation we need to discuss in order to complete our fermionic tensor network framework is the variational optimization. This is at the heart of algorithms like DMRG and TDVP, although the realization and computation details might be different, either due to the operation used or e.g. multi orbital update schemes. It should be mentioned that operations like the variational truncation of states or the variational application of operators share the same framework due to a large similarity. In principle one always takes an input state and defines a function which one tries to minimize while changing the state. In the case of DMRG this function is the energy, which we try to minimize through application of the Hamiltonian in a sophisticated way [Sch11]. For TDVP one tries to minimize the distance between the application of the Hamiltonian and the solution to the time-evolution via the Schrödinger equation by projection onto a certain MPS manifold [HCO+11, HLO+16]. Similar are the variational truncation and application, where one tries to sweep through the system and find a close representation to the state itself or an operator-application to the state while keeping the bond dimension small [Sch11]. Let us look at the DMRG case exemplary, where we define the optimization function to be

$$f(M^{n_i}, M^{n_i *}) = \langle\psi|\hat{H}|\psi\rangle - \lambda \langle\psi|\psi\rangle \ , \tag{3.58}$$

where the Lagragian-multiplier λ ensures normalization [Sch11]. Finding the minimum of f with respect to the L matrices $\{M^{n_i}\}$ is a highly non-linear complicated problem, which one usually trades for an iterative linear optimization with respect to single variational parameters, i.e.

$$\frac{\partial f}{\partial M^{n_i *}} = 0 \ . \tag{3.59}$$

Now we want to analyze the different parts of the derivative in order to find out how we should operate on the tensor network. As we discussed in the previous sections the overlap can be written in terms of the left-and right-contractions

$$\frac{\partial \langle\psi|\psi\rangle}{\partial M^{p*}} = \frac{\partial}{\partial M^{p*}} \mathrm{tr}_r \left(|l'\rangle \langle l| \circ |l\rangle |p\rangle \langle r| \circ |r'\rangle \langle p| \langle l'| \circ |r\rangle \langle r'| \right) \ , \tag{3.60}$$

where we usually use the canonical normalization of the tensor network to collapse $|l'\rangle \langle l|$ and $|r\rangle \langle r'|$ to be identity matrices. Then the derivate reduces to

$$\begin{align} &\frac{\partial}{\partial \left(|\bar{r}\rangle \langle\bar{p}| \langle\bar{l}| \right)} \left(P_{|r|} \, |l\rangle |p\rangle \langle r| \circ |r\rangle \langle p| \langle l| \right) \tag{3.61} \\ &= P_{|r'|} \, |\bar{l}\rangle |\bar{p}\rangle \langle\bar{r}| \ , \tag{3.62} \end{align}$$

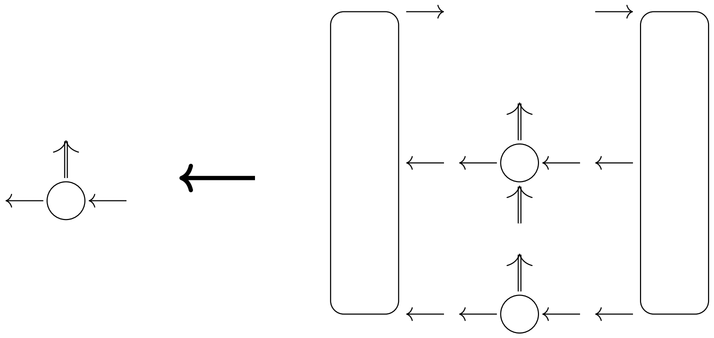

Figure 3.8: DMRG update scheme assignment for arbitrary number of orbitals involved (indicated by the double arrow). Note that physical-branching contractions work similarly just with two blocks to the right. The same holds true for single-site branching updates.

which looks like the usual MPS form eq. (3.25), however with a parity prefactor of $P_{|r|}$ coming from the right block. Note that we exchanged the parity of the right leg with the one of the conjugated right leg, as they are the same in any case.

Now we need the same analysis for the energy expectation value, i.e.

$$\frac{\partial \langle\psi|\hat{H}|\psi\rangle}{\partial M^{p*}} = \frac{\partial \, \mathrm{tr}_{r\tilde{r}} \left(|l'\rangle \langle\tilde{l}| \langle l| \circ |l\rangle |p\rangle \langle r| \circ |\tilde{l}\rangle |p'\rangle \langle p| \langle\tilde{r}| \circ |r'\rangle \langle p'| \langle l'| \circ |r\rangle |\tilde{r}\rangle \langle r'| \right)}{\partial \left(|\bar{r}\rangle \langle\bar{p}| \langle\bar{l}| \right)} \tag{3.63}$$

$$= P_{|r'|} \; |\bar{l}\rangle \langle\tilde{l}| \langle l| \circ |l\rangle |p\rangle \langle r| \circ |\tilde{l}\rangle |p'\rangle \langle p| \langle\tilde{r}| \circ |r\rangle |\tilde{r}\rangle \langle\bar{r}| \tag{3.64}$$

$$= P_{|r'|} \; P_{|p||\tilde{r}|} \, |\bar{l}\rangle |\bar{p}\rangle \langle\bar{r}| \;, \tag{3.65}$$

where it is again found that the same structure holds, including the parity from the right block $P_{|r|}$ and the physical Jordan-Wigner parity $P_{|p||\tilde{r}|}$. Due to conservation rules we can change the parity over the double index $r\tilde{r}$ for the parity of the conjugated leg r'. Now comes the crucial point for the derivation of our DMRG substitution rule. While the parity of the expectation value in eq. (3.64) is desired in order to guarantee for the expectation value to be a trace, the one in the new site tensor eq. (3.62) is certainly not. Therefore we have to invert the parity to obtain the substitution rule displayed in fig. 3.8

$$|l\rangle |p\rangle \langle r| \longleftarrow P_{|r'|} \; |l'\rangle \langle\tilde{l}| \langle l| \circ |l\rangle |p\rangle \langle r| \circ |\tilde{l}\rangle |p'\rangle \langle p| \langle\tilde{r}| \circ \left(P_{|r'|} \, |r\rangle |\tilde{r}\rangle \langle r'| \right) \;. \tag{3.66}$$

This means that when computing the updated site tensor (usually by means of the super-trace) one has to multiply the right contraction with a parity prefactor corresponding to the occupation of the conjugated right leg. In order to not mix up the parities it is important to keep in mind that according to our findings in section 3.3.5 we do not compute right blocks, but right blocks with parity prefactors, as each right block inherits the parity recursively and as can be seen in the last bracket of eq. (3.66). Therefore we have found the correct substitution rule in the fermionic Hilbert space framework and can just continue to work with bosonic tensors. One only has to multiply a parity prefactor during the eigensolver iterations into each vector in order to get the correct assignment. A particulalry important point which should not be forgotten is that typical eigensolvers like, e.g. the Krylov- or Davidson-method also make use of norms of the vectors and overlaps between them. Since our substitution rule returns the vectors without any parities we can make use of the norm and overlap functions defined in section 3.3.1 without hesitating. This means that during a call of such a function all ingoing legs of the vector (or equivalently all outgoing legs of the conjugated vector) need to be multiplied with a parity prefactor.

In principle one could also do the same derivation for a single branching node or for a combination of an arbitrary number of physical and branching nodes, some of which are shown in fig. 3.9. However, we do not need to go through all the details again, it is sufficient to say that in principle one could always merge the two right blocks from a binary node configuration into a single one by means of merge tensors. The same can be done with the current site tensors of the state and operator. Even though this procedure should not be chosen, since it is computationally very expensive, from the theoretical point of view it will result in the update scheme in eq. (3.66) again, just with a product parity $P_{|r'|} = P_{|a'|}P_{|b'|}$, after handling with the emerging Jordan-Wigner -and swap-gate parities. In general we can then just apply a parity to all ingoing legs of all right blocks and always obtain the

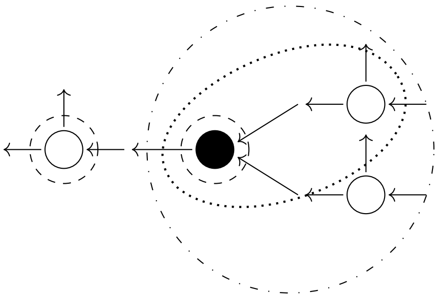

Figure 3.9: Different possible update schemes in a T3NS, showing here in an exemplary fashion: Single node update and physical branching contractions with one or two physical nodes. Whenever two or more indices are involved in the optimization the variational subspace between the two orbitals gets infinite dimensional and therefore only truncated through the SVD procedure of separating the tensors. However, if less than two physical indices are involved one should employ a subspace expansion [HMSW15].

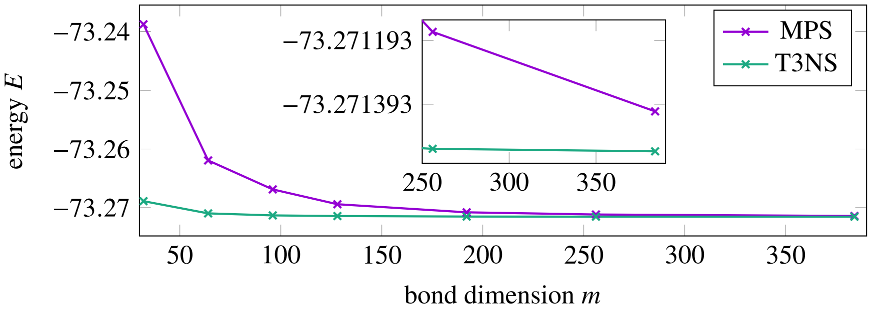

Figure 3.10: Energy convergence of a three-band Hubbard-Kanamori Hamiltonian with $L = 120$ sites.

correct result.

$$|l\rangle\,|p\rangle\,|b\rangle\,|a\rangle \longleftarrow P_{|a'|}P_{|b'|}\ \ |l'\rangle\,\langle\tilde{l}|\,\langle l| \circ |l\rangle\,|p\rangle\,|b\rangle\,|a\rangle \circ |\tilde{l}\rangle\,|p'\rangle\,\langle p|\,\langle\tilde{b}|\,\langle\tilde{a}| \circ |a\rangle\,|\tilde{a}\rangle\,\langle a'| \circ |b\rangle\,|\tilde{b}\rangle\,\langle b'| \tag{3.67}$$

Equipped with these set of rules we are able to do a variety of different operations. As already mentioned this also holds true for variational truncation and application of T3NOs and for the TDVP. However, whenever encountering a new operation during implementation of these types of tensor networks it is always good to come back to the set of rules defined in section 3.2.2 and write down the contractions in order to figure out potential parity prefactors. Even if the lack of a pure sign might not sound severe at first, a wrong implementation will cause randomly fluctuating results very fast. Especially during variational optimization, e.g. the energy starting to jump between very large negative and positive numbers, which destroys the results immediately. For observables, the situation is even more dangerous if incorrectly implemented since wrong signs might cancel each other out, making only some results wrong. When simulating systems without pre-existing benchmarks this becomes a highly dangerous game. Therefore, any handling of these fermionic tensor networks should involve a careful and sophisticated prior calculation and extensive testing.

Orbital order 3.4

So far we discussed the topology and how we can use it to optimize tensor network methods, however the topology is not the only screw we can adjust to simulate a quantum system. Independent of topology the question arises, how to map the single particle orbitals to nodes in the network. In contrast to the case of 1d spin- or Hubbard-chains there is no such thing as an à priori clear mapping for either higher dimensional systems or quantum chemical systems where all orbitals couple to each other

$$\hat{H} = \sum_{ij,\sigma} t_{ij}\, \hat{c}^{\dagger}_{i,\sigma}\hat{c}_{j,\sigma} + \frac{1}{2}\sum_{\substack{spqr\\ \sigma\sigma'}} v_{spqr}\, \hat{c}^{\dagger}_{s,\sigma}\hat{c}^{\dagger}_{p,\sigma'}\hat{c}_{r,\sigma'}\hat{c}_{q,\sigma} \ . \tag{3.68}$$

As portrayed, the matrices t and v are model dependent dense objects which are degenerate in the spin indices due to lack of spin-orbit coupling, which is why we suppress the spin indices [MG02, SC12]. For systems going beyond the BO approximation similar global couplings, depictured as Fermi-Bose mixtures, can be found [Fre31a, Fre31b]. The coefficients arise from the transition to second quantization as matrix elements of the electronic Hamiltonian with the single particle orbital basis as

$$t_{ij} = \left\langle \phi_{j,\sigma}(\vec{r}) \left| \frac{-\Delta}{2m} + \sum_{I} \frac{-Ze^2}{\left|\vec{r} - \vec{R}_I\right|} \right| \phi_{i,\sigma}(\vec{r}) \right\rangle \tag{3.69}$$

$$v_{spqr} = \left\langle \phi_{s,\sigma}(\vec{r}_1)\phi_{p,\sigma'}(\vec{r}_2) \left| \frac{e^2}{|\vec{r}_1 - \vec{r}_2|} \right| \phi_{r,\sigma}(\vec{r}_1)\phi_{q,\sigma'}(\vec{r}_2) \right\rangle \ . \tag{3.70}$$

We can interpret the diagonal elements of t as chemical potential of the respective orbital, while the off-diagonals give the hopping probability between orbitals. Furthermore, the elements of v describe the coupling strength of the two body interactions.

As we have argued in chapter 2 the factor controlling the validity of the approximation of a wave function on a tensor network is the entanglement entropy as a proxy to the needed kept singular values during the truncation. However, the entanglement entropy is an inherent basis dependent quantity [LS03, MHR05, CS11, RNW06], as can be seen in the following simplified example. Consider the Hubbard tight-binding chain with periodic boundaries in 1d

$$\hat{H}/t = -\sum_{i,\sigma} \hat{c}^{\dagger}_{i,\sigma}\hat{c}_{i+1,\sigma} + \hat{c}^{\dagger}_{i+1,\sigma}\hat{c}_{i,\sigma} \ . \tag{3.71}$$

This model is translationally invariant, therefore one usually transforms it into momentum space (labeled by k)

$$\hat{H}/t = -2\sum_{k,\sigma} \cos k\ \hat{n}_{k,\sigma} \ , \tag{3.72}$$

where we introduced the particle number $\hat{n}_{k,\sigma}$ for the momentum algebra of $\hat{a}_{k,\sigma}$ and $\hat{a}^{\dagger}_{k,\sigma}$. Now, one can solve the model easily by successively filling up the Fermi-sea from momenta $k = 0$. For instance, the two particle singlet ground state can be written by momentum excitations transformed from the vacuum and back to real space as

$$|\psi\rangle = a^{\dagger}_{k=0,\downarrow}a^{\dagger}_{k=0,\uparrow}\,|0\rangle = \frac{1}{L}\sum_{ii'} \hat{c}^{\dagger}_{i,\downarrow}\hat{c}^{\dagger}_{i',\uparrow}\,|0\rangle \tag{3.73}$$

$$= \frac{1}{L}\Big(|{\downarrow\uparrow}\ 0\ 0\ \dots\ 0\rangle + |{\downarrow}\ {\uparrow}\ 0\ \dots\ 0\rangle + \dots + |{\downarrow}\ 0\ 0\ \dots\ {\uparrow}\rangle + |0\ {\downarrow\uparrow}\ 0\ \dots\ 0\rangle + \dots \Big) \ . \tag{3.74}$$

While the former is a simple product state of bond dimension $m = 1$ and therefore bipartition entropy zero, the latter is a linear combination of all distributions of two particles with opposite spin onto L lattice sites. Even though the representation of the latter with L^2 terms might be reduced to a smaller number through truncation (we found a final bond dimension of $m = 4$ during DMRG, for a $L = 30$ site system), it is not a product state, which resembles the entropy spectrum being non-zero. Quite in contrast, the form of the bipartite entropy is given by the famous Calabrese-Cardy formula [CC04]

$$S(x) = \frac{c}{3}\ln\left(\frac{L}{\pi}\sin\left(\frac{\pi x}{L}\right)\right) + c' \ , \tag{3.75}$$

with the central charge c being the number of independent gapless single particle excitations [FK90].

The essential message from this small gymnastics is, that the choice of basis matters much in tensor networks. Not only must one be careful in what basis to use but also in how to assign it to an MPS or a TTNS. Despite the absence of a recipe or general strategy there are powerful tools to use in order to find out how to perform accordingly. Usually it is illustrative to think about how much "connection" is between two orbitals, e.g. due to physical intuition. For instance in a chemical system it is always a decent starting point to group orbitals of the same point group symmetry together, since a direct hopping between orbitals of different irreducible representations (irreps) is symmetry forbidden [WVN14b, CKG04, LS03].

In general, one needs to take care of two parts. First we have to find an optimal (or at least better than the present one) order after which we need to change the order in the network according to this map. In the following we shall discuss the key points how to do both.

Swap-gates 3.4.1

Assume we want to exchange the degrees of two degrees of freedom on a lattice, for simplicity they are neighboring. We require an operator $\hat{U}$ mapping a state to another one with permuted basis elements. For the many-body vacuum, this means changing the bookkeeping of orbitals, i.e.

$$|0\rangle = |0_1 0_2 \ldots 0_L\rangle = |0_2 0_1 \ldots 0_L\rangle \ , \tag{3.76}$$

whereas for the operator algebra we already know what is to do from section 3.2.2. In order to clarify what this symbolic notation means it is instructive to recall the relation between a basis ket and the original single particle orbital. $|n_1 n_2 n_3\rangle$ means we have n_i particles in orbital number i. This corresponds to the wave function

$$\det \begin{bmatrix} \phi_1(\vec{x}_1) & \ldots & \phi_1(\vec{x}_N) \\ \phi_2(\vec{x}_1) & \ldots & \phi_2(\vec{x}_N) \\ \phi_3(\vec{x}_1) & \ldots & \phi_3(\vec{x}_N) \end{bmatrix} / \sqrt{N!} \ , \tag{3.77}$$

with the particles distributed accordingly (for bosons it would be the permanent). Therefore a swap of the nodes on our tensor network just corresponds to a redefinition of the single particle orbitals, i.e. $\tilde{1} = 2$ and $\tilde{2} = 1$, and therefore another bookkeeping in the Fock-space, i.e. $|0_{\tilde{1}} 0_{\tilde{2}} \ldots\rangle$. Even though this swapping of degrees of freedom is not restricted to homogenous lattices, i.e. Hilbert spaces where each orbital obeys the same occupation properties, it is especially easy for these. This is because only the occupation numbers of the basis kets have to be exchanged and the coefficients in the expansion have to be adjusted accordingly. For an inhomogeneous lattice one has to take a careful tensor product of the individual Hilbert spaces of the sites and exchange the degrees of freedom in the joint space.

On a tensor network this operation becomes somewhat more local, since we do not need to operate on the full coefficient tensor, but it is enough to operate on the two site Hilbert space, just like in the case of a DMRG step. For our special case of a system containing branching nodes we just contract three sites with two physical indices, but this does merely introduce additional complication. The question remains on how to obtain these gates generically without an additional implementation effort. For this, one can make use of the merge tensors, which are essential to any implementation and therefore should be preexisting. They are defined as an identity taking two Hilbert spaces to a joined one, therefore merging two indices together, or vice versa splitting an index to two separate Hilbert spaces. Taking the two physical indices p_1 and p_2 of the sites we want to swap, we create two merges, first with the order p_1, p_2 and then with p_2, p_1 yields two rank-three tensors. Their contraction along the large Hilbert spaces yields

$$U^{p_1',p_2'}_{p_1,p_2} = \sum_p M^p_{p_1,p_2} M^p_{p_1',p_2'} \ , \tag{3.78}$$

which is the swap-gate we have been looking for. This rank-four tensor is a generalization of eq. (3.9) (which is for spinless fermions) to an arbitrary basis.

Once we are able to construct this transformation, we can construct arbitrary changes in representation by successive application of these gates, which is outlined in alg 1. In this algorithm we start at the bottom of the tree (or the right side of the MPS) and exchange the nodes of the tensor network until it is in the desired position. Then we go up iteratively until the entire network has the desired ordering. The algorithm is bounded by $L(L+1)/2$

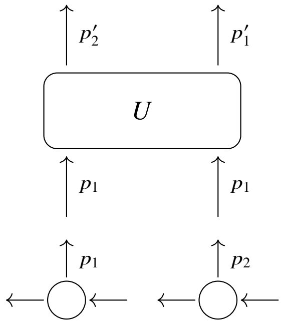

Figure 3.11: Application of a swap-gate to a MPS in order to exchange two sites. The same pattern is applied twice to the operator with the transformation and its complex-conjugate.

Algorithm 1: Successively swap sites in order to implement new ordering p.

```
Data: $|\psi\rangle$ and $\hat{H}$ w.r.t. to input order $[1, 2, \dots, L]$ and a new order $p = [p_1, p_2, \dots, p_L]$.
Result: $|\psi\rangle$ and $\hat{H}$ w.r.t. to $p$.
Def swap:
    $\psi_{lp_1p_2r} \leftarrow \psi^1_{lp_1x} \circ \psi^2_{xl_2r}$;
    $\psi_{lp_1p_2r} \leftarrow U^{p_1'p_2'}_{p_1p_2} \circ \psi_{lp_1p_2r}$;
    $\psi^1_{lp_1x}, \psi^2_{xl_2r} \leftarrow$ split $\psi_{lp_1p_2r}$ via SVD;
    $\hat{H} \leftarrow \hat{H}^1 \circ \hat{H}^2$;
    $\hat{H} \leftarrow \hat{U} \circ \hat{H} \circ \hat{U}^\dagger$;
    $\hat{H}_1, \hat{H}_2 \leftarrow$ split $\hat{H}$ via SVD;
    exchange $c_n$ and $c_{n+1}$;
    return;
current position $i \leftarrow$ bottom-most node (if more than one exists then right-most of them);
current order $c = [c_1, \dots, c_L] \leftarrow [0, 1, \dots]$;
while $i \neq root$ do
    if $c_i \neq p_i$ then
        $j \leftarrow$ index of element of $c$ which is equal to $p_i$;
        $\vec{x} \leftarrow$ path from $j$ to $i$ (going from top to bottom);
        $n \leftarrow j$;
        while $n \neq i$ do
            swap $(n, n+1)$;
            $n \leftarrow n + 1$;
        end
    end
    $i \leftarrow$ next left mode in layer, if none exists go to right-most node of layer above;
end
```

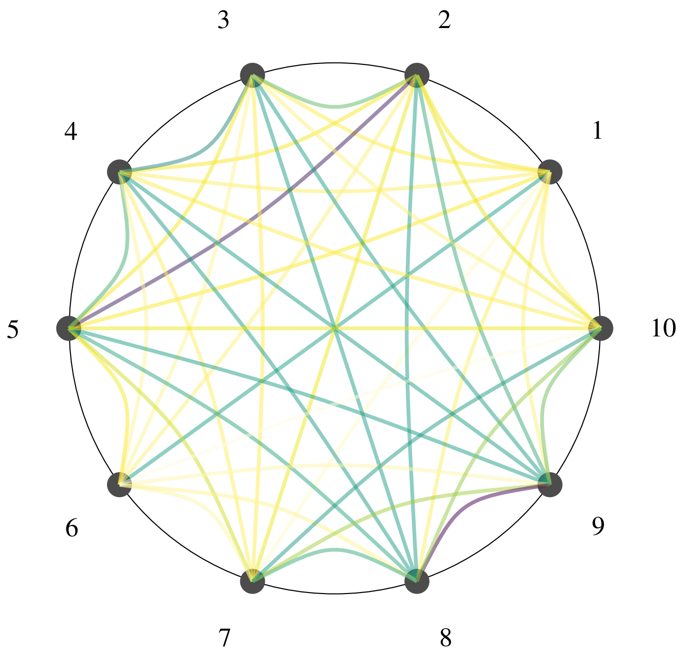

Figure 3.12: Schematic graph connecting each node in the tensor network with a value, darker color means higher value. This graph does not correspond to the MPS topology but rather represents the correlations between orbitals in eq. (3.68). In this particular example (a converged naphthalene molecule in $(10\text{e}, 10\text{o})$) all sites are talking to each other, while certain orbitals seem to be correlated stronger.

swaps (if every node is maximally distant to its target position) where each swap consists out of a rather cheap multiplication and a rather expensive SVD.

The advantage of the described procedure is the reuse of the existing state and operator, without the need to redo calculations or reconstruction. Especially when doing time-evolution, this proves to be convenient. However the main problem is that since operators can not be normalized, the SVD can cause errors in the truncation [HMS17] and therefore destroy the validity of the Hamiltonian. Therefore, in cases where the Hamiltonian can be reconstructed cheaply and one can re-obtain the state (e.g. DMRG) it can also be worthwhile discarding everything and restarting directly with the optimized order p.

Fiedler reordering 3.4.2

Now that we have talked about how to perform a reordering, we want to come back to the question how to find a good order. This is by no means a trivial question and there is no closed answer, i.e. there is no black-box-like procedure, which can give good mappings with low costs for arbitrary systems. Here, a connection to graph theory comes in handy, namely we can enlist all the nodes $\{i\}$ in the network and interconnect them to each other. We give each connection between two nodes i and j a weight I_{ij} [BLMR11], as can be seen in fig. 3.12. Each node represents an orbital, while the weight we give to the node corresponds to some measure telling us how strongly correlated the two orbitals are. This measure is usually chosen to be the mutual information between the two sites [RNW06], which is defined via the entanglement of orbital RDMs. Given two sites i and j we can compute the RDMs by tracing out everything except the respective orbitals

$$\hat{\rho}_i = \mathrm{tr}_{\{a\}\backslash i} |\psi\rangle\langle\psi| \ , \tag{3.79}$$

$$\hat{\rho}_{ij} = \mathrm{tr}_{\{a\}\backslash\{ij\}} |\psi\rangle\langle\psi| \ , \tag{3.80}$$

where we defined the set $\{a\}$ to include all basis-kets. From these we can compute the orbital entropies

$$S(\hat{\rho}) = -\,\mathrm{tr}(\hat{\rho}\ln\hat{\rho}) \ , \tag{3.81}$$

for the respective subset of the total Hilbert space. The mutual information is defined as the Kulback-Leibler divergence of the probability distribution of the individual spaces and the two orbital spaces [DMD⁺21]. Assuming the probability distribution for excitations is given by eqs. (3.79) and (3.80), we write

$$I_{ij} = \sum_{n_i n_j} \rho_{n_i n_j} \ln \frac{\rho_{n_i n_j}}{\rho_{n_i}\rho_{n_j}} \tag{3.82}$$

$$= \left(S(\hat{\rho}_i) + S(\hat{\rho}_j) - S(\hat{\rho}_{ij})\right)\left(1 - \delta_{ij}\right) \ , \tag{3.83}$$

where we defined the excitation probability for n_i in orbital i as the real number ρ_{n_i}, etc. The Kronecker delta ensures that the diagonal elements are zero. This is sometimes also referred to as the amount of information which is in the joint Hilbert space, but not in the individual ones [Sha48]. It should be mentioned that this framework can be generalized to an arbitrary number of involved orbitals [SBS⁺17], however usually the costs for computing higher order RDMs get very expensive fast.

From this point Legeza et al. [BLMR11] suggested to create a scalar function for optimization by incorporating the distance between sites $|i - j|$ in the tensor network, i.e. defining

$$f(p) = \sum_{ij} I_{ij} \, |p(i) - p(j)|^{\eta} \ , \tag{3.84}$$

where η is a coefficient to weigh the impact of the distance and $p\colon \mathbb{N}^L \to \mathbb{N}^L$ is a bijection. Note that we are optimizing with respect to the order p for which f gets minimal, i.e. formally defined [ABH98]

$$p(i) < p(j) < p(k) \Rightarrow I_{ij} \geq I_{ik} \text{ and } I_{jk} \geq I_{ik} \ . \tag{3.85}$$

This can be read as putting the orbitals with large mutual information close to each other, while others which are stronger correlated can be put into distance and is also called the seriation problem. Trying to brute force all combinatorial possibilities is obviously NP-hard in the system size [GP97]. In the special case where $\eta = 2$, i.e. we can write the cost function as a matrix vector product, there exists a closed feasible solution [ABH98]. The rigorous proof is very technical, therefore we restrict ourselves to sketching the basic idea. First, one has to replace the integer permutations by continuous variables. Since we do not want the trivial solution of all elements of the vector being zero, we have to enforce normalization by an additional constraint. Furthermore, the arbitrariness of the ordering with respect to global translation is fixed by demanding the one norm of the solution being zero. Therefore, the problem becomes an optimization problem

$$\min_{x} \left(\sum_{ij} I_{ij}(x_i - x_j)^2 - \lambda \sum_{i} x_i - \lambda' \left(\sum_{i} x_i^2 - 1 \right) \right) \tag{3.86}$$

in a real valued vector space. By defining the Laplacian of the mutual information matrix $L_I = I - D$, where

$$D = \operatorname{diag}\left(\sum_i I_{1i} \quad \sum_i I_{2i} \quad \dots \right) \ , \tag{3.87}$$

the problem reduces to diagonalizing the Laplacian of I [ABH98]. As the graph is connected, the first eigenvalue will be zero and the second one is the Fiedler value with the accompanying Fiedler vector [Fie73, Fie89] which gives the solution for the optimal order defined in eq. (3.85).

In practice one can then perform the following steps in order to find a better ordering.

1. Perform a DMRG with low bond dimension, such that the computational costs are cheap, but push it far enough such that the basic physics are captured.
2. Compute the mutual information matrix I_{ij} from the reduced systems.
3. Diagonalize its Laplacian L_I.
4. Compute the Fiedler-vector.
5. Reorder (and possibly repeat to further optimize).

This quite simple procedure enables us to find a good ordering of arbitrary systems just by probing its Hamiltonian. As previously mentioned, usually small bond dimensions $m \approx 512$ are enough to obtain good results and since one can perform several iterations it is not catastrophic if the first runs do not capture the entire physics. Due to the decreased resource requirement the next run is going to capture more of the system and the reordering will improve to a greater degree.

It should be mentioned for this algorithm that it can make sense to restrict the transformation space to certain permutations. For instance, in [BLMR11] it is argued that orbitals belonging to the same symmetry group (discussed in section 4.2) are kept tight, i.e. permutation within blocks and of total blocks are allowed, but not of orbitals of different symmetry irreps. At least in the chemical context one can say that hopping between orbitals of different symmetry irreps is prohibited, only the interaction term can connect distant orbitals. Also in another context this hand-imposed constraints can make sense, e.g. in DMFT when one wants to restrict permutations between baths. In both cases one prevents the algorithm from doing senseless orderings due to local minima by suppressing these manually.

Simulated annealing 3.4.3

Although the Fiedler reordering can improve convergence of non-local Hamiltonians on artificially mapped tensor networks [LS04, BLMR11, LS03], it is somewhat difficult to use non-MPS-like topologies. The reason is that the output of this algorithm is a vector of permutations, optimizing the distance between sites with high mutual information. However, the representation in a vector has a somewhat planar origin and therefore needs a careful mapping on higher order topologies as well as a careful thought on distance measures. Furthermore, for the iterative approach of the minimization with low amount of resources it can be beneficial not to do greedy optimizations.

Luckily Fiedler is not the only reordering algorithm, another one worth mentioning is the simulated annealing. It was even brought in contact with tensor networks earlier [TVF02, RNW06] than the Fiedler algorithm. Simulated annealing is basically very familiar to the Metropolis algorithm [MRR⁺53] in that it tries to approximate a solution of exponentially many configurations by a stochastic minimum search. A variety of interesting problems can be targeted by simulated annealing. Apart from the already mentioned Monte Carlo algorithms, industrial relevant problems like the traveling salesman [MGPO89, KGV83] and quantum algorithms trying to break cryptographic systems [Sho97, MOI20] are some of the many to mention.

The basic idea is to mimic the behavior of a metal cooling down, where we substitute the energy, which is usually minimized by the configuration of the system by some other objective function $I(p)$ depending on the configuration p. One starts with the initial configuration and does random operations changing the ordering. In our special case we choose to change two random sites or two neighboring random sites in an alternating fashion. For each new configuration we compute the relative change in the cost function I and keep the change if it decreased the cost or keep it with the probability of the Boltzmann weight if it did not. Doing so, we successively decrease the cost, while we circumvent local minima in the minimization landscape with the possibility of jumping out of them with a certain probability. However, these "hoppings" get less possible with increasing simulation time, since the temperature T is chosen as a monotonically decreasing function of the iteration step. This way the system is going to always going to find a minimum in the optimization landscape, yet will be kicked out of minima more often, the higher the temperature. If the problem is somehow well behaved, usually the first minimum which the system can not be kicked out of is going to be a global minimum or at least a minimum deeper than the minima in the proximity. Since we are typically interested in decreasing the cost function and will iterate multiple times, it is thus sufficient to operate like this to find a good representation, which will be improved over time and finally converges to the true solution. In many cases we found better results by annealing, even on the MPS, than by means of the Fiedler reordering.

It should be addressed that for system sizes becoming large (e.g. for us the heuristic threshold was $L \approx 40$) the sheer number of configurations (as already mentioned growing like $L!$) might make it necessary to run the annealing for many iterations. This can be circumvented by mixing the annealing procedure with a divide and conquer-like approach. Furthermore, a crossover with the genetic algorithm might be of value. Let us briefly comment on both of them. Divide and conquer basically explains itself, employing several workers who run over different parts of the system and only exchange within these subparts. Doing so, the number of configurations is diminished by a lot at the expense of long range exchanges getting possible only through successive multiple permutations. This makes sense since usually we start with an ordering which is not completely off, e.g. with clustering of irreps,

Algorithm 2: Finding an optimized order via simulated annealing.

```
Data: Objective function $I(c)$ and temperature function $T(i)$ ($i$ being the iteration step, the temperature
      decreasing with increasing number of iterations), threshold $\epsilon$ and maximum iterations $i_{\max}$.
Result: Optimized order $p$ which has $I(p) < I([0, 1, 2, \dots])$ and in the best case is the global minimum.
$c \leftarrow [0, 1, \dots, L]$;
$p \leftarrow [0, 1, \dots, L]$;
while $i < i_{\max}$ or $|I_{i-1} - I_i| > \epsilon$ do
    Pick random index $1 < a < L$;
    if $i$ is even then
        Pick another random index $a < b < L$;
        $c' \leftarrow [c_1 \; \dots \; c_b \; \dots \; c_a \; \dots \; c_L]$;
    else
        $c' \leftarrow [c_1 \; \dots \; c_{a+1} \; c_a \; \dots \; c_L]$;
    end
    $\delta \leftarrow \frac{I(c')-I(c)}{I(c')+I(c)}$;
    if $\delta < 0$ or $\mathrm{e}^{-\delta/T(i)} >$ random number then
        $c \leftarrow c'$;
        if $I(c) < I(p)$ then
            $p \leftarrow c$;
        end
    end
    $i \leftarrow i + 1$;
end
```

which we do not want to separate anyways, as mentioned before. Additionally, we can employ parallelization over multiple threads in the implementation, which is always desired. The genetic algorithm [TUR50, Rec71] is very close to the ideas of simulated annealing, we used it as an additional layer within the buckets of each worker. The basic principle is again to do random permutations and also recombinations (mimicking the behavior of cells in nature) in order to create new generations of settings. By iterating and creating several generations, which then in turn are subject to some kind of selection process, we include an additional measure, speeding up convergence but also enabling the system to be kicked out of local minima. The genetic algorithm is usually limited due to its slow convergence, and the sheer number of possibilities one has to realize through several generations. But using it as a tool in combination with simulated annealing we achieved some decent results with it.

Chemistry tools

4

Reduced density matrices

4.1

Often when computing observables from wave functions, it is essential to have access to RDMs of the system. A RDM is a matrix containing all physical information about a subpart of the Hilbert space, which one can obtain from the full state by a subsequent integration of unnecessary degrees of freedom. In the following we do not want to deal with RDMs in detail but merely with their efficient construction on tensor networks. We basically distinguish between two kinds of reduced systems. When integrating out particles we talk about particle reduced density matrices (pRDMs), while for the orbital case we say orbital reduced density matrices (oRDMs). The former has applications when doing electronic structure theory, e.g. complete active space self-consistent field (CAS-SCF) [ZN08], while some of the applications of the latter we already discussed in section 3.4.2.

A pRDM is defined from the total system $|\psi\rangle$ via integration over all respective particles, e.g. for one or two particles

$$\gamma_{ij,\sigma} = \langle\psi|\hat{c}^\dagger_{i,\sigma}\hat{c}_{j,\sigma}|\psi\rangle \tag{4.1}$$

$$\Gamma_{spqr,\sigma\sigma'} = \langle\psi|\hat{c}^\dagger_{s,\sigma}\hat{c}^\dagger_{q,\sigma'}\hat{c}_{r,\sigma'}\hat{c}_{p\sigma}|\psi\rangle \ . \tag{4.2}$$

From these we can compute any single- and two-particle observables. Note that they are highly symmetric, e.g. that γ is hermitian and therefore it holds that $\Gamma_{spqr,\sigma\sigma'} = \Gamma_{psrq,\sigma\sigma'} = \Gamma_{qrsp,\sigma'\sigma} = \Gamma_{rqps,\sigma'\sigma}$. This will later reduce the number of matrix elements we need to compute by a lot.

As already mentioned, the oRDM can be computed of the wave function by integrating out everything except a few sub orbitals

$$\hat{\rho}_i = \mathrm{tr}_{\backslash i}\,|\psi\rangle\langle\psi| = \sum_{\substack{n_1\ldots n_{i-1}\\ n_{i+1}\ldots n_L}} \langle n_1\ldots n_{i-1}n_{i+1}\ldots n_L|\psi\rangle\langle\psi|n_1\ldots n_{i-1}n_{i+1}\ldots n_L\rangle \ . \tag{4.3}$$

This means we mute all degrees of freedom in the orbitals, except for the sites under investigation. The case of two orbitals is fairly straight forward

$$\hat{\rho}_{ij} = \sum_{\substack{n_1\ldots n_{i-1}\\ n_{i+1}\ldots n_{j-1}\\ n_{j+1}\ldots n_L}} \langle n_1\ldots n_{i-1}n_{i+1}\ldots n_{j-1}n_{j+1}\ldots n_L|\psi\rangle\langle\psi|n_1\ldots n_{i-1}n_{i+1}\ldots n_{j-1}n_{j+1}\ldots n_L\rangle \ , \tag{4.4}$$

where we chose $i < j$, without loss of generality.

It should be mentioned that the generalization to more than two particles or orbitals can sometimes be utilized (e.g. [SBS+17]), and conceptually goes in the same spirit. However, due to the high computational cost to obtain these quantities, and since they were not needed during the course of this thesis, we do not describe them here.

Particle reduced density matrix

4.1.1

Computing eqs. (4.1) and (4.2) brute force results in a horrible runtime behaviour. Apart from the aforementioned symmetries of these objects, one also has to compute contractions of large dimensional states several times redundantly. Usually the dimensionality of the involved operators is small and their application to the state does not change it significantly. In order to get a speedup it is crucial to reuse contractions as often as possible and compute all matrix elements involved in them.

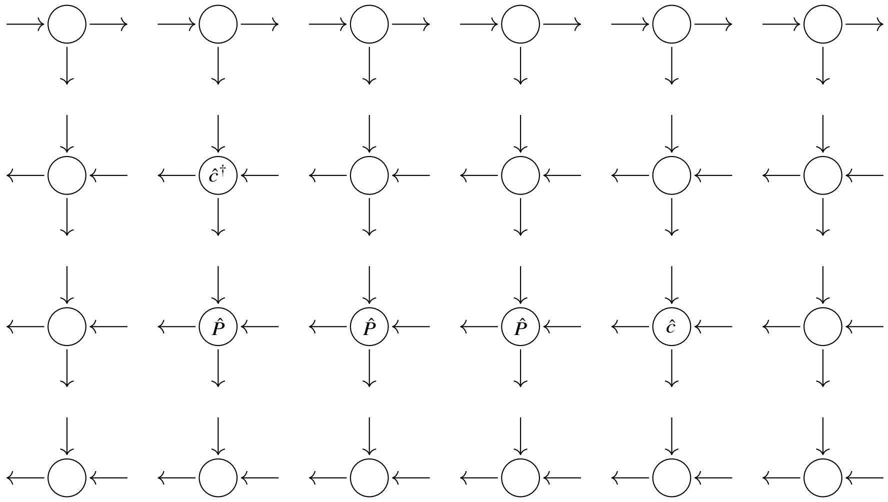

Figure 4.1: Tensor network written out pictographically for one element of γ. The symbol $\hat{P}$ either refers to a Jordan-Wigner parity or an identity, depending on the utilized framework.

Starting off with the easiest example, i.e. the 1pRDM of a MPS, as is depicted in fig. 4.1. In order to minimize the amount of needed operations, we will first left-normalize the network inbetween entirely. This way all operations which need to be performed are focussed on the area between i and j, if we keep right-normalizing after each iteration step. Of course for the last site this is the entire system, but sweeping through the chain, the amount of work continuously decreases until the final site which only needs one computation. This is an expression of the hermiticity of γ, i.e. the number of independent (complex) elements reduces to $L(L+1)/2$. Therefore we proceed as follows

1. Left-normalize the state.
2. Compute the occupation of the site, i.e. $\gamma_{jj} = \langle\psi|\hat{n}_j|\psi\rangle$ and store it.
3. Compute the right block $R_{r\tilde{r}r'}$ on site j consisting of the state site tensor ψ, its conjugate and the local representation of $\hat{c}$.
   (a) Compute $\gamma_{kj} = \langle\psi|\hat{c}_k^\dagger\hat{c}_j|\psi\rangle$ from R, ψ and $\hat{c}^\dagger \cdot P$ for the site to the left.
   (b) Extend the right-block with P and ψ to the site on the left.
   (c) Reiterate until the last site is reached.
4. Right-normalize the current site and continue to the left.

While the naive computation would have L times a cubic cost for each element in γ, i.e. $\sim L^2 \cdot Lm^3$, we can reduce it through this scheme to $\sim L^2m^3$. So we gained an order of magnitude, as can also be observed in fig. 4.2.

The generalizations necessary for the 2pRDM are far from trivial, but conceptually in the same spirit. We again try to exploit permutation symmetries of the Γ matrix and furthermore reuse contractions as often as possible. This involves a sophisticated procedure in which the RDMs are treated for each possible combination of indices. We start with the easy case, namely the ones which can be reduced to the form of 1pRDMs, for which we already know an efficient procedure, i.e.

$$\Gamma_{ijjj,\sigma\bar{\sigma}} = \langle\psi|\hat{c}_{i,\sigma}^\dagger\hat{c}_{j,\bar{\sigma}}^\dagger\hat{c}_{j\bar{\sigma}}\hat{c}_{j\sigma}|\psi\rangle \ , \tag{4.5}$$

where we include both cases, $i = j$ and $i \neq j$. The more complicated case is the one where either two indices are different or all of them are. We renounce to sketch the algorithm in detail for this here, since it would become rather extensive, but as an example we demonstrate the flow tree in fig. 4.3. Last but not least, we want to mention that the generalization to a tree is conceptually straightforward but encorporates some advanced bookkeeping. We need to introduce an artificial order, e.g. top nodes are labeled before bottom nodes and nodes on the left come before the ones one the right. Then one only has to compute the overlap elements for each site with all sites below and to the left.

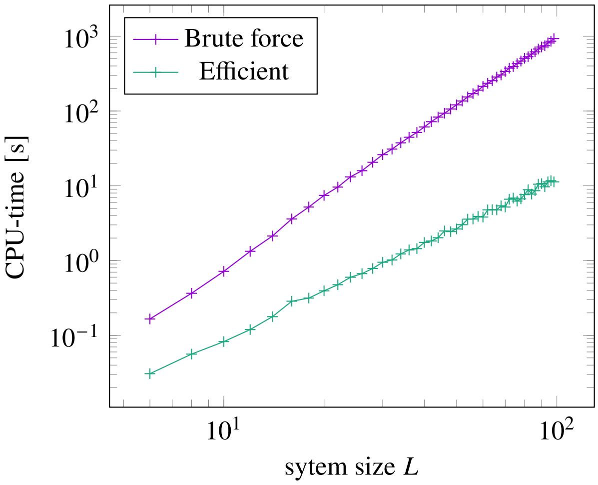

Figure 4.2: Computation time for the pRDM of a half filled Hubbard wave function of bond dimension $m = 10$ scaling with system size. Note that with increasing system size overheads get smaller and we even obtain two orders in magnitude by virtue of sparse tensors.

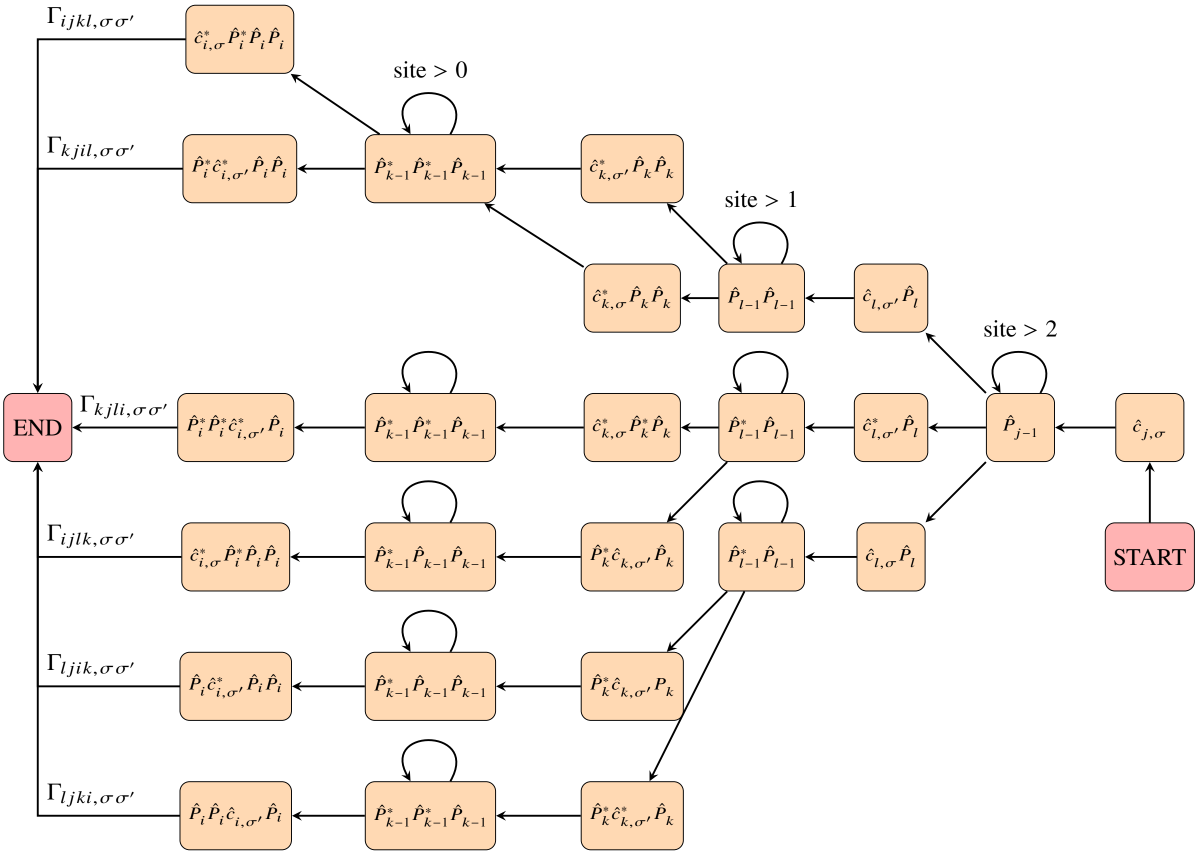

Figure 4.3: Flowchart showing how to reuse the tensors most efficiently.

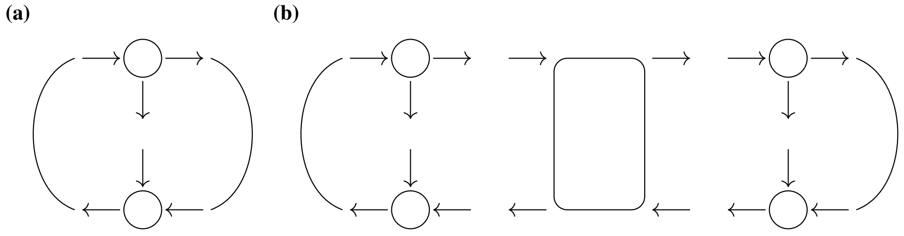

Figure 4.4: Pictographic representation of 1oRDMs and 2oRDMs assuming canonical normalization for all sites not involved.

Orbital reduced density matrix 4.1.2

The computation of oRDMs is somewhat different, since the definition is more abstract than just using expectation values. Taking the definitions in eqs. (4.3) and (4.4) and plugging in the tensor network ansatz we obtain

$$\langle n_1 \dots n_{i-1} n_{i+1} \dots n_L | \psi \rangle = \sum_{n'_i} A^{n_1} \dots A^{n_{i-1}} M^{n'_i} B^{n_{i+1}} \dots B^{n_L} \, |n'_i\rangle \tag{4.6}$$

$$\Rightarrow \hat{\rho}_i = \sum_{\vec{n}' \setminus n'_i} \sum_{n_i \tilde{n}_i} A^{n'_1} A^{n'_{i-1}} M^{n_i} B^{n'_{i+1}} B^{n'_L} \, |n_i\rangle \langle \tilde{n}_i| \, {A^{n'_1}}^\dagger {A^{n'_{i-1}}}^\dagger {M^{\tilde{n}_i}}^\dagger {B^{n'_{i+1}}}^\dagger {B^{n'_L}}^\dagger \tag{4.7}$$

$$= \sum_{n_i \tilde{n}_i, ab} M^{n_i}_{ab} {M^{\tilde{n}_i}_{ab}}^\dagger \, |n_i\rangle \langle \tilde{n}_i| \ , \tag{4.8}$$

if we assume canonical normalization. If the Hamiltonian from which we computed the state is symmetric under some transformation, by virtue of the Wigner-Eckart theorem [Wig27, Eck30] we can even say that $n_i = \tilde{n}_i$, i.e. the matrix is only non-zero on its diagonals. Pictographically this reduces to a remarkably easy representation, as can be seen in fig. 4.4. We just need to left-/right-normalize all the sites on the left/right of the orbital whose RDM we are seeking and then contract over the virtual indices. This even extends naturally to higher order RDMs on any network, e.g. 2oRDMs can be computed by starting from one of the orbitals, leaving the virtual legs in the direction of the other one open. Then we contract with the state and its conjugate, muting the physical indices until we reach the target site. For TTNS it is basically the same, only that branching nodes do not have physical indices, so they are completely contracted in. Here, it is instructive to remind oneself of the concept of root-normalization (see section 3.3.2) in order to obtain a correct result. Furthermore, one should again reuse the existing contractions as often as possible, since for high bond dimension states their computation is still expensive. So when we need several RDMs like e.g. in sections 3.4.2 and 3.4.3 it is worthwhile first to compute for each site involved the 1RDM and then recursively the block and the 2RDMs. For the tree this again involves an artificial ordering, as in the section before.

One last remark to make is that there exists an approach based on matrix elements in order to compute each element of the RDM without direct tensor manipulations [RNW06, BTB⁺13]. In this approach each matrix element is computed by one matrix element, e.g.

$$\langle 0 | \hat{\rho}_i | 0 \rangle = \langle \psi | (1 - \hat{n}_{i,\downarrow})(1 - \hat{n}_{i,\uparrow}) | \psi \rangle \ . \tag{4.9}$$

Usually it is computationally very expensive to use this approach, but we employed it in one particular case, when we had ground states in the HF basis, but we desired the RDM in a natural orbital (NO) basis. It can be cheaper than transforming the Hamiltonian into a new basis and starting simulations from zero. If we obtain the eigensystem, e.g. the NOs from the 1pRDM

$$\begin{aligned} \text{eigensystem} \colon \mathbb{C}^{L \times L} &\to \{\mathbb{R}^L, \mathbb{C}^{L \times L}\} \\ \gamma &\mapsto \begin{pmatrix} \lambda_1 \\ \vdots \\ \lambda_L \end{pmatrix}, U \end{aligned} \tag{4.10}$$

we can transform the operators algebra via

$$\hat{c}_\alpha = \sum_{i=1}^{L} \langle\alpha|i\rangle\, \hat{c}_i = \left(U \cdot \begin{pmatrix}\hat{c}_1\\ \vdots \\ \hat{c}_L\end{pmatrix}\right)_\alpha \tag{4.11}$$

$$\hat{c}^\dagger_\alpha = \sum_{i=1}^{L} \langle i|\alpha\rangle\, \hat{c}^\dagger_i = \left(U^\dagger \cdot \begin{pmatrix}\hat{c}^\dagger_1\\ \vdots \\ \hat{c}^\dagger_L\end{pmatrix}\right)_\alpha \quad . \tag{4.12}$$

Note that while U is an unitary, it is multiplied both times from the left, which means the transformation of two operator terms is not trivial, i.e.

$$\hat{n}_\alpha = \sum_{ii'} U^*_{i\alpha} U_{\alpha i'} \hat{c}^\dagger_i \hat{c}_{i'} \ . \tag{4.13}$$

We shall not discuss this procedure in detail, since it is of mere technical nature, we just refer to the tables 4.1 and 4.2 for an overview on how to compute the individual elements for a Hubbard basis [RNW06, BTB⁺13].

$O^{(1)}$	$1 - \hat{n}_\uparrow - \hat{n}_\downarrow + \hat{n}_\uparrow \hat{n}_\downarrow$
$O^{(2)}$	$(1 - \hat{n}_\uparrow)\hat{c}_\downarrow$
$O^{(3)}$	$(1 - \hat{n}_\downarrow)\hat{c}_\uparrow$
$O^{(4)}$	$\hat{c}_\downarrow \hat{c}_\uparrow$
$O^{(5)}$	$-(1 - \hat{n}_\uparrow)\hat{c}^\dagger_\downarrow$
$O^{(6)}$	$(1 - \hat{n}_\uparrow)\hat{n}_\downarrow$
$O^{(7)}$	$\hat{c}^\dagger_\downarrow \hat{c}_\uparrow$
$O^{(8)}$	$\hat{n}_\downarrow \hat{c}_\uparrow$
$O^{(9)}$	$(1 - \hat{n}_\downarrow)\hat{c}^\dagger_\uparrow$
$O^{(10)}$	$\hat{c}^\dagger_\uparrow \hat{c}_\downarrow$
$O^{(11)}$	$\hat{n}_\uparrow (1 - \hat{n}_\downarrow)$
$O^{(12)}$	$\hat{n}_\uparrow \hat{c}_\downarrow$
$O^{(13)}$	$\hat{c}^\dagger_\uparrow \hat{c}^\dagger_\downarrow$
$O^{(14)}$	$-\hat{n}_\downarrow \hat{c}^\dagger_\uparrow$
$O^{(15)}$	$\hat{n}_\uparrow \hat{c}^\dagger_\downarrow$
$O^{(16)}$	$\hat{n}_\uparrow \hat{n}_\downarrow$

	–	↓	↑	2
–	1			
↓		6		
↑			11	
2				16

Table 4.1: Definition of the operators necessary for the computation of matrix elements and representation of the 1oRDM.

Molecular symmetries 4.2

So far the role of symmetries in a tensor networks has not been addressed. In almost all branches of physics, symmetries play a crucial role, from guiding to theoretical arguments, to simplifying calculations. As we are interested in quantum many-body problems, where the problems usually suffer from the curse of dimensionality, it is common to heavily exploit symmetries to impose conditions decreasing the number of degrees of freedom. In order to understand how this works, we shall give a simplified example [Sch11]. Assume we have a system whose Hamiltonian commutes with some total particle number, i.e. $\left[\hat{N}, \hat{H}\right] = 0$. This implies that due to a common

	(0, 0)	(1, −1/2)	(1, 1/2)	(2, −1)	(2, 0)	(2, 1)	(3, −1/2)	(3, 1/2)	(4, 0)
	−−	−↓ ↓−	−↑ ↑−	↓↓	−2 ↓↑ ↑↓ 2−	↑↑	↓2 2↓	↑2 2↑	22
−−	1/1								
−↓		1/6 2/5							
↓−		−5/2 1/6							
↑−			1/11 −3/9						
−↑			9/3 11/1						
↓↓				6/6					
−2					1/16 2/15 3/14 4/13				
↓↑					5/12 6/11 7/10 8/9				
↑↓					9/8 10/7 11/6 12/5				
2−					13/4 14/3 15/2 16/1				
↑↑						11/11			
↓2							6/16 −8/14		
2↓							14/8 16/6		
↑2								11/16 12/15	
2↑								−15/12 16/11	
22									16/16

Table 4.2: Representation of the 2oRDM from matrix elements.

eigenbasis the eigenvectors $|\psi\rangle$ of $\hat{H}$ are labeled by eigenvalues of $\hat{N}$

$$\hat{N}\,|\psi\rangle = \hat{N}\sum_{n_i ab}\psi^{n_i}_{ab}\,|a\rangle\,|n_i\rangle\,|b\rangle = N\,|\psi\rangle\ , \tag{4.14}$$

where we assumed a canonical MPS representation of the wave function and N is the total particle number. The action of the global number operator on the number kets is rather trivial, since it is just defined via a tensor product

$$\hat{N}\,|n_i\rangle = n_i\,|n_i\rangle\ . \tag{4.15}$$

The same way we can obtain the action on the left- and right-bases, e.g.

$$\hat{N}\,|a\rangle = \hat{N}\sum_{n_1\ldots n_{i-1}} A^{n_1}\ldots A^{n_{i-1}}\,|n_1\ldots n_{i-1}\rangle = (n_1+\ldots+n_{i-1})\,|a\rangle = n_a\,|a\rangle\ . \tag{4.16}$$

With the last equality we introduced the notion of the "particle number of a leg". This directly implies that either $n_a + n_i + n_b = N$, or the elements $\psi^{n_i}_{ab}$ are zero. This rather primitive example is the consequence of a much deeper and more sophisticated statement, namely the Wigner-Eckart theorem [Wig27, Eck30]. It basically states that a tensor invariant under a symmetry transformation decomposes into a tensor product of smaller blocks which are labeled by irreducible representations (irreps) of this symmetry transformation and tensors of numbers only determined by the symmetry group called Clebsch-Gordon coefficients (CGCs). In our case of the Abelian particle number group, the CGCs are just identities multiplied with Kronecker deltas which exactly enforce the statement given by eq. (4.14) [SPV10, SPV11].

From a numerical point of view, we can just store the tensor blocks themselves with their irreps and leave away the zeros. This is advantageous from several aspects, e.g. that the neglected zeros do not occupy the memory or do not need to be taken into account during tensor operations. Furthermore during contractions, we can just ignore tensors whose quantum numbers do not fit, instead of painfully computing them just to find that their norm is (close to) zero in the end. This results in an improved scaling by typical factors of 10 – 1000, depending on the model.

We should mention that in the condensed matter context we usually talk about global symmetries, i.e. the symmetry transformation under which the Hamiltonian is invariant does not depend on the orbital itself. For instance in the particle number case, the symmetry transformation associated with the conserved number is often something like the transformation of the operator algebra

$$\hat{c}_i \to \mathrm{e}^{\mathrm{i}\alpha}\hat{c}_i \qquad \hat{c}^\dagger_i \to \mathrm{e}^{-\mathrm{i}\alpha}\hat{c}^\dagger_i\ , \qquad \alpha\in\mathbb{R},\ \forall i \tag{4.17}$$

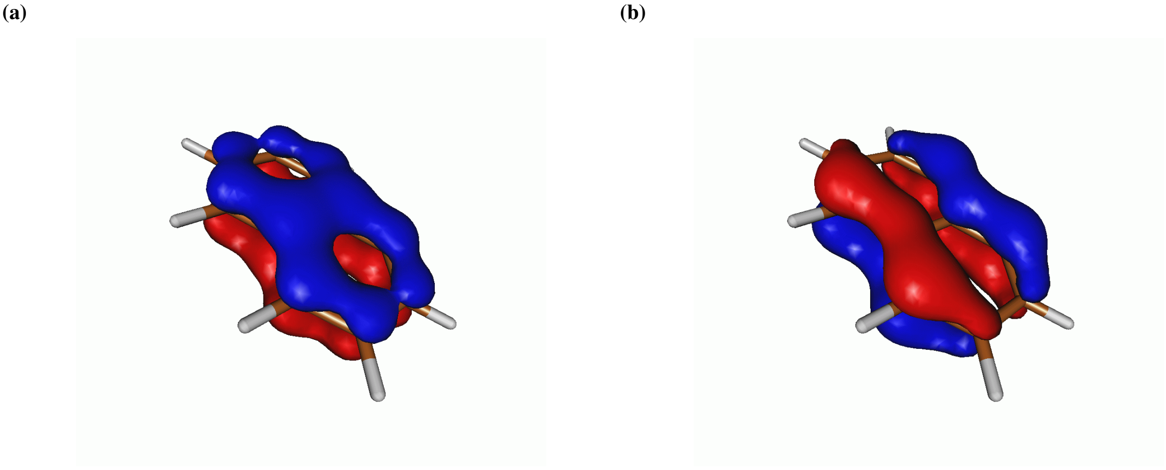

Figure 4.5: Molecular single particle orbitals of naphthalene in a (10e, 10o) cc-pVDZ basis.

which leaves two body Hamiltonians (e.g. eq. (3.68)) invariant. In other context, e.g. high energy or lattice gauge theories, the symmetry transformation is local, depending on the orbitals position, i.e. $\alpha \rightarrow \alpha_i$. This can be accounted for in the traditional tensor network approach by doubling the size of the MPS [ZCR13, BHVA$^+$14, BCC$^+$19]. However, these methods were not used in the scope of this thesis and therefore we only want to mention them for the sake of completeness.

With this powerful symmetry framework at hand we can decompose the tensor network with arbitrary symmetries, e.g. common ones are $\mathbb{Z}_k$, $U(1)$ but even $SU(2)$ and $SU(3)$. One solely requires the irreps belonging to the basis state and the CGCs, which can be constructed generically, even if the procedure itself is very complicated and needs to be reimplemented for every group [Wei12]. When dealing with chemical problems an essential class of groups is the molecular symmetry groups. These are the symmetries which can be attributed to single particle orbitals of the molecule. Before we continue to a systematic characterization, we shall give a brief example by studying the molecular orbitals in fig. 4.5. These real space wave functions are obtained by the HF method on a linear combination of atomic orbitals (LCAO) ansatz. The sign of the wave function is represented by different colors. The crucial point is what happens when changing the position of the molecule in space. The molecule or its quantum dynamics do not know about the coordinate system we set up, therefore all quantities measured must remain the same. However, we can observe that e.g. rotating the molecule along the plane in which it lies in fig. 4.5a exchanges the sign of the wave function, while in fig. 4.5b it stays invariant. Still since the electronic density is the absolute value of the wave function this does not affect observables. To phrase it differently, both are symmetric, just in another fashion as we shall experience shortly.

As for now, we will progress in the theory. Usually, the important symmetries for a molecule are characterized by the k-fold rotation or cyclic group C_k (sometimes also called $\mathbb{Z}_k$), the mirror symmetry C_s, the inversion symmetry C_i and the group of joint rotation and reflection called improper rotations S_k [AdP06]. As the name already suggests the cyclic group C_k characterizes molecules which are invariant under a rotation of $2\pi/k$ around a certain axis, e.g. the water or the hydrogen peroxide molecule. Many molecules posses more than one symmetry axis, therefore one usually refers to the one of the highest degree k, which is referred to as principal axis [AdP06]. The mirror symmetry C_s describes when a molecule can be mirrored along some 2d area and remains the same. Prominent planes are, e.g. the ones parallel to the principal axis (called σ_v) or the one orthogonal to it (called σ_h) [AdP06]. Examples would be the water molecule or benzene here again. Then there is the inversion symmetry C_i simply multiplying every coordinate vector with a global minus sign. Molecules like naphthalene or ethane are transformed into themselves by such. Finally, the concatenations of rotations and reflections are called improper rotations S_k. Restricting to mirror plane axis we arrive at the chemically important Dieder group D_k, which is, e.g., realized in ethylene, and is non-Abelian for any $k > 2$ [AdP06]. Concluding, it shall be mentioned that there are more molecular symmetry groups which partially contain other symmetry groups or themselves are subgroups to other groups [AdP06].

How is this related to tensor networks and their numerical representation? Assuming our Hamiltonian to be constructed from matrix elements of these single particle orbitals as described in eqs. (3.69) and (3.70), restricts the values of the t and v matrices which can be non-zero. Since integrals of molecular orbitals are scalars and therefore do not change under symmetry transformations, the orbitals must pair up in such a way under the integral that the signs introduced by the transformation cancel out, otherwise the matrix element is zero [AdP06]. This means for instance that hopping elements between sites of different transformation behavior must vanish, as well as interaction terms which do not respect the symmetry. The wave function itself is defined in a certain symmetry sector and the application of the Hamiltonian can not change this particular sector to another one.

The last piece needed in order to connect our molecular symmetry framework to the Wigner-Eckart type of tensor decomposition are character tables. We take the finite group G and would like to represent its (linear) action via a set of matrices Γ by some map ρ

$$G = \{g_1, \dots, g_n\} \xrightarrow{\rho} \{\gamma_1, \dots, \gamma_n\} = \Gamma \ . \tag{4.18}$$

In general, there exist multiple representations of a group, however, there is a particularly interesting subset of representations called the irreps. An irrep is a special map which represents the elements of G in such a way, that

$$\nexists W \subsetneq \Gamma \text{ except } W = \{0\} \text{ such that } \rho(g) \cdot w \in W \qquad \forall w \in W,\ g \in G \ . \tag{4.19}$$

In other words there is no subset (except for the trivial ones) whose elements will end up in that subgroup again upon arbitrary group action. Usually, representations are no irreps, however, for our molecular symmetry cases the elements of the representation can be brought into the form of a direct sum of irreps [Mas98, Hal15],

$$\gamma = \gamma_1 \oplus \gamma_2 \oplus \ldots \oplus \gamma_m = \begin{bmatrix} \boxed{\gamma_1} & & & \\ & \boxed{\gamma_2} & & \\ & & \ddots & \\ & & & \boxed{\gamma_m} \end{bmatrix} , \tag{4.20}$$

where each γ_i matrix operates on its subspace only. Qua constructio the action of the matrices will not be further decomposable onto smaller subspaces. The number of existent irreps is determined by the number of conjugacy classes. The conjugacy classes contain operations of the same type or more formally speaking the conjugacy class of an element γ is defined as

$$\{\gamma' \in \Gamma \mid \exists\, \eta \in \Gamma \text{ such that } \gamma' = \eta^{-1}\gamma\eta\} \ . \tag{4.21}$$

The number of classes is simply equivalent to the number of irreps [AdP06]. We will use this to visualize the representations of a group in square character tables. The columns are labeled by the conjugacy classes of the group, while the rows are labeled by the irreps. The entries are then given by the trace of one of the transformation matrices in this irrep and called characters. Since the elements of the conjugacy class are related by a similarity transformation and the trace is cyclic under permutations, all elements of the class have the same character. An example for this is shown in table 4.3, where two common Abelian symmetry groups are presented. The characters describe the action of group elements categorized by the irrep. Characters may also have special properties, e.g. the one of the identity operation is equal to the degeneracy of orbitals belonging to this irrep.

At this point we return to the application to tensor networks [LS03, CKG04, WVN14b]. Basically, the key point here is to observe that many-body kets inside the Hilbert space and its subspaces transform under irreps of the symmetry group which the Hamiltonian is invariant under. Or, to phrase it differently, we restrict the Hilbert space to be spanned by vectors which are part of a sub Hilbert space in accordance with the symmetry. This makes it possible to label every element in this Hilbert space by an irrep. We just extend this with the molecular symmetries, as is usually done by the spin symmetry and now write [WVN14b]

$$|n = 0, s_z = 0, A = 0\rangle\,,\ |n = 1, s_z = 1/2, A = a\rangle\,,\ |n = 1, s_z = -1/2, A = a\rangle\,,\ |n = 2, s_z = 0, A = 0\rangle \ . \tag{4.22}$$

$\mathbb{Z}_4$	0 mod 4	1 mod 4	2 mod 4	3 mod 4
Γ_1	1	1	1	1
Γ_2	1	i	−1	−i
Γ_3	1	−1	1	−1
Γ_4	1	−i	−1	i

C_{2v}	E	C_2	σ_v	σ'_v
A_1	1	1	1	1
A_2	1	1	−1	−1
B_1	1	−1	1	−1
B_2	1	−1	−1	1

Table 4.3: Two examples for customary character tables. The cyclic group $\mathbb{Z}_k$ might be familiar from the condensed matter context, where one uses it to represent 2π periodic momenta, e.g. in hybrid lattices. In this context it characterises rotations of multiples of 90° around an axis. The C_{2v} group is probably most prominent for being the symmetry group of the water molecule. It describes (apart from the trivial identity operation E) the rotation of 180° around the axis going through the oxygen atom while symmetrically bisecting the hydrogens. Furthermore, there is the mirror plane in which the molecule itself lies and the mirror plane going through the oxygen flipping the hydrogens.

The extension to $SU(2)$ works with the same principle. Here, we used a as a placeholder for the symmetry irrep to which the respective orbital belongs to, i.e. which determines the transformation of e.g. the HF orbital the matrix elements originated from. The notation $A = 0$ refers to the empty or doubly filled orbital belonging to the trivial representation of the group which maps all elements to the identity element of the algebra Γ. The advantage of this method now is, as mentioned before, that a contraction of two vectors belonging to different irreps is immediately zero and does need next to no CPU-time. However, in order to be able to perform all the operations necessary for our variational optimizations or to compute observables the tensor product of two irreps is required

$$|n, s_z, A\rangle \otimes |n', s'_z, A'\rangle \ . \tag{4.23}$$

In most of the cases this is not going to be an irrep itself, luckily there exists a way to decompose it into a direct sum of such through the means of CGCs [Hal15]. Since we worked solely with Abelian point groups, the incorporation of CGCs is not the sophisticated procedure usually necessary. Rather we can easily decompose the product

$$|n, s_z, A\rangle \otimes |n', s'_z, A'\rangle = |\tilde{n}, \tilde{s}_z, \tilde{A}\rangle \tag{4.24}$$

by means of the character table. The element on the right hand side is just determined by multiplying the characters of the elements on the left hand side and searching in the character table for the correct result [AdP06]. Before we demonstrate this for a particular example, please note that in our case this direct sum only has one addend, but usually it would be more, e.g. in the $SU(2)$ case

$$|S = 1/2\rangle \otimes |S = 1/2\rangle = |S = 0\rangle \oplus |S = 1\rangle \ . \tag{4.25}$$

Serving the purpose of better understanding, two examples are highlighted, one with $\mathbb{Z}_4$ and the other one with C_{2v}. If we multiply Γ_2 and Γ_4 we arrive at the trivial representation Γ_1, just as we expected. On the other hand, $A_2 \otimes B_2 = B_1$ by means of table 4.3.

To briefly summarize the approach to implement molecular symmetries in a tensor network:

1. Denote the irreps by some label, e.g. integer numbers or the labels common in chemical literature.
2. Define the product decomposition via the character table. In the Abelian case it is just a hard-coded function connecting two elements to another one. In the non-Abelian case we need the correct computation of CGCs.
3. Create an inhomogeneous lattice where the sites are labeled with respect to their transformation behaviour under the group action by irreps. Empty and doubly occupied orbitals belong to the trivial representation here. Up-and down-spin belong to the same orbital if there exists an exchange symmetry.
4. Proceed with the tensor network methods in an ordinary fashion.

Time evolution

5

As mentioned previously, DMRG was originally designed for systems in equilibrium and is incredibly powerful for their description by solving the time independent many-body Schrödinger equation

$$H \left|\psi\right\rangle = E_0 \left|\psi\right\rangle \ , \tag{5.1}$$

in order to obtain the state $\left|\psi\right\rangle$ with the lowest energy E_0, and possibly some low lying excitations. However, many interesting features of physical many-body systems are no properties of the static system but need to incorporate dynamics. Therefore, early on, people tried to extend the DMRG to be able to compute time dependent properties [Hal95, Jec02, KW99]. Interestingly, these works did not try to construct the time dependent wave function from the ground state but rather tried to compute momentum space correlators with the help of the momentum representation of operators. Doing so, they basically extended the DMRG algorithm for a rather expensive construction of powers of the Hamiltonian applied to the ground state, which is superficially similar to computing the time evolution via the application of the operator exponential

$$\left|\psi(t)\right\rangle = \mathrm{e}^{-\mathrm{i}t\hat{H}} \left|\psi(0)\right\rangle = \left(1 - \mathrm{i}t\hat{H} - \frac{t^2}{2}\hat{H}^2 + \ldots\right) \left|\psi(0)\right\rangle \ . \tag{5.2}$$

Here, we defined the Hamiltonian to be time independent, otherwise we would need a Dyson-series [Dys49].

These approaches are not perfect, one needs to struggle in manifold ways, e.g. one needs to run the entire algorithm for each frequency [Jec02], furthermore, an explicit construction of several Lanczos vectors is always required. Since these get increasingly expensive, usually the approximation gets unfaithful for high energy excitations, which can be treated by more involved techniques and the additional representation of the vectors in a truncated basis (it is DMRG after all) comes in additionally [KW99].

This motivated to look for a way to compute time-dependent states from an initial state (e.g. an excited state or a ground state to a different Hamiltonian), unfortunately time evolution is somewhat different from ground state searches. While the MPS ansatz is custom tailored to 1d quantum states, i.e. the solution gets increasingly accurate during the simulation. Time evolution does not have this convenient feature. This means we can afford to not find the perfect ground state during a DMRG sweep, the error will be corrected later on, while a wrong time evolved state is plainly wrong. Due to this a variety of time evolution methods for tensor networks were established [PKS⁺19], ranging from explicit integration [LXW03, CM02] to the Trotterization [Suz76a] of the time evolution operator [Vid03] today known as time-evolving block decimation (TEBD). It shall be mentioned these can also be used for imaginary time, for instance to do calculations at finite temperature [VGRC04].

Each of these methods suffer from shortcomings, to begin with, the explicit construction of the powers of $\hat{H}$ (applied to the state), also referred to as global Krylov method, is enormously expensive in CPU-time and memory, while in turn very precise. Since norms of MPOs grow exponentially in the system size L, one can usually not construct the full time evolution operator, the number of vectors necessary would be beyond any reason. However one can exploit the propagator property of the time evolution operator, i.e.

$$\hat{U}(t, 0) = \exp\left(-\mathrm{i}(t - 0)\hat{H}\right) = \exp\left(-\mathrm{i}(t - t')\hat{H}\right) \exp\left(-\mathrm{i}(t' - 0)\hat{H}\right) \tag{5.3}$$

to decompose the total time $t = \Delta t/n$. If n is large enough, the convergence of the Krylov subspace is given via a few vectors and we just have to apply the evolution operator many times. The primary cost is then the zip-up application of the operator to the state as we already discussed in section 3.3.3, followed by a direct truncation. Both operations can be estimated cubically in the bond dimension m for each lattice site. TEBD also involves the application of operators, but in the form of several two site gates. The basic principle is to divide the Hamiltonian into sub-lattices whose operator algebras commute, such that one can exponentiate $\hat{H}$ explicitly very cheaply, provided the time step is small again. That reduces the time evolution to sweeps through the system, creating two orbital Hilbert spaces and applying the respective gate. However, while the splitting into disjoint sublattices is easy for local Hamiltonians, running TEBD for generic systems is rather tricky. It involves a complicated procedure in which one swaps orbitals (compare to section 3.4.1), such that the respective sites for the next gate application lie next to each other. After a successful application one has to swap the sites back.

This served as a motivated to look for the construction of a solution for the time evolution of tensor networks which can operate on arbitrary systems while intrinsically making use of the locality of the ansatz and being (hopefully) cheap enough to evolve to long times. The currently best method to do so is time-dependent variational principle (TDVP), which we will be discussing in the following.

Time-dependent variational principle 5.1

TDVP is the application of the Dirac-Frenkel principle [Dir30, Fre34] for the time evolution of quantum states to a tensor network. Broadly speaking it is a time evolution method for any variational state ansatz. Dirac tried to time evolve Hartree states, i.e. product state ansatzes for many body wave functions (which in our framework would have bond dimension $m = 1$). He realized that the time evolution will not preserve the product state property, i.e. the state will become a correlated state. As a solution he proposed to project down the state back to a product state, with the projector keeping the disturbance of the state minimal. In a more modern language one says that the number of all states with a fixed bond dimension formulates a manifold as a subregion of the Hilbert space [LOV15]. In order to keep the state expressible in the MPS form during the time evolution process one needs to formulate a projector into the tangent space of the state.

We begin with the Schroedinger equation, giving the time evolution of a state at a certain time

$$|\psi(t)\rangle^{\bullet} = -\mathrm{i}\hat{H}\,|\psi(t)\rangle \ , \tag{5.4}$$

connecting the time derivative of the wave function with itself. Enforcing that the time evolution stays within the original Hilbert space we extend this to

$$|\psi(t)\rangle^{\bullet} = -\mathrm{i}\hat{P}_{\psi}\left(\hat{H}\,|\psi(t)\rangle\right) \tag{5.5}$$

with the projector $\hat{P}_{\psi}$ taking state from one manifold to a reduced bond dimension manifold [HLO+16, PKS+19]. This way we ensure that, even though we can not represent the state correctly with the original amount of resources, it is as close as possible to the true state. Following the argument of [HLO+16] we need the basis vectors of the tangent space

$$\frac{\partial\,|\psi\rangle}{\partial M^{n_i}_{\alpha\beta}} = \sum_{\vec{n}\backslash n_i} (M^{n_1}\dots M^{n_{i-1}})_{\alpha}\,(M^{n_{i+1}}\dots M^{n_L})_{\beta}\,|n_1\dots n_L\rangle = |\alpha\rangle\,|n_i\rangle\,|\beta\rangle \tag{5.6}$$

in order to compute elements of this space. Therefore, any state can be expanded as

$$|\Theta[B]\rangle = \sum_{\alpha\beta n_i} B^{n_i}_{\alpha\beta}\,|\alpha\rangle\,|n_i\rangle\,|\beta\rangle \ , \tag{5.7}$$

where B are arbitrary coefficients. Our aim is then to find the representation of $\hat{P}_{\psi}$, such that it satisfies

$$\min_{B}\left\|\left(1-\hat{P}_{\psi}\right)\hat{H}\,|\psi\rangle\right\| \quad \Rightarrow \quad \min_{B}\sum_{n_i}\mathrm{tr}\left(B^{n_i}B^{n_i\dagger} - B^{n_i}\tilde{M}^{n_i\dagger} - \tilde{M}^{n_i}B^{n_i\dagger}\right) \ . \tag{5.8}$$

Together with the definition of the left-and right-bases $|\alpha\rangle\,,|\beta\rangle$ this gives the shape of the projector [HCO+11, HLO+16]

$$\begin{aligned}\hat{P}_{\psi} &= \sum_{i=1}^{L}\left(\sum_{\alpha}|\alpha\rangle_{i-1\ i-1}\langle\alpha|\right)\otimes\hat{1}_i\otimes\left(\sum_{\beta}|\beta\rangle_{i+1\ i+1}\langle\beta|\right) - \sum_{i=1}^{L-1}\left(\sum_{\alpha}|\alpha\rangle_{i\ i}\langle\alpha|\right)\otimes\left(\sum_{\beta}|\beta\rangle_{i+1\ i+1}\langle\beta|\right) && (5.9)\\ &= \sum_{i=1}^{L}\hat{P}^{L}_{i-1}\otimes\hat{1}_i\otimes\hat{P}^{R}_{i+1} - \sum_{i=1}^{L-1}\hat{P}^{L}_{i}\otimes\hat{P}^{R}_{i+1} \ . && (5.10)\end{aligned}$$

For the moment this did not make the solution of the equation easier, but rather a lot trickier, as we are now confronted with

$$|\psi(t)\rangle^{\bullet} = -\mathrm{i}\left(\sum_{i=1}^{L} \hat{P}^{L}_{i-1} \otimes \hat{1}_i \otimes \hat{P}^{R}_{i+1} - \sum_{i=1}^{L-1} \hat{P}^{L}_{i} \otimes \hat{P}^{R}_{i+1}\right) \hat{H}\,|\psi(t)\rangle \ . \tag{5.11}$$

This can be dissolved by Trotterization of eq. (5.11), meaning that instead of the full equation we seek a solution for each summand individually [Tro59, Suz76b, Suz85]. Therefore, we arrive at an hierarchy of differential equations for wave functions $|\psi_i\rangle$ and $|\phi_i\rangle$, where i is the hierarchy step and ψ_i is the solution of the first term, while ϕ_i corresponds to the second term [PKS+19]. We begin with the first site and evolve for a small time step Δt

$$|\phi_1(t)\rangle^{\bullet} = -\mathrm{i}\left(\hat{P}^{L}_{0} \otimes \hat{1}_1 \otimes \hat{P}^{R}_{2}\right) \hat{H}\,|\phi_1(t)\rangle \quad \text{with } |\phi_1(t=0)\rangle = |\psi(0)\rangle \tag{5.12}$$

$$|\psi_1(t)\rangle^{\bullet} = -\mathrm{i}\left(-\hat{P}^{L}_{1} \otimes \hat{P}^{R}_{2}\right) \hat{H}\,|\psi_1(t)\rangle \quad \text{with } |\psi_1(t=0)\rangle = |\phi_1(\Delta t)\rangle \ . \tag{5.13}$$

For a canonically normalized state we can close from the left side with the conjugate bases $\langle\beta|\,\langle n_1|\,\langle\alpha|$, therefore we obtain differential equations soley for the local site tensors

$$\dot{M}^{n_1'}_{\alpha'\beta'} = -\mathrm{i}\sum_{\alpha\beta n_1} \langle\beta' n_1' \alpha'|\hat{H}|\alpha n_1 \beta\rangle\, M^{n_1}_{\alpha\beta} = -\mathrm{i}\sum_{\alpha\beta n_1} (H_{\text{eff}})^{n_1' n_1}_{\alpha'\beta',\alpha\beta} M^{n_1}_{\alpha\beta} \tag{5.14}$$

$$\dot{C}_{\bar{\alpha}'\alpha'} = \mathrm{i}\sum_{\bar{\alpha}\alpha} \langle\bar{\alpha}'\alpha'|\hat{H}|\bar{\alpha}\alpha\rangle\, C_{\bar{\alpha}\alpha} = \mathrm{i}\sum_{\bar{\alpha}\alpha} (H_{\text{eff}})_{\bar{\alpha}'\alpha',\bar{\alpha}\alpha} C_{\bar{\alpha}\alpha} \ , \tag{5.15}$$

where C is the transfer tensor which naturally arises when trying to obtain the bond bases by exploiting $|\bar{\alpha}\rangle = \sum_{\alpha n_1} A^{n_1}_{\alpha\bar{\alpha}}\,|n_1\rangle$ for the left-normalized MPSes. Looking at the indices as multi-indices, these equations both have the charm of matrix-vector multiplications, which can be solved by exponentiating the tensor, e.g. via a Lanczos procedure as

$$M^{n_1}_{\alpha\beta}(\Delta t) = \mathrm{e}^{-\mathrm{i}\hat{H}_{\text{eff}}\Delta t} \cdot M^{n_1}_{\alpha\beta}(0) \tag{5.16}$$

$$C_{\bar{\alpha}\alpha}(\Delta t) = \mathrm{e}^{\mathrm{i}\hat{H}_{\text{eff}}\Delta t} \cdot C_{\bar{\alpha}\alpha}(0) \ . \tag{5.17}$$

We proceed now site by site and always use the integrated solution at time-step Δt as an input to the next, i.e. for any iteration step we do

$$|\phi_i(t)\rangle^{\bullet} = -\mathrm{i}\left(\hat{P}^{L}_{i-1} \otimes \hat{1}_i \otimes \hat{P}^{R}_{i+1}\right) \hat{H}\,|\phi_i(t)\rangle \quad \text{with } |\phi_i(t=0)\rangle = |\psi_{i-1}(\Delta t)\rangle \tag{5.18}$$

$$|\psi_i(t)\rangle^{\bullet} = -\mathrm{i}\left(-\hat{P}^{L}_{i} \otimes \hat{P}^{R}_{i+1}\right) \hat{H}\,|\psi_i(t)\rangle \quad \text{with } |\psi_i(t=0)\rangle = |\phi_i(\Delta t)\rangle \ . \tag{5.19}$$

Note that if we keep shifting the orthogonality center in order to maintain canonical normalization, the equations always collapse to differential equations for one rank three (or two) tensor.

Next we want to prove that our expansion scheme actually is equivalent to the full solution of the time-dependent Schroedinger equation, i.e. that $|\psi_L(\Delta t)\rangle = |\psi(\Delta t)\rangle$. For this we define the shorthands

$$\hat{H}^{j}_{f} = \left(\hat{P}^{L}_{i-1} \otimes \hat{1}_i \otimes \hat{P}^{R}_{i+1}\right) \hat{H} \tag{5.20}$$

$$\hat{H}^{j}_{b} = \left(\hat{P}^{L}_{i} \otimes \hat{P}^{R}_{i+1}\right) \hat{H} \tag{5.21}$$

and expand the i-th iteration step as

$$|\psi_i(\Delta t)\rangle = |\psi_i(0)\rangle + \Delta t\,|\psi_i(0)\rangle^{\bullet} + \frac{\Delta t^2}{2}\,|\psi_i(0)\rangle^{\bullet\bullet} + \dots \tag{5.22}$$

$$= \left(1 + \mathrm{i}\Delta t \hat{H}^{b}_{j-1} - \frac{\Delta t^2}{2}\hat{H}^{b}_{j-1}\hat{H}^{b}_{j-1} + \dots\right) \underbrace{|\psi_i(0)\rangle}_{=|\phi_i(\Delta t)\rangle} \tag{5.23}$$

$$= \left(1 + \mathrm{i}\Delta t \hat{H}^{b}_{j} - \frac{\Delta t^2}{2}\hat{H}^{b}_{j}\hat{H}^{b}_{j} + \dots\right)\left(1 - \mathrm{i}\Delta t \hat{H}^{b}_{j} - \frac{\Delta t^2}{2}\hat{H}^{f}_{j}\hat{H}^{f}_{j} + \dots\right) |\psi_{i-1}(0)\rangle \ , \tag{5.24}$$

i.e. the i-th step depends on the $i-1$-iteration step. Recursively putting this formula into itself for $|\psi_L(t)\rangle$ until one arrives at $|\psi_0(0)\rangle$ yields up to second order [PKS+19]

$$\begin{aligned}|\psi(\Delta t)\rangle &= |\psi_L(\Delta t)\rangle\\ &= \left(1+\mathrm{i}\Delta t\hat{H}^b_{L-1}-\frac{\Delta t^2}{2}\hat{H}^b_{L-1}\hat{H}^b_{L-1}+\dots\right)\left(1-\mathrm{i}\Delta t\hat{H}^f_{L-1}-\frac{\Delta t^2}{2}\hat{H}^f_{L-1}\hat{H}^f_{L-1}+\dots\right)\\ &\quad\cdot\ldots\cdot\left(1+\mathrm{i}\Delta t\hat{H}^b_1-\frac{\Delta t^2}{2}\hat{H}^b_1\hat{H}^b_1+\dots\right)\left(1-\mathrm{i}\Delta t\hat{H}^f_1-\frac{\Delta t^2}{2}\hat{H}^f_1\hat{H}^f_1+\dots\right)|\psi(0)\rangle \qquad (5.25)\\ &= \left(1-\mathrm{i}\Delta t\underbrace{\left(\sum_{j=1}^{L}\hat{H}^f_j-\sum_{j=1}^{L-1}\hat{H}^b_j\right)}_{=\hat{H}}-\frac{\Delta t^2}{2}\hat{H}^2-\frac{\Delta t^2}{2}\left(\text{commutators of }\hat{H}^f_j\text{ and }\hat{H}^b_j\right)+\dots\right)|\psi(0)\rangle\ . \qquad (5.26)\end{aligned}$$

This is equal up to first order to the true solution

$$\left(1-\mathrm{i}\Delta\hat{H}-\frac{\Delta t^2}{2}\hat{H}^2+\dots\right)|\psi(0)\rangle\ , \tag{5.27}$$

or to put it differently, if the time-step is small enough the solution is correct. We make use of the composition property and split the entire time evolution into small slides.

We can even improve this further by taking half the time-step $\Delta t/2$ and making a forward and a backward evolution. By this we get rid of all the commutators in second order, since they cancel each other due to reversed order and the anti-symmetry of the commutator [PKS+19]. This doubles the price of the exponentiation of the effective Hamiltonian (which is usually the most expensive in variational algorithms), however the necessary contractions are all already preexistent and therefore the algorithm is exact in second order while usually staying below twice the CPU-time.

The careful reader might have raised the questions why we actually want to stay on the original MPS manifold, i.e. why we want to keep the bond dimension fixed. After all we have no guarantee that the state we are seeking is well represented with the bond dimension profile of the initial state. The case is even worse since usually correlations grow exponentially in time for 1d quantum systems [Osb06, GKSS05, CC05]. They usually saturate for some long time limit but this just means that the necessary bond dimension is huge [CC05]. Eventually, this can destroy the area law which originally made the tensor network ansatz possible in the first place. However, for many setups it can still be possible to do time evolution of tensor network states and reach excellent results for intermediate and long times [Sch11]. In order to be able to do so we need to allow the bond dimension to grow such that it can leave the subspace of the initial state. This is usually done by the two-site algorithm which just mimics the two-site optimization scheme of DMRG. For ground states, one gradually updates two sites, then shifts to the next site continuing with updated site and a new site (like a [12] 3 4$\cdots\rightarrow$ 1 [23] 4... scheme). Therefore, the tangent space is needed with respect to the two orbital subspace, i.e. we again have an infinite amount of variational parameters between them. By splitting the two orbital tensor when moving on to the next site we truncate this to a predefined value m' or $\omega=\sum_r s_r$, which is hopefully enough to describe the state correctly. The two site tangent space elements are in analogy to eq. (5.7)

$$|\Theta[B]\rangle = \sum_{\alpha\beta n_i n_{i+1}} B^{n_i n_{i+1}}_{\alpha\beta}\,|\alpha\rangle\,|n_i n_{i+1}\rangle\,|\beta\rangle\ , \tag{5.28}$$

where we are now looking at the two site variational subspace [HLO+16]. This leads to a projector of the form [HLO+16]

$$\begin{aligned}\hat{P}_\psi &= \sum_{i=1}^{L-1}\left(\sum_\alpha|\alpha\rangle_{i-1\ i-1}\langle\alpha|\right)\otimes\hat{1}_i\otimes\hat{1}_{i+1}\otimes\left(\sum_\beta|\beta\rangle_{i+2\ i+2}\langle\beta|\right)\\ &\quad-\sum_{i=1}^{L-2}\left(\sum_\alpha|\alpha\rangle_{i\ i}\langle\alpha|\right)\otimes\hat{1}_{i+1}\otimes\left(\sum_\beta|\beta\rangle_{i+2\ i+2}\langle\beta|\right)\ .\end{aligned} \tag{5.29}$$

The application and Trotterization then lead to the local update scheme [PKS+19]

$$\dot{M}^{n'_i n'_{i+1}}_{\alpha'\beta'} = -\mathrm{i} \sum_{\substack{\alpha\beta n_i \\ n_{i+1}}} \langle \alpha' n'_i n'_{i+1} \beta' | \hat{H} | \alpha' n_i n_{i+1} \beta' \rangle \, M^{n_i n_{i+1}}_{\alpha\beta} \tag{5.30}$$

$$\dot{M}^{n'_{i+1}}_{\bar{\alpha}'\beta'} = \mathrm{i} \sum_{\alpha\beta} \langle \bar{\alpha}' n'_{i+1} \beta' | \hat{H} | \bar{\alpha} n_{i+1} \beta \rangle \, M^{n_{i+1}}_{\alpha\beta} \ . \tag{5.31}$$

The solution to this is the evolution in the two orbital Hilbert space

$$M^{n_i n_{i+1}}_{\alpha\beta}(\Delta t) = \mathrm{e}^{-\mathrm{i}\hat{H}_{\mathrm{eff}}\Delta t} \cdot M^{n_i n_{i+1}}(0) \tag{5.32}$$

followed by the back evolution of the site in sweep direction

$$M^{n_{i+1}}(\Delta t) = \mathrm{e}^{\mathrm{i}\hat{H}_{\mathrm{eff}}\Delta t} \cdot M^{n_{i+1}}(0) \ . \tag{5.33}$$

If one splits the evolution into back-and forward-sweep while taking half the time step, one again arrives at a second order integrator just like for the single site case [PKS+19].

One last thing to mention is that apart from the usually dominant truncation error and the Trotter error we discussed, there are two more possible sources of errors in TDVP. First, the exponentiation of the effective Hamiltonian to construct the local solutions in eqs. (5.16) and (5.17) is not exact since we cut it off after some finite value [PKS+19]. This error is usually controlled by the time step and therefore very much under control. The second possible source is the projection error originating from the fact that the definition of the projectors eq. (5.10) is only exact if $|\psi\rangle$ is actually the true state. When truncating the state this will disturb the projector and lead to wrong results [PKS+19]. This error is usually also subdominant and can be improved by increasing the bond dimension, just as for the truncation error. Furthermore, it can be well monitored by comparing the variance of the state with local methods like the two site variance [HHS18].

TDVP on TTNS 5.2

Now we want to generalize our finding for the time evolution of MPS to trees what we are going to do mostly according to [BA20]. Basically, it is the same procedure again, the site tensors just have more than two virtual legs. For this we have to break with the locality of the ansatz and define an artificial ordering of modes and branching tensors again. In our cases we always chose it to be from top to bottom and from left to right, i.e. the last node is the right-most and bottom-most one. Consider a contraction between a branching and a physical node, canonically normalized as it was described in section 3.3.2

$$|\psi\rangle = \sum_{rabn_i} M^{n_i}_{rab} \, |r\rangle \, |n_i\rangle \, |b\rangle \, |a\rangle \ . \tag{5.34}$$

For our setup we did not only test this scheme, but also the case where one has solely one node, be it physical or branching and the contraction of two physical and a branching node as we shall discover soon. For didactical reasons we will perform the calculations on this one. Elements of our tangent space are again parametrized in the following way [HLO+16, BA20]

$$|\Theta[B]\rangle = \sum_{rabn_i} B^{n_i}_{rab} \, |r\rangle \, |n_i\rangle \, |b\rangle \, |a\rangle \ , \tag{5.35}$$

where B are again the coefficients of the vector expansion. As in the MPS case, the kernel of the map Θ represents is not empty but rather

$$\ker\Theta = \left\{ B^{n_i}_{rab} \,\middle|\, B^{n_i}_{rab} = \sum_c \Big(N(r)^{n_i}_{cab} X_{cr} \,\mathrm{sgn}(r \to L) + N(a)^{n_i}_{rcb} X_{ca} \,\mathrm{sgn}(a \to L) + N(b)^{n_i}_{rac} X_{cb} \,\mathrm{sgn}(b \to L) \Big) \right\} . \tag{5.36}$$

Where the X objects are arbitrary matrices and $N(x)^{n_i}$ is the site tensor when the entire network is normalized towards the x neighbour of site i [BA20]. Here, we also introduce the sign of the leg, which is one if the leg is pointing towards the last node and minus one otherwise. This is an artefact of the fact that the tensor network ansatz has more degrees of freedom than necessary (as also discussed in section 3.3.2) which need to be gauge-fixed. We change notation to label the indices with greek symbols, with which we want to indicate that this works for any of the bonds and there is no particular connection between the ordering of the indices and the topology and more, and impose the gauge constraint

$$\sum_{\alpha\gamma n_i} \left(B^{n_i}_{\alpha\beta'\gamma}\right)^\dagger N(\beta)^{n_i}_{\alpha\beta\gamma} = 0 \qquad \forall\beta,\beta', \forall i \neq L\ . \tag{5.37}$$

This will be our Lagrange multiplier to the otherwise same optimization problem as in eq. (5.8)

$$\min_B \left[\sum_{n_i\,\alpha\beta\gamma} B^{n_i}_{\alpha\beta\gamma}{}^\dagger B^{n_i}_{\alpha\beta\gamma} - B^{n_i}_{\alpha\beta\gamma}{}^\dagger F^{n_i}_{\alpha\beta\gamma} - F^{n_i}_{\alpha\beta\gamma}{}^\dagger B^{n_i}_{\alpha\beta\gamma} - \sum_{i=1}^{L-1}\sum_{\beta\beta'}\lambda^i_{\beta\beta'}\sum_{\alpha\gamma n_i} B^{n_i}_{\alpha\beta'\gamma}{}^\dagger N(\beta)^{n_i}_{\alpha\beta\gamma}\right]\ . \tag{5.38}$$

This objective can be minimized by taking the derivative $\partial/\partial B^{\bar{n}_i}_{\bar{\alpha}\bar{\beta}\bar{\gamma}}$ which yields

$$B^{n_i}_{\alpha\beta\gamma} = F^{n_i}_{\alpha\beta\gamma} + \sum_{i=1}^{L-1}\sum_{\beta'}\lambda^i_{\beta'\beta}N^{n_i}_{\alpha\beta'\gamma} \tag{5.39}$$

or plugging in the Lagrange multiplier

$$B^{n_i}_{\alpha\beta\gamma} = F^{n_i}_{\alpha\beta\gamma} - \sum_{\tilde{\alpha}\tilde{\gamma}n_i'} N(\beta)^{n_i}_{\alpha\beta'\gamma}N(\beta)^{n_i'}_{\tilde{\alpha}\beta'\tilde{\gamma}}F^{n_i'}_{\tilde{\alpha}\beta\tilde{\gamma}} \tag{5.40}$$

which gives the form of the projector as [BA20]

$$\begin{aligned}\hat{P}_\psi =& \sum_{i=1}^{L}\left(\sum_\alpha |\alpha\rangle_{i-1\ i-1}\langle\alpha|\right)\otimes\hat{1}_i\otimes\left(\sum_\beta |\beta\rangle_{i+1\ i+1}\langle\beta|\right)\otimes\left(\sum_\gamma |\gamma\rangle_{i+2\ i+2}\langle\gamma|\right)\\ &-\sum_{i=1}^{L-1}\left(\sum_\alpha |\alpha\rangle_{i\ i}\langle\alpha|\right)\otimes\left(\sum_\beta |\beta\rangle_{i+1\ i+1}\langle\beta|\right)\otimes\left(\sum_\gamma |\gamma\rangle_{i+2\ i+2}\langle\gamma|\right)\ .\end{aligned} \tag{5.41}$$

Note, that we arbitrarily chose α to connect to the root node of i and that the notation $i+1,\ i+2$ is meant symbolically as the left and right leaves.

With these powerful equations at hand we have the possibility to formulate the single-site, the two-node and the two-site TDVP for T3NS. The application of the projector again leads to a modified Schrödinger equation which is then solved by Trotterizing into a hierarchy of differential equations. The canonical normalization reduces the problems to local ones, one forward and one backward in time. However, what does actually change is the pattern in which we apply our effective Hamiltonian and what the sites are which are back-evolved, as we demonstrate in alg 3. As we can see the concepts of forward evolution of the variational Hilbert space and the subsequent backward evolution stay the same. However, apart from the concept of an artificial (planar) ordering a new important concept comes into play, the one of the leg pointing towards the end of the path through this ordering. So we do not update the nodes in order but rather only update if we do not come along this node again following the path through the system. Otherwise, we just normalize the entire network to work with local equations, i.e. we canonically normalize the state and compute new contractions for the system. When actually using a true two orbital algorithm we can spare one additional evolution by checking if we would need to later on do so and if so, not evolving back. Regarding the sweeping patterns they are rather trivial with the exception of the two site update, which is described in fig. 5.1. Usually coming from the top we perform the update ① first before recursively visiting the subtree on the left. When coming back from there we do ② and afterwards visit the subtree on the right. And finally returning from there we go up by performing ③.

Before closing this quite technical section let us write a few words on the difference between the two-node and the two-site TDVP. Since the two-node version has a factor of d less entries the computations are usually

Algorithm 3: Performing TDVP on a T3NS.

```
Data: MPS state $|\psi(0)\rangle$ and MPO Hamitlonian $\hat{H}$
Result: Evolved state $|\psi(\Delta t/2)\rangle$
Def evolveSingle:
    Compute time evolution of single site $M(\Delta t/2) \leftarrow \mathrm{e}^{-\mathrm{i}H_{\mathrm{eff}}\Delta t/2} M(0)$;
    Split away the bond $AC = M$ (e.g. via an SVD);
    $M \leftarrow A$;
    Compute $C \leftarrow \mathrm{e}^{\mathrm{i}H_{\mathrm{eff}}\Delta t/2} C$;
    Multiply $C$ into the next site.;
    return;
Def evolveTwoNode:
    Compute time evolution of physical branching contraction $M(\Delta t/2) \leftarrow \mathrm{e}^{-\mathrm{i}H_{\mathrm{eff}}\Delta t/2} M(0)$;
    Split the two tensors again shifting the orthogonality center into the sweep direction $PSB = M$;
    Store the one which is not in sweep direct;
    Back evolve the other one $M \leftarrow \mathrm{e}^{\mathrm{i}H_{\mathrm{eff}}\Delta t/2} M$;
    return;
Def evolveTwoSide:
    Compute time evolution of physical branching physical contraction $M(\Delta t/2) \leftarrow \mathrm{e}^{-\mathrm{i}H_{\mathrm{eff}}\Delta t/2} M(0)$;
    Split into two tensors, the current physical site tensor and a physical branching contraction in the sweep direction. Multiply the singular values weights into the latter. $PC = M$;
    if update direction ≠ direction on the path to $L$ then
        Back evolve the entire remainder $C \leftarrow \mathrm{e}^{\mathrm{i}H_{\mathrm{eff}}\Delta t/2} C$;
    end
    Split the remaining site tensor into branching and physical again $BP' = C$ shifting the orthogonality center into the physical site;
    if update direction = direction on the path to $L$ then
        Back evolve the second physical tensor $P' \leftarrow \mathrm{e}^{\mathrm{i}H_{\mathrm{eff}}\Delta t/2} P'$;
    end
    return;
Def update:
    if sweeping direction = current element on path $p_i$ then
        if $i$ is a physical node then
            Update according to one of the pattern, i.e. evolveSingle, evolveTwoNode or evolveTwoSide.;
        end
        if $i$ is a branching node then
            if doing an update involving two physical nodes then
                Normalize network towards sweeping direction;
            else
                Update according to pattern;
            end
        end
    else
        Normalize network towards sweeping direction;
    end
    return;
Define a path going from the root to the last node $L$ and store it $p \leftarrow [p_1, \ldots p_{L-1}]$;
Start on the root: $i \leftarrow root$;
while $i \neq L$ do
    update;
    Follow path to next node;
    return;
end
while $i \neq root$ do
    update;
    Go path backwards to previous node;
    return;
end
```

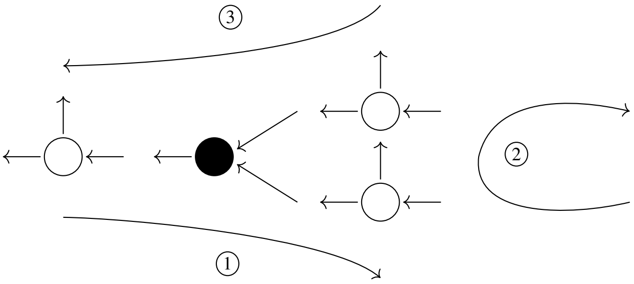

Figure 5.1: Showing three possible ways to perform an update, involving two physical nodes and a branching node.

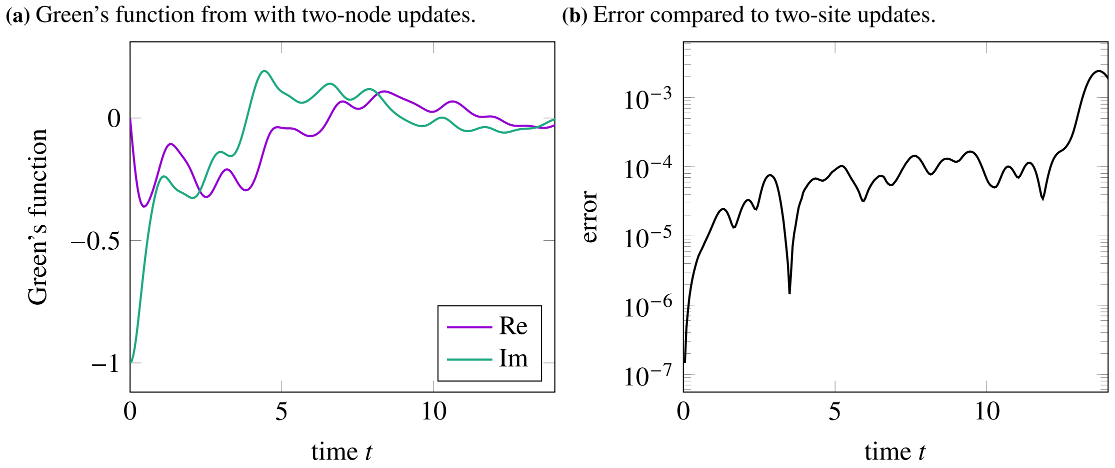
(a) Green's function from with two-node updates.

(b) Error compared to two-site updates.

Figure 5.2: Green's function for an $L = 660$ real time DMFT calculation of a three band model with different time evolution schemes.

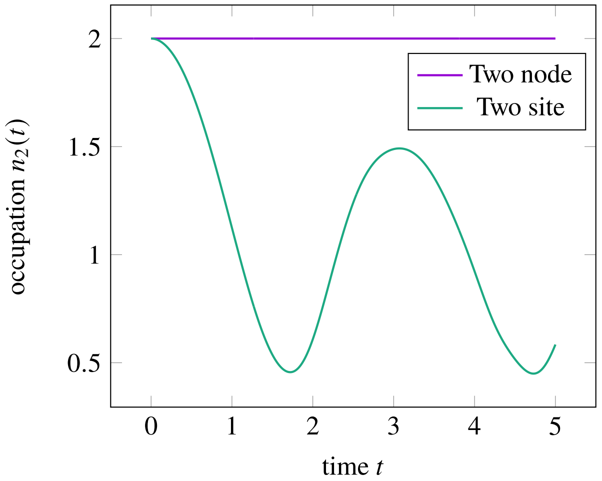

Figure 5.3: Time evolution of the occupation of the initially doubly occupied site.

faster, especially when using larger local Hilbert spaces. However, it is not a pure single site algorithm since the variational space of subsequent steps overlaps by always one node. This way, it can be very practical when the propagation of excitations is too fast for single site [CC05] but we still do not want to employ the full two site algorithm. We benchmarked a numerically challenging DMFT calculation where an improvement up to the factor of the local dimension d can be achieved in fig. 5.2. However, it is still not a total substitute for the full algorithm, since it can get stuck and display wrong results thereafter. As an example for this we included the benchmark of a three site system, initialized with a double occupation on one site. The dynamics are governed by the Hamiltonian

$$\hat{H} = -\sum_{\langle i,j\rangle} \hat{c}_i^\dagger \hat{c}_j^\dagger + \sum_{i=1}^{3} \hat{n}_{\uparrow\downarrow,i} \; , \tag{5.42}$$

i.e. the system penalizes double occupancies. The result of this can be seen in fig. 5.3 where we recognize that the initial occupation decays to different modes, as it should, for the two-site algorithm but that the system freezes for the physical branching complex. In retrospective this is not all too surprising, since a double occupancy is an excitation for this model, however the system can not re-distribute the particle somewhere else. Therefore, excitations of these kind are stuck on the orbital permanently and results will be wrong. However, nothing forces one to just use one algorithm, i.e. we made good experiences with hybrid approaches. One can save a lot of runtime

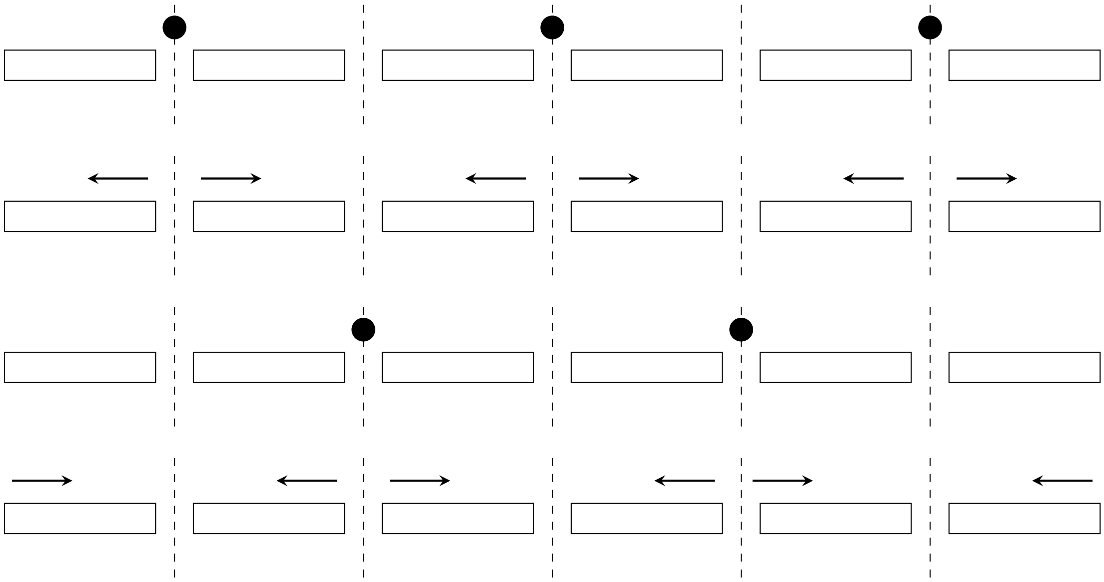

Figure 5.4: Sweeping pattern for six subchains in the MPS. We start by synchronizing the links which have a circle above them, either through a two site update for the boundaries or by three single site updates such that each site gets the updated environment of the other worker. Then we sweep in the direction of the arrow followed by another sync and a subsequent backsweep.

by running TDVP first with two sites, intermediately with just two nodes and at the end, when the system allows it, run the pure single site algorithm. The knowledge when to switch from one algorithm to another is however model dependent and often has to be acquired by a trial and error like approach, e.g. by scaling the bond dimension and checking whether it is converged or not [KLR18].

Parallel TDVP 5.3

In the following we will approach the real space parallelization of TDVP [SGL+20]. Certainly, the term "real space" might be misleading since we do not always work in a position basis. What we are constating is that the orbitals which make up the nodes in the tensor network are variationally optimized in parallel. This idea came up originally in the ground state context [SW13], where different workers (i.e. cores on a CPU, CPUs or even computers) simultaneously perform the application of the effective Hamiltonian in subchains of the MPS. Therefore each subchain has to have the opposite sweeping direction of its neighbors. This way, each worker will need to have the resources an individual worker will have, e.g. when parallelizing over tensor blocks, each worker will need the respective number of threads and the amount of memory a serial run would require. The runtime will be the one of the slowest worker, therefore we need to split the workers in such a way that they all approximately need the same time. A dynamic adaption can be reasonable in cases where the bond dimension profile changes during the course of the optimization.

When two workers meet at the boundary of their area they do a joint update, sometimes also referred to as synchronization. The four core steps of the iterative pattern are summarized graphically in fig. 5.4. The basic idea is that since DMRG is an inherently local method, information about an orbital is shifted successively to all other orbitals via the sweeping. Therefore, if nodes are far apart from each other, the optimization will still be correct even if the environment is outdated, because updates which were performed on one bucket are unknown to the others. Of course this works best for strictly local Hamiltonians. If the convergence is not smooth enough one can mix the serial and the parallel procedure at the cost of having to recompute contractions. Apart from some cases, e.g. when systems build up irreversible domain walls, this is a valid procedure, after all we continuously improve the state.

From a technical point of view the main difficulty is to get a mixed canonical representation in each worker. We rely heavily on the system being left- and right-normalized for the equations to get local and stable, since we do not want to deal with generalized eigenvalue problems. For this to be possible we must introduce several orthogonality centres, which can be done to arbitrary high order by inverting the singular value tensor, e.g.

$$|\psi\rangle = \sum_{\vec{n}} A^{n_1} \cdot M^{n_2} \cdot B^{n_3} \cdot B^{n_4} \cdot \ldots |\vec{n}\rangle = \sum_{\vec{n}} A^{n_1} \cdot A^{n_2} \cdot S \cdot B^{n_3} \cdot B^{n_4} \cdot \ldots |\vec{n}\rangle \tag{5.43}$$

$$= \sum_{\vec{n}} A^{n_1} \cdot A^{n_2} \cdot S \cdot S^{-1} \cdot S \cdot B^{n_3} \cdot B^{n_4} \cdot \ldots |\vec{n}\rangle = \sum_{\vec{n}} A^{n_1} \cdot M^{n_2} \cdot S^{-1} \cdot M^{n_3} \cdot B^{n_4} \cdot \ldots |\vec{n}\rangle \ , \tag{5.44}$$

where A are left-normalized, B are right-normalized and M is the orthogonality center [SW13]. In order to establish one orthogonality center for each worker we need to compute one matrix of inverse singular values for each worker except for the last one, which can be done quite easily while normalizing the state. Basically nowhere in eq. (5.25) the order of the Trotterization plays a role. Up to the order we expand we are free to choose any application pattern for the local solution of the differential equation, i.e. no one forces us to update $1 \to 2 \to 3 \to \ldots$. We usually proceed this way, because it minimizes the number of contractions to compute. Even the application of the projector eq. (5.29) leads to local equations eqs. (5.32) and (5.33) again, since we can always absorb $S^{-1}M = A$ or B. The fact that changes if we proceed in parallel is that we do not go through with the recursive chain eq. (5.25) but we basically do it for the subsystems disconnectedly and put together the local tensors in the end. To phrase it differently, the environment at the connecting point is always outdated after the first optimization of the adjacent worker. If the Hamiltonian would be local, this would not be a problem, however the more non-local the system gets, the larger the error of the parallel approach will become. Nevertheless, we certainly had a decent experience with the parallel approach and for reasonable mappings the errors are well controlled.

We can therefore formulate the parallel TDVP algorithm [SGL+20] by the following steps.

1. Prepare the state with several orthogonality centers and set the workers to be at the boundary of adjacent bins.

2. Contract to obtain the two site Hilbert space

$$\psi_{ab}^{n_i n_{i+1}} = \sum_x M_{ax}^{n_i} \cdot S_{xx}^{-1} \cdot M_{xb}^{n_{i+1}} \ . \tag{5.45}$$

3. Compute and store the time-evolution with a half time-step.

4. Split ψ again into M^{n_i}, S^{-1} and $M^{n_{i+1}}$.

5. Compute and store the contractions with S^{-1} multiplied into the right MPS for the left worker and vice versa.

6. Back evolve the left MPS in the left worker and vice versa with a half time-step.

7. Sweep through the subsystems in a regular fashion with a half time-step.

8. Do the two-site evolution, build the contractions according to item 5 and do the back transformation with a full and a half time-step, respectively.

9. Sweep back to the original position.

10. Do only a forward evolution with a half time-step.

This procedure breaks the separation of the forward and backward sweep explicitly in item 8, however we made the experience that it is not only faster but also deviates less from the serial TDVP. At the end we arrived at a state evolved by the two-site TDVP to the next step on the time grid. The reason we do not use the single-site algorithm is that we can always implement the boundary synchronization as a joint update.

It is useful to implement this in both shared memory and distributed memory models. The shared memory model exploits several cores in a node to run the parallelization, e.g. by means of an open multi-processing (open MP) [Ope08] for loop. The implementation of this is rather unchallenging since it only needs a compiler directive for the sweeping being done in parallel. The synchronization is done by handing over the necessary data from one worker to its neighboring one. The distributed memory model using the message passing interface (MPI) [mpi93] is a bit more involved. Here, each machine starts a sweep on the respective sub-part of the tensor network to then synchronize over the network connection.

Next we want to get a sense for the size of the error caused by the parallelization, therefore we are going to have a look at the distance between the serial and parallel evolved states

$$\left\| |\psi_1\rangle - |\psi_i\rangle \right\|^2 , \tag{5.46}$$

where i is the number of real-space workers used. This difference is shown in figs. 5.5a and 5.5c. For the real time case we used a $L = 32$ Hubbard-Holstein model in the intermediate coupling regime, both for electrons and phonons. The ground state we excited with a bosonic particle in the middle of the chain. As we can see, the difference is in a still numerically controllable fashion, however it is increasing monotonously. Furthermore we observe no big additional error due to the use of additional workers, which we attribute to the locality of the model. For the imaginary time case we tested the time-evolution of an excitation above the ground state in a $L = 35$ impurity model that was obtained within the first iteration of DMFT. As we can see, there is a sharp increase of the error at the simulation start followed by an almost constant error only depending on the segment size. All in all, the error is smaller than would be relevant for the DMFT application, meaning that the parallelization is a well controlled algorithm in this case.

Furthermore, we want to look at the norms, e.g. as a proxy of the unitarity breaking in real-time evolution. The relative norm distance

$$\frac{\left\| |\psi_1\rangle (t) \right\| - \left\| |\psi_i\rangle (t) \right\|}{\left\| |\psi_1\rangle (t) \right\|} \tag{5.47}$$

is shown in figs. 5.5b and 5.5d. We choose to look at the relative distance since the norm decays quite fast in imaginary time, therefore differences are in different orders of magnitude. It is to mention that its decay is actually of physical significance in order to compute observables, therefore its precision is of high value. The magnitude of the norm difference compared to the serial run as a proxy measure of the projection error is in accordance with the error previously observed. However, in real time applications, usually the norm starts deviating at some point and afterwards grows quite rapidly [SGL+20]. This point was not reached in our simulations yet, since they are merely for demonstration purposes, but usually one can renormalize the wave function if so. In many cases this does not strongly affect observables computed from the state and they are still in good agreement with the serial run. For the imaginary time case we can observe a similar behaviour as before, there is a strong increase before saturating to a constant value. With increasing number of workers the error increases as before, however it is not constantly rising as can be seen by the difference between two and four workers compared to four and eight workers. The sharp minima at early times we attribute to the change of sign in the norm difference.

Last but not least we want to have a look at the runtime, whose improvement was the aim of this attempt in the first place. Figure 5.5e shows the real time (not the CPU-time) for different number of workers in the real time evolution. First we observe the plateau between two and four workers, meaning that the additional involvement of workers did not improve the performance in this area. From our experience this is a typical behaviour for intermediate number of workers, as mentioned before the total runtime is dominated by the slowest worker. Therefore, the additional workers might take load of the former workers, however there is still a region whose optimization takes significantly longer than the other ones. This is also the reason for the weak scaling of higher number of workers, e.g. an speedup of three for eight workers. We can address this in two ways, i.e. either we can adapt the bounds dynamically or we can chose them manually. For the latter one we simulate a test run and log the runtimes of each individual optimization. Using this method, we gain a good estimation on how to set the workers, such that the runtimes of each worker in the manual definition are the same. The dynamic worker adaption needs to estimate the runtimes of the individual segments as well, however through some algorithm we move the worker bounds during the synchronization of the second half step. As long as the shift does not violate the bounds of another worker it is sufficient to perform a regular two site update followed by the construction of new environment tensors into the moving direction as well as a new canonical normalization of the state.

Now that we have seen the extent of the errors one might be curious if they can be accounted for. Our claim was always, that there might be a way to account for the wrong-doing in such a way, that we subtract the introduced deviance in eq. (5.25) in order to arrive at eq. (5.26) again. To investigate this one might look at the easiest possible system, i.e. two workers splitting the chain in the middle at the first time-step. The first synchronization is still correct and the two half sweeps in the individual workers are also undisturbed (at least for each subsystem). What one would have to do to obtain the correct TDVP evolved wave function is to continue the sweeping in the other

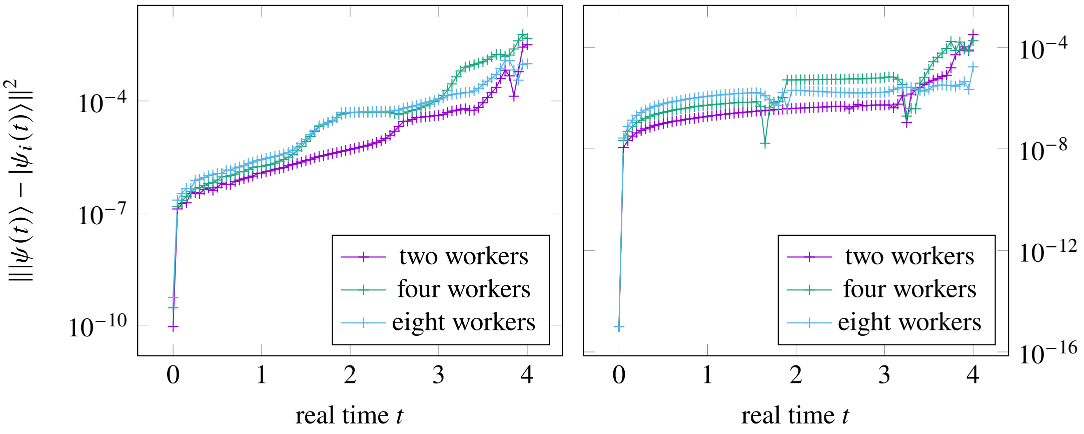

(a) Error in real time PTDVP.

(b) Norm deviance in real time PTDVP.

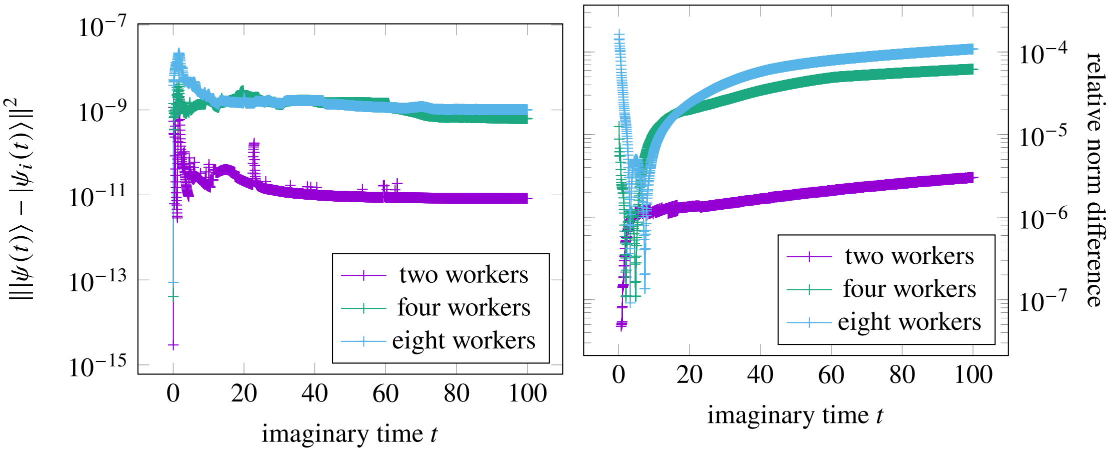

(c) Error in imaginary time PTDVP.

(d) Norm deviance in imaginary time PTDVP.

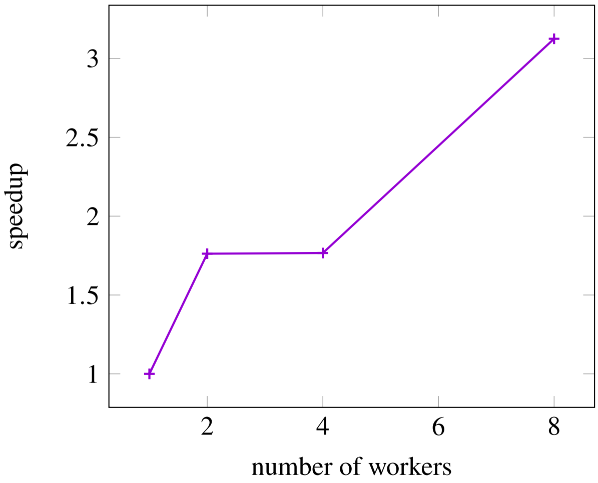

(e) Speedup plotted against the number of workers for equally distributed worker sizes.

Figure 5.5: Different numerical control parameters for real and imaginary time evolution in parallel (always compared to the serially evolved state).

half of the respective worker, instead of putting the local tensors into the same state and performing another sync. However, the problem in identifying the necessary terms here is that the Trotterization happens on the global wave function level and the application of the projector reduces everything to local equations, while the PTDVP directly operates on the local tensors. We believe that a future investigation could deal with the question how to bring back the local solutions performed in the neighboring subsystem of a worker to the trotterized form and expand them in order to learn more about the errors of the algorithm. This way one could account for them fully or at least create an estimate on the error made for the respective type of the system. Otherwise, one relies on heuristic studying of case-by-case Hamiltonians in order to pinpoint the stability of the algorithm.

Mode transformation

6

As of now the reader is likely aware of the importance of the orbital basis when doing non 1d calculations in tensor networks. Usually, when operating on molecular ground state problems the starting point is the HF method. First, one chooses a set of atomic orbitals, i.e. a full basis of real space wave functions $\{\phi_i(\vec{x})\}_{i\in I}$. This basis does not have to be an eigenbasis of the actual atomic problem, it just needs to be orthonormal, such that one can expand the true problem. Often one chooses basis-sets with useful properties, e.g. the Gaussian or Slater basis whose radial part looks like

$$\phi_i(r) = \mathrm{e}^{-\alpha r^2} \tag{6.1}$$

$$\phi_i(r) = r^n \mathrm{e}^{-\alpha r} \ . \tag{6.2}$$

After multiplying with the spherical harmonics and normalizing the entire product to one, one obtains a total atomic orbital. From these we form an LCAO ansatz [SO96]

$$\chi_j(\vec{x}) = \sum_{i\in I} R_{ji}\phi_i \tag{6.3}$$

to obtain molecular orbitals. Note that choosing R to be a permutation (i.e. to consist of zeros and ones only) corresponds to a reordering of modes as in section 3.4. This implies the interpretation of mode transformation as a “natural extension” of the reordering idea.

For the many-body wave functions the Slater determinant (or permanent) ansatz looks like

$$\psi(\vec{x}_1,\dots,\vec{x}_N) = \frac{1}{\sqrt{N!}} \det \begin{bmatrix} \chi_1(\vec{x}_1) & \dots & \chi_1(\vec{x}_N) \\ \vdots & \ddots & \vdots \\ \chi_L(\vec{x}_1) & \dots & \chi_L(\vec{x}_N) \end{bmatrix} , \tag{6.4}$$

whose energy we seek to minimize by means of the electronic Hamiltonian [SO96]

$$E[\psi] = \langle\psi|\hat{H}|\psi\rangle \ . \tag{6.5}$$

For this purpose we optimize with respect to the elements R_{ij}. The solution is obtained by a quite sophisticated mapping to an eigenvalue problem, which gives us a numerically cheap spectrum, exact in the $m = 1$ approximation. However, this is not the scope of this chapter and therefore we refer the determined reader to the excellent derivation in [SO96]. The point we are trying to highlight is the following: it is true that the energy can be seen as a functional of the wave function, but what the HF method actually does is to view it as an optimization problem for the $L\times L'$ dimensional matrix R (the number of atomic and molecular orbitals is not necessarily the same)

$$\min_{\psi} E[\psi] = \min_{R} E(R) \ . \tag{6.6}$$

Since the normalization of the wave function fixes the prefactor this is the only optimization target. Once one has the converged result, one can compute an active space via eqs. (3.69) and (3.70) and include correlations into the calculations. This means that we superpose linear combinations of the determinaant with arbitrary coefficients. In this context it makes sense to extend the problem from a pure basis optimization to one simultaneously operating on the basis and the variational parameters

$$\min_{R} E(R) \rightarrow \min_{R,c} E(c_{n_1\dots n_L}, R) \ , \tag{6.7}$$

where $c_{n_1\dots n_L}$ are the usual ED coefficients.

A common form of doing this simultaneous optimization is the well known CAS-SCF method [Roo80, SAHR81, RTS80] and in particular the implementation using tensor networks [ZN08]. Here, one self-consistently optimizes the wave function variationally for the basis and the energy, starting from an initial basis. Thereafter, one can compute from the converged result the one and two pRDMs, which are related to the gradient and Hessian of the energy functional. By searching for a minimum in the energy functional optimization space with respect to the basis rotation, one can achieve an optimal R. This we reiterate until the desired convergence in the state and its basis is achieved.

The idea of mode transformation [KVLE16, GL21] is conceptually similar but different in implementation. Since the determination of a global U is in general very challenging, we rather try to achieve a global transformation through subsequent application of rotations of the single particle basis $U \in \mathbb{C}^{L\times L}$ as

$$U = \ldots \cdot U_3 \cdot U_2 \cdot U_1 \;, \tag{6.8}$$

where each $U_i \in \mathbb{C}^{L\times L}$ takes the form

$$U_i = 1^{(1)} \otimes 1^{(2)} \otimes \ldots \otimes T^{(i,i+1)} \otimes \ldots \otimes 1^{(L)} \;, \qquad T^{(i,i+1)} \in \mathcal{H}_i \otimes \mathcal{H}_{i+1} \;. \tag{6.9}$$

The key point is, that after each local optimization of the variational parameters for the energy, we optimize the basis as well. Therefore we obtain rotations on the two orbital Hilbert space, which do not change the computational basis itself, but just superpose the elements in it in a different fashion. This connects the algebras of the two bases via eqs. (4.11) and (4.12). Since the optimized nodes overlap with the nodes targeted next, not only can a non-local U be reached this way, but rather it is immediately reached after the first sweep. Therefore, we have to deal with a dense Hamiltonian the entire time, which comes with its own caveats as we shall see in the upcoming sections.

Our aim is now to figure out how the transformation of the single particle basis

$$\begin{pmatrix}\phi_1\\ \phi_2\end{pmatrix} \longrightarrow \begin{bmatrix}T_{11} & T_{12}\\ T_{21} & T_{22}\end{bmatrix}\begin{pmatrix}\phi_1\\ \phi_2\end{pmatrix} \tag{6.10}$$

acts on our MPS system. Note that in principle this is tensored with all the other $L-2$ orbitals which are in turn hit by an identity matrix. However, since we only operate on the two orbital subspace we can leave away the remaining system for this consideration and keep in mind that 1 and 2 might later on refer to any adjacent sites. Since this representation of the rotation in first quantization is a bit difficult to work with, we would rather have the direct impact onto the second quantized Hilbert space. Therefore we write e.g. the creation operator in its most general form and insert two identities

$$\begin{aligned}
\hat{c}^\dagger_\alpha &= \sum_{n=0}^{d-2} \eta(n)\,|n+1\rangle_\alpha\,{}_\alpha\langle n| = \left(\sum_{n'i'} |n'\rangle_{i'}\,{}_{i'}\langle n'|\right) \sum_{n=0}^{d-2} \eta(n)\,|n+1\rangle_\alpha\,{}_\alpha\langle n| \left(\sum_{n''i''} |n''\rangle_{i''}\,{}_{i''}\langle n''|\right) && (6.11)\\
&= \sum_{\substack{i'i''\\ n,n',n''}} \eta(n)\,{}_{i'}\langle n'|n+1\rangle_\alpha\,{}_\alpha\langle n|n''\rangle_{i''}\,|n'\rangle_{i'}\,{}_{i''}\langle n''| \;, && (6.12)
\end{aligned}$$

where we assumed a finite local Hilbert space of size d. $\eta(n)$ is a normalization factor, that depends on the specific model and which is not of any further interest right now. The overlap elements ${}_{i'}\langle n'|n+1\rangle_\alpha$ and ${}_\alpha\langle n|n''\rangle_{i''}$ are numbers and can be obtained, e.g. by integration. If overlaps of different occupation give zero we even reobtain the super-diagonal structure of the creation operator in the α basis. However, this is a slightly complicated task so for now we will restrict to fermions, which will restrict all occupations to either zero or one and therefore simplify to

$$\hat{c}^\dagger_\alpha = \sum_i \langle i|\alpha\rangle\,\hat{c}^\dagger_i = T_{\alpha 1}\hat{c}^\dagger_1 + T_{\alpha 2}\hat{c}^\dagger_2 \;. \tag{6.13}$$

Since any tensor is spanned by the elements of the Hilbert space which are created by successive application of creators onto the vacuum, this gives a path to proceed. If we want to rotate a tensor out of our network into another single particle basis we just apply the transformation matrix T to the coefficients. The detailed impact on a fermionic basis is going to be demonstrated in section 6.1.

In order for us to be able to work solely on the coefficients we need to confirm the following. Usually, one does not keep track of the basis states in a tensor network implementation. Upon multiplying the transformation into the coefficients and relabelling the basis we crucially rely on the algebra of creation and annihilation operators being preserved. The transformation can be obtained through

$$\left[\hat{c}_{\alpha}^{(\dagger)}, \hat{c}_{\beta}^{(\dagger)}\right] = \sum_{ij} T_{\alpha i}^{(*)} T_{\beta j}^{(*)} \underbrace{\left[\hat{c}_{i}^{(\dagger)}, \hat{c}_{j}^{(\dagger)}\right]}_{=0} = 0 \tag{6.14}$$

$$\left[\hat{c}_{\alpha}, \hat{c}_{\beta}^{\dagger}\right] = \sum_{ij} T_{\alpha i} T_{\beta j}^{*} \underbrace{\left[\hat{c}_{i}, \hat{c}_{j}^{\dagger}\right]}_{=\delta_{ij}} = \sum_{i} T_{\alpha i} T_{\beta i}^{*} = \sum_{i} T_{\alpha i} T_{i\beta}^{\dagger} = \delta_{ij} \ , \tag{6.15}$$

for any bilinear function $[\,\cdot\,,\,\cdot\,]$, in our case the anti-commutator. Therefore, by choosing T unitary we have the advantage of preserving the distances and angles inside the Hilbert spaces and furthermore would automatically keep U unitary.

The attentive reader might have noticed a contradiction by now. Originally we claimed that we are going to optimize an energy function with respect to variational parameters and the single particle basis, but our choice of unitary transformations will keep the energy constant qua construction. Therefore, we need a different criterion to minimize. Usually one chooses proxy measures to reduce the mutual information, typically local accessible quantities like functions of the singular value spectrum. These have the advantage that they can be computed quite cheaply from already present objects during twosite DMRG. Hence, if the optimization is successful, we will reach a better energy in the next step with a lower bond dimension.

This harmless seeming choice enhances the optimization problem by a component already present in DMRG type of ansatzes, namely we enforce the state to have low entanglement and low energy. In customary DMRG, the SVD truncation during sweeping implicitly chooses a bond basis which minimizes the overall entanglement of the state. With mode transformation this effect tends to get even more weight in the optimization, since not only the bond basis is optimized for minimal entropy but also the single particle basis. In applications where the desired state is minimal in energy and entropy this can be a convergence booster. However, there are models in which energy and entanglement optimization are competing aims, probably most prominently the doped 2d Fermi-Hubbard model at intermediate coupling [QCS+20]. Here, the ground state and the low lying excitations are very close in energy, while the excitations have the lower entanglement [QCS+20]. This interplay usually makes DMRG calculations not only a matter of resources, but in addition one needs to force the model into the correct low energy state, e.g. by use of magnetic pinning fields [SW12, EWN17, QCS+20]. Therefore, the use of mode transformation needs to be carefully controlled in order to avoid producing wrong results, as mistaking a low lying excitation for the ground state.

Fermionic mode transformation 6.1

In this section we want to demonstrate the algorithmic details of the application of mode transformation to electrons [KVLE16]. As mentioned in chapter 6, a general recipe is more complicated due to the structure of the transformation and ambiguities between first and second quantization, and has not been implemented yet to present day. We therefore restrict ourselves to two special cases. The first are fermions without spin, i.e. the only implemented symmetry for the tensors is a $U(1)_n$ particle number conservation. The second one are fermions with particle number and z component of their spins conserved, i.e. the symmetry group is $U(1)_n \otimes U(1)_z$. Assuming we are at a twosite DMRG step of an MPS, the wave function takes the form

$$|\psi\rangle = \sum_{\substack{abn_i \\ n_{i+1}}} \psi_{ab}^{n_i n_{i+1}} |a\rangle\, |b\rangle\, |n_i n_{i+1}\rangle \ . \tag{6.16}$$

The application to a general tensor network active site tensor (in our case it was the T3NS) works completely analogous, since all operations are planar and additional virtual legs are not involved in the algorithm to follow. In other words we just substitute $|b\rangle \to |b\rangle\,|c\rangle$ and continue with the same recipe. As aforementioned the rotation of the single particle orbitals $\phi_i(x)$ and $\phi_{i+1}(x)$ only acts on the physical basis $|n_i n_{i+1}\rangle$. The way it acts on the basis ket depends on the possible symbols n can take and the commutation relations of the occupied states.

We will commence with the easiest case, i.e. spinless fermions, which are either occupied or not $n \in \{0, 1\}$. The two orbital Hilbert space is of size four and spanned by the basis

$$
\begin{aligned}
\underline{n=0}: &\qquad |0\rangle \ , \\
\underline{n=1}: &\qquad |10\rangle\,, |01\rangle \ , \\
\underline{n=2}: &\qquad |2\rangle \ .
\end{aligned}
\tag{6.17}
$$

The first element of the basis belongs to the $n = 0$ irrep, while the middle ones belong to $n = 1$ and the last one to $n = 2$. As the first and the last element are one dimensional, their transformation may only be a complex phase $\mathrm{e}^{\mathrm{i}\alpha}$, otherwise they would not be unitary. We implemented the mode transformation both with real and complex valued matrices, the difference being the number of free parameters of the rotation matrices to optimize. Of course number of iterations necessary to converge increases with the number of free parameters, since the parameter space gets larger. However, the additional degree of freedom did usually not bring any advantages in the basis and therefore we mostly worked with the real representation, i.e. we can fix the transformation in the empty and doubly occupied sectors to be one. From this point on we shall therefore specialize to $U \in \mathbb{R}^{L\times L}$. Returning to the spinless fermions, only the single particle sector is non-trivial and transforms as

$$|10\rangle = \hat{c}_1^\dagger \,|0\rangle \to \left(U_{11}\hat{c}_1^\dagger + U_{12}\hat{c}_2^\dagger\right)|0\rangle = U_{11}\,|10\rangle + U_{12}\,|01\rangle \tag{6.18}$$

$$|01\rangle = \hat{c}_2^\dagger \,|0\rangle \to \left(U_{21}\hat{c}_1^\dagger + U_{22}\hat{c}_2^\dagger\right)|0\rangle = U_{21}\,|10\rangle + U_{22}\,|01\rangle \ . \tag{6.19}$$

The transformation behaviour of the basis can be written compact in matrix-vector notation, i.e.

$$\begin{pmatrix} |0\rangle \\ |10\rangle \\ |01\rangle \\ |2\rangle \end{pmatrix} \to U(\alpha)\cdot \begin{pmatrix} |0\rangle \\ |10\rangle \\ |01\rangle \\ |2\rangle \end{pmatrix} \tag{6.20}$$

with the rotation matrix on the two orbital sub Hilbert space being defined as

$$U(\alpha) \doteq \begin{array}{c|cccc|c} & |0\rangle & |10\rangle & |01\rangle & |11\rangle & \\ \hline & \boxed{1} & & & & |2\rangle \\ & & \cos\alpha & -\sin\alpha & & |00\rangle \\ & & \sin\alpha & \cos\alpha & & |01\rangle \\ & & & & \boxed{1} & |11\rangle \end{array} \ , \tag{6.21}$$

where α is the parameter describing the rotation. Note, that the trigonometric functions come from the representation of the U_{ij} in SO(2), the group of two dimensional real unitaries. Setting aside the task how to find a reasonable α, we notice that in principle, the application of this twosite gate into the variational tensor rotates the wave function into the new single particle basis

$$|\psi\rangle = \sum_{lnr} \psi^n_{lr}\,|lnr\rangle = \sum_{lnrn'} \psi^n_{lr}\delta_{nn'}\,|ln'r\rangle = \sum_{lnrn'c} \psi^n_{lr}U_{nc}U^*_{cn'}\,|ln'r\rangle = \sum_{lcr} \underbrace{\left(\sum_n \psi^n_{lr}U_{nc}\right)}_{=\tilde{\psi}^n_{lr}} \underbrace{\left(\sum_{n'} U_{cn'}\,|ln'r\rangle\right)}_{=|lcr\rangle} \ , \tag{6.22}$$

where we combined n_i and n_{i+1} into a multi-index n for convenience. Note, that we made use of the fact that the local degrees of freedom do not change which causes the preservation of the operator algebra in eq. (6.15) through our special choice of U. Otherwise, the redefinition of the last equality sign would not be possible, but we would need to introduce a new local Hilbert space with new labelings, respecting the algebra of the transformed basis. However here, we just apply the gate which disentangles the two sites the most and repeat with the site into sweeping direction and its next neighbor.

The same game can be played for fermions carrying spin indices, however it is a bit more bookkeeping. In principle we already have encountered the two orbital reduced subspace for spinfull fermions in table 4.2. Therefore we know that it is 16 dimensional, decomposes into nine sectors and is spanned by the kets

$$\begin{aligned}
\underline{n=0, s_z=0}: &\quad |0\rangle\ ,\\
\underline{n=1, s_z=-1/2}: &\quad |0\ \downarrow\rangle\,,|\downarrow\ 0\rangle\ ,\\
\underline{n=1, s_z=+1/2}: &\quad |0\ \uparrow\rangle\,,|\uparrow\ 0\rangle\ ,\\
\underline{n=2, s_z=-1}: &\quad |\downarrow\downarrow\rangle\ ,\\
\underline{n=2, s_z=0}: &\quad |0\,2\rangle\,,|\downarrow\uparrow\rangle\,,|\uparrow\downarrow\rangle\,,|2\,0\rangle\ ,\\
\underline{n=2, s_z=+1}: &\quad |\uparrow\uparrow\rangle\ ,\\
\underline{n=3, s_z=-1/2}: &\quad |\downarrow\ 2\rangle\,,|2\ \downarrow\rangle\ ,\\
\underline{n=3, s_z=+1/2}: &\quad |\uparrow\ 2\rangle\,,|2\ \uparrow\rangle\ ,\\
\underline{n=4, s_z=0}: &\quad |4\rangle\ .
\end{aligned} \tag{6.23}$$

Due to the fact that every single particle orbital can be occupied by an up- and a down-spin (actually itself being a tensor product of species of the previous case in eq. (6.21)) we need to proceed with caution, since every species itself transforms like

$$\begin{pmatrix}\phi_{1\sigma}(x)\\ \phi_{2\sigma}(x)\end{pmatrix} \rightarrow U(\alpha_\sigma)\begin{pmatrix}\phi_{1\sigma}(x)\\ \phi_{2\sigma}(x)\end{pmatrix}\ , \tag{6.24}$$

in first quantization. We account for this by introducing two independent rotations for the degrees of freedom $\sigma \in \{\uparrow,\downarrow\}$, a setup commonly known as unrestricted Hartee Fock (UHF) [PN54]. If we write down the rotations in each subsector we arrive at the total transformation matrix $U(\alpha_\uparrow,\alpha_\downarrow)$. Again we find ourselves in the situation that all one dimensional subsectors are only allowed to transform trivially by a factor of one. Not particularly surprising in the one particle subsectors, each element transforms with the unitary itself. Interestingly, the three dimensional subspaces transform with the rotation matrix of the empty degree of freedom and a flipped sign of α_σ. The former is due to the property of unitarity matrices to have determinant one, which cancels some coefficients in the transformation, and the fact that no orbital can be occupied twice. The latter is because of the anti-commutation of creation operators. Finally, the complicated two particle sector can be, as already mentioned, decomposed into up- and down-kets

$$\begin{pmatrix}|2\,0\rangle\\ |\uparrow\downarrow\rangle\\ |\downarrow\uparrow\rangle\\ |0\,2\rangle\end{pmatrix} = \begin{pmatrix}|1\rangle_\uparrow\,|0\rangle_\uparrow\\ |0\rangle_\uparrow\,|1\rangle_\uparrow\end{pmatrix} \otimes \begin{pmatrix}|1\rangle_\downarrow\,|0\rangle_\downarrow\\ |0\rangle_\downarrow\,|1\rangle_\downarrow\end{pmatrix}\ , \tag{6.25}$$

which explains the form of an dyadic product of the individual transformations $U(\alpha_\uparrow)\odot U(\alpha_\downarrow)$. Bringing together all these results we arrive at the total transformation matrix $U(\alpha_\uparrow, \alpha_\downarrow)$ given by

$$
\left[\begin{array}{ccccccccc}
\begin{array}{c} |0\rangle \\ 1 \end{array} & & & & & & & & \\
& \begin{array}{cc} |\downarrow\ 0\rangle & |0\ \downarrow\rangle \\ \cos\alpha_\downarrow & -\sin\alpha_\downarrow \\ \sin\alpha_\downarrow & \cos\alpha_\downarrow \end{array} & & & & & & & \\
& & \begin{array}{cc} |\uparrow\ 0\rangle & |0\ \uparrow\rangle \\ \cos\alpha_\uparrow & -\sin\alpha_\uparrow \\ \sin\alpha_\uparrow & \cos\alpha_\uparrow \end{array} & & & & & & \\
& & & \begin{array}{cccc} |2\,0\rangle & |\uparrow\downarrow\rangle & |\downarrow\uparrow\rangle & |0\,2\rangle \\ \cos\alpha_\uparrow\cos\alpha_\downarrow & -\cos\alpha_\uparrow\sin\alpha_\downarrow & -\sin\alpha_\uparrow\cos\alpha_\downarrow & \sin\alpha_\uparrow\sin\alpha_\downarrow \\ \cos\alpha_\uparrow\sin\alpha_\downarrow & \cos\alpha_\uparrow\cos\alpha_\downarrow & -\sin\alpha_\uparrow\sin\alpha_\downarrow & -\sin\alpha_\uparrow\cos\alpha_\downarrow \\ \sin\alpha_\uparrow\cos\alpha_\downarrow & -\sin\alpha_\uparrow\sin\alpha_\downarrow & \cos\alpha_\uparrow\cos\alpha_\downarrow & -\cos\alpha_\uparrow\sin\alpha_\downarrow \\ \sin\alpha_\uparrow\sin\alpha_\downarrow & \sin\alpha_\uparrow\cos\alpha_\downarrow & \cos\alpha_\uparrow\sin\alpha_\downarrow & \cos\alpha_\uparrow\cos\alpha_\downarrow \end{array} & & & & & \\
& & & & \begin{array}{c} |\downarrow\downarrow\rangle \\ 1 \end{array} & & & & \\
& & & & & \begin{array}{cc} |2\ \downarrow\rangle & |\downarrow\ 2\rangle \\ \cos\alpha_\uparrow & \sin\alpha_\uparrow \\ -\sin\alpha_\uparrow & \cos\alpha_\uparrow \end{array} & & & \\
& & & & & & \begin{array}{c} |\uparrow\uparrow\rangle \\ 1 \end{array} & & \\
& & & & & & & \begin{array}{cc} |2\ \uparrow\rangle & |\uparrow\ 2\rangle \\ \cos\alpha_\downarrow & \sin\alpha_\downarrow \\ -\sin\alpha_\downarrow & \cos\alpha_\downarrow \end{array} & \\
& & & & & & & & \begin{array}{c} |4\rangle \\ 1 \end{array}
\end{array}\right] . \tag{6.26}
$$

The application is completely analogous to eq. (6.22), since this is also a twosite gate of square matrix dimension d^2.

For some applications it might be useful to write the blocks parametrized through α_σ via an exponential function, i.e.

$$
U = \exp\left(\mathrm{i}\sum_i J_i \alpha_i\right) . \tag{6.27}
$$

Therefore, we want to note the individual generators of the blocks, e.g. for the two dimensional subspaces we have

$$
J = \pm \begin{bmatrix} 0 & -1 \\ 1 & 0 \end{bmatrix} , \tag{6.28}
$$

where the positive sign belongs to one particle subspace and the negative sign to three particles. The same calculation for the two particle subspace yields the two generators

$$J_\uparrow = \begin{bmatrix} 0 & 0 & -1 & 0 \\ 0 & 0 & 0 & 1 \\ 1 & 0 & 0 & 0 \\ 0 & -1 & 0 & 0 \end{bmatrix} \qquad J_\downarrow = \begin{bmatrix} 0 & 1 & 0 & 0 \\ -1 & 0 & 0 & 0 \\ 0 & 0 & 0 & -1 \\ 0 & 0 & 1 & 0 \end{bmatrix} . \tag{6.29}$$

So far we only talked about the wavefunction, however, it is also necessary to switch the computational basis of all operators. We already encountered the transformation behaviour of local operators, which can be done at any point by virtue of the matrix U and arithmetic MPO operations [HMS17]. However, since the operator algebra gets superposed, we end up with single orbital creation and annihilation operators of dimension L. This accounts for a scaling of at best bond dimension $\mathrm{O}\left(L^{2p}\right)$, where p is the number of particles the operator involves. Upon naive construction, it is even one order higher, not to speak of the cost of truncation algorithms for MPOs [HMS17]. Therefore, we rather proceed by applying the scheme sketched in fig. A.1, where we sandwich the operator with the transformation and its hermitian conjugate, such that the MPO is also transformed to the new basis. The twosite MPO is present during variational optimization anyways, in order to compute the effective Hamiltonian [Sch11], and the multiplication of the two gates into it is usually very cheap. Furthermore, we only have to do it once we have found a transformation we want to actually keep, in contrast to the state, as we are going to see in a second. The only trouble is the bond dimension of the Hamiltonian. Since the underlying Hamiltonian is now dense, the SVD we use to separate the two orbitals from each other is not going to find a representation as sparse as for the input Hamiltonian. In our experience a combination of a rescaled SVD without truncation and delinearization [HMS17] followed by a global truncation after a few sweeps gives the best results. Nevertheless, the bond dimension will increase, even in the best cases and the additional cost is going to condense into the most extensive part of tensor network algorithms. Therefore a careful balance needs to be found between the input MPO bond dimension and the growth during the mode transformation, as well as the speedup gained by disentanglement compared to the additional complexity of the operator application.

We discussed earlier in this section why it is important to be careful with the number of free parameters introduced into the transformation and how particles of different species might decouple through use of different rotation matrices. For our typical benchmark system the energy was much lower with less sweeps, when we made use of two parameters instead of just one, i.e. when we chose $\alpha_\uparrow \neq \alpha_\downarrow$. Of course, the optimization took longer due to more parameters, but that might seem like a price to pay. However, recent developements [Leg21] tend to point into the direction that the short term energy drop due to more freedom in the parameter space is bought with a high price. Namely, for some of the models we described before, in particular the 2d Fermi-Hubbard, where there is a strong competition between entropy and energy minimization [QCS+20] the UHF can increase the problem by creating a heavy imbalance between the (originally exchange symmetric) up- and down-spin. Therefore, a careful investigation and a shift away from the greedy optimization scheme can be very useful in order to avoid getting stuck in wrong states. This can be done quite easily by enforcing the α_σ to be equal.

Determining the transformation matrix 6.1.1

Now, that we have a stable framework to rotate a fermionic basis and have found the transformation matrices, let us come to the question of how to find a suited matrix U. For this, we first want to look at the functions we actually want to optimize. First of all, the transformation matrices in eqs. (6.21) and (6.26) are periodic with respect to shift of the arguments $\alpha \longrightarrow \alpha + 2\pi$. Therefore, our search space is restricted to $[0, 2\pi[$ for each species we want to treat independently. However, in order to find a meaningful optimization criterion it is necessary to find a scalar objective which can be optimized for a minimum, i.e. we are searching for a cost function $f(U) = f(\alpha)$. There is a lot of room for playing around with this and the resulting basis is going to depend strongly on the choice of the objective. Two particular choices of cost functions proved very useful to us, therefore we want to introduce them here briefly. First, there is the 1-norm of the singular value spectrum [KVLE16], which we obtain when splitting the two orbital wavefunction into individual orbitals again via an SVD

$$\psi_{ab}^{n_i n_{i+1}} = \sum_x A_{ax}^{n_i} \cdot S_{xx} \cdot B_{xb}^{n_{i+1}} . \tag{6.30}$$

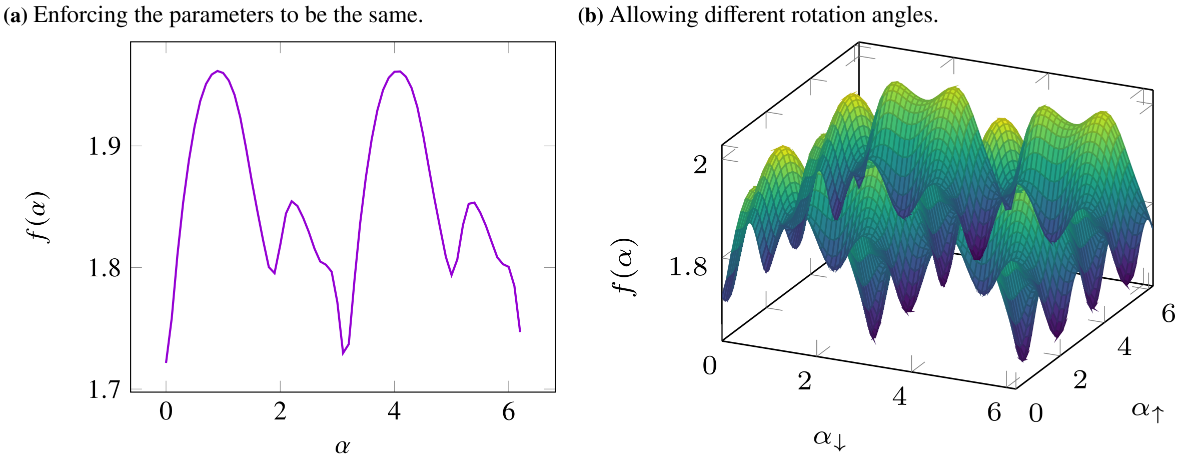
(a) Enforcing the parameters to be the same.

(b) Allowing different rotation angles.

Figure 6.1: Example optimization landscape of a 2d Fermi-Hubbard model for the 1-norm cost function defined in eq. (6.31).

A normalized state has singular values ranging from zero to one, however through the application of the effective Hamiltonian this bound is shifted above one. As we have argued in eqs. (2.6) and (2.9) the spectrum is somewhat connected to the bipartition entropy and therefore to the computational resources required. Hence, we can define the function to minimize as

$$f(\alpha) = \sum_x |s_x(\alpha)| \ , \tag{6.31}$$

where the α dependency is hidden in the application of the unitary and a subsequent SVD. The advantage of this cost function is that it treats all singular values on equal footing, therefore we found it to be especially useful for early stages of, e.g., the DMRG.

When one wants to use the 1-norm on a T3NS, a minor modification is needed. Since a two site update involves the joint space of two physical and a branching node we will always have two individual bonds with their spectra involved. However, the two Hilbert spaces of the bonds (introduced by two subsequent SVDs) have completely unrelated bases, so comparing them to each other (what we do, when we sum up the spectra) is not well defined. We circumvented this problem by normalizing the total function with respect to the initial cost function value. This we need to compute and store anyways, such that we can reject transformations which did not meet our acceptance criteria (which we are going to discuss in a second). Therefore, we add up the relative change in bases for both bonds

$$\tilde{f}(\alpha) = \frac{\frac{f_1(\alpha)}{f_1(0)} + \frac{f_2(\alpha)}{f_2(0)}}{2} \ , \tag{6.32}$$

which results in eq. (6.31) for a single MPS bond.

The second possibility is to take the logarithm of the (fourth power of the) 4-norm of the singular value spectrum [KVLE16], i.e.

$$f(\alpha) = \ln\left(\sum_x s_x(\alpha)^4\right) \ . \tag{6.33}$$

which has the advantage that it suppresses long singular value tails and hence was often used by us in advanced stages. Furthermore, it can be constructed without an explicit SVD by means of the tensor contractions in fig. 6.2,

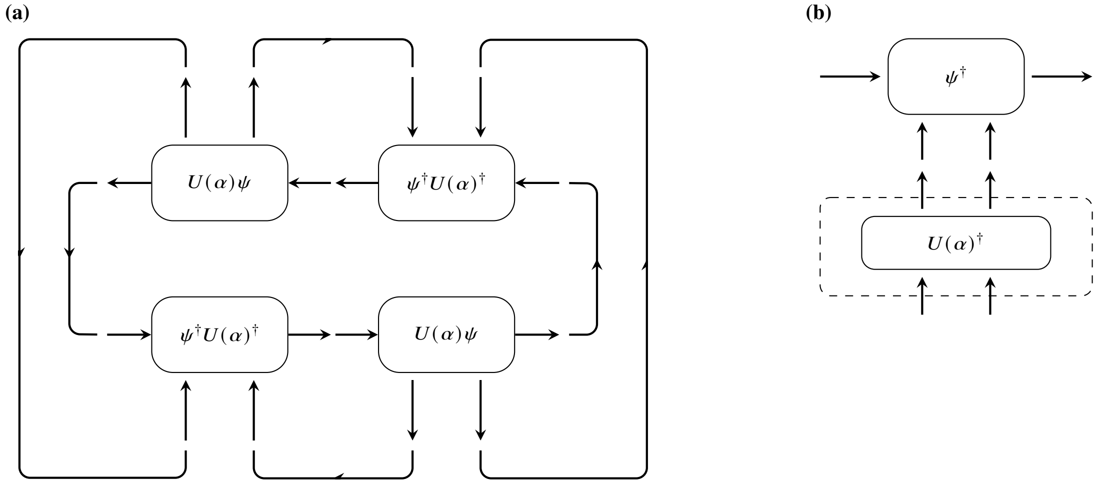

Figure 6.2: Computation of the 4-norm of the singular value spectrum from contractions for a canonically normalized state.

assuming the state is canonically normalized

$$\sum_{\substack{n'bn''a'\\ \tilde{n}b'na}} \psi^{nn'}_{ab}\psi^{n'n''*}_{a'b}\psi^{n''\tilde{n}}_{a'b'}\psi^{n\tilde{n}*}_{ab'} = \sum_{\substack{n'bn''a'\\ \tilde{n}b'na\\ xx'cc'}} A^{n}_{ax}S_{xx}B^{n'}_{xb}B^{n'*}_{bx'}S_{x'x'}A^{n''*}_{x'a'}A^{n''}_{a'c}S_{cc}B^{\tilde{n}}_{cb'}A^{n*}_{ac'}S_{c'c'}B^{\tilde{n}}_{c'b'*} \tag{6.34}$$

$$= \sum_{xx'cc'} \underbrace{\left(\sum_{an} A^{n}_{ax}A^{n*}_{ac'}\right)}_{=\delta_{xc'}} \underbrace{\left(\sum_{bn'} B^{n'}_{xb}B^{n'*}_{bx'}\right)}_{=\delta_{xx'}} \underbrace{\left(\sum_{n''a'} A^{n''}_{a'c}A^{n''*}_{x'a'}\right)}_{=\delta_{x'c}} \underbrace{\left(\sum_{\tilde{n}b'} B^{\tilde{n}}_{cb'}B^{\tilde{n}*}_{c'b'}\right)}_{=\delta_{cc'}} = \sum_{x} s_x^4 \,, \tag{6.35}$$

with a cost scaling like $\sim \mathrm{O}\left(d^3m^3\right)$ similar to the scaling of the SVD. Another advantage of this cost function is that its Jacobian and Hessian with respect to α can be computed with moderate effort by means of the chain rule

$$\frac{\partial}{\partial\alpha^*} = \frac{\partial U^{n'\tilde{n}'*}_{n\tilde{n}}}{\partial\alpha^*}\frac{\partial}{\partial U^{n'\tilde{n}'*}_{n\tilde{n}}} \,. \tag{6.36}$$

Often the additional information about the optimization space proves useful in order not to get stuck in local minima and speed up the convergence. While the first term is rather trivial for our representations of the unitary eqs. (6.21) and (6.26), the derivate(s) of the 4-norm with respect to the unitary needs some involved algebra. However, the diagrammatic representation in fig. 6.2b makes the derivative a lot easier here. The Jacobian is given by the sum of the contraction of the diagram without one of the $U^\dagger$ each, while for the Hessian we can just leave out both occurrences of $U^\dagger$.

Finally, we arrive at the algorithm necessary for the determination of the minimum of the objective with respect to the rotation. For the derivative free version of the optimization in eq. (6.31), i.e. we only have access to function evaluations, we usually use the well known Nelder-Mead scheme [NM65, TVF02] (sometimes also referred to as Downhill-Simplex method). This algorithm is specialized to non-linear optimization problems and in our application found a minimum of the cost function within typically $\sim$ 30 iterations for each free parameter. In order not to get stuck, we do a global reordering approximately every seven to ten sweeps and either restart with the reordered Hamiltonian (e.g. in DMRG) or also reorder the state (e.g. in TDVP). The basic idea is to form a simplex in the optimization space of dimension d, i.e. an object with $d+1$ corners and use geometric operations to go down the cost function, while decreasing the surface of the simplex to a desired accuracy. Therefore, we bisect the area within the optimization space for so long, until we are sure to be in a minimum. As one can image, the method is highly dependent on the initial value, which usually does not bother us, since we are working iteratively. Methods involving derivates shall not be mentioned in this section, since we will encounter the first derivative in section 6.2.1. Second derivative methods, like e.g. Dogleg [POW70], are in principle possible and are expected to increase performance but were not part of the work of this thesis.

Generic ansatz 6.2

Up until now we discussed how to change single particle bases, and implemented a framework to do so for fermionic bases with Abelian symmetries without changing distances and angles inside the Hilbert space. We chose this particularly easy case, since fermionic orbitals can only be occupied or unoccupied, therefore the transformation behaviour of the kets in eq. (6.12) is simplified a lot. However, we might be curious to see, if this can be extended towards several directions. Our aim is to have a generic transformation, written down in a fully automated fashion, regardless of the particle content of the Hilbert space. In order to derive this from a pedagogical point-of-view, let us look at bosons with local occupation $n = 2$. The two orbital joint Hilbert space of the local bases $\{|0\rangle, |1\rangle, |2\rangle\}$ is given by

$$\begin{aligned}
\underline{n=0}: &\quad |0\rangle \ , \\
\underline{n=1}: &\quad |01\rangle, |10\rangle \ , \\
\underline{n=2}: &\quad |02\rangle, |11\rangle, |20\rangle \ , \\
\underline{n=3}: &\quad |12\rangle, |21\rangle \ , \\
\underline{n=4}: &\quad |4\rangle \ .
\end{aligned} \tag{6.37}$$

Some transformations might be trivial again, like the zero and the four sector or the one particle sector, which we expect to transform similarly, as before. But, how does e.g. the two particle transformation look like? We again want to write each basis ket as application of single orbital operators on the vacuum and derive its transformation under rotations of the basis by the transformation of the operator algebra. If we could find a closed form and the algebra would be preserved, we would have a chance to write down a similar transformation as before. Introducing for instance a rotation of the basis elements $1, 2$ to new elements $\tilde{1}, \tilde{2}$, has according to eq. (6.12), the impact

$$\begin{aligned}
\hat{b}^\dagger_\alpha = \sum_{n=0}^{1} \eta(n) \Big[& {}_{\tilde{1}}\langle n+1|n+1\rangle_\alpha \ {}_\alpha\langle n|n\rangle_{\tilde{1}} \ \underline{|n+1\rangle_{\tilde{1}} \, {}_{\tilde{1}}\langle n|} + {}_{\tilde{1}}\langle n+1|n+1\rangle_\alpha \ {}_\alpha\langle n|n\rangle_{\tilde{2}} \ \underline{|n+1\rangle_{\tilde{1}} \, {}_{\tilde{2}}\langle n|} \\
& + {}_{\tilde{2}}\langle n+1|n+1\rangle_\alpha \ {}_\alpha\langle n|n\rangle_{\tilde{1}} \ \underline{|n+1\rangle_{\tilde{2}} \, {}_{\tilde{1}}\langle n|} + {}_{\tilde{1}}\langle n+1|n+1\rangle_\alpha \, {}_\alpha\langle n|n\rangle_{\tilde{2}} \ \underline{|n+1\rangle_{\tilde{2}} \, {}_{\tilde{2}}\langle n|} \Big] \qquad \alpha = 1, 2 \ .
\end{aligned} \tag{6.38}$$

on the algebra. Even though it might be tempting to redefine the underlined elements in the transformation as $\hat{b}^\dagger_{\tilde{1}}$, $\hat{b}^\dagger_{\tilde{1}}\hat{b}_{\tilde{2}}$, $\hat{b}^\dagger_{\tilde{2}}\hat{b}_{\tilde{1}}$ and $\hat{b}^\dagger_{\tilde{2}}$, a closer look reveals that this is not as easily done as in the fermionic case. The reason for this is the sum over more than one element. In the fermionic case $\eta(n) = 1$ and the sum collapses to one term due to the Pauli exclusion principle. Therefore, we can simply define the content of the overlaps of the two bases as optimization coefficients and search for them. Here, the prefactors depend on the occupation number itself. This is why we can not just pull them out of the sum in order to define a new operator algebra, unspoken of the normalization of two operator terms. Note that this is really just a matter of two particles occupying the same level. For instance, hard core bosons with the same space as eq. (6.17) can be exposed to this procedure, while $SU(2)$ fermions with the properties

$$\begin{aligned}
\underline{n=0, S=0}: &\quad |0,0\rangle \ , \\
\underline{n=1, S=1/2}: &\quad |1,1/2;\ 0,0\rangle, |0,0;\ 1,1/2\rangle \ , \\
\underline{n=2, S=0}: &\quad |2,0;\ 0,0\rangle, |1,1/2;\ 1,1/2\rangle, |0,0;\ 2,0\rangle \ , \\
\underline{n=2, S=1}: &\quad |1,1/2;\ 1,1/2\rangle \ , \\
\underline{n=3, S=1/2}: &\quad |2,0;\ 1,1/2\rangle, |1,1/2;\ 2,0\rangle \ , \\
\underline{n=4, S=0}: &\quad |4,0\rangle \ .
\end{aligned} \tag{6.39}$$

fail again due to up- and down-spin occupying the same spinor.

This was our starting point where we wondered whether it is possible to apply mode transformation to generic systems without knowing the exact details of the rotation, which we most likely could not enforce correctly anyway.

Therefore, we took away the restriction that the unitary needed to depicture the rotation of single particle orbitals. This rather simple statement changes the setup entirely, for good and for worse, as we shall see in the following. Assuming we have a twosite gate, i.e. a square matrix of dimension d^2, the only restrictions are that it

i. does not violate the symmetry of the computational basis,

ii. preserves the nature of the physical degrees of freedom and

iii. is unitary, such that it preserves the Hilbert space structure.

Any rotation matrix U, living on the two orbital Hilbert space $\mathcal{H}_1 \otimes \mathcal{H}_1$ which is block diagonal in the irreps of the symmetry transformation and whose blocks are unitary themselves, fulfils these three properties.

However, there are several problems with this approach. First, making the entries of the unitary themselves, the variation parameters introduced more degrees of freedom than allowed. If you look at eq. (6.26) for instance, even fixing the one dimensional blocks, there remain 32 parameters. For most non-convex optimization algorithms this is too costly to operate on. Furthermore, typical optimization algorithms will also not find an unitary solution, but only try to minimize the objective, two tasks which are nearly always not compatible with each other. For instance, a simple gradient descent search will look for the direction of the steepest descent and basically just executes

$$U \leftarrow U - \varepsilon \frac{\partial f(U)}{\partial U} \ , \tag{6.40}$$

with ε being a parameter. As is seen quite easily, this is not unitary anymore, i.e. we obtain

$$\left(U - \varepsilon \frac{\partial f(U)}{\partial U} \right)^{\dagger} U - \varepsilon \frac{\partial f(U)}{\partial U} = 1 - 2\varepsilon \operatorname{Re} \left(U^{\dagger} \frac{\partial f}{\partial U} \right) + \varepsilon^2 \left\| \frac{\partial f}{\partial U} \right\|^2 \ , \tag{6.41}$$

a quantity which is far from being unitary. Of course a subsequent QR decomposition might account for this, but in our experience the QR usually destroys the minimum character of the solution.

In order to handle these severe shortcommings, we came up with a different ansatz for the unitary. Due to the constraint that each block of the matrix needs to be unitary itself (or even more restrictive, be a member of the $SO(n)$), we can make the following statement. Each block $U^{(i)}$ inside U, belonging to the symmetry species i can be written as

$$U^{(i)} = \exp\left(\mathrm{i} \sum_j J_j^{(i)} C_j \right) \ , \tag{6.42}$$

where J_j are the generators of the $SO(n)$, C_j are arbitrary coefficients and the sum over j runs over as many elements, as the group has degrees of freedom. For example, $SO(2)$ has the previously encountered single degree of freedom, $SO(3)$ has three degrees of freedom, and $SO(4)$ has six. Higher block dimensions can in principle be constructed automatically, however, for non of our investigated cases they were necessary. Note that a complex transformation would utilize the $SU(n)$ as symmetry group, which has higher dimension, but not twice as high, due to the restrictions of the symmetry group. Since the individual Hilbert spaces are disjoint we can finally write the total transformation matrix as

$$U = \exp\left(\mathrm{i} J \cdot C\right) \ , \tag{6.43}$$

where J is the total generator

$$J = \begin{bmatrix} \boxed{} & & & \\ & \boxed{J^{(2)}} & & \\ & & \boxed{\quad J^{(3)} \quad} & \\ & & & \boxed{} \end{bmatrix} \tag{6.44}$$

System	Single particle basis free parameters	Total unitary free parameters
$U(1)$ spinless fermions	1	1
$U(1)$ hard-core bosons	1	1
$U(1) \times U(1)$ spinfull fermions	2	10
$SU(2) \times U(1)$ spinfull fermions	1	5
$U(1)$ bosons $n = 2$	1	5
$U(1)$ bosons $n = 3$	1	14

Table 6.1: Number of free parameters compared for different systems. It is important to emphasize, that not for all of the systems a closed expression for the mode transformation exists. As a rule of thumb we had a linear scaling of 30 iterations per species in the number of parameters for the Nelder-Mead-based, derivative-free optimization. All values are given for a completely real transformation matrix.

and C is a vector of the length of the total unitary optimization subspace. This is an important fact that is worth reemphasizing, by constructing the form of the unitary explicitly. In that way, we optimize only in the subspace of the unitary rotations and therefore do neither have too many open parameters, nor have to do a QR of the matrix afterwards. The only thing remaining is to construct the full J matrix (as a rank-three tensor), which can be done once initially and reused afterwards. Note that the additional leg is a vacuum dummy leg which is mirrored on the vector C. For non-Abelian cases, the only extension is the necessity for CGCs. These we can easily take from merging tensors for the generator, since they are of rank three as well. The vector gets a singleton, since its values are optimized anyways and therefore the initial CGCs are not important.

Even though we have reduced the number of parameters significantly, we still have a high-dimensional non-convex optimization problem to tackle at each energy optimization step. To get a feeling for the spaces involved, we want to refer to table 6.1. It becomes very apparent that, the space got drastically reduced, but in some cases is still quite high dimensional. As we have previously mentioned, the incorporation of more information about our objective is definitely going to be beneficent for the convergence behaviour and the resource consumption. However, it is for example not a priori straightforward to obtain the derivate of an arbitrary cost function with respect to C. Thus, we will be discussing how this becomes possible.

Automatic differentiation 6.2.1

As discussed in the last section, the more we know about our objective, the easier it gets to optimize. Apart from a few special cases however, it is difficult to obtain the generic derivative of f when operating numerically, let alone in tensor networks. However, a way to compute semi-analytical gradients for arbitrary functions exists, called automatic differentiation (AD) [Wen64]. This technique is a highly flexible tool which is broadly used among many areas, e.g. from environmental science over finance mathematics to neural networks (for an overview the interested reader might have a look at [BC05]).

Basically, the idea of AD works as follows, assuming we can write the function evaluation as a concatenation of operations on an input data leading to an output data. Furthermore we presume, that we know the derivative for each of these operations. The former statement is formalized as

$$
\begin{aligned}
f \colon \mathbb{C}^n &\longrightarrow \mathbb{R} \\
C &\mapsto f(C) = (f_m \circ f_{m-1} \circ \ldots \circ f_1)(C) \qquad (6.45) \\
f_i \colon \mathbb{C}^{n_i} &\longrightarrow \mathbb{C}^{n_{i+1}} \\
y_{i-1} &\mapsto y_i = f_i(y_{i-1}) \,, \qquad (6.46)
\end{aligned}
$$

where C and all the f_i can be multi-dimensional, but are not necessarily of the same dimensions or rank. For f itself, we always know we have a scalar objective. The only necessity is that the data structure of the inputs is the same as the previous outputs, e.g. $n_0 = n$ and $n_{m+1} = 1$. Being interested in the total gradient, we write by means

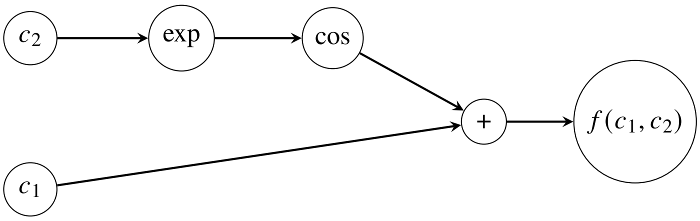

Figure 6.3: The compute graph of eq. (6.49).

of the chain rule

$$\nabla_C f = \frac{\partial f}{\partial y_1} \cdot \frac{\partial f_1(C)}{\partial C} = \left(\frac{\partial f}{\partial y_2} \cdot \frac{\partial f_2(y_1)}{\partial y_1} \right) \cdot \frac{\partial f_1(C)}{\partial C} \tag{6.47}$$

$$= \ldots = \frac{\partial f_m}{\partial y_{m-1}} \cdot \ldots \cdot \frac{\partial f_2}{\partial y_1} \cdot \frac{\partial f_1}{\partial C} \,, \tag{6.48}$$

noting that the individual gradients are contracted over their mutual indices, as is indicated by the " · " symbol. This is where the second assumption comes in. If we know how to compute the derivative of each operation, we can compute the total gradient relatively easy. We follow the flow of operations recursively back from the result to the inputs and compute each derivate element, a pattern known as backward sweep AD. At each step we contract the gradient into the previous gradients. Finally, we obtain a numerical exact representation of the gradient without the need to use numerically unstable difference quotients. The entire pattern is visualized in fig. B.2 for our 1-norm cost function eq. (6.31) and the generic ansatz (described in section 6.2).

The implementation in tensor networks [LLWX19, Hub19] is technically a bit sophisticated but conceptually straight forward. For this, the input tensor for the computation of f gets extended by an object we call "compute node". This compute node stores all the data necessary for the flow back to the initial input node, in addition to the aforementioned partial gradients, e.g. by previous compute nodes and cached objects. Of course for the input tensor itself the compute node is trivial. Starting from the input tensor, each new operation successively instantiates a compute node of the applied operation. When the final result is then obtained, we flow back the compute graph and compute each partial derivative from the cached data while contracting it with the results of the previous compute node. In the syten toolkit [HLL$^+$] this is especially easy due to the use of automated tensor leg contractions of the "STensor" class.

In order to understand this concept better, the following presents a simple one dimensional analytic example with the function

$$f(c_1, c_2) = c_1 + \cos \mathrm{e}^{c_2} \,. \tag{6.49}$$

Together with the partial functions

$$f_1(C) = \begin{pmatrix} c_1 \\ \mathrm{e}^{c_2} \end{pmatrix} = y_1 \,, \quad f_2(y_1) = \begin{pmatrix} (y_1)_1 \\ \cos(y_1)_2 \end{pmatrix} = y_2 \,, \quad f_3(y_2) = (y_2)_1 + (y_2)_2 \,, \tag{6.50}$$

we are able to write the function, whose compute graph is visualized in fig. 6.3, as $f(c) = f_3(f_2(f_1(c)))$. The gradient then resolves via the partial derivates as

$$\frac{\partial f}{\partial C} = \frac{\partial f_3}{\partial y_2} \cdot \frac{\partial f_2}{\partial y_1} \cdot \frac{\partial f_1}{\partial C} = \begin{pmatrix} 1 \,, & 1 \end{pmatrix} \begin{bmatrix} 1 & 0 \\ 0 & -\sin(y_1)_2 \end{bmatrix} \begin{bmatrix} 1 & 0 \\ 0 & \mathrm{e}^{c_2} \end{bmatrix} = \begin{pmatrix} 1 \,, & -\mathrm{e}^{c_2} \sin \mathrm{e}^{c_2} \end{pmatrix} \,. \tag{6.51}$$

As we see, we obtain the (trivial) correct gradient, just by the means of the partial objects. Once implemented correctly, this provides us with an extremely powerful framework to differentiate any tensor network with respect to any constituent tensor within it, which is as exact as our numerics allow, and relatively cheap to obtain. Usually, the cost of the derivative evaluation is around the same order of magnitude as the function evaluation itself.

Apart from the trivial implementation of functions like tensor-tensor addition or contraction, there are recipes of highly non-trivial functions in the AD community. For instance, for our implementation the QR decomposition [WLL10] or the SVD [Tow16] were highly important. Each function operating on a tensor needs to be therefore equipped with the necessary information to generate its own compute node or cancel if called without such functionality.

In principle, this closes our discussion of the generic application of unitaries to two orbital Hilbert spaces. Basically, we now know everything needed in order to implement the rotation matrix and optimize its parameters efficiently in tensor networks.

Derivative of matrix exponential | 6.2.2

Before discussing results of the method introduced, we would like to discuss the derivative of one function, which is not completely trivial. Basically, we neglected the question of how to obtain the specific partial gradients up until now. Looking at the compute graph in fig. B.2 we see a lot of functions, whose gradient is not a priori clear. Fortunately, except for one of them, we where able to find literature on the partial gradients, as described in the previous section. However, the derivative of the exponential of a matrix was not easily obtained. As a disclaimer, we would like to mention here, that we firmly believe that someone has solved this problem before, but there is no immediate literature on this, therefore we tried to derive it ourselves.

The question is, given the function

$$f(I) = \mathrm{e}^{tI} \in \mathbb{C}^{n\times n} \tag{6.52}$$

with the input matrix $I \in \mathbb{C}^{n\times n}$ and t being a number, how can we obtain a closed form of

$$\frac{\partial f}{\partial I_{ij}} \tag{6.53}$$

from quantities available, i.e. f, I, etc? In the fashion of the gradient as derivate along a direction in a vector space, we define the unit “vectors” in the matrix space as

$$(E_{ab})_{ij} = \delta_{ij}\delta_{ab} \quad \Leftrightarrow \quad E = 1 \odot 1 \ . \tag{6.54}$$

For each entry in the matrix this gives a matrix only containing zeros and unity for the respective direction, e.g.

$$E_{11} = \begin{bmatrix} 1 & 0 & \dots & 0 \\ 0 & 0 & \dots & 0 \\ \vdots & \vdots & \vdots & \vdots \\ 0 & 0 & 0\dots & 0 \end{bmatrix} . \tag{6.55}$$

By means of this we can define the directional partial derivative via the limit [Coo15]

$$\frac{\partial \exp(tI)}{\partial I_{ij}} = \lim_{h\to 0} \frac{\mathrm{e}^{t(I+hE_{ij})} - \mathrm{e}^{tI}}{h} \ , \tag{6.56}$$

which resembles the definition of the usual (scalar) exponential function. Therefore, the derivative is expected to be the function itself multiplied with some factor, our aim should now be to bring the derivative in this form. However, we can not just pull out the exponential, since the terms consist of non-commuting matrices. Therefore, we make use of the Zassenhaus formula (closely related to the Baker-Campbell-Hausdorff formula (BCH) [Bak01, Cam97, Hau06] and the Suzuki-Trotter decomposition [Tro59, Suz76b, Suz76a])

$$\begin{aligned} \exp\left(t(I + hE_{ij})\right) = \exp\left(tI\right) \cdot \exp\left(thE_{ij}\right) &\cdot \exp\left(-\frac{t^2}{2}\left[I, hE_{ij}\right]\right) \\ &\cdot \exp\left(\frac{t^3}{6}\left(2\left[hE_{ij}, \left[I, hE_{ij}\right]\right] + \left[I, \left[I, hE_{ij}\right]\right]\right)\right) \\ &\cdot \exp\left(\frac{-t^4}{24}\left[\left[\left[I, hE_{ij}\right], I\right], I\right] + \mathrm{O}\left(h^2\right)\right) \mathrm{O}\left(t^5\right) \ . \end{aligned} \tag{6.57}$$

We recognize a power expansion in t with the exponents having a term of order $\mathrm{O}(h)$ and for the higher powers, terms scaling at least quadratically in h. Since we are interested in the small h limit, we can Taylor expand, which leads us, up to first order, to

$$\frac{\partial \exp(tI)}{\partial I_{ij}} = \frac{\mathrm{e}^{tI}}{h}\left(\left(1+thE_{ij}+\mathrm{O}\left(h^2\right)\right)\left(1-\frac{t^2}{2}[I,hE_{ij}]+\mathrm{O}\left(h^2\right)\right)\left(1+\frac{t^3}{6}[I,[I,hE_{ij}]]+\mathrm{O}\left(h^2\right)\right)\cdot\mathrm{O}\left(t^4\right)-1\right) \tag{6.58}$$

$$= \frac{\mathrm{e}^{tI}}{h}\left(1+thE_{ij}-\frac{t^2}{2}\left[I,hE_{ij}\right]+\frac{t^3}{6}\left[I,hE_{ij}\right]_2+\ldots+\mathrm{O}\left(h^2\right)-1\right) \tag{6.59}$$

$$= \frac{\mathrm{e}^{tI}}{h}\left(\sum_{n=1}^{\infty}\frac{(-1)^{n-1}t^n}{n!}\left[I,hE_{ij}\right]_{n-1}+\mathrm{O}\left(h^2\right)\right) , \tag{6.60}$$

where we defined the n-th nesting of the commutator as $[\,\cdot\,,\,\cdot\,]_n$. Executing the limit $h \longrightarrow 0$ we arrive at the closed form

$$\frac{\partial \exp(tI)}{\partial I_{ij}} = -\mathrm{e}^{tI}\left(\sum_{n=1}^{\infty}\frac{(-t)^n}{n!}\left[I,E_{ij}\right]_{n-1}\right) , \tag{6.61}$$

which is the matrix product of the original exponential and some factor introduced by the derivative, in analogy to the scalar case.

In principle, this is sufficient to compute the derivative, we can just truncate the series after some n terms and compute the gradient from the objects I, E and $f(I)$, to which we have quite easy access. We can even compute each term in the sum from the previous term, i.e. set up a recursive pattern to decrease the cost. However, the norm of the commutator decreases quite slowly, such that we typically needed around 20 iterations until we reached convergence, e.g. for fermionic sites. This makes the computation not only quite costly, but also prone to catastrophic cancellation [Gol91] due to the alternating sign in the series. We solved this problem by reformulating the series in an exact fashion, without the need to truncate.[1] The key observation of the procedure [Bra20], is the fact that $[\,\cdot\,,\,\cdot\,]_n$ is a bilinear map from two matrices to another matrix. Therefore, if we map the space of matrices to an isomorphic space of vectors, the operation $[I,\,\cdot\,]_n$ is the pendant of a matrix multiplication with a vector. Such a bijection $\beta(i,j)$ could for instance be a fuse or split tensor multiplied into the matrix to which $[I,\,\cdot\,]_n$ is applied. The central claim now is that higher order commutators behave like powers of the matrix application, i.e.

$$[I,\,\cdot\,]_n = [I,\,\cdot\,]^n\ . \tag{6.62}$$

This claim we prove via induction, i.e. starting from

$$[I,\,\cdot\,]_0 B = B = [I,\,\cdot\,]^0 B \tag{6.63}$$

$$[I,\,\cdot\,]_1 B = [I,B] = [I,\,\cdot\,]^1 B \tag{6.64}$$

we can make the step

$$[I,\,\cdot\,]_{n+1} B = [I,[I,B]_n] = [I,\,\cdot\,][I,\,\cdot\,]^n B = [I,\,\cdot\,]^{n+1} B\ . \tag{6.65}$$

With respect to the scalar product defined by the Frobenius norm, we can investigate the (anti-) hermiticity properties of the matrix for two arbitrary vectors A, B

$$\langle A|[I,B]\rangle = \mathrm{tr}\left(A^\dagger[I,B]\right) = \mathrm{tr}\left(\left[A^\dagger,I\right]B\right) = \pm\,\mathrm{tr}\left([I,A]^\dagger B\right) = \pm\,\langle [I,A]|B\rangle\ , \tag{6.66}$$

where plus sign holds for I being hermitic and the minus sign for I being anti-hermitic, i.e. the matrix in our isomorphic space inherits its hermiticity properties from I. Finally, we write down the representation of the matrix

$$\Gamma_{\beta(k,l),\beta(i,j)} = \left(\left[I,E_{ij}\right]\right)_{kl}\ , \tag{6.67}$$

---

[1] For historical reasons we referred to this procedure internally as the “first Bramberger solution”.

with which we can write eq. (6.61) as

$$M(\Gamma) = \sum_{n=1}^{\infty} \frac{(-t)^n}{n!} \left[I, E_{ij}\right]_{n-1} = \sum_{n=1}^{\infty} \frac{(-t)^n}{n!} \underbrace{\Gamma^{n-1}}_{=(\xi^*\gamma)^{n-1}} = \sum_{n=1}^{\infty} \frac{(-t)^n}{n!} \xi^{*n-1} U D^{n-1} U^\dagger \tag{6.68}$$

$$= U \frac{1}{\xi^* D} \left(\mathrm{e}^{-t\xi^* D} - 1\right) U^\dagger \ . \tag{6.69}$$

Here, we defined the hermitian matrix γ and the residual prefactor ξ, which is one in the case of a hermitian matrix and i for an anti-hermitian one. Since we diagonalized the matrix it now can be easily exponentiated

$$M(\Gamma) = U \operatorname{diag}\left[\frac{\mathrm{e}^{-t\xi^* d_1} - 1}{\xi^* d_1}, \frac{\mathrm{e}^{-t\xi^* d_2} - 1}{\xi^* d_2}, \dots, \frac{\mathrm{e}^{-t\xi^* d_n} - 1}{\xi^* d_n}\right] U^\dagger \ . \tag{6.70}$$

It is worthwhile stepping back for a second an observing the result again. We have achieved to map our problem from a numerically highly unstable series to the problem of merging the correct legs of a tensor and diagonalizing a relatively small hermitian matrix. This makes it possible to compute the derivative for arbitrary exponents I, we just have to transform the result back into the original basis. We formalize the entire algorithm.

1. Compute e^{tI}.
2. Construct E.
3. Compute the commutator $\Gamma = \left[I, E_{ij}\right]$.
4. Merge the matrix legs of Γ into one leg and the index legs i, j into another, therefore obtaining a true matrix.
5. Diagonalize Γ, obtaining $UDU^\dagger$.
6. Set each element of D to
   i. $\exp\left(\mathrm{e}^{-td} - 1\right)/d$, if the eigenvalue $d > 0$, or
   ii. use l'Hopital's rule and set the element to $-t$ otherwise.
7. Multiply to $\Gamma = UDU^\dagger$ again.
8. Demerge into the original matrix legs and i, j.
9. Multiply Γ with $-\mathrm{e}^{tI}$ to obtain the final derivative.

Finally, we have everything to implement and compute the general unitary and its derivative and can therefore start benchmarking the algorithm.

Operator bond dimension 6.2.3

Overcoming the rotation of single particle orbitals in eq. (6.38) and introducing the ansatz in eq. (6.43) we hid one thing, namely the behaviour of the operator under this transformation. As we mentioned in previous sections and visualized in fig. A.1, we sandwich the Hamiltonian with the adjoint of the rotation from the left and the rotation itself from the right. Starting from the most general Hamiltonian, which restricts to maximally two particle interaction (and suppressing the spin indices from eq. (3.68), as they are not important for the argument)

$$H = \sum_{ij} t_{ij} \, \hat{c}_i^\dagger \hat{c}_j + \sum_{spqr} v_{spqr} \, \hat{c}_s^\dagger \hat{c}_p^\dagger \hat{c}_q \hat{c}_r \tag{6.71}$$

and rotating

$$\hat{c}_i^{(\dagger)} \to U_{i1} \hat{c}_1^{(\dagger)} + U_{i2} \hat{c}_2^{(\dagger)} \tag{6.72}$$

we will maximally change the content of the t and v objects. However, the operator bond dimension $w = \mathrm{O}\left(L^2\right)$ bound [HMS17] remains valid at any time. This of course only goes under the assumption, that we use the usual tricks [HMS17] in order to avoid numerical garbage piling up in the operator and hence finding a good representation. When one uses the pre-MPS way to construct Hamiltonians from partially pre-summed complementary operators [CKN$^+$16, KVLE16] the same logic holds. There, only the operator terms which belong to changed orbitals have to be updated by recomputation. Since we have direct access to the global U matrix, we do need to transform further observables, they can just be reconstructed after the optimal basis has been found.

For our construction scheme in eq. (6.43) which only restricts itself to be unitary, this is no longer the case. We do know that the transformed Hamiltonian will be representable in some second quantized basis, but its representation in this basis might contain arbitrary high particle interactions

$$\hat{H} = \sum_{ij} t^1_{ij}\ \hat{c}^\dagger_i \hat{c}_j + \sum_{spqr} t^2_{spqr}\ \hat{c}^\dagger_s \hat{c}^\dagger_p \hat{c}_q \hat{c}_r + \sum_{ijspqr} t^3_{ijspqr}\ \hat{c}^\dagger_i \hat{c}^\dagger_j \hat{c}^\dagger_s \hat{c}_p \hat{c}_q \hat{c}_r + \dots\ , \tag{6.73}$$

which in turn shifts the bond dimension bound to $\mathrm{O}\left(L^\iota\right)$, where ι is the highest interaction introduced. Of course, this does not mean that this immediately happens, but depending on the system at hand and the truncation procedure after the rotation, this can have severe consequences. For instance, we have observed systems whose bond dimension reaches $\mathrm{O}\left(20\,000\right)$ after just two sweeps with this method. Of course the computational speed-up in the state bond dimension is then completely destroyed by this scaling. Therefore a careful observation and control of the algorithm is of high relevance for its application and we are not able to currently offer a manual for procedure. This has to be the subject of future research efforts.

One path we followed, was to extend the cost function by the bond dimension of the operator and a scaling factor η, i.e.

$$f(C) \to f(C) + \eta \tilde{f}(W)\ , \tag{6.74}$$

where W is the twosite MPO tensor. η can be utilized to choose how much one wants to weigh the operator. Please note, that we are again comparing spectra of different Hilbert spaces, therefore a relative measure as in eq. (6.32) is necessary. As f we chose the four norm of the spectrum eq. (6.33), as we can compute it with the same scaling as the one norm, as discussed before, but we avoid taking SVDs. Since operators can not be normalized, in contrast to wave functions, and their norms usually grow exponential in system size, the spectra consists of quite large numbers, even when using the rescaled SVD. What we found is that the additional term complicates the optimization landscape (described in fig. 6.1) so much that our usual algorithms do not find minima in a reasonable number of iteration steps. However, it would be feasible to find a way in the future to get better control of the operator bond dimension, in order to push this method to new potential domains, irrespective of the fermionic or generic ansatz chosen.

One last remark we want to make is that using the generic ansatz prevents rotation of the original basis to the new one in order to compute observables the usual way. However, we can use the same method as before, i.e. sandwiching the Hamiltonian, on an arbitrary operator, e.g. the identity MPO. This way we obtain the global representation of the unitary as an MPO itself and can then rotate global quantities between the different bases by means of operator-operator applications, see section 3.3.4. Of course, here the same catastrophic scaling can happen, which would then make the calculation useless, apart from trivial quantities, e.g. entropies and energies.

2d Fermi-Hubbard model benchmarks 6.3

The Hubbard model [HF63, Kan63, Gut63] has been of physical interest for over half a decade now. Its basic idea is as simple as the model itself is written down: How does the tendency of spinfull electrons to delocalize play out against their repulsion due to electrostatic effects and Pauli's principle [Pau25]? This is manifested through the simple looking Hamiltonian model (given in the canonical ensemble)

$$\hat{H}/t = - \sum_{\langle i,j \rangle \sigma} \hat{c}^\dagger_{i\sigma} \hat{c}_{j\sigma} + U/t \sum_i \hat{n}_{\uparrow\downarrow,i}\ , \tag{6.75}$$

where the former is controlled through the tunnelling amplitude t and the latter via the on-site repulsion U. This can be a good model to approximate an atomic grid, in which the atoms keep their electrons tightly bound to themselves,

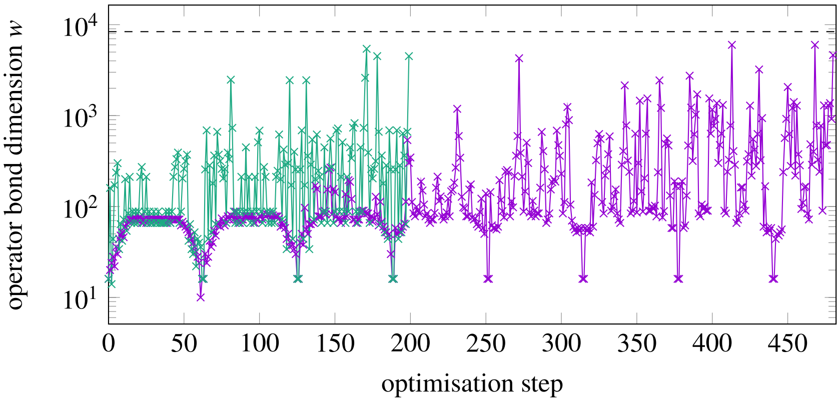

Figure 6.4: Bond dimension of the operator in fermionic (—×—) and AD (—×—) orbital optimization plotted against the optimization step. The system at use is an 8×8 Fermi-Hubbard model with $U = 8$ and $1/8$-th doping. Note, that the periodic decreasing comes from the trivial bond dimensions at the edges of the MPO. Furthermore, the theoretical bound (- - -) on a fully dense quartic MPO bond dimension is $w \leq 2L^2 + 3L + 2 = 8386$ [HMS17], which is not violated. The initial bond dimension before mode transformation was $w = 6$.

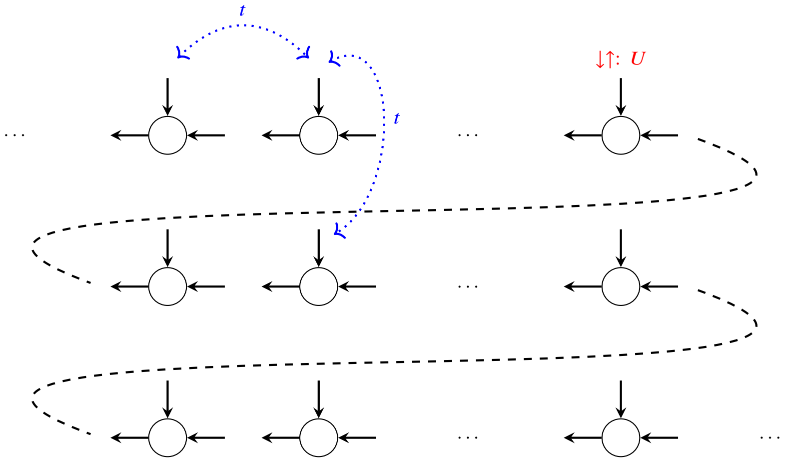

Figure 6.5: Schematic representation of the Z-mapping of a 2d lattice to a MPS. While the hoppings along the x-axis can be attributed to neighbouring nodes, the hopping along the y-axis always will be L_x nodes away. Double occupancies are penalized with an energy contribution of U. Note, that one could also do a snake mapping, i.e. connecting the edges of the rows. This would make the number of nodes between rows variable between one and $2L_x - 1$, in our case depending on how far the upper node is from the right edge.

however the individual atoms are close enough, such that hopping can occur between nearest neighbours. The geometry of the grid is basically left open in this formulation and can be arbitrary, however, in our case the grid shall be a 2d square lattice as is shown in fig. 6.5. The interaction between electrons of different grid points is neglected, only the double occupation of two electrons of opposite spin is penalized with an energy gain of U. We consider each atom to have only one non-degenerate electronic orbital, e.g. because higher lying orbitals are separated through a large energy gap.

Of course, this is a simplification of reality and far from being ab-initio, however the idea is to isolate interesting physics and attribute it to simple origins. In particular, the Hubbard model and related models are candidates for modelling high T_c superconductivity [BM86, Dag94] in cuprates [And87, ZR88]. For ordinary superconductors the microscopic origin [BCS57a, BCS57b] can be attributed to the instability of the Fermi-sea towards perturbations with an attractive electron-electron interaction [Coo56] and the subsequent formation of composite bosonic particles, so called Cooper pairs. However, due to the low binding energy of Cooper pairs their formation is restricted to low temperatures, i.e. above $T_c \gtrsim \mathrm{O}\,(10\,\mathrm{K})$ the composite particles break into their constituents again. Therefore, one can also see the Hubbard model as a "natural" extension, asking how superconductivity can occur given repulsion

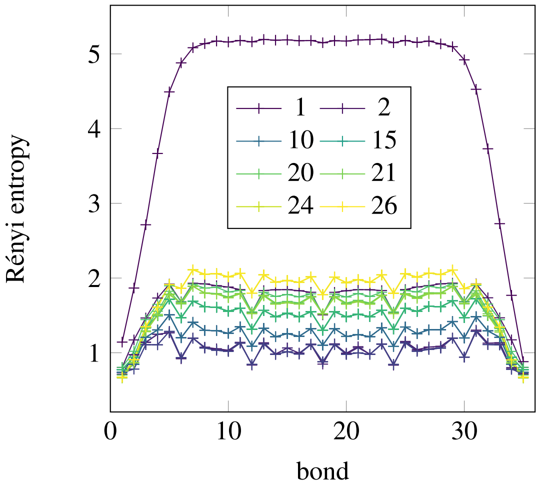

Figure 6.6: Bond entropies for the $L = 6$ lattice at half filling getting brighter with increasing number of iterations.

of the constituents.

Coming back to the model and neglecting its applications, we can see that it is solely controlled by two parameters. Being only interested in the singlet ground state, we have the ration between hopping and repulsion and the number of particles present, i.e. the filling factor $\rho = {}^{N}/_{L}$, as parameters. It is also common to work with the doping of the model, i.e. how much the particle number is away from being half filled $\rho = 1 + \delta$). Even though the model is quite simple looking, it is far from trivial to solve for large systems sizes. There exists a variety of literature for different regimes, e.g. for the under-doped model [ZCC+17, TLJ+13, AM07] or at half filling [LAB+15, SWicv+21, QSA+21]. Especially the latter can be well accessed by Monte-Carlo methods, since it does not suffer from the sign problem [Hir85]. However, the doped case, which is of particular physical interest, just recently got treated in a conclusive manner, where it was found that the ground state consists of stripes and that it is not superconducting [QCS+20].

For our test of the fermionic mode transformation we ran quadratic lattices with two system sizes, i.e. $L = 6$ and $L = 8$ at $U/t = 8$. Furthermore, the transformation matrix of the spin species were enforced to have the same rotation angle α, a procedure which has higher energies during the optimization process than UHF calculations. However, this resembles the physical situation of the system, i.e. an invariance under exchange of up-and down-spin. We chose periodic boundary conditions since the mode transformation is able to find the momentum space representation for translationally invariant systems in 1d and this might be also beneficial in higher dimensions. For the doping we used half filling and the doping of $\delta = 1/8$ which was employed in [QCS+20]. As discussed in the latter, the competition between entropy and energy minimization, in combination with the large system sizes necessary, makes a faithful simulation quite difficult. Furthermore, the suspected stripe ground state has a mean-field wavelength of $\lambda = 1/\delta$ [VT18], which would tend to make systems below width of $L = 8$ frustrated in simulations.

We initiate our simulation by a run at bond dimension $m = 512$ which results in a quite high Rényi entropy, as can be seen in fig. 6.6. This can be attributed to the artificial 1d → 2d mapping which introduces long range hopping in the MPS. This is followed by a reordering of the modes according to the mutual information criterion (as was explained in section 3.4) which causes an immediate drop of the overall entropy. In the subsequent steps, the bond dimension grows up to the final value of $m = 2048$ which leads to a growth of the entropy. However, the mode transformation counteracts this growth by minimizing the singular value spectrum.

As for the energy, we clearly see large drops in fig. 6.7 in some of the iterations after mode transformations have been applied, even though bond dimension is kept constant at these iterations. This resembles the fact, that we did not choose the local transformations to be greedy, in order to avoid getting stuck in local minima, as the search for good modes takes several iterations. The particle densities and spins in fig. 6.8 show the typical antiferromagnet (AFM) order in the half filled 2d Fermi-Hubbard model [HT89]. The particles try to maximally delocalize in order to minimize the energy and therefore the distribution is not differing more than 1×10^{-5} from unity, while the spins are alternating.

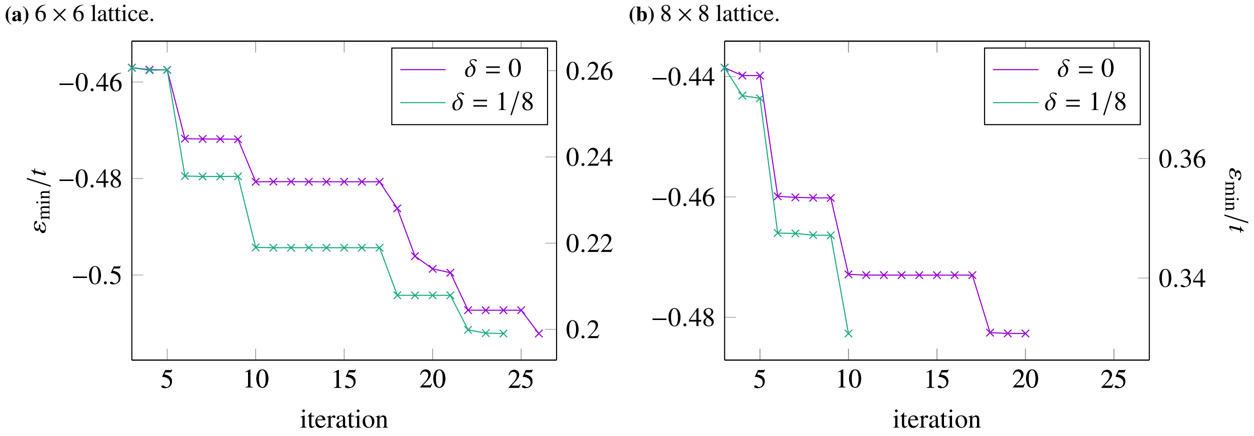

Figure 6.7: Minimal energy density for each iteration during the DMRG mode transformation process for a 2d Fermi-Hubbard model with periodic boundaries. Half filling ($\delta = 0$) is shown on the left y-axis and the doped model is shown on the right.

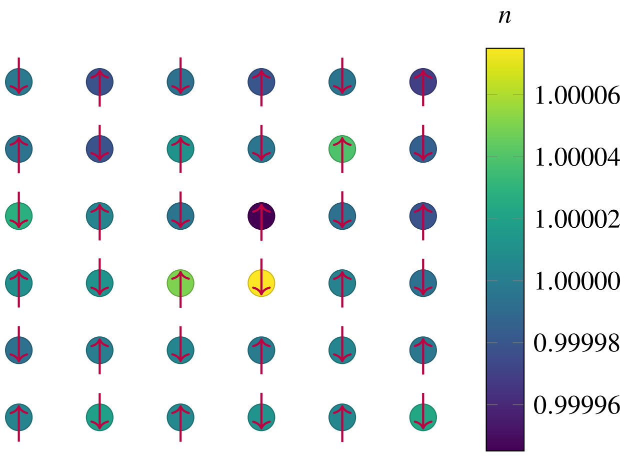

Figure 6.8: Density and spin expectation values for the half filled Fermi-Hubbard model with mode transformation. The spins resemble AFM order and are depicted true to scale.

Projected purification

7

So far, we have encountered systems in- and out-of-equilibrium, but we have not yet talked about systems beyond the BO approximation. We mentioned in section 3.4, that Hamiltonians for such systems exist, but did not dive into any further detail. Therefore, prior to discussing on tensor network methods for such systems, we will spare a moment to explain their derivation from the Schrödinger equation.

Basically, the idea of Born and Oppenheimer [BO27] is to split off the nuclear motion in the molecular Hamiltonian eq. (1.3) and treat each problem separately. In order to do so, we introduce a mean nuclear mass M and define $\chi = (m/M)^{1/4}$, where m is the electron mass. This enables us to write the total Hamiltonian as

$$H = T_e(\nabla_i) + U(x_i, x_I) + T_n(\nabla_I) = H_0 + \chi^4 H_1 \ , \tag{7.1}$$

where lower case indices i are counting electrons, while capital indices I count nuclei. This way, the nuclear motion can be treated perturbation-like, with the parameter χ being very small, even for the lightest nuclei. One common physical picture is that the electrons are so much lighter than the nuclei, that their motion follows instantaneously. The authors then argue that the solution of the $\chi = 0$ limit, i.e. frozen nucleus motion $x_I = \text{const.}$ leads to an electronic wave function $\varphi_{x_I}(x_i)$, only parametrically depending on the nuclear positions. Furthermore, we obtain corresponding eigen energies $E^{(0)}$, which only depend on the relative nuclear coordinates, a concept nowadays referred to as potential energy surface (PES). A subsequent expansion of the relative nuclear coordinates with respect to small changes χ leads to a series of differential equations for the total molecular wave function [BO27]. The zeroth and first order corresponds to the lattice being in equilibrium, especially the former is solved by a product state ansatz of the nuclear and electronic wavefunctions. The second and third order belong to lattice vibrations and are therefore more complicated to solve. This originates in the fact that the second order correction is the first term containing contributions from H_1 [BO27]. Higher order corrections give higher order lattice corrections, which are usually not of particular interest to us. Expanding the solutions of the perturbed electronic wave functions in the nuclear frozen electronic basis leads to a total wave function representation [BO27]

$$\psi(x_i, x_I) = \sum_k \xi_k(x_I)\varphi_{x_I,k}(x_i) \ , \tag{7.2}$$

where the $\xi_k(x_I)$ are some functions for the nuclei, yet to be determined.

In order to derive the validity of this ansatz we plug the total wave function back into the eigenvalue eq. (7.1) and eliminate the electronic part of the wave function, which leads to [Gla44, SIS⁺15, Mus16]

$$(H_{\text{el}} + H_{\text{n}})\, \xi(x_I) = E\xi(x_I) \ . \tag{7.3}$$

Here, H_{el} is a diagonal matrix of the electronic energies and H_{n} is defined via the remaining terms as

$$H_{\text{n}}(x_I) = \begin{bmatrix} \langle\varphi_1|T_n|\varphi_1\rangle & \dots & \langle\varphi_1|T_n|\varphi_K\rangle \\ \vdots & \ddots & \dots \\ \langle\varphi_K|T_n|\varphi_1\rangle & \dots & \langle\varphi_K|T_n|\varphi_K\rangle \end{bmatrix} . \tag{7.4}$$

Since the derivative with respect to nuclear coordinates hits the parametric dependency of the electronic wave functions as well, we thus obtain three terms for the nuclear part [Gla44, Mus16]

$$\sum_{k'} \left(\delta_{kk'} T_n + \langle\varphi_k|T_n|\varphi_{k'}\rangle + \sum_I \langle\varphi_k|p_I|\varphi_{k'}\rangle \frac{p_I}{M_I} \right) \xi_{k'}(x_I) \ . \tag{7.5}$$

As long as the second and third term in eq. (7.5) can be neglected, we can treat the electronic and nuclear systems separate from each other and just form product wave functions. The second term is a scalar, which is somewhat related to the change of the electronic wave functions with nucleus position. As argued previously, this is not exactly relevant to our cause. On the other hand we have the last term, whose diagonal elements are zero for time reversal invariant systems and whose off-diagonals can be shown to be negligible, if the PESes do come close anywhere in the parameter space [Smi69].

If we want to go beyond the adiabatic approximation, we rely on the incorporation of the nuclear grid and its motion. Especially when dealing with calculations from first principles, we need to depicture the correct interaction and can not make use of effective models. In order to restore the diagonal character of eq. (7.3), it is therefore common to do a diabatic transformation of the electronic levels [Lic63, Smi69]. This introduces a unitary rotation in such a way, that the total matrix becomes diagonal.

From here, one can start to investigate at the molecule in the presence of nuclear vibrations. The dependency of the PES on the lattice coordinates is usually a slightly complicated configuration. However, we are only interested in the proximity to some minimal configuration, i.e. corrections to the equilibrium. Therefore, it is common practice to approximate the PES as harmonic oscillator around this minimum position [Mus16]. This is expressed in a Taylor series of the potential $E^{(0)}(x_I)$ up to the second order. Together with the kinetic energy of the nuclei, we can therefore write

$$\sum_I \left(\frac{p_I^2}{2M_I} + \frac{M_I \omega_I^2}{2} x_I^2 \right) , \tag{7.6}$$

which translates in second quantization to the well known

$$\sum_I \omega_I \left(\hat{n}_I + 1/2 \right) . \tag{7.7}$$

The occupation numbers n counts the quasi-particle excitations of the lattice vibrations, called phonons. Phonons are bosonic particles, i.e.

$$\left[\hat{b}_i^{(\dagger)}, \hat{b}_j^{(\dagger)} \right] = 0 , \tag{7.8}$$

$$\left[\hat{b}_i, \hat{b}_j^\dagger \right] = \delta_{ij} , \tag{7.9}$$

whose individual levels might count occupations $n \in [0, \infty[$.

As for the third term in eq. (7.5), this is the vibronic coupling term, which is proportional to $\langle \varphi_k | \partial_{x_I} | \varphi_{k'} \rangle$ and connects the electronic and the phononic orbitals. Here strikes the advantage of a diabatic transformation [Lic63, Smi69]: We can exchange the derivative of the electronic functions on the nuclear coordinate and get a term depending on the transformation matrix between adiabatic and diabatic orbitals and the PESes only. As the excitation energy is then usually approximated to be linear in the displacement of the nucleus [SIS+15], we arrive at the electron-phonon coupling term to the second quantized Hamiltonian

$$\sum_{ijI} g_{ij,I} \left(\hat{b}_I^\dagger + \hat{b}_I \right) \hat{c}_i^\dagger \hat{c}_j . \tag{7.10}$$

As we shall see in section 9.1, there also exist Hamiltonians which couple the electronic algebra to higher powers of the displacement $\hat{b}_I^\dagger + \hat{b}_I$. The diagonal terms $i = j$ can be interpreted as the proximity to electronic density, causing the vibrating nuclei to change motion and therefore change the energy. The off-diagonal terms $i \neq j$ in turn belong to vibrations which are influenced by electrons hopping to other orbitals.

Common methods 7.1

In order to study the impact these additional new degrees of freedom have on our tensor network approach, let us have a look at one of the easiest possible models incorporating lattice vibrations, i.e. the Holstein model [Hol59]

$$H/t = - \sum_{\langle i,j \rangle} \hat{c}_i^\dagger \hat{c}_j + U \sum_{\langle i,j \rangle} \hat{n}_i \hat{n}_j + \omega_0 \sum_I \hat{n}_I + g \sum_{i,I} \left(\hat{b}_I^\dagger + \hat{b}_I \right) \hat{n}_i . \tag{7.11}$$

While this model exhibits the usual fermionic particle number conservation due to the symmetry $\hat{c}^{(\dagger)} \to \mathrm{e}^{\pm \mathrm{i}\alpha}\hat{c}^{(\dagger)}$, no such symmetry exists for the bosonic particles. This is caused by the electron-phonon coupling, which transforms non-invariant. The physical picture is plausible, since lattice vibrations can be triggered by certain processes from "nowhere", as long as energy is conserved. However, this leads to higher occupation of the vibrational orbitals with phonons. For our usual tensor network ansatz this is quite severe, since the exploitation of symmetries in the tensor representation is crucial to the feasibility of solutions, as we explained in section 4.2. Without it, the tensors are not going to be as sparse, resulting in a significantly increased usage of CPU-time and memory consumption (we will show examples in chapter 9). For realisticly large systems this can be a curse, confining their exact first principle studies to strong limitations.

The situation gets aggravated by the fact that the vibration modes can technically be occupied by an arbitrary particle number, since they do not obey Pauli's exclusion principle. We certainly need to truncate the local Hilbert space at some finite value n_{ph}, since we are operating on a computer. However, the value for the truncation needs to be high enough, such that the system does not see the truncation. If states which are necessary to describe the wave function correctly are cut off, this will result in plain wrong results. For DMRG-like ansatzes, which were developed for a low number of local degrees of freedom the scaling can be quite challenging when n_{ph} gets large. Several methods exist to handle these type of systems [SKM+21]. Before detailing out the method we used, a brief overview is in order.

In the condensed matter community, probably one of the earliest is the pseudo-site method [JW98, ZJW99]. In order to avoid large local Hilbert spaces the representation of $0, 1, \ldots, n_{\mathrm{ph}}$ on a single orbital is therefore decomposed onto several auxiliary sites, all having a local basis of e.g. $0, 1$. The occupation of higher values are then in turn expressed through their binary representation at the cost of introducing couplings between the auxiliaries, e.g. on a single site this reads

$$|3\rangle = |1\rangle_{2^0} \otimes |1\rangle_{2^1} \otimes |0\rangle_{2^2} \otimes |0\rangle_{2^3} = \bigotimes_{i=0}^{\epsilon} |b_i\rangle_{2^i} \ . \tag{7.12}$$

Here, we have a total eight-dimensional local Hilbert space $d = 8$, going up to $n_{\mathrm{ph}} = 7$, and as a consequence, each phononic site will become $\epsilon = \lceil \ln d / \ln 2 \rceil$ new sites. This works quite well for systems with local electron-phonon coupling, however for the molecular systems treated within this thesis, which have long range couplings anyway, this results in an unreasonable high demand for resources. For instance, the bosonic creation operator looks like

$$\hat{b}^\dagger = \sum_{n=0}^{n_{\mathrm{ph}}-1} \sqrt{n+1}\, |n+1\rangle \langle n| = \sum_{n=0}^{n_{\mathrm{ph}}-1} \sqrt{n+1} \bigotimes_{ij} |b_i\rangle_{2^i}\, {}_{2^j}\langle b_j| \ , \tag{7.13}$$

obviously multiplying this with other operators results in dense long range couplings.

Another method dealing with large local Hilbert spaces is the local basis optimization (LBO) [ZJW98, BDV+15]. The basic idea is to optimize the local basis with respect to the phononic oRDM (see section 4.1.2) at each optimization step, in order to find an optimal representation [SKM+21], similar as DMRG does for the site tensor. First, we extend each site tensor by a matrix containing the basis rotation, i.e. $M^{n}_{lr} \to \sum_{n'} M^{n'}_{lr} V^{n'n}$. Then, at each optimization step of the canonical site tensor, we compute the SVD with respect to the physical bond. Subsequently, we perform a DMRG like optimization of the contraction of the transfer tensor and the rotation matrix, which is subsequently again split via a SVD. Finally, the transfer tensor is multiplied back into the site tensor, leaving the MPS open for an iteration on all sites and the transformation matrix again as an unitary. The improvement of the local basis due to these operations will be a reduction of the local dimension to a value between $1 \leq \tilde{d} \leq d$.

Finally, we want to mention the existence of a method very common in the chemistry community, namely the MCTDH [MMC90, Man08, Man09, ZXJL16, RCT19, MMC92]. Here, the idea is to decompose the many-body wave function in first quantization (particularly in real space representation) into a recursive TTNS representation and make use of the Dirac-Frenkel variational principle [Dir30, Fre34]. This leads to equations of motion for the expansion coefficients and the basis functions, which are superficially similar to those of TDVP. The local degrees of freedom of the tree then become the discretized positions in space. One of the main problems however, is the representation of the Hamiltonian in a fashion which makes the ansatz solvable. Similar to the application of H_{eff} to the wave function being the most expensive part of TDVP, this becomes the most expensive part of MCTDH. One of the down-sides here is that, due to the representation in real space, the incorporation of symmetries becomes very non-trivial. The necessary symmetry groups are substancially complicated, typically non-Abelian ones, which makes the implementation effort rather complex.

In order to handle the earlier problems, we now want to introduce the projected purification (PP) mapping [KSP21, SKM+21, Pae20], a technique which handles various difficulties of phononic models at once, which was the main method used for this thesis.

Mapping 7.2

Assume we have a wave function expanded in orbitals which are labeled by the irreps of some global conserved quantity $\hat{N} = \sum_{i=1}^{L} \hat{n}_i$

$$|\psi\rangle = \sum_{n_1 \dots n_L} c_{n_1,\dots,n_L} |n_1, \dots, n_L\rangle \ . \tag{7.14}$$

We want to emphasize, that this procedure is not restricted to particle number symmetries, in principle any global (Abelian) symmetry can be restored like this.[1] However, depending on "how much" the Hamiltonian is violating the quantum number conservation, we are going to see more blocks (discussed in detail in section 8.2). Continuing, we introduce a somewhat artificial doubling of the total Hilbert space [KSP21, SKM+21, Pae20], i.e. every orbital i becomes two orbitals $(i, \bar{i})$, i.e.

$$|\psi\rangle = \sum_{\substack{n_1 \dots n_L \\ \bar{n}_1 \dots \bar{n}_L}} c_{n_1,\dots,n_L,\bar{n}_1 \dots,\bar{n}_L} |n_1, \dots, n_L, \bar{n}_1, \dots, \bar{n}_L\rangle \ . \tag{7.15}$$

These are called "physical" and "bath" orbitals and are visualized in fig. 7.1. The attentive reader might recognize the similarity in notation to purification in finite temperature MPS approaches [VGRC04, Sch11]. However, the key difference is, that we will restrict ourselves to the sub-manifold of the original Hilbert space entirely. In order to do so we impose a gauge-condition on the coefficients of the state

$$n_i + \bar{n}_i \neq n_{\mathrm{ph}} = d - 1 \qquad \Rightarrow \qquad c_{n_1 \dots n_L \bar{n}_1 \dots \bar{n}_L} = 0 \ . \tag{7.16}$$

Plugging eq. (7.16) back into eq. (7.15) we obtain the new representation of the wave function

$$|\psi\rangle = \sum_{n_1 \dots n_L} \underbrace{c_{n_1,\dots,n_L,n_{\mathrm{ph}}-n_1 \dots,n_{\mathrm{ph}}-n_L}}_{=c_{n_1,\dots,n_L,n_{\mathrm{ph}}}} |n_1, \dots, n_L, n_{\mathrm{ph}} - n_1, \dots, n_{\mathrm{ph}} - n_L\rangle \ , \tag{7.17}$$

where we obtained the new unknown coefficients c which only depend on the original degrees of freedom and n_{ph}. If we now define the total particle number operator

$$\hat{\tilde{N}} = \hat{N} + \hat{\bar{N}} \ , \tag{7.18}$$

we see that we restored the particle number conservation

$$\begin{aligned} \left(\hat{N} + \hat{\bar{N}}\right) |\psi\rangle &= \sum_{n_1,\dots,n_L} c_{n_1,\dots,n_L,n_{\mathrm{ph}}} \left(\hat{N} + \hat{\bar{N}}\right) |n_1, \dots, n_L\rangle \, |n_{\mathrm{ph}} - n_1, \dots, n_{\mathrm{ph}} - n_L\rangle \\ &= \sum_{n_1,\dots,n_L} c_{n_1,\dots,n_L,n_{\mathrm{ph}}} L n_{\mathrm{ph}} |n_1, \dots, n_L\rangle \, |n_{\mathrm{ph}} - n_1, \dots, n_{\mathrm{ph}} - n_L\rangle = L n_{\mathrm{ph}} |\psi\rangle \end{aligned} \tag{7.19}$$

at the cost of introducing some additional nodes. Therefore, we can just introduce the total (physical and bath) particle number as a conserved quantity again, irrespective of the Hamiltonian commuting with the individual terms or not. This transforms the dense blocks of local dimension d to d sparse blocks of reduced dimension one. This has manifold advantages compared to the standard approach. Mainly, a lot of unnecessary zeros are left out therefore saving resources in CPU and memory. This can make calculations several orders of magnitude faster [KSP21, SKM+21, Pae20, MXY+21], especially when exploiting the usual parallelization over tensor blocks. Also, we make operations numerically more stable due to smaller blocks. Furthermore, the relation between the

---

[1] Non-Abelian symmetries should obey the same logics but need a more complicated gauge condition.

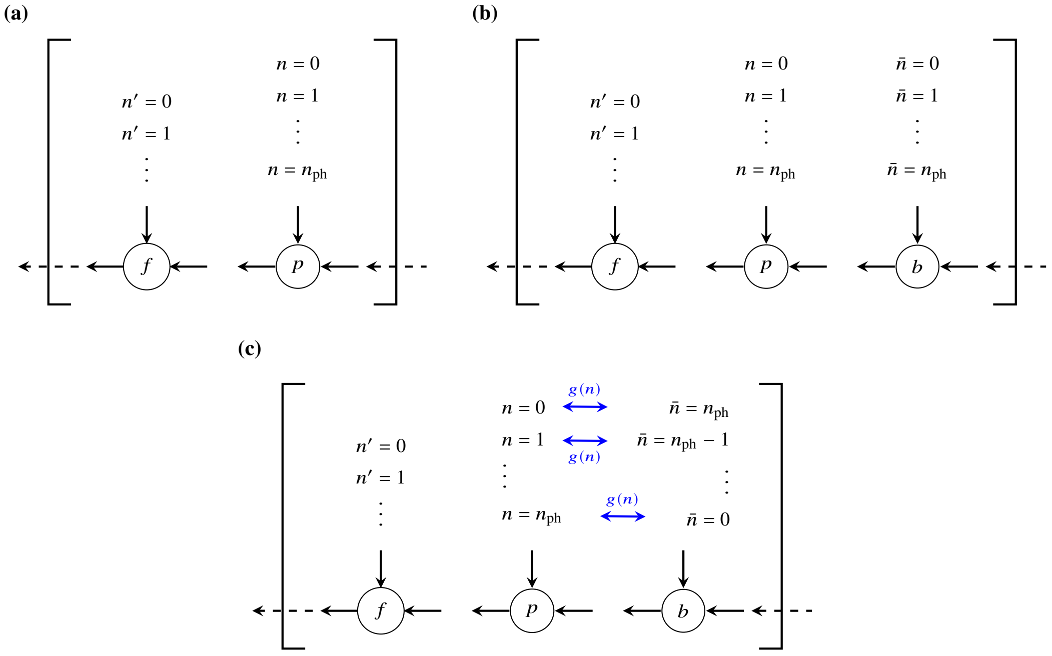

Figure 7.1: Demonstration of the PP mapping. Figure 7.1a demonstrates a state with two types of orbitals, f belongs to the symmetry which is not violated, p to the one which we want to restore. The notation with the brackets is borrowed from chemistry and means repeat as often as necessary. The super site could be for instance a tight binding like electronic orbital, energetically well separated from the higher orbitals and a vibrating lattice component. Figure 7.1b is the usual doubling, also applied in purification [VGRC04], where we introduce a larger total Hilbert space. Figure 7.1c then finally shows the state projected into the subspace of the purification by means of the function $\bar{n} = g(n)$.

truncation of the bonds between the physical and bath sites and the 1oRDM of the phononic super-site is of high interest, as we shall see in a second.

Before we continue discussing the projected purification (PP) mapping, we shall take a step backwards and prove that the representation eq. (7.15) together with the gauge condition eq. (7.16) is actually isomorphic to the original problem. In order to do so, we want to prove that a set of all functions spanned by variation of the c in eq. (7.14) is isomorphic to the set of all functions in eq. (7.17), given the gauge is enforced [KSP21]. First we define for convenience

$$\bar{n} = g(n) = n_{\mathrm{ph}} - n \, , \tag{7.20}$$

and note that with each $\delta_{\bar{n}_i, g(n)}$ we introduce to the wave function in eq. (7.15), we eradicate n_{ph} degrees of freedom. Therefore, the resulting total dimensionality of the purified subspace $\mathcal{H} \otimes \mathcal{H}$ is of the original size d^L. Furthermore, we note that we can form a joint Hilbert space of the physical and bath sites by means of contraction with an isomorphism [SPV10, SPV11, SV12]. Such isomorphism, commonly also referred to as merge tensors, takes two legs, e.g. of dimension d, and upon contraction results in a merged local Hilbert space of size d^2. Contracting the physical and bath site over their mutual link, and the physical legs with an isomorphism, results in a dense tensor which belongs solely to the irrep of n_{ph} but is of dimension d if the gauge condition was imposed. However, inside the original Hilbert space $\mathcal{H}$, the structure is preserved. If there were no symmetry-violating terms in the state, one can even reconstruct the decomposition into irreps, otherwise it will be truly dense. As one can easily check, the subsequent contraction of all physical and bath sites will lead to the representation of the MPS in the original basis. Therefore, we have found an isomorphism between the two spaces.

For the usual DMRG/TDVP procedure we need an initial state before we can start the algorithm. This can be easily constructed from pre-existing methods by restricting the occupation number (or any other symmetry) of the purified and the bath sites to the vacuum and afterwards applying a transformation MPO. This MPO contains only

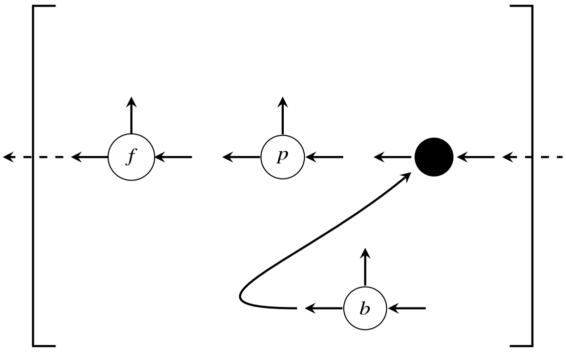

Figure 7.2: Possible mapping to combine the advantages of the T3NS with the PP mapping. Actual physical sites are aligned in the chain, while the bath sites are split away by means of the branching nodes.

identity operators, mapping everything to itself on all sites except the bath orbitals where we apply the matrix

$$T \doteq \begin{array}{c} \begin{array}{cccc} |0\rangle & |1\rangle & \dots & |d{-}1\rangle \end{array} \\ \begin{bmatrix} 0 & 0 & \dots & 0 \\ 0 & 0 & \dots & 0 \\ \vdots & \vdots & \vdots & \vdots \\ 1 & 0 & \dots & 0 \end{bmatrix} \end{array} . \tag{7.21}$$

After that, we can prepare the symmetry-violated orbitals in any way we wish, usually by the application of creation and annihilation operators, see section 7.4. It should be mentioned, that there also exists the possibility to map any state from $\mathcal{H} \otimes \mathcal{H}$ onto the purified subspace by application of a projection MPO. However, we found that the bond dimension of the MPO grows quite fast and therefore the application and the handling of the state afterwards gets quite tedious. Once our subspace representation is obtained, we can simply proceed with ordinary tensor network methods.

One special property of the PP mapping is that, since we have decomposed one orbital into several sites, the two-site DMRG method [Sch11] works as an effective single site update scheme. We mainly focused on two ways, in order to map the electronic and phononic degrees of freedom. Either we chose a joint representation of the electronic and the physical orbital in fig. 7.1c, or we actually split all three into separate orbitals. The former was the original method presented in [KSP21], however we found the latter to be advantageous, mainly because the local Hilbert space of the merged sites is of size $n_\mathrm{f} \times n_\mathrm{ph} \sim 100$. Nevertheless, since the largest bond dimension is usually the one between purified and bath site, it would be interesting for future investigations to apply a mapping, merging the bath and the fermionic site and therefore creating a homogenous bond dimension profile. Also, ansatzes where one combines TTNS and PP, as is demonstrated in fig. 7.2, might be beneficient to the system.

However, in order to overcome this effective reduction of the variational Hilbert space, we found it useful to do a lot of low accuracy sweeps with the single site update pattern [HMSW15] at the beginning of the run. This basically constructs the next iteration step in the Krylov subspace and expands the basis with it before the truncation happens. Therefore, it can help to overcome these artificially introduced convergence preventers.

As a final remark we would like to mention, that single orbital observables of the purified sites now involve two actual orbitals. Therefore, their computation needs additional care, if one does not want to be wasteful of resources. We found it particularly useful to implement the evaluation of typical observables via hand-crafted functions which perform the contractions between physical and bath sites in the correct fashion.

Automatic truncation 7.3

Through the PP mapping we have recovered the $U(1)$ particle number symmetry of our phononic systems again, which was desirable from a computational perspective. However, we have not yet discussed the large number of local degrees of freedom present in the typical setup. By initializing the system the way we explained it before, i.e.

by the vacuum and the full orbital for the purified and bath sites respectively, only the bonds between super-sites will not belong to product states. Therefore, even if we are depicting all possible occupations $n = 0, \dots, n_{\mathrm{ph}}$, we only keep track of one sparse block of dimension one, i.e. the choice of n_{ph} is unimportant for the cost of the state. Of course the magic is hidden in the representation of the Hamiltonian, as it has to contain all possible mappings from all quantum numbers of the state $|\psi\rangle$ to all quantum numbers of the state $|\hat{H}\psi\rangle$, which the given system can do under the gauge condition eq. (7.16). This leads to the Hamiltonian usually having the full local dimension d. However after truncation, which has do be done only once in the beginning of the simulation, the operator bond dimension is usually quite small ($\sim \mathrm{O}(10)$), which enables us to work with the reduced one dimensional blocks efficiently.

So how does the PP mapping influence the local dimension of the state, e.g. in a variational procedure? The first impression might be that through the application of the Hamiltonian, we introduce new possible occupations on the MPS, resulting in the local dimension getting denser with increasing simulation time. Particles will be shifted from the bath sites into the physical system and superposition of different combinations will be introduced into the state. After all we do not expect the system to be a product state between the super-sites, or the fermionic orbitals and the physical-bath complexes. However, the interesting question arises, almost naturally, about the interpretation of the bonds between physical and bath sites. In order to understand this, we need to understand the relation between the RDM of the (physical) phononic system.

From basic quantum mechanics we know that the diagonal entries of the RDM are related to the probability of finding the system in the corresponding state. If we want to know, e.g. what is the probability to find two phonons on orbital i, we need to compute $\hat{\rho}_i$ (as described in eq. (4.8)) and look at the diagonal entry belonging to $n = 2$. It is important to note, that here by orbital i we mean the product space between i_P and i_B. We already know about the connection between the RDM and the SVD truncation from eq. (2.9), however we now are interested in the RDM of the physical site only. Therefore, following the argument from [KSP21, Pae20], we define the map, bringing states in $\mathcal{H}$ to the purified subspace of the doubled Hilbert space as I. The action on operators in the PP space therefore is given by

$$P \ni \hat{O}_P = I\hat{O}I^{-1} \ , \quad \forall \hat{O} \in \mathcal{H} \ , \tag{7.22}$$

where we called the set of all states in the doubled spaces respecting the gauge condition P. From this definition immediately follows

$$\begin{aligned} \left\langle \tilde{n}_1 \dots \tilde{n}_L \middle| \hat{O}_P \middle| \tilde{n}'_1 \dots \tilde{n}'_L \right\rangle &= \langle \bar{n}_L | \langle n_L | \dots \langle \bar{n}_1 | \langle n_1 | \, I\hat{O}I^{-1} \, | n_1 \rangle | \bar{n}_1 \rangle \dots | n_L \rangle | \bar{n}_L \rangle \\ &= \left\langle n_1 \dots n_L \middle| \hat{O} \middle| n'_1 \dots n'_L \right\rangle \end{aligned} \tag{7.23}$$

that the tensor coefficients are equivalent in the different bases. For the special case of the expectation value of the local particle number excitation we therefore obtain [KSP21, Pae20]

$$\sum_{n_i} \rho_{n_i n_i} n_i = \langle \hat{n}_i \rangle = \left\langle \hat{\tilde{n}}_i \right\rangle = \sum_{\tilde{n}_i} \rho_{\tilde{n}_i \tilde{n}_i} \tilde{n}_i \ , \tag{7.24}$$

which promptly implies, that the diagonals of the 1oRDM are the same for the super-site and for the local physical site in the PP mapping only. If we now compute the RDM with eq. (4.8), which we derived earlier, but shift the orthogonality center away from the orbitals, such that all orbitals are either left- or or right-normalized but connected through the singular value bond we recognize that

$$\rho_{n_i n_i} = \sum_{ab} M^{n_i}_{ab} M^{n_i *}_{ab} = \sum_{abb'b''} \left(A^{n_i}_{ab'} S_{b'b''} V_{b''b} \right) \left(A^{n_i *}_{a\bar{b}} S^*_{\bar{b}\bar{\bar{b}}} V^*_{\bar{\bar{b}}b} \right) = \sum_b s_b^2 \ . \tag{7.25}$$

This relation demystifies the nature of the virtual bond between physical and bath site, the strength of its truncation simply controls the approximation of the local Hilbert space size. By choosing a singular value threshold t, we demand that phononic excitations, whose probability is smaller than this, are discarded. If we are to choose a truncated weight w as sum of discarded singular values we discard phononic excitations until this threshold is reached. If we just set hard cut-off on the bond dimension m, the m most important phononic modes are going to be incorporated. However, the important message is that due to our mapping, the system is always going to choose as many phonons as are necessary in order to describe the system with the predefined accuracy. This is a somewhat automatic truncation, with the restriction that the total Hilbert space can not exceed the predefined value n_{ph}. For large systems with different requirements in d, in order to describe the state correctly, this is a guaranteed way to always use exactly as many phonons as necessary. As such, we never waste resources, given a reasonable choice of the initial parameters.

Finally, we would like to mention that it might be beneficial to choose an inhomogeneous truncation depending on which bond we are actually truncating. Especially for non-1d systems, physical correlation between super-sites might build up, which need to be translated through the system by the sweeping pattern. This resembles a high bond dimension in the bulk of the chain. However, it might be possible to truncate the bonds between the physical and bath sites stronger than the ones between the super-sites, without losing much accuracy. At present time, this remains a highly experimental procedure, which needs to be hand-crafted every time and will need more careful investigation in the future.

Operators 7.4

The final question of this chapter is of more practical relevance: How do we actually construct Hamiltonians in the new mapping? We know, that there is an isomorphism, i.e. there exists exactly one element in P for each element in $\mathcal{H}$. The urging question on how to actually find it comes to mind. Usually, one needs to know the representation of the SSOs, from which one can then construct the Hamiltonian according to a recipe, like eq. (3.68), irrespective of the method [Sch11, CKN+16, HHS18, PKM17, KDTR15]. Therefore, our aim is going to be finding a representation of the creators and annihilators.

We know from eq. (7.23), that the matrix elements of the operators themselves should not change. Furthermore, we know from eq. (7.19) that however the SSO acts on the orbital, the total change should be compensated, such that the total particle number is conserved. This motivates the representation of the operators as [KSP21, Pae20]

$$\hat{b}_i = \sum_{n=0}^{d-1} \sqrt{n+1}\, |n\rangle_{i\,i}\langle n+1| \otimes |n+1\rangle_{i\,i}\langle n| \tag{7.26}$$

$$\hat{b}_i^\dagger = \sum_{n=0}^{d-1} \sqrt{n+1}\, |n+1\rangle_{i\,i}\langle n| \otimes |n\rangle_{i\,i}\langle n+1|\ , \tag{7.27}$$

if the operator breaks the global $U(1)$ symmetry in the original Hilbert space $\mathcal{H}$. Otherwise, all operators are just tensored with identities in the auxiliary space. Please note, that the matrix elements of the bath sites are always ones, irrespective of the occupation or the particle content's nature. For instance, if we purify fermions, we will not use Jordan-Wigner parities on the bath sites.

As now one can easily verify, the application of operators build up from these building blocks always stays within the given sub-manifold, provided that the state was originally in the purified subspace. The bath nodes just act as reservoirs for the physical system, particles can jump from it to the physical part of the system, where they will interact with each other or e.g. fermions. Of course the reverse process of jumping back to the reservoir is also possible. We will always preserve the gauge condition, which guarantees the description of the correct physical system.

With this recipe we close our technical discussion, define a system, double the degrees of freedom for all sites which do not preserve the symmetry in the Hamiltonian, and construct the operators according to eqs. (7.26) and (7.27). The remaining algorithms can be used in the usual pre-existing fashion.

Applications

8 The Hubbard-Holstein model

We have already encountered Hubbard like models in section 6.3 dealing with the idealized interplay between individual electronic delocalization and pairwise repulsion. What went without saying in the pure Hubbard model [HF63, Kan63, Gut63]

$$\hat{H}_{\mathrm{el}}/t = -\sum_{\langle i,j\rangle\sigma} \hat{c}^{\dagger}_{i\sigma}\hat{c}_{j\sigma} + U/t\sum_{i}\hat{n}_{\uparrow\downarrow,i} \ , \tag{8.1}$$

was, that we made use of the BO approximation (also see chapter 7), assuming that the particles are much lighter than the nuclei. In this course, we described the motion of the electrons alone and assumed that they would follow the motion of the several orders of magnitude heavier grid points instantaneously. Intuitively, the validity of this approximation increases with heavier cores. However, we have already discussed that the striking criterion for the BO approximation to be valid is the separation of all PESes. Then we could model the nuclei as static and incorporate the electrons in the conduction band as freely tunnelling among electronic orbitals, one belonging to each grid point.

However, there might be cases where one wants to model the Hubbard interaction of the electrons but also take into account motion of the nuclei. Hydrogen for example, is suspected to become metallic and even superconducting at low temperatures and high pressures and therefore is currently a topic of great interest [WH35, Ash68, BSOG04, KY11, ZSS16, HM21]. This could be modelled by a grid consisting of the protons (and neutrons, depending on the isotope) and electrons which are tightly bound to the s orbital but could transition between the nuclei. Other interesting applications like fullerenes where individual carbon atoms are replaced with alkali metals exist as well. Here, one also needs to take into account both inter electronic and electron-lattice interactions [TES⁺91, HRH⁺91, Gun97, TAA07]. But apart from applicability it is an interesting theoretical task to investigate the interplay between inter electronic and electron-phonon interactions.

As discussed in previous chapters, a good description for the motion of the grid can be achieved via the incorporation of harmonic vibrations. This introduces contributions to the Hamiltonian twofold. First, we can argue that the vibrational motion of the cores is typically described well by the perturbations around a stable minimum [Jon24b, Jon24a]. The second order expansion around this minimum gives us (as already mentioned in eq. (7.6)) a harmonic oscillator, which in second quantization leads to an energetic contribution of

$$\hat{H}_{\omega}/t = \omega_0/t\sum_{I}\hat{b}^{\dagger}_{I}\hat{b}_{I} \ . \tag{8.2}$$

Here, we assumed a homogenous vibration frequency ω_0 for each node in the system [Hol59]. Note that we introduced uppercase roman indices for phononic orbitals while sticking with lowercase latin indices for electronic orbitals to provide a better explanation. It is common practice to drop the separation for cases in which each site has one orbital of both types and just refer to the "supersite" as the total orbital $i \longleftarrow i \otimes I$. Second, we have a contribution to the energy from the coupling of lattice vibrations to the electronic density. Intuitively, proximity to electrons might cause nuclei to start motion and nuclear motion influences electronic motion in turn. This is given by the first order Taylor expansion of the PES with the coupling strength g [Hol59]

$$\hat{H}_{\mathrm{c}}/t = -g/t\sum_{i}\left(\hat{b}^{\dagger}_{i} + \hat{b}_{i}\right)\hat{n}_{i} \ . \tag{8.3}$$

Note that in this type of coupling the phonons can not distinguish between up- and down-spin and therefore make the system completely symmetric under spin exchange. The sum of these four contributions is the Hubbard-Holstein model [Hol59]

$$\hat{H} = \hat{H}_{\mathrm{el}} + \hat{H}_{\omega} + \hat{H}_{\mathrm{c}} \ , \tag{8.4}$$

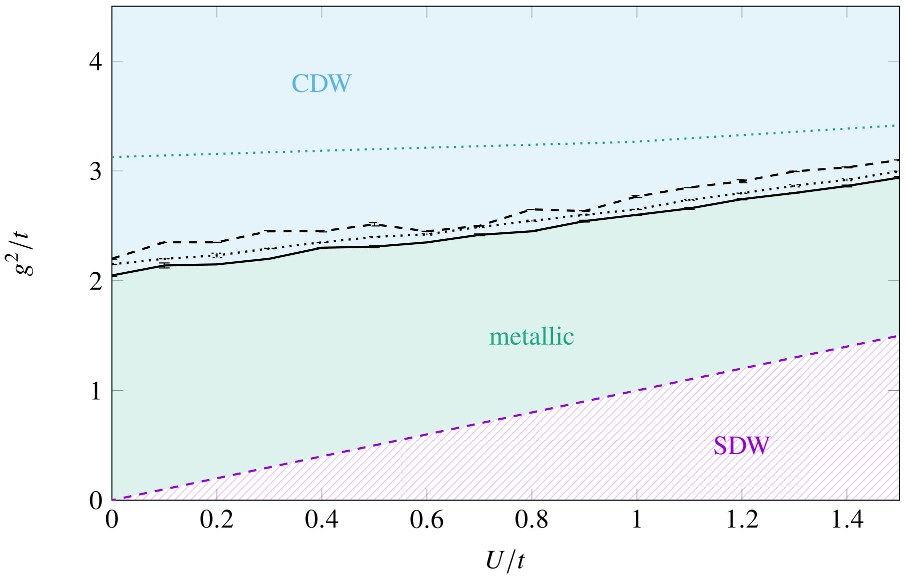

Figure 8.1: Phase boundaries of the 1d Hubbard-Holstein model for different system sizes. The angle bisector (- - -) marks the transition from the spin density wave (SDW) to the metallic phase while the black lines show the critical coupling obtained from fitting the charge density wave (CDW) order parameter in eq. (8.12) for various system sizes ($L = 64$ - - - , $L = 96$ ······, $L = 128$ ——). Previous DMRG results for the phase boundary obtained from [TAA07] are also displayed (······).

which introduces the coupling to the lattice via Einstein phonons, i.e. dispersionless phonons which only couple among each other indirectly via the electrons. This model, just like the pure Hubbard model itself, is not ab-initio but depends on the choice of the prefactors to the individual Hamiltonians in a cartoonish way. However, again the aim is not to describe a realistic system with this Hamiltonian but to investigate the effect simple mechanisms have in a quantum mechanical setup.

The Hubbard-Holstein model has previously been investigated in various fashions for many of the different parameter configurations introduced by the dimensionality d, the particle doping δ, ω_0, U and g. Among the many scientific works before us we want to mention that there are mean-field [HF83, Nas87, Tak96], ED [Tak96, Hir85], RG [CB84, YI96], Monte-Carlo [HF83, MSJ04] and DMRG [TAA07] investigations for 1d [HF83, Tak96, PA00, TC03] and 2d [PA00, MSJ04] lattices. These were conducted for the adiabatic ($\omega_0 \to 0$) [HF83, Nas87] and the anti-adiabatic ($\omega_0 \to \infty$) [HF83, Nas87, PA00] limit. Furthermore, various fillings were investigated [Hir85, YI96, BPK74]. The application of couplings beyond the dispersionless Einstein phonons, as well as anharmonic couplings are also present [HF83, LSC17, PHCS+21].

In the following we want to give an overview of our results for the simulation of the Hubbard-Holstein model by means of PP-DMRG. These results have not fully converged into a coherent picture yet, as the interpretation of the data is currently still work in progress. However, a few interesting observations can already be settled with the existing data.

Phase diagram 8.1

Due to the large amount of free parameters the system can exhibit various rich phases. We focussed mainly on the region where the hopping and the lattice vibrations are of comparable magnitude, i.e. $\omega_0/t = 2$ to be more precise. We did so, since it is a difficult regime, both to analytics as well as numerics. Around half filling ($\delta = 0$), there is often a characteristic behavior depending on the effective coupling $\lambda = 2g^2/\omega_0 - U$ [TAA07, GHW+15, MNH+17, KS17, CSYS20], depicted in fig. 8.1. Typically, when the on site repulsion is stronger than the electron-phonon interaction, i.e. we are in the regime $\lambda < 0$, we have a spin density wave (SDW) order. Here, the system becomes an AFM consisting of alternating spins and hence is a Mott insulator. In contrast, for regions where the electron-phonon interaction is much larger than the electronic repulsion, i.e. $\lambda \gtrsim 1.5$, the system undergoes a Peierls transition resulting in an translationally invariant charge density wave (CDW) which is also insulating.

We fixed our calculations to the simplest case, namely 1d, and the particle number to be at half filling. In accordance to the previous works, we did not only find a phase transition between the described orders, but also a third phase above $\lambda > 0$, before the system becomes Peierls insulating due to the large effective coupling. Previous DMRG investigations found the size of this phase to be growing with the frequency ω_0 [TAA07]. However, it is worthwhile spending some time in investigating this region as its nature was described differently depending on the method employed. The main candidate natures for this region were insulating, metallic or with a dominating pairing correlation [GHW$^+$15]. As in this phase not only interactions are not negligible but also competing, controlled analytical results are difficult to obtain. Methods like ED and Monte-Carlo suffer from typical problems like system size or finite temperature. And the DMRG approach is quite tricky due to the large local Hilbert space and the $U(1)$ symmetry violation of the electron-phonon coupling. However, this makes this model seem custom tailored to our PP approach which we are going to employ for ground state searches now.

Following the DMRG investigation in [TAA07], we wanted to investigate the dominating order in the system. For this we need to set up some order parameters and compute them as observables from our converged ground states $|\psi\rangle$. The candidates for the order in the chain are spin, charge and pairing correlations, depicted by the matrices

$$C_\sigma(i,j) = \langle\psi|\hat{s}^z_i \hat{s}^z_j|\psi\rangle \qquad \text{spin correlator,} \tag{8.5}$$

$$C_\rho(i,j) = \langle\psi|\hat{n}_i \hat{n}_j|\psi\rangle - \langle\psi|\hat{n}_i|\psi\rangle\, \langle\psi|\hat{n}_j|\psi\rangle \qquad \text{charge correlator,} \tag{8.6}$$

$$C_s(i,j) = \langle\psi|\hat{c}^\dagger_{\uparrow i}\hat{c}^\dagger_{\downarrow i}\hat{c}_{\downarrow j}\hat{c}_{\uparrow j}|\psi\rangle \qquad s\text{-wave correlator,} \tag{8.7}$$

$$C_p(i,j) = \frac{1}{2}\langle\psi|\left(\hat{c}^\dagger_{i\uparrow}\hat{c}^\dagger_{i+1\downarrow} + \hat{c}^\dagger_{i\downarrow}\hat{c}^\dagger_{i+1\uparrow}\right)\left(\hat{c}_{i+1\downarrow}\hat{c}_{i\uparrow} + \hat{c}_{i+1\uparrow}\hat{c}_{i\downarrow}\right)|\psi\rangle \qquad p\text{-wave correlator,} \tag{8.8}$$

$$C_d(i,j) = \frac{1}{2}\langle\psi|\left(\hat{c}^\dagger_{i\uparrow}\hat{c}^\dagger_{i+1\downarrow} - \hat{c}^\dagger_{i\downarrow}\hat{c}^\dagger_{i+1\uparrow}\right)\left(\hat{c}_{i+1\downarrow}\hat{c}_{i\uparrow} - \hat{c}_{i+1\uparrow}\hat{c}_{i\downarrow}\right)|\psi\rangle \qquad d\text{-wave correlator.} \tag{8.9}$$

For our investigation we did not account p- and d-wave correlations, as they were found subdominant to the others in [TAA07]. This is also in accordance with previous findings indicating s-wave to be the important mechanism for the region, where the electron-phonon coupling is larger than the on-site repulsion [YZS99]. All simulations were performed for the system size $L = 128$ and final bond dimension of $m = 8192$, if not stated differently, in order to mimic the thermodynamic limit.

We start off with analyzing them by plotting the correlation functions exemplarily for the three characteristic regimes of the system in fig. 8.2. In order to minimize boundary effects we measured the correlations of the system from the center site. Beginning with the SDW region of the phase diagram, the envelope of all three curves clearly shows algebraic decay. The spin correlations are the ones decaying slowest, just as expected. It is interesting to observe that there is a region in the middle of the maximal distance to the center site where the graph is a perfect line, making it possible to extract a good decay coefficient here by fitting. Nonetheless, this region is quite narrow. Furthermore, we have characteristic oscillations in the short range and boundary regimes which get weaker as we approach the middle region. Previous investigations often fitted the decay by just taking into account a subset of sites, e.g. just every second site [TAA07], (the maxima) or measured in multiples of five site distances [GHW$^+$15]. We note that the maxima of our curve also provide a relatively straight line. Deep in the CDW, phase the correlations of the system are rather different. Here, we clearly have an exponential decay of all curves, which we cut off after 30 sites for the sake of visualization. As the value approaches numbers below the numerical precision, i.e. the flat region for spin and charge, the exact values of the results are no longer faithful, but given the low order of magnitude can just be considered zero. As always, the most interesting region is the one where both interactions are competing due to comparable strength, as can be seen for the effective coupling of $\lambda \sim 0.1$ and $\lambda \sim 1$. In this metallic regime the decay seems to be algebraic again for both cases if one fits the maxima and neglects the boundaries. However, while shortly after the transition from the AFM the oscillations are quite large and the possible exponents are strongly competing, the charge gets progressively dominant with increasing electron-phonon coupling.

The investigation of the intermediate regime is worthwhile continuing as its phenomena are very rich. We would like to get a deeper understanding of its properties and also investigate the mechanism behind the emergence of this state, as we shall do in the following.

(a) $U = 1.5$, $g = 0.5$ in the SDW.

(b) $U = 0.5$, $g = 2$ in the CDW.

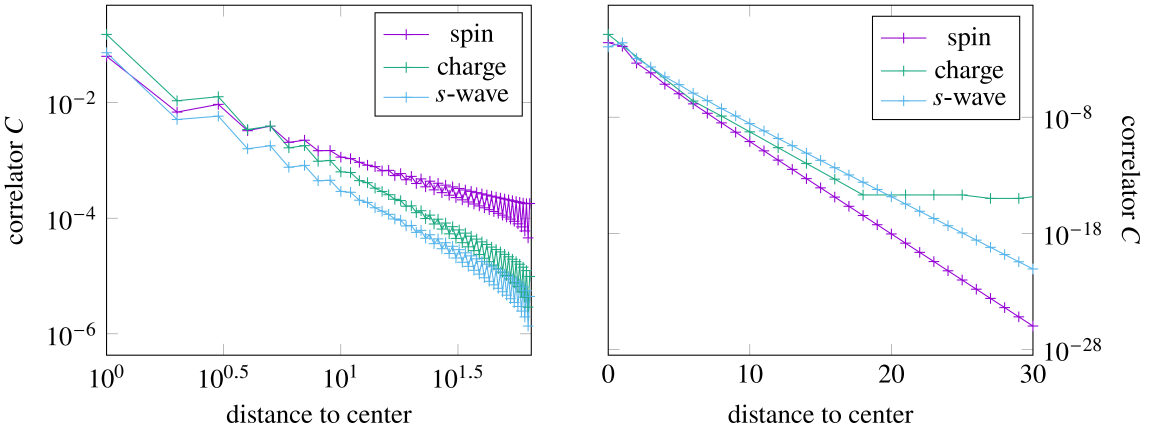

(c) $U = 0.5$, $g = 0.77$ in the intermediary region.

(d) $U = 0.5$, $g = 1.22$ in the intermediary region.

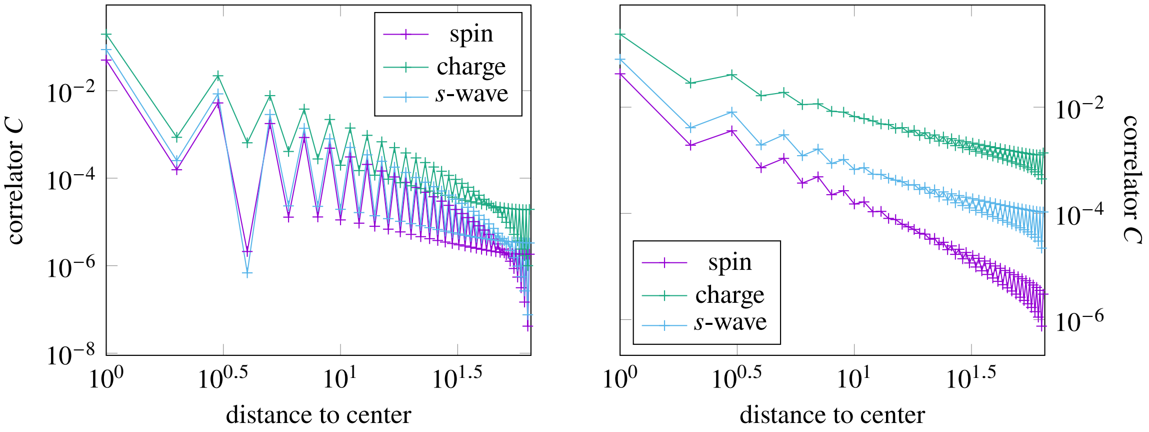

Figure 8.2: The three correlation functions described in eqs. (8.5) to (8.7) plotted against the distance to the middle for characteristic points in the (U, g) plane. The system at use is exemplarily chosen to be $L = 128$ with a final bond dimension of $m = 8192$.

Phonon distribution 8.2

Now that we have an introductory overview over the physics of the Hubbard-Holstein model, we want to investigate the influence of the phonons on the electronic systems. We know that generally, the electrons tend to organize in an AFM order through the electron repulsion at half filling and that the effective interaction mediated by the phonons attracts the electrons to each other. Until we hit the phase boundary of $U = g^2$, the electron-phonon coupling mainly renormalizes the value of U to a smaller value but going beyond this boundary results in the electrons feeling more and more attractive interaction. Therefore, we want to investigate the role the phonons play in this procedure by means of the RDM of the phononic orbital in the middle of the system $I = L/2 = 64$, i.e.

$$\hat{\rho}_I = \mathrm{tr}_{\setminus I} \left|\psi\right\rangle \left\langle\psi\right| \ . \tag{8.10}$$

Note that this definition also involves integrating out the electronic orbitals. In particular, we are interested in the diagonal elements $f_I(n)$ depicted in fig. 8.3, as they determine the excitation probability of this phononic occupation mode. Here we show the distribution for the four characteristic cases discussed earlier in section 8.1.

All four curves in fig. 8.3a share the fact that the maximum of the distribution is at $n = 0$, as the excitation of phonons costs energy through the vibration part of the Hamiltonian eq. (8.2). Furthermore, they all show a kind

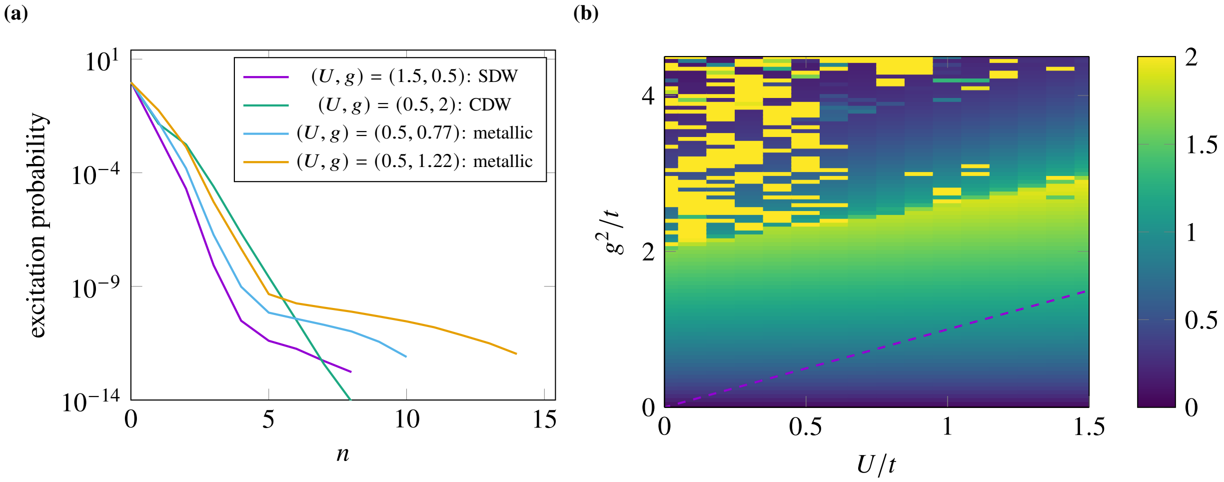

Figure 8.3: The phononic excitation probability in the middle of the chain for the points presented in fig. 8.2 is shown in 8.3a. Furthermore, we investigate the width of the distribution for the entire phase diagram in 8.3b by means of the Shannon entropy of the distribution extrapolated to $m \to \infty$.

of exponential decay for the low lying modes accompanied by a tail behaviour for the higher ones. In the SDW phase the decay of the curve is quite steep as one would expect due to the low electron-phonon interaction. The excitation probability for modes above $n > 9$ is so small that it is not resolved by our numerics with a truncated weight of 1×10^{-14} and also cuts off singular values below that value immediately. For the CDW we recognize a slower decay for which however approximately the same number of phonons' excitation probability lies above our truncated weight. This means that higher occupations are more likely found than in the SDW but there is also an interplay with the tendency of the electrons to localize in this regime due to effective electron attraction. The distribution has a long tail with excitation probabilities below the numerical precision going up to $n = 27$, which we cut off for accuracy and visualization reasons.

The two distributions in the metallic phase exhibit an interesting behaviour between the two extreme cases, as the electron-phonon coupling is quite strong in this regime but the electrons are also still mobile. Both distributions have a width between the distributions of SDW and CDW and show an interesting kink aroung $n = 5$. After that there is quite a long tail of excitation probabilities going up to $n = 10$ and $n = 15$. However, it is fairly tedious to discuss every distribution in the distinct parameter regimes by visualization and therefore we want to introduce a (scalar) measure for the broadness of the distribution. A meaningful way to do so is through the Shannon entropy of the distribution function

$$S(\hat{\rho}) = -\sum_{n} f(n) \ln f(n) \ . \tag{8.11}$$

This quantity is basically a measure for the amount of $U(1)$ symmetry breaking of the phononic occupations and gives us a good estimate for the role the phononic interaction play in the system for various parameters. We plotted the Shannon entropy for the entire phase diagram of the Hubbard-Holstein model in the regime investigated by us in fig. 8.3b. It is interesting to observe, that the role of the phonons is basically independent of the value of U before crossing the phase boundary from the AFM to the metallic phase, i.e. $U = g^2$. The phononic distribution has the same broadness for all values of the electron repulsion. When entering the metallic regime there are two possible behaviors. For the electron-phonon coupling still below a certain value, the independence pattern of the AFM is reproduced just with a slightly higher value width. However, before going to the Peierls phase there is an interesting region of comparatively high phonon distribution width tilted with the effective interaction line $U = g^2$. This twofold nature of the metallic phase is quite remarkable and was not described before to our knowledge. It is currently still under our investigation and will be characterized in more detail in our future work. Finally, when going into the CDW phase we see an immediate drop of the distribution function attributed to the double occupation pattern and hence the immobility of the electrons. This phase boundary is also tilted with the angle bisector. The mosaic patterns, mainly in the above left corner, can be most likely attributed to the difficulty of DMRG calculations due to frustration and the formation of domain wall-like patterns here.

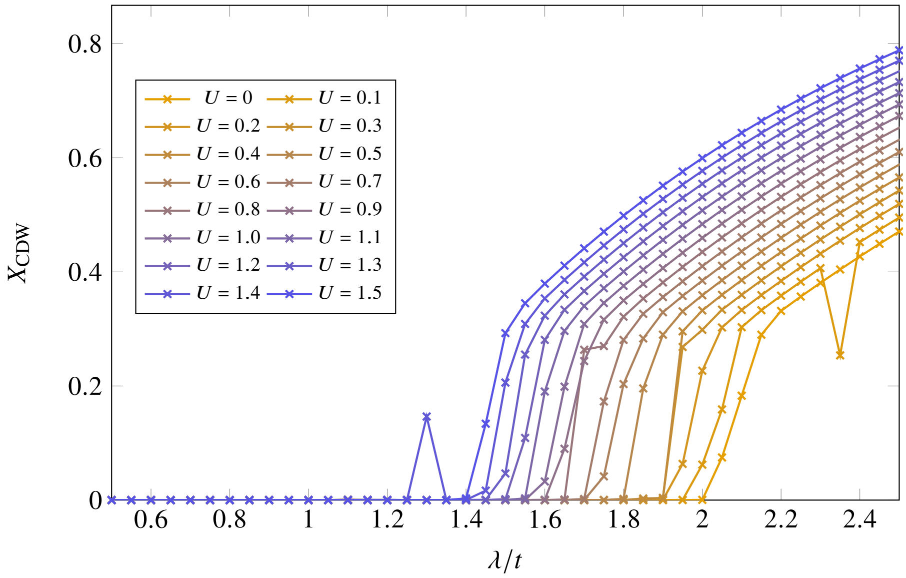

Figure 8.4: CDW order parameter extrapolated to $m \to \infty$ plotted against the effective coupling λ for various values of U.

To conclude with the final discussion of this section, we will be looking at the CDW phase and its phononic observables in greater detail. For this we have chosen the CDW order parameter [JW98, SKM+21]

$$X_{\mathrm{CDW}} = \frac{1}{L}\sum_i (-1)^i \langle\psi|\hat{b}_i^\dagger + \hat{b}_i|\psi\rangle \tag{8.12}$$

depending on the phonon displacement $\hat{x} = \hat{b}^\dagger + \hat{b}$. This is easily extracted from the converged wave function $|\psi\rangle$ by an expectation value computation even though some additional attention is required due to the PP mapping. The results depending on λ are shown for various electron repulsion strengths U, in fig. 8.4. Meaningful observations can be extracted from this plot. First of all, we see that all curves are strictly zero in the SDW phase, just as we would expect it and there clearly is a transition to a phase which is a CDW. Also a few outlying points can be observed where the calculations had a hard time converging, however, the overall trend can be seen and is quite striking. There is a discontinuous jump which moves from around $\lambda \approx 2$ to $\lambda \approx 1.4$ with increasing value of U, just as expected from looking at fig. 8.3b.

Central charge 8.3

In order to look a deeper look into the twofold nature of the metallic phase, we want to investigate the central charge now. We have already encountered the central charge c during our discussion of orbital order in section 3.4 as a prefactor occuring in the Calabrese-Cardy formula [CC04]. However, there we used the formula for a system with periodic boundaries since we needed the k-space representation of the ground state. The modification for open boundaries, as was used for our investigation of the Hubbard-Holstein model is given by [CC04]

$$S(x) = \frac{c}{6}\ln\left(\frac{L}{\pi}\sin\left(\frac{\pi x}{L}\right)\right) + \tilde{c}\ , \tag{8.13}$$

where $\tilde{c}$ is now a different constant than before but not of interest to us right now. In itself, this formula is quite remarkable as it is valid for any 1d model, irrespective of its nature, as long as it can be derived from conformal field theory (CFT). Therefore, the result is exact for a critical system, however, once a gap opens up (also due to finite size effects) we will only obtain an approximate fit to this function. Nevertheless, the central charge is a decent measure to obtain the independent number of gapless excitations above the ground state [Gia04]. Since we are seeking to get a grasp on the nature of the highlighted region in fig. 8.3b this information is useful in the interpretation.

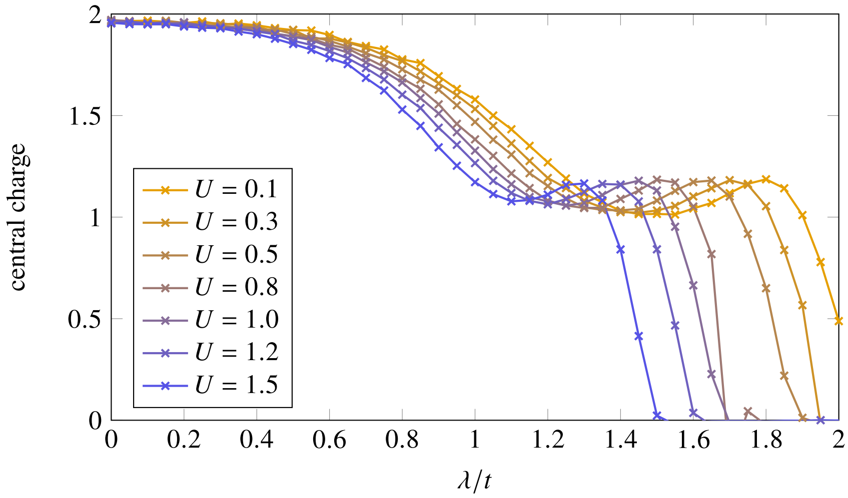

Figure 8.5: Central charge obtained from the scaling to the middle method [STC19] and extrapolated to $m \to \infty$.

From the MPS side we can obtain the entanglement entropy easily by sweeping through the system via an SVD keeping the system canonically normalized (see section 3.3.2). From the sigular values s_α obtained at each bond x one can compute the entanglement entropy easily via summation as

$$S(x) = -\sum_\alpha s_\alpha^2 \ln s_\alpha^2 \ . \tag{8.14}$$

The only remaining thing is to fit these functions to the functional form in eq. (8.13). It should be mentioned that the entanglement entropy is a basis dependent quantity, but if the state is actually converged, i.e. the bond dimension is large enough, the sweeping procedure only fixes a gauge resulting in the same value. However, since we have a finite system we will always encounter boundary effects in the entanglement entropy measured. Previous works have used sophisticated methods in order to get this under control, e.g. [MWS20] extended the fit function by a contribution suppressing the boundary values resulting in an increased weight for the bulk. We implemented this method and experienced an improvement in the stability of the fits and the obtained values. However, we decided to go with another method as the aforementioned method introduces additional parameters whose tuning were not straightforward to us. We followed the “scaling to the middle” ansatz introduced by Campbell et al [STC19]. In this method one uses the central charge fit eq. (8.13) but restricts it to a domain size D symmetrically including all nodes left and right the middle of the chain. One starts from a domain size $D = L$ and subsequently reduces the size by the same amount of nodes left and right until one reaches a desired cutoff value. This will generate a sequence of $D \mapsto c$ which is a function itself for each fitted value of the domain size. The scaling to the middle consists then, as the name already says, by fitting these values to function form itself and extracting the true value by the extrapolation to $D \to 0$. One can also restrict the maximum and minimum domain size D to values below L and above too small values in order to suppress overfitting and edge effects [STC19]. Overall, we were able to extract quality central charges by this method, as we shall discuss in the following.

We have visualized the central charge in dependency of the effective coupling λ in fig. 8.5. We can clearly see that after the transition to the metallic phase from the SDW, the number of independent gapless modes is two, i.e. up and down electrons. In the CDW, phase both gaps are expected to open up and become rather large. Therefore, the notion of the central charge becoming zero for the large λ limit also seems reasonable. However, what happens in between is immensely interesting, i.e. there seems to be a phase were the number of gapless particles is one. The region seems to coincide with the region in the metallic phase where the Shannon entropy of the phonon distribution function gets large. Up until now we have not figured out, what the nature of this region is but hope to do so in future investigations. What can be said is that we currently do not believe that the mechanism visible here is s-wave pairing due to theoretical arguments. Namely, it was shown [HF83] that integrating out the phonons at finite frequencies ω_0 results in a Hamiltonian local in space and slightly off-local in time. The latter is exponentially suppressed with increasing value of ω_0. Hence, due to the Mermin-Wagner theorem [MW66] and the duality between thermal and quantum phase transitions in d and $d - 1$ [Sac11], respectively, no breaking of a continuous symmetry can be established here.

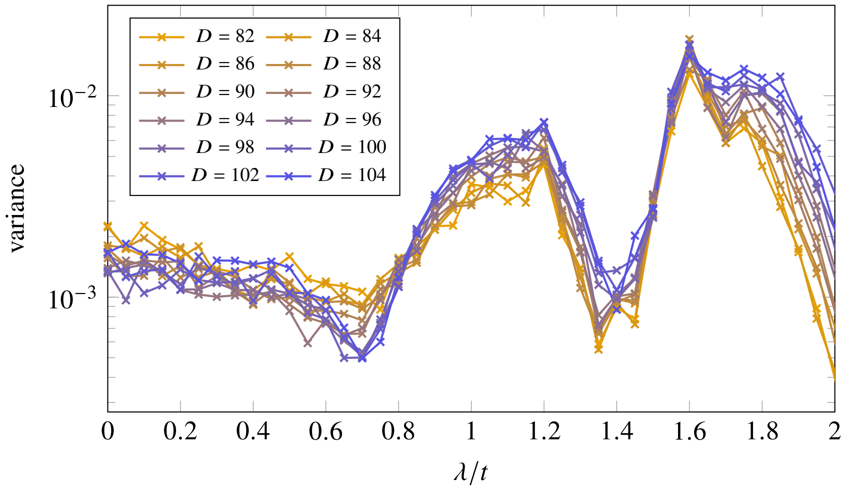

Figure 8.6: Variance of the central charge fit to eq. (8.13) for various domain sizes D for $U = 1$.

It seems appropriate to mention that in [STC19] it was also discussed that the scaling to the middle method can be used for more than just determining central charges. Turning the usual disadvantages of finite numerics to ones own advantage the authors pointed out there, that due to the fact that one needs a gapless system for the Calabrese-Cardy formula to be exact, the emergence of a bad fit indicates a gap. Therefore, they suggested to use the variance of the fit to the functional form as an order parameter proxy to distinguish a transition between two gapped states and tested it quite successfully for the extended Hubbard model. In order to get a feeling where our system might be gapped, we did the same in fig. 8.6. One needs to proceed with caution here since too small domain values D will not show the critical behavior we anticipate and too large ones are going to incorporate the boundaries again. Therefore, we chose to plot the variance of the domain sizes from 82 to 104 in our $L = 128$ system size model by means of heuristics. We can see that for the area directly after the transition to the metallic phase the variance is of $\mathrm{O}\left(10^{-3}\right)$ indicating a small gap. Around $\lambda = 0.7$ there is a minimum of the function which could be connected to an unknown feature of the metallic phase, as in the remaining region until the system crosses over to the CDW the system seems to have a large gap. The question if the system becomes gapless at this transition point is still open to us. Going into the CDW phase, the error first becomes larger which is intuitive as the system has a large spin and charge gap here, followed by a decline of the variance to small values. This can be attributed to the fact that the central charge becomes zero in this regime and therefore the prefactor of the fit eq. (8.13) just vanishes, i.e. making the fit well suited without telling us anything about the gap.

Thus we are able to confirm that, even though the variance of the central charge fit is a purely numerical quantity with no physical equivalent, it might serve as a proxy to tell us something about the system. All in all there seems to be an interesting feature when both interactions present in the system are of comparable size shortly before the electron-phonon coupling becomes dominating, which was unknown prior to the best of our knowledge. In this region the number of gapless modes becomes one while there has to be a gap opening of unknown nature.

Gaps 8.4

To finalize our discussion of the gaps we want to evaluate two kinds of gaps which are especially accessible within the symmetry protected DMRG setup, i.e. the spin gap Δ_s and the charge gap Δ_c. In order to obtain both of them we need to search for the lowest energy state in a doped regime of the Hubbard-Holstein Hamiltonian. For this we introduce the notation $S = (N, s_z)$ for the sector of the total many-body Hilbert space $\mathcal{H}$ which has N particles and z component of the spin s_z. As we are interested in the behaviour at half filling we fixed the chemical potential such that the ground states lives in the $(N = L, s_z = 0)$ space. For the gaps we need the lowest lying excitations in the sectors $(L, 1)$, $(L+2, 0)$ and $(L-2, 0)$, whose energy we refer to as E_s, E_2 and E_{-2}, respectively. Then we can

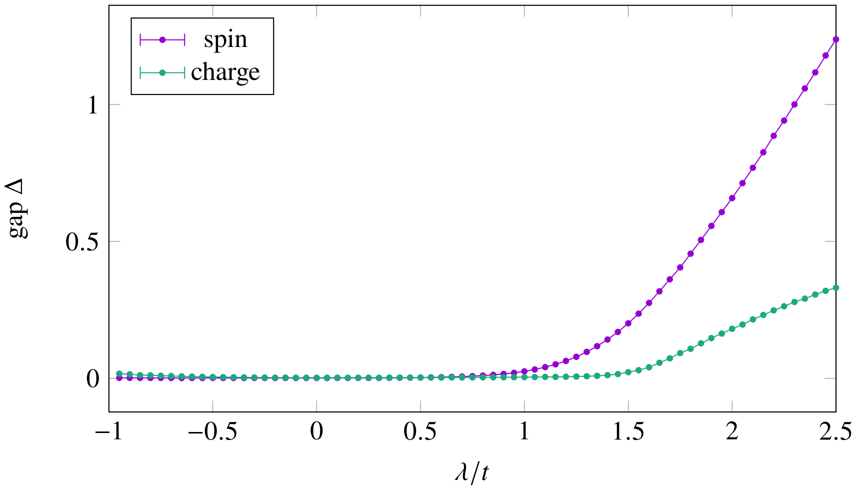

Figure 8.7: Spin and charge gap for $U = 1$ plotted against the effective coupling, extrapolated to $m, L \longrightarrow \infty$. Note that this time also the SDW region, i.e. negative effective couplings, are included in the figure.

define the gaps as

$$\Delta_s = E_s - E \qquad \text{spin gap,} \tag{8.15}$$

$$\Delta_c = E_2 + E_{-2} - 2E \qquad \text{charge gap,} \tag{8.16}$$

where E is the energy of the half filled ground state. The former corresponds to replacing one down spin with an up spin while the latter corresponds to adding or withdrawing two particles in such a way that the total spin stays constant.

For visualisation reasons we have again chosen to demonstrate one slice out of the phase diagram in fig. 8.7, as the larger/smaller values of U just move the transition point to the left/right, respectively. We can clearly see that both gaps are near zero in the SDW region ($\lambda < 0$) and in the metallic regime. However, given finite numerics it is always a bit difficult to state if the gap is closed or just exponentially small. To this end, a finite size extrapolation $1/L \longrightarrow 0$ is crucial to observe a qualitativly right result. Increasing the electron-phonon coupling g we see that first the spin gap opens up slightly before $\lambda = 1$, whereas the charge gap opens up later around $\lambda = 1.4$.

This pattern of two different behaviours in the metallic phase and close to the CDW transition might help us again to interpret the nature of the metallic phase. Apparently, the gapless single particle excitation we encountered in section 8.3 in this regime does not have a charge gap but is spin gapped. This might indicate that these gapless modes are spin up and down pairs, as the additional spins cost the system energy.

Molecular dynamics | 9

Now, we want to deal with the out-of-equilibrium dynamics of realistic molecules with lattice vibrations incorporated. One might wonder why anyone would do so, since we spend quite of lot of effort on arguing how the solution of the electronic system decouples from the nuclear motion (see chapter 7). However, there are many chemical phenomena where it is by now well established, that a pure electronic description is not sufficient [BG17, MKW$^+$17, BMK$^+$16, TR17, SM10, Cas18, STM$^+$19]. As described before, this gets necessary due to the PESes getting close to each other for some nuclear configuration.

In order to do so, we typically rely on converged many-body calculations of the electronic system for several configurations, e.g. the ground state and an excited state. These can be obtained e.g. through DFT [HK64] or, as in our case, CAS-SCF [ZN08] (excited state) calculations. Once these are given, we know the energy and transition amplitudes between different levels which lead to the Hamiltonian description of the system via the many-body modes i, j

$$\hat{H}_{\mathrm{el}} = \sum_{ij} t_{ij}\, \hat{c}_i^\dagger \hat{c}_j \ . \tag{9.1}$$

Here, as in the remaining part of this chapter, we will stick to the notation, that electronic levels are labeled by lowercase latin indices. The diagonal elements of t are the level energies and the off-diagonals are coupling among them. Since our particles are excitons, the nature of the creation and annihilation algebra is typically the same as for hard-core bosons. Nevertheless, we usually do not have more than one "particle" in the electronic system, i.e. anti-commutation and commutation are the same.

To study the dynamics, we typically initialize the system in an excited state $|\psi(0)\rangle$, or a superposition of such, and observe the Hamiltonian time evolution

$$|\psi(t)\rangle = \exp\left(-\mathrm{i}t\hat{H}\right) |\psi(0)\rangle \ , \tag{9.2}$$

mostly using TDVP. This resembles the experimental preparation of the molecule in an excited state, e.g. through a laser or other incoming radiation. Of course eq. (9.1) is not particularly interesting, since it is an integrable system [Deu18] and therefore can be solved quite easily. Not to mention of the small Hilbert space size, since we are after all only interested in a few low lying states. Furthermore, the system can not thermalize [Deu18], resulting in the time-evolution being Rabi-like oscillations between the eigenstates. This means that as long as the particle number is conserved the "density" will change between the levels periodically [ZXJL16].

When we include the vibronic Hamiltonian, this is changed due to indirect coupling mediated through the phonons. Now energy can be transferred from the electronic system into lattice vibrations and vice versa, leading to richer dynamics. In turn, this makes the system more complicated to solve for the typically required number of vibrational modes. In order to handle the complex requirements imposed by the molecule, we make use of the previously described PP mapping to restore the broken $U(1)$ particle number conservation symmetry. Of course the particle number of the electronic system is also conserved and can be exploited however, the small number of electronic modes usually makes this part not as challenging. This way the Hamiltonian is quite sparse and the entire tensor network decomposes into symmetry protected tensors. Furthermore we do not need to investigate each mode's local Hilbert space size, we just choose a number which is large enough and let the automatic truncation do the rest.

Before we continue to detail specific models, let us spare a few words on the time-scales, which can be reached. Initially, the electronic state is either a product state (in the case of an excitation) or a state of low bond dimension (for superpositions of excitations). This is due to the fact that our excitons are eigenstates of the electronic energy Hamiltonian. The initial state of the phononic Hilbert space was set to be the vacuum in the course of this thesis. This is due to the fact, that we always operated at zero temperature. In principle, one could, e.g. by means of a second purification [BKP$^+$22], start the PP time-evolution from a finite temperature state which would result in an initial occupation of lattice vibrations. However, this goes beyond the scope of our investigation and is going

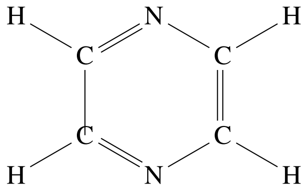

Figure 9.1: Chemical skeleton of the pyrazene molecule. Note, that the notation with the double bonds inside the ring is symbolic, in reality the electrons delocalize.

to be subject of future research efforts. During time-evolution, the bond dimension typically grows exponentially [CC05, Sch11, PKS+19]. But since we start from a very low value, the coefficient of the scaling is essential for the regime until we can time evolve. Heuristically, we can make the statement, that we were usually able to reach several hundreds of femtoseconds with our simulations, depending on the structure of the electronic system. Typically, the constraining factor is the bond dimension between the most relevant physical and bath sites in the vibronic system which gets large due to a high number of phonons necessary. This then leads to an enormous demand for computational resources (after all m and d are now large) which typically exceeds the memory available. In cases where only the runtime was high, we made careful use of the PTDVP [SGL+20] algorithm (see section 5.3). However, typically the memory demand was the most problematic point, restricting us to common random-access memory (RAM) availability in high-performance computing (HPC) of 1 TB to 2 TB. This makes our method especially promising for all kinds of first principle out-of-equilibrium applications where the essential physics take place on short time scales. It is to mention that other methods exist which can reach up to several thousand picoseconds [ETDW03, WLX+21], e.g. Redfield theory [RED65] which basically has no limitation on evolution time. Here, one approximates the vibronic subsystem as bath for the electronic subsystem, an approximation which is often valid and leads to good results in the weak coupling regime. But for the systems we investigated, i.e. with strong coupling, the Redfield theory produces qualitatively different results than our first principles study, implying its invalidity for this domain and depicting the competition between time scales and coupling strength.

Pyrazine 9.1

We began our investigation with Pyrazine, an organic molecule with the formula $C_4H_4N_2$, whose chemical structure is shown in fig. 9.1. Pyrazine has long been a benchmark model for any first principles calculation of molecular dynamics [RWMC99, XLY+19, BR19]. Our model involves the two lowest electronic singlet states S_1 and S_2, both at the equilibrium position. As the former belongs to the B_{3u} and the latter to B_{2u} of the molecular symmetry D_{2h} (see section 4.2), they do not couple to each other [RWMC99]. They only contribute to the Hamiltonian through their energy gap 2Δ, i.e.

$$\hat{H}_{\mathrm{el}} = \Delta\left(\hat{c}^{\dagger}_{s_2}\hat{c}_{s_2} - \hat{c}^{\dagger}_{s_1}\hat{c}_{s_1}\right) . \tag{9.3}$$

The nuclear system is represented by 24 modes, ordered in ascending frequency

$$I \in \{16_a, 16_b, 6_a, 6_b, 4, 11, 10_a, 17_a, 5, 1, 12, 18_b, 18_a, 14, 9_a, 3, 19_b, 19_a, 8_b, 8_a, 13, 7_b, 2, 20_b\} , \tag{9.4}$$

and whose matrix elements we obtained from [RWMC99]. Note, that we refer to phononic orbitals with uppercase latin indices. Our system is now described by the total Hamiltonian [Fre31a, Fre31b]

$$\hat{H} = \hat{H}_{\mathrm{el}} + \sum_I \omega_I \hat{b}^{\dagger}_I \hat{b}_I + \frac{1}{\sqrt{2}} \sum_{ij,I} g_{ij,I} \left(\hat{b}^{\dagger}_I + \hat{b}_I\right) \hat{c}^{\dagger}_i \hat{c}_j + \frac{1}{2} \sum_{ij,IJ} G_{ij,IJ} \left(\hat{b}^{\dagger}_I + \hat{b}_I\right)\left(\hat{b}^{\dagger}_J + \hat{b}_J\right) \hat{c}^{\dagger}_i \hat{c}_j . \tag{9.5}$$

We recognize again the energy contribution from the vibrations of the phonons, with each individual contribution given by the vibration frequency ω. Furthermore, we have the already encountered linear coupling g between the displacement $\hat{x} = \left(\hat{b}^\dagger + \hat{b}\right)/\sqrt{2}$ and the excitonic density. Last but not least, there is the second order expansion term which results in a bilinear and quadratic coupling, given by G. Through this coupling, there is indirect mediation between the electronic states. The target goal of the simulation is going to be to find out how the excitation decays.

Our starting point for the size of the local Hilbert space were previous investigations [XLY+19], where a maximum of $n_{\text{ph}} = 24$ was needed. Therefore, we fixed our n_{ph} to be 31 maximally however, we also performed calculations with $n_{\text{ph}} = 63$ to make sure our approximations were justified. As mentioned before, the initial size of the local Hilbert space only leads to a minor increase of computational complexity during the Hamiltonian construction. We initialize the system to be entirely in the excited state, i.e.

$$|\psi(0)\rangle = |s_2\rangle \tag{9.6}$$

and use two-site TDVP to time evolve. The growth of bond dimension during the sweeping is truncated by a truncated weight of $\delta = 1 \times 10^{-7}$ while restricting the accuracy of the individual vectors to 1×10^{-5}, according to the criterion of Hochbruck and Lubich [HL97].

As we have by now extensively discussed, the question of ordering is crucial in order to be able to maintain the calculation for as long as possible. We compared the two mappings described in fig. 9.2 to each other, i.e. first putting the electronic modes to one side of the MPS, and second putting them in the center of the chain [XLY+19]. Of course many more possibilities exist to map the nodes, but not only that but we can also rotate the coefficient tensors g and G, in order to describe the coupling in a different fashion, as is usual in e.g. DMFT [KRU08, dVSW15, BMG+21]. However, this was not investigated in the course of this thesis and shall be target of future research efforts.

Numerical stability 9.1.1

The first thing we wanted to check is the numerical stability of the algorithm, as the combination of the PP mapping and TDVP was previously never used with a non-local Hamiltonian. Therefore, we chose a relatively small time-step of $\Delta t = 0.2\,\text{eV}^{-1}$ which kept the exponentiation error well controlled (see section 5.1). The total calculation took around $5.8 \times 10^3\,\text{s} \approx 1.5\,\text{h}$ real time to reach a simulation time of 131 fs, which is roughly one order of magnitude smaller than the reference calculation in [XLY+19]. As a proxy for the projection error [PKS+19] we chose the norm deviation from the initial state. Even though this is a rough approximation, the degree to which the time-evolution violates unitarity gives a good estimate of the error occurred. If one wanted to compute the actual projection error in twosite TDVP, one could compute the variance of $|\psi(t)\rangle$ and its single and twosite variance, according to [HHS18]. However, for Hamiltonians with such large local Hilbert spaces and global coupling between the orbitals such a calculation would be highly expensive which made it numerically unfeasible for our calculations. Especially squaring the Hamiltonian for the total variance is usually a highly expensive task, which is also prone to catastrophic cancellation [HMS17, PKM17, HHS18]. We mentioned before, that we do not restrict the bond dimension but rather define a truncated weight δ, which controls the validity of the approximation [Sch05, Sch11]. In practice this means defining a very high value for m, such that this bound is never actually saturated. Therefore, another control criterion to check suitable description of the state within the sub-manifold defined by the simulation parameters is the evolution of the bond dimension profile. Finally, we want to check if the local Hilbert space size is converged. For this we proceed with the same simulation with the two different values of $d = 32$ and $d = 64$. The results for all these numerical control parameters are shown in fig. 9.3. The norm error seems to be of constant order of magnitude throughout the entire simulation, independent of the system setup. Furthermore, it is consistent with the truncated weight we chose, i.e. $\delta = 1 \times 10^{-7}$. However, we notice, that while the projection error seems to be insensitive to the local Hilbert space size, mapping the electronic nodes to the middle makes the projection error around 30 % larger. This observation is also in agreement with the fact that the maximum bond dimension necessary increases quite drastically for the middle mapping. After all we remember, that the TDVP projector is exact in the infinite bond dimension limit (see section 5.1 and [PKS+19]). As the information between vibrational modes of the same frequency must be transported delocally and through the excitonic sites, the resource requirement increases such that the calculation went out of memory around 30 fs. Here, a mapping which orders the nodes in increasing frequency along one half and continues along the other half might be beneficial. Since

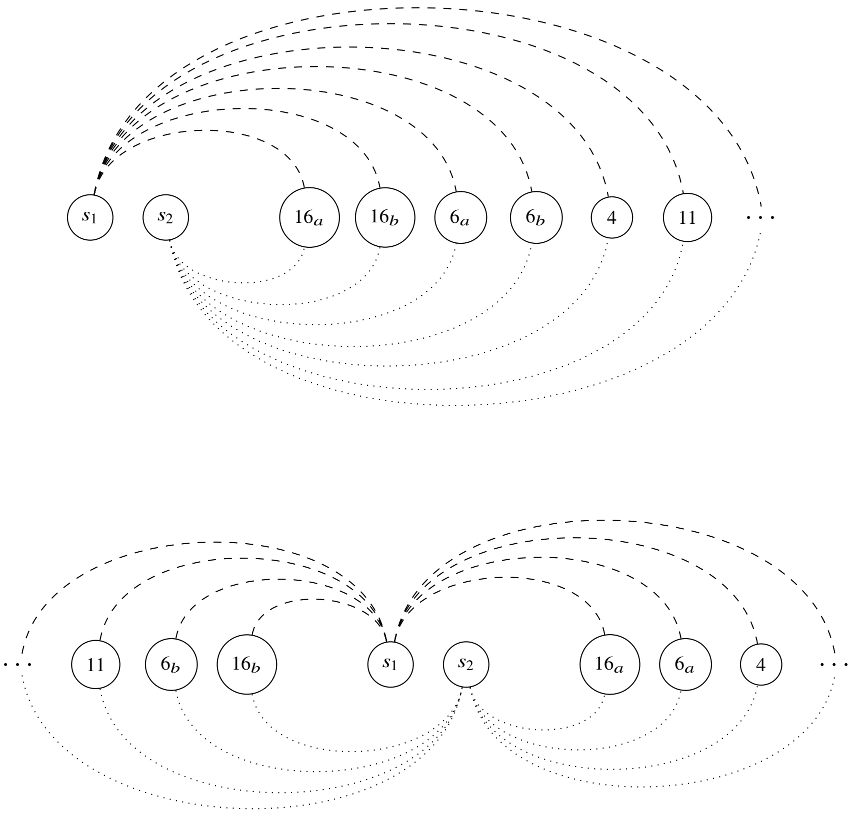

Figure 9.2: Different possible mappings of the pyrazine Hamiltonian to a chain. We can either try to put the electronic levels to the edge of the system or put them into the middle. As the coupling of the vibration modes is global, they will all be connected to each other. Therefore, the bonds will have to communicate the action of the Hamiltonian through the entire system.

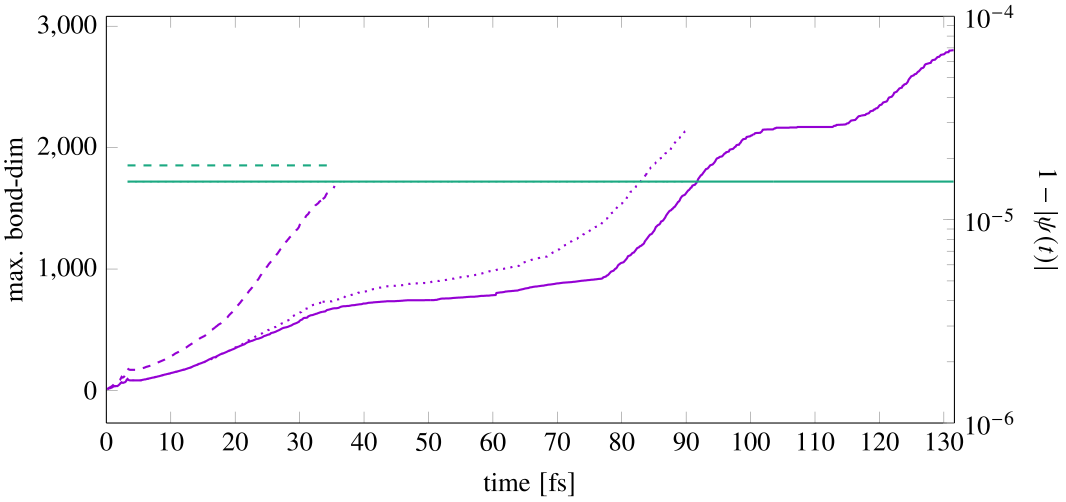

Figure 9.3: Numerical control parameters for two electronic and 24 vibrational modes. The deviation from the initial norm is shown on the left axis for the electronic nodes in the middle of the MPS and $n_{\mathrm{ph}} = 63$ (- - -) and at the edge of it, for $n_{\mathrm{ph}} = 31$ (——) and $n_{\mathrm{ph}} = 63$ (⋯⋯). Furthermore, we show the maximum bond dimension on the right axis for the electronic nodes in the middle (- - -) and at the edge, with the small (——) and the large (⋯⋯) local Hilbert space.

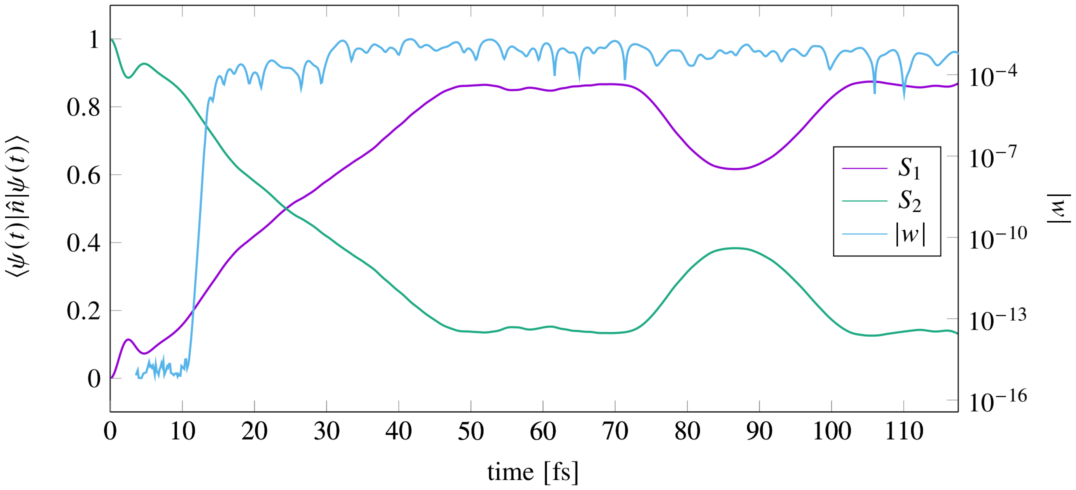

Figure 9.4: Time-evolution of the electronic densities. In addition to the occupation of the electronic levels we also plotted the magnitude of the off-diagonal elements of the electronic RDM, which is a measure for the coherence of the two states.

this would again involve long range couplings between nodes of approximately the same vibration frequency, we decided against this mapping and continued with the electronic nodes at the left edge of the MPS. In this ordering the maximum bond dimension is never saturated during the simulation time and the memory requirements are easier to handle. Furthermore, we can observe two plateau-like regimes in fig. 9.3, which might indicate different regimes in the time-evolution. It is also interesting to see that the larger local Hilbert space results in a slightly larger bond dimension requirement from the point where the middle mapping breaks down, and where the first plateau for the edge mapping sets in. This might be attributed to singular value tails, which were otherwise cut away but now slightly increase the dimension of physical-branching bonds. However, the impact is remarkably small and as we shall note shortly, observables are not affected, making calculations with the smaller Hilbert space well converged. Therefore, our requirement for the number of local phononic modes is in accordance with previous results [XLY+19].

Electronic properties 9.1.2

Now that we are confident that our calculations are numerically well controlled, we would like to investigate the decay behavior of the excitation S_2. For this we take a look at the electronic densities in fig. 9.4, which are obtained for the edge mapping and local Hilbert space size $d = 32$, as was described in the last section. We observe the total tendency of the system to decay to the S_1 state with some additional features. The initial kink around at early times < 5 fs we attribute to the time it takes for the phonon dynamics to set in. However, it does not influence the decay of the S_2 population until around 30 fs, where there is the inversion of the two graphs. Excitingly, this coincides with the point where the simulation either goes out of memory or reaches the first plateau. After that, there is a long region where the system seems to be steady, i.e. a plateau in occupation. Our interpretation of this is, that the light phononic modes set in early and after their dynamics has subsided, the system reaches this area. With some delay then the excitation of heavier vibrations set in, which causes the bump with the peak around 90 fs. However, this is not sufficient to push the system out of the previous state and the occupation of S_2 again decays in favour of S_1. Finally, almost all electronic density is attributed to the lower lying level and the system does not seem to change any longer.

In order to further understand the electronic system, we investigate the RDM with all the phonos integrated out

$$\hat{\rho}_{\mathrm{el}} = \mathrm{tr}_{\mathrm{ph}} |\psi(t)\rangle \langle\psi(t)| \ . \tag{9.7}$$

As we are working in the reduced subspace of one excitonic particle only, the electronic space is spanned by the two vectors $|S_1 = 1, S_2 = 0\rangle$ and $|S_1 = 0, S_2 = 1\rangle$. Therefore, we write the RDM as

$$\hat{\rho}_{\mathrm{el}} = \begin{bmatrix} \rho_0 & w \\ w^* & 1 - \rho_0 \end{bmatrix} , \tag{9.8}$$

which we can always do, as the matrix has to be hermitian and of trace one, i.e. it only has two independent degrees of freedom. While the diagonal elements fix the occupation of the individual elements, $w \in \mathbb{C}$ tells us if the system is in a coherent superposition. In particular, the magnitude $|w|$ gives a measure for the "delocalization" between the two electronic states, which is why we plotted it on the right axis of fig. 9.4. Even though, there is a jump of several orders of magnitude shortly before the crossing, the mixing is always within the range of quite small number and therefore never reaches the maximal coherent superposition which would correspond to $|w| = {}^1\!/_2$. Therefore, the electronic dynamic can be described purely classical.

The above observations motivated us to claim the hypothesis that the phonons serve as bath for the excitonic system. Given this would be true, we could make the ansatz that near the equilibrium we have an effective Hamiltonian, such that

$$\hat{\rho}_{\mathrm{el}} \approx \mathrm{e}^{-\beta \hat{H}_{\mathrm{eff}}} . \tag{9.9}$$

As the RDM in eq. (9.7) lives in the two-dimensional one particle subspace, so does $\hat{H}_{\mathrm{eff}}$. Based on the previous observation that the electrons do not delocalize but instead are captured by a nearly classical mixture we make the ansatz

$$\hat{H}^0_{\mathrm{eff}} = -\Delta \cdot \begin{bmatrix} \hat{n}_{S_1} & 0 \\ 0 & \hat{n}_{S_2} \end{bmatrix} + \text{const.} , \tag{9.10}$$

in which we assume the effective Hamiltonian is diagonal in the occupations of the electronic levels. In order to analyze the effect of the phononic bath we study the time evolution of the eigenvalues of the electronic RDM by rotating into the eigenbasis

$$\hat{\rho} = \frac{1}{1 + \mathrm{e}^{-\beta H^0_{\mathrm{eff}}}} \begin{bmatrix} \mathrm{e}^{-\beta H^0_{\mathrm{eff}}} & 0 \\ 0 & 1 \end{bmatrix} \equiv \begin{bmatrix} \rho_1 & 0 \\ 0 & \rho_0 \end{bmatrix} , \tag{9.11}$$

which allows us to write down the quotient

$$p_1 = {}^{\rho_1}\!/_{\rho_0} = \mathrm{e}^{-\beta H^0_{\mathrm{eff}}} . \tag{9.12}$$

Therefore, if we can fit β in such a way that the ratio of the RDM diagonals and the Boltzmann weight are the same, we have found the effective temperature. We do so by a heuristic fit to $\beta\Delta = 3/2$ in fig. 9.5, where we interpret the level with the smaller occupation as the ground state with energy ϵ_0. As one can see, the agreement is quite exact, even though the fitting procedure consisted merely of guessing the number. This excellent match between the postulated, classical density matrix description and the found dynamics of the diagonal elements of the Hamiltonian also implies an adiabatic time-evolution, since the effective temperature is merely constant.

Autocorrelation function & phononic properties 9.1.3

In the following we are going to discuss the remaining observables of the system. We begin by looking at the auto-correlation function

$$C(t) = \langle \psi(0) | \psi(t) \rangle , \tag{9.13}$$

which is easily obtained from the wave function and the initial state and shown in fig. 9.6. As we can see, the states are initially nearly parallel, a feature which decays within the initial time period which is reasonable as the Hilbert space is exponentially large and we exploit highly excited states through the time-evolution. However, it is also interesting to see that a transient phase between the two states builds up in the imaginary part of the overlap.

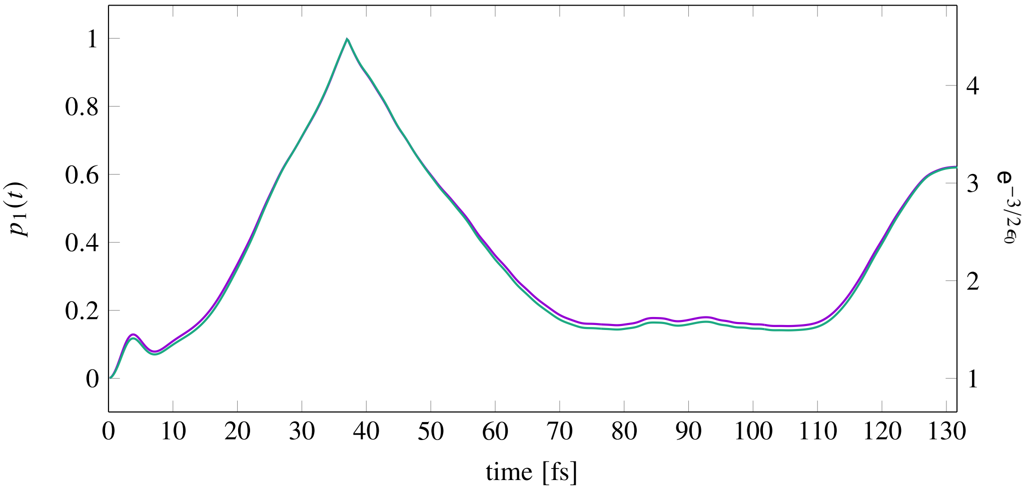

Figure 9.5: Fitting the eigenvalues of the electronic RDM (on the left axis, —) to the Boltzmann weight of the lowest energy state (on the right axis, —).

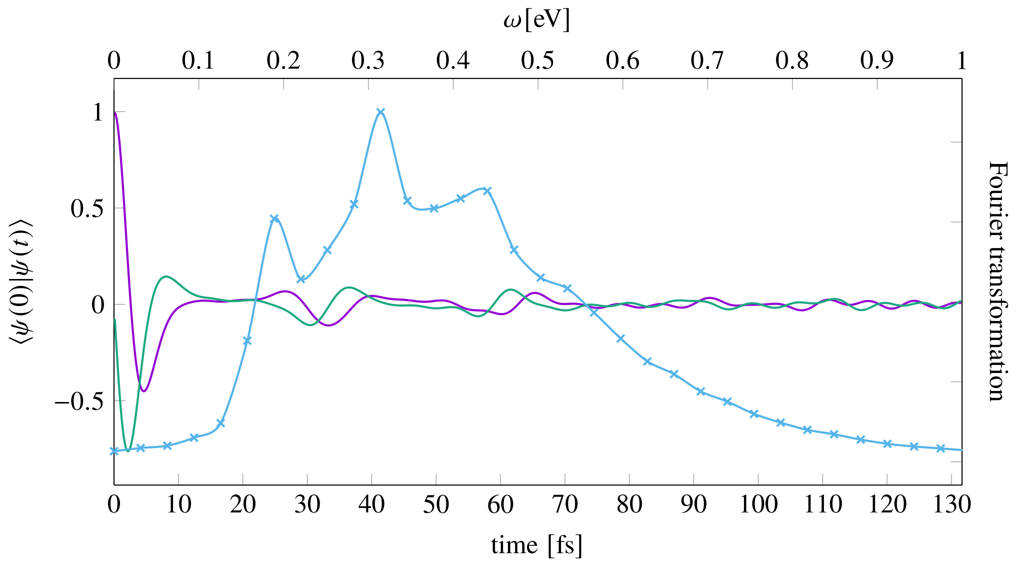

Figure 9.6: Real (—) and imaginary (—) part of the overlap of $|\psi(t)\rangle$ with the initial excitation S_2 are plotted on the left axis with the corresponding time steps at the bottom. In addition, we plotted the Fourier transform (—×—) on the right axis with the corresponding energies at the top. For the latter we used $\tau = 66\,\mathrm{fs}$.

Furthermore, fig. 9.6 exhibits an oscillatory behaviour around the envelope of orthogonality to the initial excitation. The nature of this oscillation is studied through the absorption spectrum, defined via the Fourier transform of $C(t)$ [Muk95]

$$I(\omega) \propto \mathrm{Re} \int_0^\infty \mathrm{d}t\, C(t) \exp\left(\mathrm{i}\omega t - t/\tau\right) \ , \tag{9.14}$$

where τ is an appropriately short effective relaxation time, sometimes also referred to as broadening. We observe good qualitative agreement to [XLY⁺19], where the absorption spectra were compared to MCTDH and experiment. The features, peaks and their relative heights are correctly reproduced in the correct energy range. However, the resolution seems to be limited through the final time and through the fact that we used a truncated weight which was one order of magnitude higher. Both are important findings which we will take over to the next section, where we want to obtain results as accurate as possible.

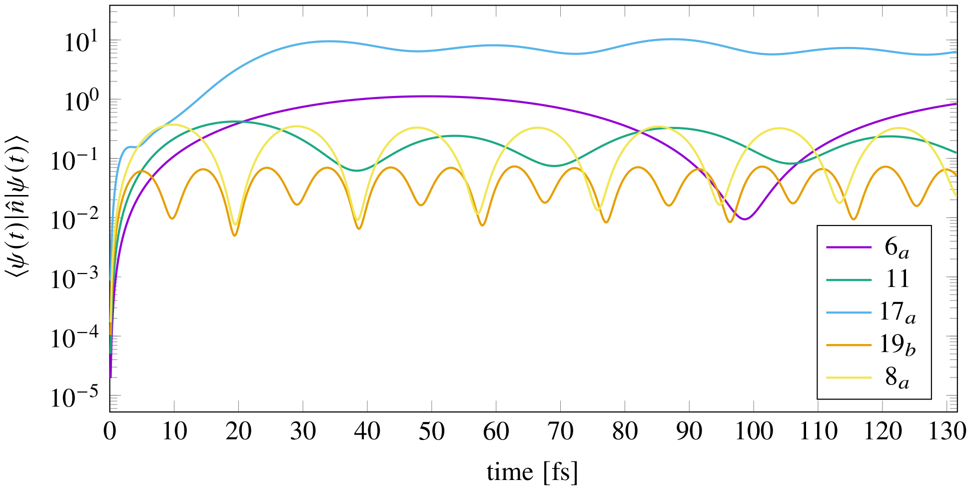

Figure 9.7: Time-evolution for the occupation of selected phononic orbitals.

The last physical property of the pyrazine molecule we want to address is the occupations of the phononic modes. For this we chose a subset of particular orbitals with rich dynamics and displayed them in fig. 9.7. The remaining modes were either quite constant in occupation after the transient regime or did not build up occupation at all. We recognize that the mode 11 has the maximal occupation of O (10) and is rather constant after the level crossing of the electronic states has occurred. However, this should not tempt us to believe that the phononic Hilbert space could have been chosen smaller. The large Hilbert space is required in order to represent the long tails of the spectrum of the RDM faithfully, as we shall discuss in section 9.2.4. The remaining nodes show interesting oscillatory behavior, with oscillations of constant frequency and amplitude. Last but not least, the interesting bump of 6_a should be noticed, whose occurrence is shortly after the depopulation of S_1, which we attributed to the heavy phononic modes. At this point in the simulation time, this mode is depopulated. However, once the electronic system goes back to being mainly S_1, it is populated again to the same level it was before.

Singlet fission 9.2

Now that we have described our experiences with benchmark systems, we want to turn to the main object of scientific interest. The highly prominent target of our calculations are molecules exhibiting singlet fission (SF), a class of systems in which excitonic coupling to lattice vibrations can not be neglected [MKW+17, BMK+16, TR17, SM10, Cas18]. SF is a process taking place in organic molecules upon photo-absorption. Thereby, a singlet exciton is converted into two triplet excitons while upholding spin conservation [ZZM10, SM10, MH17, Cas18]. In doing so, SF can increase the yield of organic semi-conductors in order to develop solar cells with higher efficiency [CLT+13, HN06]. However, a systematic approach to understand the mechanism and categorizing materials which are of use is still in the scientific process. Therefore, our aim was to perform a first principles simulation for possible candidate materials. As it turned out, the exact coupling of large number of vibrational modes to the diabatic states was in fact crucial for this. Even though many orbitals could be neglected, the amount of necessary modes is still relatively high for tensor network methods. Our previous ansatzes proved to be highly fruitful in order to obtain reliable results.

Before we go on with our discussion of SF and the material we simulated, we shall pay some attention to limiting factors in photo-absorption.

The Shockley-Queisser limit & multiple exciton generation 9.2.1

The basic functioning principle of the photo-absorption [Ein05] in a solar cell is easily explained, without going to much into detail. Electrons in the valence band are excited into the conduction band by a photon, leaving back a hole in the former. In the conduction band they are free and can be subject to electrical fields inducing motion, e.g. by a p-n junction. The difference in energy between the two bands is the band-gap Δ which needs to be smaller than the photon's energy in order to excite the particle. However, the question arises, what size of the band-gap is optimal to maximize the output of the construction. Small Δ leads to many excitations which are short-living due to their scattering with the nuclear grid, while large Δ leads to few particles which are in turn energetically highly excited. As one can already estimate, there is some kind of interplay with an optimum in between.

When Shockley and Queisser formulated their bound on the efficiency η of a single p-n junction [SQ61], semi-empirical results on the efficiency of solar cells were known [Lof56, Pri55, PVR54, CFP54]. However, they pursued a rather different approach idealizing the solar cell subject to light from the sun as an object exposed to black-body radiation. This way they were able to make a statement about the maximal efficiency of any material, irrespective of the actual real world setup, a property which is compared by them to the second law of thermodynamics [Car24, Cla50, Cla54, Tho52]. There, the maximal efficiency of no process might be larger than the efficiency of the Carnot process [Car24], i.e. it just depends on the ratio of temperature differences between the reservoirs.

Since the calculations necessary to arrive at the previous bound are quite extensive, we restrict ourselves to sketching the proofs idea and refer the interested reader to [SQ61]. First, Shockley and Queisser put a solar cell at $T_c = 0$ into a cavity with temperature T_s, assuming that the former has an energy gap of Δ. Then, they continue with the computation of what they call ultimate efficiency, i.e. the idealization that photons with energy below Δ do not cause anything while photons above Δ cause an electric charge at the corresponding voltage. Lastly, they make use of Planck's distribution [Pla01] to write down the number of photons absorbed

$$Q_s \propto \int_{\omega_g}^{\infty} \mathrm{d}\omega \, \frac{\omega^2}{\mathrm{e}^{-\beta_s \hbar\omega} - 1} \tag{9.15}$$

and compare it to the total energy density the sun emits

$$P_s \propto \int_{0}^{\infty} \mathrm{d}\omega \, \frac{\omega^3}{\mathrm{e}^{-\beta_s \hbar\omega} - 1} \, . \tag{9.16}$$

The ratio of these two quantities gives (up to factors) the ultimate efficiency. They argue that the function has a maximum and determine it by numerical means at 44 % for a band-gap of $\Delta = 1.1\,\mathrm{eV}$. However, they are even able to refine this bound by taking into account the radiative combination, i.e. the decay of an electron-hole pair upon emission of a photon, and finite solar cell temperature. Furthermore, also formation and decay of excitons without photonic involvement and the removal of an electron-hole pair are taken into account. Finally, they define a rate equation and demand, that the total rate of all processes is zero which leads them to a new value for η. This value is the ultimate efficiency multiplied with some correcting functions [SQ61]. The maximum of this function is also determined to be $\eta \approx 30\,\%$ at $\Delta = 1.1\,\mathrm{eV}$ for $T_s = 6000\,\mathrm{K}$ and $T_c = 300\,\mathrm{K}$.

Thus, for a quite long time the statement that single junction solar cells could not get more efficient was believed to be true. However, this belief got challenged by a new development in organic semi-conductors research, otherwise we would of course not be dealing with it. In the derivation of the Shockley-Queisser limit [SQ61] the explicit assumption was made, that each photon gets translated to one electron hole pair in the semi-conductor. Around the millennium this idea got challenged by the observation of more than one particle-hole pair created by incoming radiation in quantum dots [SK04, SPK05, EBJ+05, SSPK06, MBN+06, NBL+10], referred to as multiple exciton generation (MEG). This was not accounted for in the original derivation of Shockley and Queisser and it motivated the rederivation of the detailed balance limit by Hanna and Nozik [HN06]. They did so by following a derivation similar to the original one however, they introduced an additional function namely, the number of excited particles and called it the quantum yield $Y = Y(E)$. This function is then multiplied into the integrand of eqs. (9.15) and (9.16) in order to account for multiple charge carriers per photon. As the true nature of this function is unknown in general, they proposed three model dependencies of the ratio between light quanta and particles. First, they looked at a step-function which increases the quantum yield every time a multiple of a certain energy is reached to model quantum dot like behavior. Second, they looked at a combination of two step-functions which are only non-zero if their corresponding energy threshold has been reached but one has twice the yield of the other. Between the gap and twice the gap the yield is one, above the gap the yield is two. In this course they also introduce singlet fission as possible mechanism to achieve a quantum yield modelled by this function. And last, a step function which turns into a linear curve after a second threshold has been reached.

These yield functions are then tested with several photo-absorbing setups, i.e. single gap absorbers, the electrolysis of water to hydrogen and oxygen and a construct they call tandem cell, consisting of two solar cells which might be coupled serially or in parallel. Various possible numbers of excitons are taken into account. Particularly interesting, already two excitons shift the maximum efficiency of the cell to being $\eta \approx 42\,\%$ if the band-gap of the chosen material is slightly smaller than in the Shockley-Queisser case [HN06] namely, around 1 eV. For the tandem solar-cell construction even values around $\eta \approx 1/2$ can be achieved in theory.

All of the above mentioned methods rely on the solar-cell material to produce multiple charge carriers per photon, a task easily described in theory but difficult to realize in an exploitable fashion in experiment. However, the decay of single excitons into two triplet excitons in some organic materials was a known phenomenon to some scientific communities [MAG69, GPV69, SS68, SJS+65] in the context of fluorescence. Therefore, after the works introduced in this section, SF became a target of scientific interest with the goal of finding candidate materials to increase the efficiency of solar-cells. In addition to inducing MEG, the products of the photo-absorption process have another striking advantage, i.e. their statistics. Since the produced excitons are triplets, they are symmetry protected from decaying back to the ground state [SM10]. This makes the typical free path length of triplet excitons ($\sim$ µm) around a hundert times larger than for the singlet case ($\sim$ 10 nm) [NLZ+10, IB11]. Of course, they could do the reverse process of singlet fusion and two of the triplets result in a singlet again which can be recombined, e.g. under photo-emission. However, this is a process which needs certain circumstances to happen, e.g. current works indicate the spatial proximity is crucial for a fusion and therefore spatially distant triplet production increases the SF yield [WLX+21].

Concluding this rather dense section, we saw that the theoretical efficiency upon photo-absorption is limited and how this limit could be shifted to a larger value upon multiple exciton generation (MEG). We also chose one mechanism to generate MEG namely singlet fission (SF) which has also the advantage of creating long living excitons. In the upcoming chapter we want to discuss the mechanism in order to induce singlet fission.

Vibronic coupling 9.2.2

SF is known to happen in two manners, intermolecular (xSF) and intramolecular singlet fission (iSF). While in the former the fission process takes place between crystalline structures of stacked molecules [JNM13a, SM10], in the latter it takes place within covalently linked chromophore units which allows much easier control of the inter-chromophore orientation and interaction [THRB+15b, BXW+15]. This is achieved by manipulation of the molecular bridging parts and the environment, e.g. via the solvent. In the course of this thesis we only dealt with iSF and will therefore sometimes refer to it simply as singlet fission. In addition, previous investigations [WLX+21, THRB+15a, ZXJL16, RCT18, CBP+13, Tao19, ZZL17, XSBF+19, THRB+15a, MST+17, BG, GB21, SXC+20, SLH+21, STM+19] have resolved two driving mechanisms behind the triplet production in organic molecules, i.e. thermally activated and coherently driven SF. Thermally activated SF typically takes place on a relatively large time-scale of more than a ps [THRB+15b]. In contrast, the coherently driven SF is a process happening much faster, i.e. typically on time-scales below 100 fs [MST+17]. As the time-scale for our simulation is set by the inverse units of the Hamiltonian[1] these ultra fast processes were of particular interest to our first principle methods.

In order to model the triplet generation faithfully it is by now a well accepted fact that one has to incorporate the vibrations of the atomic lattice [SM10, Cas18]. In fact, in many models the electronic states decouple due to small hopping amplitudes between them or symmetry forbidden transitions [ZZM10, EBJ+05]. The lattice vibrations then induce coherence between the otherwise unrelated excitonic levels and thereby cause an effective mediated transition possibility. The necessity to go beyond the Born-Oppenheimer approximation (BO approximation) when modelling was discussed in a theoretical context [ZZM10, BHR14, ASD15, TR17], as well as through the investigation of materials exhibiting SF by spectroscopy [MKW+17, BMK+16]. In particular, the former typically showed that the

---

[1] The units of the Hamiltonian are $[\hat{H}] = \mathrm{eV}$, whose inverse corresponds to $1\,\mathrm{eV}^{-1} \mathrel{\hat{=}} 0.658\,212\,\mathrm{fs}$ for $\hbar = 1 = c$.

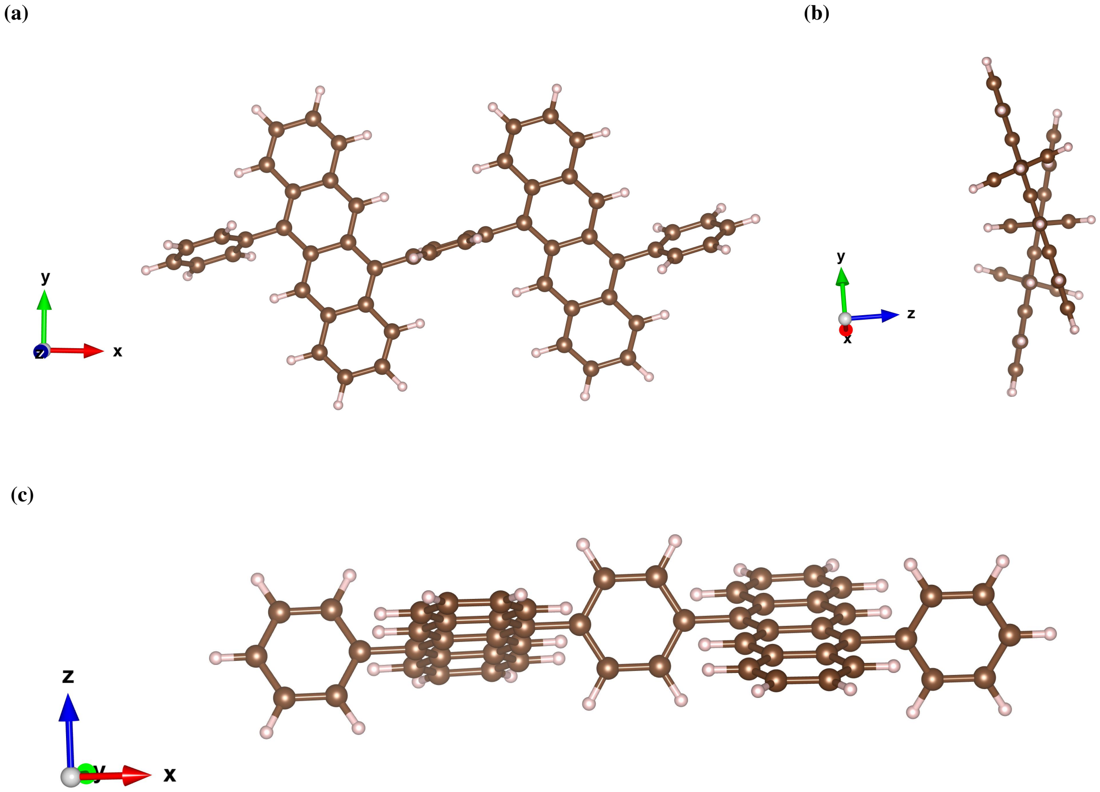

Figure 9.8: Chemical structure of the tetracene para-dimer resolved from different perspectives.

coupling of the identified electronic states gets enhanced by the phonons in such a way, that an ultra fast triplet population is achieved, otherwise no “density” is distributed to the electronic many-body levels belonging to the triplets. The experimental results backed up this claim in particular by identifying signals belonging to vibrational modes and relating these to conical intersection in the potential energy surface (PES), just as we discussed in chapter 7.

Model 9.2.3

Motivated by all these prior results and in particular by the investigation in [WLX$^+$21], in which the iSF in tetracene oligomers was explored, we began our analysis of the 1,4-bis(11-phenyltetracen-5-yl)benzene (tetracene para-dimer), shown in fig. 9.8. Tetracene ($C_{18}H_{12}$) is a hydrocarbon basically consisting of four benzene rings attached to each other and is the building block for these molecules. The chemical convention distinguishes between the carbon atoms which the individual units dock to via the ortho, meta and para keyword, i.e. if the tetracene units dock on nearest neighboring, next to nearest neighboring or second to next carbon atoms. These units are then attached to each other covalently by a phenyl group to form oligomers. In particular, the aforementioned work dealt with the question of the relevance of spatial distance for the triplet yield of the system experimentally, i.e. they looked at dimers, trimers and tetramers. For us the yield itself was not the immediate guiding question, rather we wanted to model with the minimal amount of approximations. Hence, we began our investigation with the dimer. This leads to the phononic Hamiltonian, given by the individual energy of the vibronic modes ω_I and the linear

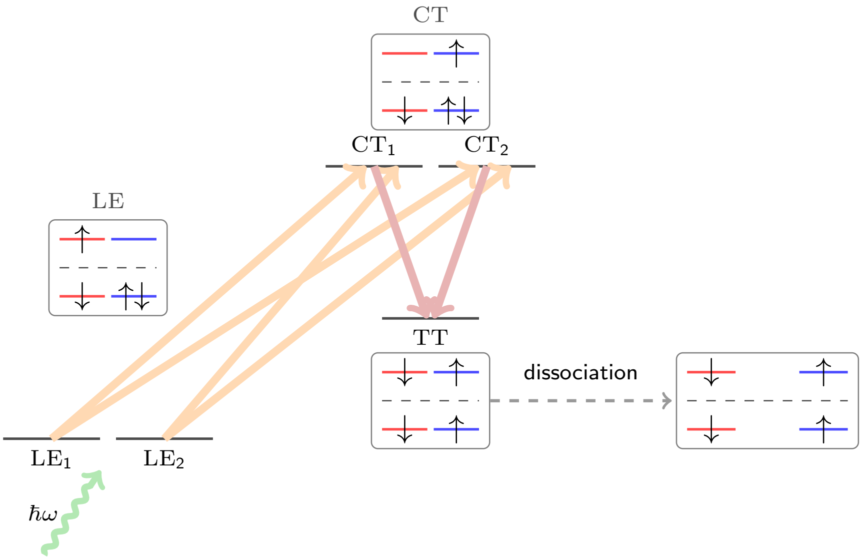

Figure 9.9: Schematic plot of the five diabatic states used to model the SF in the tetracene para-dimer. The position of the levels on the y-axis corresponds to the energies of the electronic many-body wavefunctions, which is the chemical potential in our exciton model eq. (9.18), but is not true to scale.

coupling between the excitonic density and the phononic displacement $g_{ij,I}$ as

$$\hat{H}_{\text{ph}} = \sum_I \omega_I \, \hat{b}_I^\dagger \hat{b}_I + \frac{1}{\sqrt{2}} \sum_{ij,I} g_{ij,I} \left(\hat{b}_I^\dagger + \hat{b}_I \right) \hat{c}_i^\dagger \hat{c}_j \, . \tag{9.17}$$

The form of the model is similar to eq. (9.5), of course with the coefficients being different. However, here we only needed to include the first order coupling in $\hat{x}$ to achieve excellent results.

Before we come to the nature of the vibronic modes, let us talk about the representation of the electronic system, which we modelled by means of five diabatic states, depicted in fig. 9.9. The locally excited (LE) states are representing the molecule after photo-absorption from the ground state. The excitation might reside in any of the chromophore units, therefore we have two of them labeled by a subscript. An analysis of the determinats belonging to this state reveals that they mostly consist of exciting one electron from the highest occupied molecular orbital (HOMO) to the lowest unoccupied molecular orbital (LUMO), as is also shown in the scheme. Furthermore, the involvement of charge transfer (CT) states is crucial for the correct description of the system. These correspond to cationic and anionic intermediate situations of the molecule in which the excitation is taken from the HOMO of the corresponding chromophore and placed in the LUMO of the neighboring tetracene unit. As one can imagine, these electrically charged non-equilibrium states are higher in energy and therefore, the molecule tries to avoid these by decaying to lower lying states. Of course, the most important constituent is still missing, namely the triplet electrons. As previous investigations have shown [ZZM10], the localized triplets in the chromophores can also be interpreted as electron-hole bound states which are correlated into an overall singlet state [SM10, JM70], here referred to as triplet pair (TT) state. Usually, the investigation of the dissociation into two spatially seperated triplets and recombination processes are detached topics [May16, MCBGZ19] and were therefore also not investigated by us. This enables us to again write down the total Hamiltonian of the tetracene para-dimer as [Fre31a, Fre31b]

$$\hat{H} = \sum_{ij} V_{ij} \, \hat{c}_i^\dagger \hat{c}_j + \sum_I \omega_I \, \hat{b}_I^\dagger \hat{b}_I + \frac{1}{\sqrt{2}} \sum_{ij,I} g_{ij,I} \left(\hat{b}_I^\dagger + \hat{b}_I \right) \hat{c}_i^\dagger \hat{c}_j \, , \tag{9.18}$$

where the energy of the electronic states is the chemical potential, i.e. the diagonals of V while the transition amplitude between electronic states is given by the off-diagonals.

The actual values for the V matrix are obtained using the state averaged complete active space self consistent field (SA-CASSCF) method for excited states [BR20]. In this method, the single particle orbital space of the electrons is divided into core, active and virtual orbitals. Subsequently, the time independent Schrödinger equation of the active space is solved variationally under optimization of the many-body coefficients and the single particle

	$\lvert\mathrm{LE}_1\rangle$		$\lvert\mathrm{LE}_2\rangle$		$\lvert\mathrm{CT}_1\rangle$		$\lvert\mathrm{CT}_2\rangle$		$\lvert\mathrm{TT}\rangle$	
$\lvert\mathrm{LE}_1\rangle$	2.9635	0.279	-0.0857	0.035	0.0431	0.039	-0.0535	0.052	0.0002	0.000
$\lvert\mathrm{LE}_2\rangle$			2.9637	0.280	0.0535	0.052	-0.0431	0.040	-0.0002	0.000
$\lvert\mathrm{CT}_1\rangle$					3.3645	0.276	-0.0007	0.001	-0.0612	0.055
$\lvert\mathrm{CT}_2\rangle$							3.3645	0.276	-0.0612	0.055
$\lvert\mathrm{TT}\rangle$									3.1493	0.516

Table 9.1: Excitonic Hamiltonian elements V_{ij} and their corresponding thermal fluctuations σ_{ij} (defined in eq. (9.21)) at 300 K in units of eV. The first entry per cell is V, while the second entry denotes σ for the given pair of diabatic states i, j.

orbitals. For our calculations we made use of the $6-31G(d)$ single particle basis set and in order to recreate the notion of locality in the delocalized molecular orbitals we used the Pipek-Mezey method [PM89]. Finally, we computed the elements of V by means of the complete active space configuration interaction (CASCI). The resulting diabatic chemical potentials and couplings are presented in table 9.1. As we have expected, the coupling between the LEs and CTs is relatively large compared to the coupling between LEs and TT. However, the indirect pathway superexchange path [BHR13a, BHR13b, JNM13b, MMW$^+$16] in which the excitation decays to the triplets via LE→CT→TT has a way higher transition probability and is going to be the main mechanism of TT population, as we are going to see.

As described in chapter 7, we then distort the equilibrium geometry along the vibrational mode Q_I to compute a PES in order to obtain the exciton-phonon coupling. From this, the resulting values for g are computed by taking the gradient with respect to the spatial coordinate

$$g_{ij,I} = \nabla_{Q_I} V_{ij}(\vec{Q}) \ . \tag{9.19}$$

In order to figure out, which vibrational modes out of the total 258 are the most relevant we computed the spectral density according to

$$J_{ij}(\omega) = \sum_I g_{ij,I}^2 \, \delta(\omega - \omega_I) \tag{9.20}$$

and plotted it in appendix C. It can be recognized, that the diagonal excitonic coupling is dominated by high frequency modes around 1400 cm^{-1}. Two modes contribute in particular to this frequency range namely, the ones at 1409.61 cm^{-1} and 1411.18 cm^{-1}. We labeled these notorious modes, which are depicted in appendix D, $I = 184$ and $I = 185$ and note, that they correspond to collective vibration of the chromophore's backbones. Due to the stark change of the molecular orbitals this induces, a change in the excitonic energies is caused which influences the chemical potentials in V. In contrast, the off-diagonal excitonic couplings seem to be stronger for modes with lower frequencies in particular, around 415 cm^{-1}. This is explained by the fact, that these modes represent the twisting of the connecting phenyl group which mainly varies the transition probabilities, as they depend on the overlap between the chromophore units. The chromophores themselves remain unaltered under this vibration. We neglect all modes which trigger relative fluctuation below 0.1 % and whose frequencies correspond to oscillation time below our simulation time. This leaves us with 76 phononic modes in total, ranging from 10.18 cm^{-1} to 1714.2 cm^{-1} (0.0013 eV to 0.2125 eV) which we need to incorporate in our simulations.

Finally, we want to justify the employment of zero temperature methods and compute the temperature-dependent fluctuations of the excitonic Hamiltonian at 300 K according to

$$\sigma_{ij} = \sqrt{\int_0^\infty \mathrm{d}\omega \, J_{ij}(\omega) \coth {}^{\beta\omega}\!/_{2}} \ , \tag{9.21}$$

which is shown in table 9.1 and appendix C. As we can see, the thermal fluctuations are quite small compared to zero temperature which makes our ansatz justified and the results compareable.

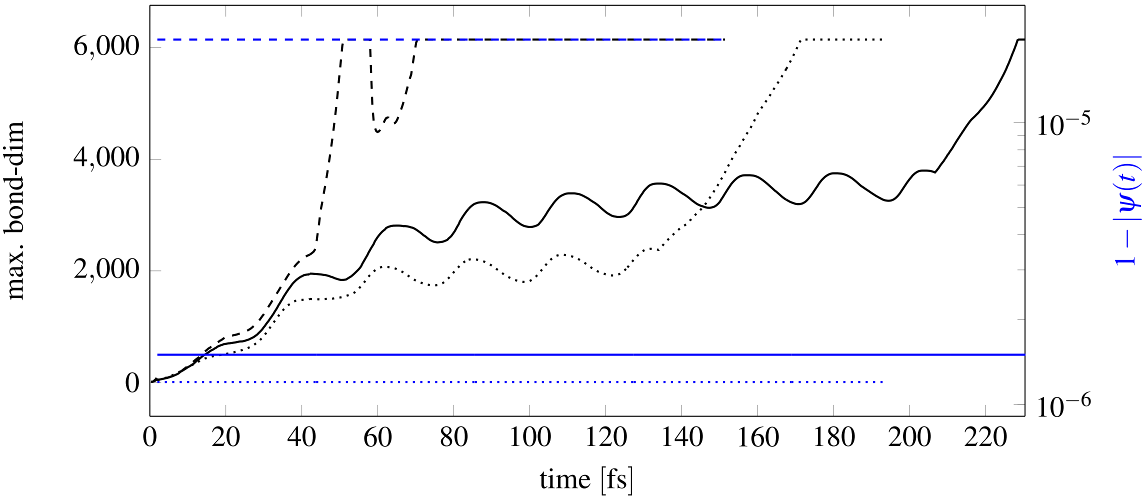

Figure 9.10: Numerical control parameters of the tetracene para-dimer for the different initial states described in the main text. ‘ The maximum bond dimension is shown in black for the localized (dotted), bright (solid) and dark (dashed) initial state. Again, we use the norm deviation as a measure for the projection error and show it in blue with the same schemes for the initial state as the bond dimension.

Numerical stability 9.2.4

Based on our previous experiences with the pyrazine molecule (see section 9.1) we chose to map the five electronic orbitals to the left of the MPS and attach the phononic modes in ascending frequency to the right, just as it is described in the upper part of fig. 9.2. However, we wanted to be assured that our numerics are well controlled and therefore investigated the two main sources of error again. Even tough TDVP has four sources of error, i.e. the projection error, the truncation error, the exponentiation error, and the Trotter error, our main targets were the former two, again. Due to the latter two the error depends on the time-step and how fast powers of the Hamiltonian decay. As the time-step is typically chosen to be small this makes the Trotter error subleading to the other types [PKS⁺19]. Furthermore, the exponentiation error is caused by the (formally) inexact solution of the local differential equation ([PKS⁺19] and section 5.1) and can be very well controlled again by the criterion of [HL97].

We truncated the growth in bond dimension by cutting off as many singular values until the threshold of $\delta = 1 \times 10^{-8}$ is reached. However, we also set an upper bond dimension of $m = 6144$ after which we cut off the smallest singular values. Until this bond dimension is not reached, we can trust the results to lie within the chosen truncated weight. After that a careful investigation of the results needs to be undertaken in order to assure the data being trustable. We modelled the system after photo-excitation by means of three possible initial states, i.e.

$$|\psi(0)\rangle = |\text{localized}\rangle = |\text{LE}_1\rangle \ , \tag{9.22}$$

$$|\psi(0)\rangle = |\text{bright}\rangle = (|\text{LE}_1\rangle + |\text{LE}_2\rangle)\,/\sqrt{2}\ , \tag{9.23}$$

$$|\psi(0)\rangle = |\text{dark}\rangle = (|\text{LE}_1\rangle - |\text{LE}_2\rangle)\,/\sqrt{2}\ , \tag{9.24}$$

which, as the names already suggest confine the excitation to one of the chromophores (as the molecule is symmetric it does not matter which one) or distributes it along both chromophores. The dark initial state can not be realized as it belongs to a forbidden transition, but was investigated out of curiosity. All phononic orbitals were prepared with an initial occupation of zero. As we can observe in fig. 9.10, there is an oscillatory growth behaviour in the maximum bond dimension and the maximum which we defined is not saturated for the two physical cases until late in simulation time. Furthermore, the maximum bond dimension which saturates the bound belongs to the bond between the physical bath construction of the mode no. 184 and does therefore not influence relations between supersites. This also explains the oscillatory behaviour, as the occupation of the phononic modes also oscillates. It originates from the high number of phononic modes necessary, as we shall see in fig. 9.12. We will observe the RDMs there and check that the results are in fact trustable. For the dark initial state the situation is undoubtedly different. While the evolution of the maximum bond dimension is quite similar to the others for the first 40 fs,

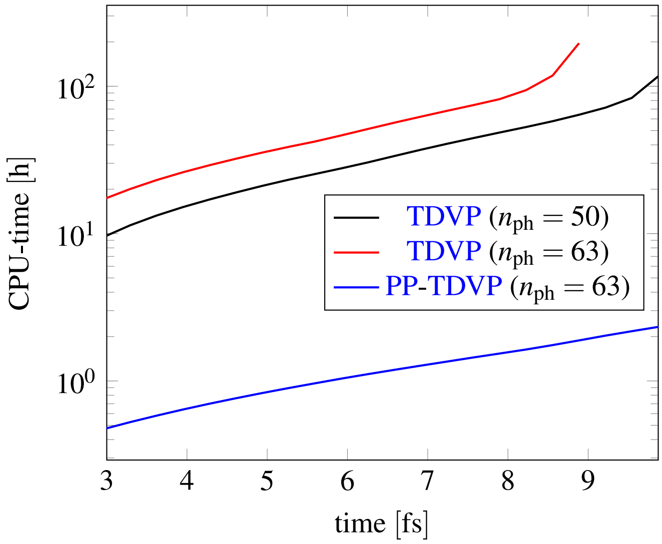

Figure 9.11: The speedup in CPU-time for the tetracene para-dimer on an Intel®Xeon®Gold 6130 CPU (2.10 GHz) with two processors and 32 cores in total. Hyperthreading was enabled on the machine but not exploited by us. Note the logarithmic scale on the y-axis.

it skyrockets after that immediately to the maximum where it stays for the rest of the simulation except for an interesting kink around 50 fs. Most likely is the system showing similar oscillatory behavior as before.

The projection error seems to be well controlled, as before, and therefore the norm deviance is of quite constant order of magnitude over time for the different initial states. While the difference in norm error of the bright initial state is approximately 50 % higher than the one for the localized one, the dark initial state is one order of magnitude higher. As the main source of projection error is an insufficient bond dimension to display the projector to the original Hilbert space sub-manifold correctly, this is reasonable given the bond dimension profile in fig. 9.10. However, it is to note that we described the formally $\sim 10^{137}$ dimensional Hilbert space of the tetracene para-dimer with a state using 1.3 GB on disk exactly, only using O (10 GB to 100 GB) of RAM during the calculations.

The resulting speedup in computation time between the molecule with and without the PP-mapping can be observed in fig. 9.11. Here, we compared the PP-mapping with a total local Hilbert space size of $d = 64$ to a pure TDVP with the same Hilbert space size and one of size of $n_{\mathrm{ph}} = 50$. This is the smallest Hilbert space size which we could choose in order to have results of the phononic RDM in accordance with our truncated weight of $\delta = 1 \times 10^{-8}$. As we can see, the PP-mapping is a factor of 100 faster than the symmetry free version which is not only caused by the parallelization over tensor blocks but also through the automatic truncation (section 7.3) of low weight blocks. Furthermore, note that the calculations without symmetry protected tensors went above the maximum memory threshold of the machine of 200 GB around 9 fs to 10 fs while we were able to maintain our calculations until 260 fs. Another convenient aspect of the employed representation is that through the suppression of unnecessary zeros in the tensor blocks, the MPO bond dimension stays quite low. While the pure MPO has a maximum bond dimension of 200, we were able to construct an operator with a bond dimension around 20. As the application of the effective Hamiltonian to the state is the most expensive part of variational optimization algorithms [Sch11] this will also save us a lot of runtime, not to speak of the construction of blocks, etc.

As a final remark on numerics and stability of the simulations we want to discuss the necessary size for the local Hilbert space, before continuing with physical observables. We already described, how choosing an insufficiently large Hilbert space will result in the system “seeing the edge” of such and therefore in wrong results. After all an RDM

$$\hat{\rho}_I(t) = \mathrm{tr}_{\setminus I} \left|\psi(t)\right\rangle \left\langle\psi(t)\right| \tag{9.25}$$

has to be of trace one therefore, the system tends to renormalize the suppressed probability to lower lying modes, if the modes necessary for the description are not present. Typically, this would result in a combination of a population inversion and explosion of the bond dimension. Therefore, we investigated the phononic RDM of the already described characteristic mode no. 184 whose bond between physical-and bath-site corresponded to

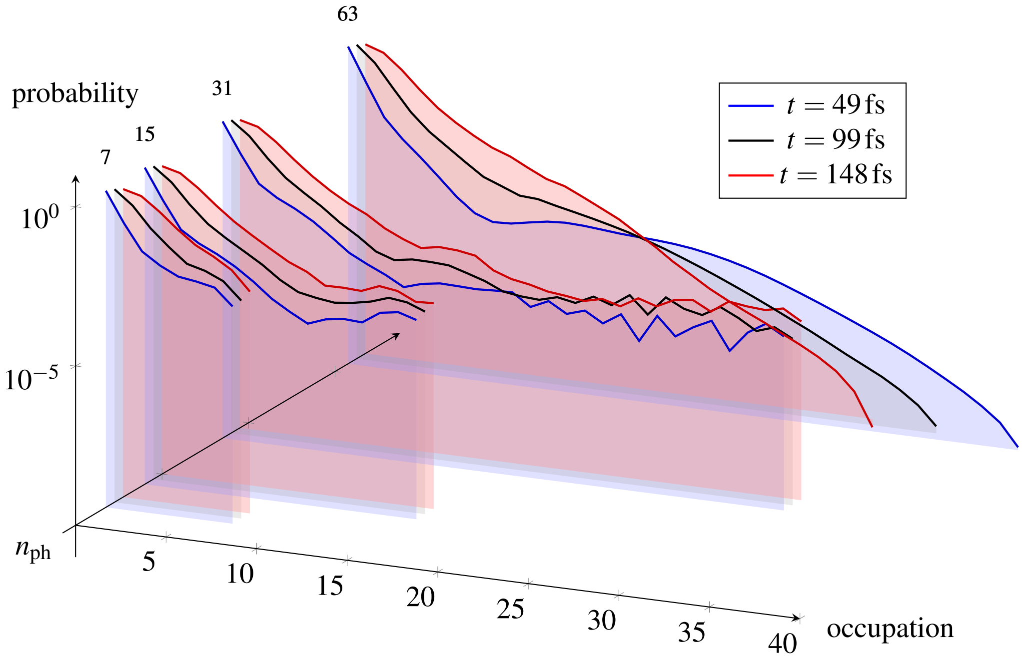

Figure 9.12: Excitation probability for phononic occupation modes of the vibrational orbital no. 184 during the time-evolution.

the maximum bond dimension in this parameter regime. The result, in the form of the diagonal elements of the phononic RDM, is presented in fig. 9.12. Here, we repeated the calculation for smaller values of d and checked the influence on the system. As we can see, the maximum of the distribution is always around the zero occupation point which indicates that no population inversion took place. Furthermore, the decay for the approximately first ten phononic modes is always correctly described, even for small local Hilbert spaces like $d = 8$. However, the results for the largest Hilbert space reveals that the tail of the phonon distribution is much longer than the smaller Hilbert spaces can provide for intermediate times. This leads to a relaxation of the distribution for later times in the simulation in the true model while the MPSes with too small local dimension can not display the decay of these excitations correctly. As a consequence, they are going to remain in an energetically higher excited state while the molecule actually would relax away from this.

We shall try estimating these errors induced by those wrong results which are of the order of $\delta(\rho_I)_{nn} \sim 10^{-5}$ for the occupations $n = 10$ to 30. The energy of the lattice vibrations enters the Hamiltonian linearly according to eq. (9.18). Therefore, the approximate error in energy introduces scales like $\langle\psi(t)|\hat{n}_I|\psi(t)\rangle = \sum_n n \cdot (\rho_I)_{nn}$ whose numerical value is given by

$$\sum_{n=10}^{30} n \cdot \delta(\rho_I)_{nn} \sim 10^{-3} \tag{9.26}$$

for each time-evolution step of the mode no. 184 in the corresponding time regime. The error for other modes might be smaller than this particular mode, however, their errors are accumulated into the total wavefunction over time and therefore make the deviance quite severe. We therefore have no other way than to use the large local Hilbert space of at least 50 phonons. As we do not have to account for too large Hilbert spaces from the computational perspective, we fixed the maximum d to be 64. All following results were obtained with this setup, if not stated otherwise.

Absorption spectrum & energy transfer | 9.2.5

Now that we are certain that our caluclations are well behaved, let us discuss the actual physically relevant data we can extract from the simulation of the tetracene para-dimer. The initial state of our time-evolution is the bright

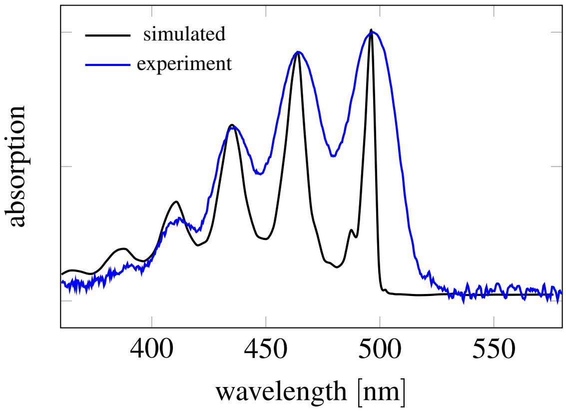

Figure 9.13: Simulated absorption spectrum compared to experimental values from [WLX+21].

excitonic state from eq. (9.23), i.e.

$$|\psi(0)\rangle = |\text{bright}\rangle \otimes |\chi(0)\rangle \ , \tag{9.27}$$

where $|\chi(0)\rangle$ is the vacuum state of the phononic sub Hilbert space (in the PP representation). The absorption spectrum is obtained similarly as before from the Fourier transform of the autocorrelation function

$$I(\omega) \propto \mathrm{Re} \int_0^\infty \mathrm{d}t \ \langle\chi(0)| \langle\text{bright}| \, \mathrm{e}^{-\mathrm{i}t\hat{H}} \, |\text{bright}\rangle \, |\chi(0)\rangle \, \mathrm{e}^{\mathrm{i}\omega t - t/\tau} \ , \tag{9.28}$$

where we choose the broadening τ in such a way that the $0-0$ and the $0-1$ peaks fit the experimental spectra [WLX+21]. With a numerical value of $\tau = 230\,\mathrm{fs}$ this is achieved and we display it in fig. 9.13. In particular, we see that the relative height of the peaks fits excellently, as well as their positions and the range of the spectrum. Even the small shoulders in the blue wavelength and adjacent to the ultraviolet (UV) spectrum are correctly resolved. However, the peak position is slightly higher than for the experiment. We attribute this and the lower valley depth of the simulated spectrum to the neglected phononic modes, i.e. the ones which were too heavy for our simulation time or had not enough spectral density (see section 9.2.2). Marginal energy contributions which would otherwise flow into these subsystems are now distributed to the existing orbitals. Nevertheless, these small deviances are certainly acceptable given the high degree of agreement to experiment and could be the subject of small future investigations.

Next, we want to look at the energy contributions of the different subsystems to the total energy. This is easily achieved by taking the Hamiltonian in eq. (9.18) and splitting into the three constituent parts, i.e. the electronic, the vibrational and the exciton-phonon coupling. The time-evolution of the energy is then obtained by computing expectation values $E_x(t) = \langle\psi(t)|\hat{H}_x|\psi(t)\rangle \, / \|\psi(t)\|$, where x corresponds to one of the three options. As we can observe in fig. 9.14, the excitonic part of the energy almost remains constant in the region of the initial value, i.e. the energy of the LEs (see table 9.1), except for a small wiggly area in the beginning. Quite in contrast, the energy of the phonons and the exciton-phonon coupling show strong oscillatory behaviour. We can see the amplitude of the oscillation itself showing damped oscillatory behaviour if we look at the envelope of the energies. In order to figure out which frequencies are the ones contributing most to the energy transfer we Fourier transformed the time dependent energies and showed them in fig. 9.14. This reveals that there are two peaks belonging to the vibrational modes dominating the energy transfer between the subsystems, they are located around $1420\,\mathrm{cm}^{-1}$ and $1620\,\mathrm{cm}^{-1}$. The modes which are employed in this frequency range are in particular

$$\begin{aligned} 1420\,\mathrm{cm}^{-1}: &\qquad \text{modes no. 184, 185 and 186} \ , \\ 1620\,\mathrm{cm}^{-1}: &\qquad \text{modes no. 209, 210 and 211} \ , \end{aligned}$$

especially the former are modes found already by previous investigations [ZXJL16, BMK+16, SAW+19] to be of high importance to the energy transfer. As formerly mentioned, these modes belong to the collective vibration of the molecule's backbone and have shown dominant peaks in the spectral densities in appendix C, particularly in the diagonal excitonic coupling.

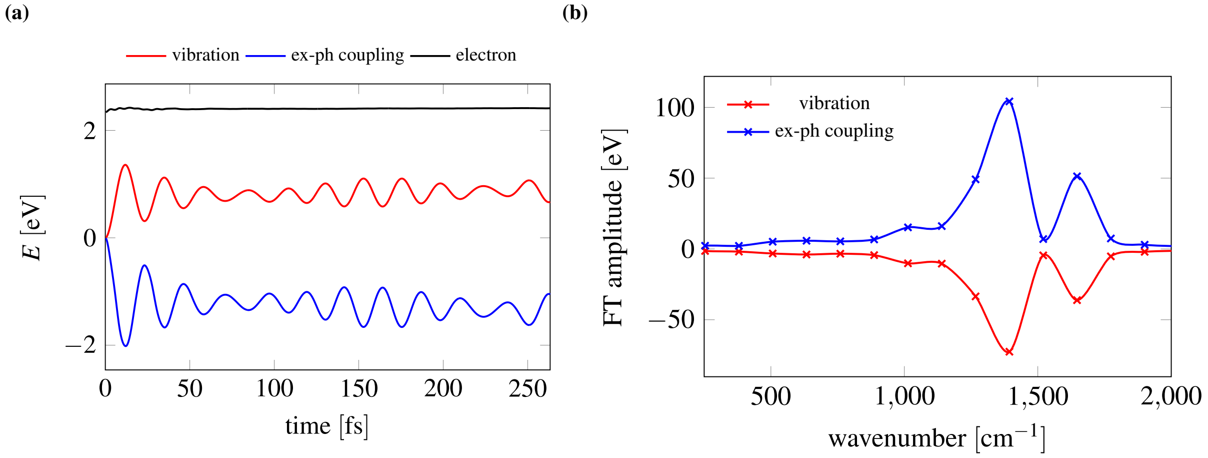

Figure 9.14: Time-evolution of the partial energies and their respective Fourier transforms.

Electronic properties & solvent polarity | 9.2.6

For practical purposes the most important question is of course the triplet yield or its slope, respectively. If the investigated material should be employed to harvest light in a solar cell we are mainly interested in how many charge carriers we can expect, but also in which parameter regimes we need to do so and how to realize these in experiment. Therefore, our starting point in this section shall be the excitonic occupations, shown in fig. 9.15. The first two cases, i.e. the localized and the bright initial state, are the physically realizable ones and show very similar behaviour. They both have a delay until the CT population builds up which emphasizes the importance of the indirect pathway. Furthermore, both are ultrafast processes in the sense that the triplet population builds up in the sub 100 fs regime by an almost constant growth rate. The LEs and CTs show oscillatory behavior in time with a frequency of about $0.12\,\mathrm{fs}^{-1}$. This frequency coincides with the energy gap of two eigenstates of the pure excitonic Hamiltonian which carry the main weight in the expansion of the eigenbasis in term of the diabatic states. This demonstrates, that the excitonic coupling is the main driving force on transient time-scales until the coherence mediated by the phonons starts to set in. The oscillations get suppressed over time which we interpreted as a sign that the phononic bath was chosen large enough for the system to achieve relaxation into an incoherent exciton dynamics, as we are also going to discuss in a second. Also, it is interesting to observe that the delocalization of the initial excitation over two chromophores results in pretty much twice the triplet yield especially, in the light of the findings of [WLX+21], i.e. the spatial delocalization as driving force for the triplet generation. Finally, we want to mention the results from the dark initial state, also shown in fig. 9.15. Here, we can see a significantly different behavior including the formation of a plateau in TT occupation for transient times, resulting in a higher final yield than in the previous two cases. Furthermore, also a decay of triplet population can be observed after approximately 80 fs, a phenomenon not present in the other two cases. However, as such an initial state after photo-absorption can not be realized, the investigation of this initial state is more of an academic motivation and less of a practical one.

Before we continue on coherence of the excitonic system, we consider it important to investigate the solvent polarity. It has been previously shown [XSF+20], that the polarity of the solvent material in which we put our organic semi-conductor will have an influence on the CTs. In particular, [WLX+21] investigated the dependency for several solvent materials, i.e. the relation between the LE and CT energy level and the inverse of the dielectric constant of the solvent. It was found, that while the LEs are mostly insensitive to the polarity, the CT states come down in energy the more polar the solvent gets. From an intuitive point of view this makes sense, as mentioned before the CTs are energetically high lying anionic and cationic intermediate states. However, the more polar the environment gets, the easier it is for these to be populated, i.e. for the system to transfer charge from chromophore to the other which resembles in the energy.

Therefore, we tried to map out a kind of phase-diagram of the tetracene para-dimer tuning its energy levels in CT and TT. It should be mentioned, that the tuning of the TT levels is not realizeable in experiment however, was done by us in order to estimate the impact in general. The resulting maximum TT occupations are shown in

(a) $|\psi(0)\rangle = |\text{localized}\rangle$. **(b)** $|\psi(0)\rangle = |\text{bright}\rangle$.

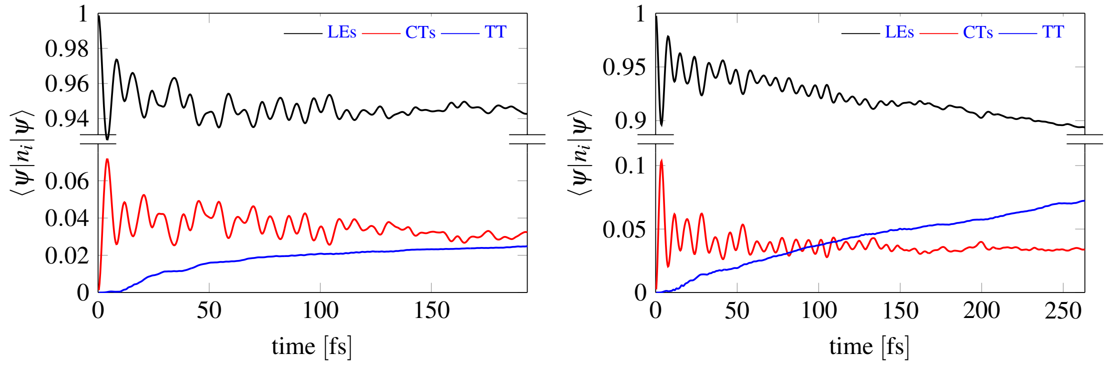

(c) $|\psi(0)\rangle = |\text{dark}\rangle$.

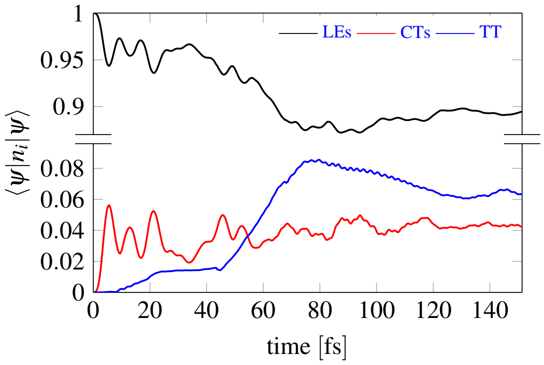

Figure 9.15: Excitonic occupations for different possible initial states, i.e. a localized, bright and dark excitation.

fig. 9.16. Here, the LE-CT gap is plotted on the x-axis while the difference between TT and CT is on the y-axis. The actual computed value for the TT energy level lies at $E_{\text{CT}} - E_{\text{TT}} = 0.2\,\text{eV}$, i.e. in the middle of the diagram. As we can observe, irrespective of the value on the y-axis the TT yield increases upon increasing of the solvent polarity. We expect the function connecting the yield and the CT energy levels to be of parabolic shape however, the minimum and the width are unknown presently. Apparently, the phonons induce hopping from the LEs to the CTs which then in turn decay into the energetically nearest state, i.e. the TT. We find the maximum number of triplet electron being 14 % to 25 % which is in quite good agreement to the experimental findings of 21 % [WLX⁺21].[2]

We also plotted the time-evolution for selected points in the phase-diagram in fig. 9.16. As expected, we see different values for the solvent polarity and the TT level resulting in different final yields. However, a striking feature exposes itself in this graph, i.e. a characteristic kink around 35 fs. This feature is completely independent of the configuration of the excitonic energy levels and stands out, as for all of the datapoints $^2/_3$ of the total triplet yield are produced until the time corresponding to this kink. The first interpretation for this might be relating to the most important phononic modes, whose period is about 25 fs, to this characteristic time-scale. As we have already argued, the effective transition from the LEs to the TT state is controlled by the effect the phonons have on the excitonic system. Mainly, the mechanism behind iSF is driven by the coherence, which is small given the pure excitonic Hamiltonian in table 9.1. However, the lattice vibrations induce phonon-assisted hoppings, following Fermi's golden rule, which leads to a coherence between the excitonic modes for a finite lifetime [CLJ⁺11, MZ15, ZXJL16, RCT18]. As previously, we wanted to investigate the quantum coherences of the molecule during the simulation and therefore computed the excitonic RDM and its eigensystem

$$\hat{\rho}_{\text{ex}}(t) = \text{tr}_{\text{ph}}\,|\psi(t)\rangle\,\langle\psi(t)| = \sum_{i,j\in X}\langle i|\hat{\rho}_{\text{ex}}(t)|j\rangle\,|i\rangle\,\langle j| = \sum_{\lambda}\lambda(t)\,|\lambda(t)\rangle\,\langle\lambda(t)|\ , \tag{9.29}$$

---

[2] Since every triplet pair decays into two triplet electrons, their number is twice the occupation of the TT level.

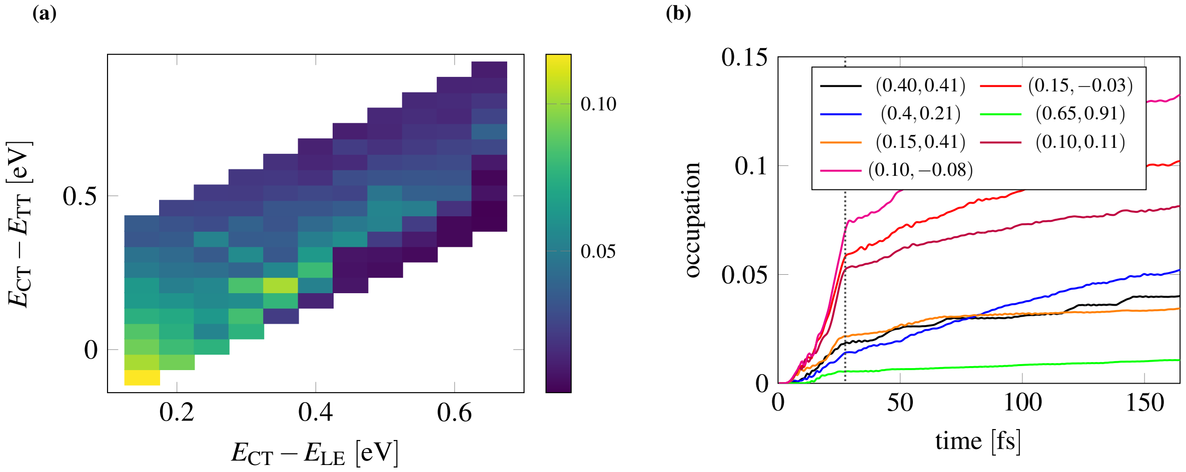

Figure 9.16: Maximum occupation of the TT yield for different values of the chemical potentials, i.e. the diagonals in V of eq. (9.18), on the left. Note, that these values belong to different times during the simulation as the highest possible occupation was always chosen over the entire range. Full time-evolution of the TT level of selected points on the right.

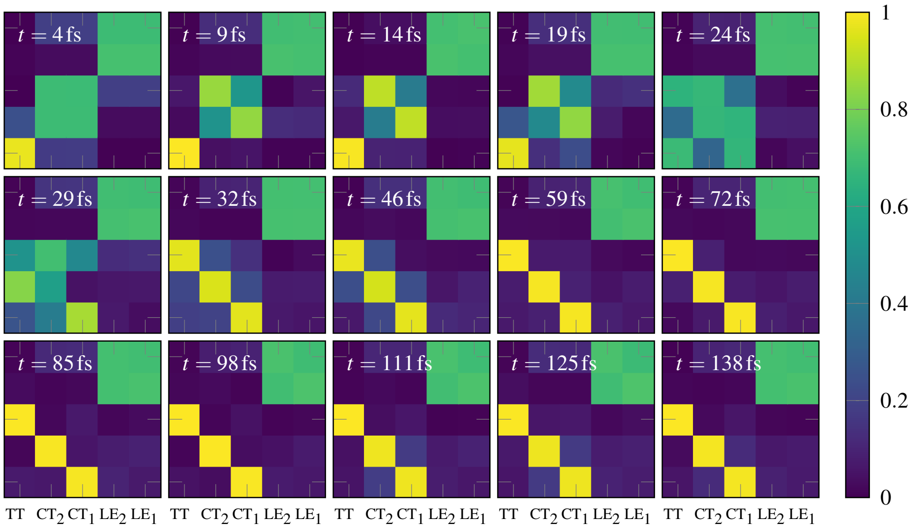

Figure 9.17: Type-evolution of the eigenvectors $|\langle\lambda|i\rangle|$ of the electronic RDM. Note, that the eigenvalues are sorted by magnitude, in our case from top (largest) to bottom (smallest).

where X is the set containing the five diabatic modes and λ labels the elements of the eigensystem of $\hat{\rho}_{ex}$. The overlap elements $\langle\lambda(t)|i\rangle$ form a matrix determining the degree of coherence between the corresponding initial basis vectors over time. We computed these from the time-evolved wavefunction and plotted it in fig. 9.17.

As one can recognize, for times $t < t_0 \approx 30$ fs the system is in coherent superpositions but between different sets of levels for different times. The LE levels are coherent over the entire simulation time which is reasonable, as they were intialized in such a state (see eq. (9.23)) and do not loose much occupation to the other levels, as is clearly seen in fig. 9.15. The CTs show similar behaviour up until ~ 10 fs which is related to the already mentioned indirect pathway. After that, they start delocalizing with the TT level which reaches its maximum around 25 fs where these three levels are basically in an equal weighted superpositon. Following that, the system basically decomposes into unrelated blocks for the rest of the simulation time, expect for the aforementioned LEs. Note that the eigenvectors of the RDM are sorted by their weight and therefore their ordering might change during time-evolution, explaining the diagonal pattern in fig. 9.17. Neglecting the subleading off-diagonal terms for $t > t_0$ we can find an approximate decomposition for the RDM

$$\hat{\rho}_{\text{ex}}(t)\Big|_{t>t_0} \approx \hat{\rho}_{\text{LE}}(t) \oplus \hat{\rho}_{\text{CT}}(t) \oplus \hat{\rho}_{\text{TT}}(t) = \exp\left(-t\left(\hat{H}_{\text{LE}} \oplus \hat{H}_{\text{CT}} \oplus \hat{H}_{\text{TT}}\right)\right)/Z(t)\ , \tag{9.30}$$

where the effective Hamiltonians governing the excitonic subsystems look like

$$\hat{H}_{\text{LE}} = -\sum_{i,j\in\{1,2\}} \left(\ln\lambda_4(t)\,\langle \text{LE}_i|\lambda_4(t)\rangle \left\langle \lambda_4(t)\middle|\text{LE}_j\right\rangle\ |\text{LE}_i\rangle\langle \text{LE}_j| + \ln\lambda_5(t)\,\langle \text{LE}_i|\lambda_5(t)\rangle \left\langle \lambda_5(t)\middle|\text{LE}_j\right\rangle\ |\text{LE}_i\rangle\langle \text{LE}_j|\right) \tag{9.31}$$

$$\hat{H}_{\text{CT}} = -\left(\ln\lambda_1(t)\ \ |\text{CT}_1\rangle\langle \text{CT}_1| + \ln\lambda_2(t)\ \ |\text{CT}_2\rangle\langle \text{CT}_2|\right) \tag{9.32}$$

$$\hat{H}_{\text{TT}} = -\ln\lambda_3(t)\ \ |\text{TT}\rangle\langle \text{TT}|\ . \tag{9.33}$$

We thus see, that time-scale of the coherences coincides with the timespan in which the main TT production is reached. After that, the systems are basically evolving decoupled from each other and classically according to their respective effective Hamiltonians. This emphasises the importance of the coherence induced among the excitonic levels by the phonons to the SF process. However, this does not explain the origin of this time-scale. How the phononic bath changes the effective Hamiltonian for the excitonic system shall be therefore discussed next.

Lang-Firsov transformation 9.2.7

In order to investigate the effect the phonons have on the excitonic system we made use of a generalized Lang-Firsov transformation [LF63, HvdL07]. Originally developed for Holstein type of models, this method makes it able to derive an effective low energy theory for composite electron-phonon systems in some limits and reveal the nature of the renormalized mass of electrons. For this we define the operator $\hat{U} = \mathrm{e}^{-\hat{S}}$ given the operator

$$\hat{S} = \sum_{ij,I} \Gamma_{ij,I}\, \hat{c}_i^\dagger \hat{c}_j \left(\hat{b}_I^\dagger - \hat{b}_I\right) \tag{9.34}$$

similar to the exciton-phonon coupling term, however with so far unknown coefficients Γ. This way, we can transform the Hamiltonian according to

$$\hat{H} = \mathrm{e}^{-\hat{S}}\left(\mathrm{e}^{\hat{S}}\hat{H}\mathrm{e}^{-\hat{S}}\right)\mathrm{e}^{\hat{S}}\ . \tag{9.35}$$

This somewhat artificial construct will soon prove to be useful as we take the inner braket and try to evaluate it. The degrees of freedom left open are the values of the Γ tensor which we will choose in such a way, that the exciton-phonon coupling vanishes, at least to first order.

As a lemma from BCH [Bak01, Cam97, Hau06] we may write the Hamiltonian product with the exponential matrices as

$$\mathrm{e}^{\hat{S}}\hat{H}\mathrm{e}^{-\hat{S}} = \sum_{n=0}^{\infty} \frac{\left[\hat{S},\hat{H}\right]_n}{n!} = \hat{H} + \left[\hat{S},\hat{H}\right] + \frac{1}{2}\left[\hat{S},\left[\hat{S},\hat{H}\right]\right] + \ldots\ , \tag{9.36}$$

where $[\,\cdot\,,\,\cdot\,]_n$ is again the regular commutator nested n times. Unfortunately, we can not evaluate this expression to arbitrary high order exactly, we can get a good approximation though by truncating after the first element of the series. Due to the linearity of the commutator the Hamiltonian in eq. (9.18) can be splitted into three terms and evaluated individually

$$\left[\hat{S},\hat{H}\right] = \left[\hat{S},\hat{H}_{\text{ex}}\right] + \left[\hat{S},\hat{H}_{\text{ph}}\right] + \left[\hat{S},\hat{H}_{\text{c}}\right]\ . \tag{9.37}$$

For the first commutator we can compute[3]

$$\left[\hat{S}, \hat{H}_{\text{ex}}\right] = \sum_{ijI} \left(A_{ijI} - A_{jiI}\right) \hat{c}_i^\dagger \hat{c}_j \left(\hat{b}_I^\dagger - \hat{b}_I\right) \tag{9.38}$$

$$A_{ijI} = \sum_a V_{ia} \Gamma_{ajI} \; . \tag{9.39}$$

Furthermore, the second commutator evaluates to

$$\left[\hat{S}, \hat{H}_{\text{ph}}\right] = -\sum_{ijI} \omega_I \Gamma_{ijI} \hat{c}_i^\dagger \hat{c}_j \left(\hat{b}_I^\dagger + \hat{b}_I\right) \; . \tag{9.40}$$

And finally, the coupling Hamiltonian's commutator looks like

$$\left[\hat{S}, \hat{H}_{\text{c}}\right] = -2 \sum_{ijab} \Omega_{ijab} \, \hat{c}_a^\dagger \hat{c}_b \hat{c}_i^\dagger \hat{c}_j + \sum_{ijIJ} \left(B_{ijIJ} - \sum_b g_{jbI} \Gamma_{ibJ} \right) \hat{c}_i^\dagger \hat{c}_j \left(\hat{b}_I^\dagger + \hat{b}_I\right) \left(\hat{b}_J^\dagger - \hat{b}_J\right) \tag{9.41}$$

$$\Omega_{ijab} = \sum_I g_{ijI} \Gamma_{abI} \tag{9.42}$$

$$B_{ijIJ} = \sum_a g_{iaI} \Gamma_{ajJ} \; . \tag{9.43}$$

By choosing $\Gamma_{ijI} = g_{ijI}/\omega_I$ we can obtain the desired cancellation of the electron-phonon coupling. Furthermore, this makes A and B symmetric in the excitonic indices which induces a cancellation in the commutators of eqs. (9.38) and (9.41). This reduces the total commutator to two terms, i.e.

$$\left[\hat{S}, \hat{H}\right] = -\sum_{ijI} g_{ijI} \, \hat{c}_i^\dagger \hat{c}_j \left(\hat{b}_I^\dagger + \hat{b}_I\right) - 2 \sum_{ijab} \Omega_{ijab} \, \hat{c}_i^\dagger \hat{c}_j \hat{c}_a^\dagger \hat{c}_b \; . \tag{9.44}$$

As mentioned before, we neglect all the higher order commutators in eq. (9.36) and obtain for the transformed Hamiltonian

$$\mathrm{e}^{\hat{S}} \hat{H} \mathrm{e}^{-\hat{S}} \approx \sum_{ij} V_{ij} \, \hat{c}_i^\dagger \hat{c}_j + \sum_I \omega_I \, \hat{b}_I^\dagger \hat{b}_I - 2 \sum_{ijab} \Omega_{ijab} \hat{c}_i^\dagger \, \hat{c}_j \hat{c}_a^\dagger \hat{c}_b \; , \tag{9.45}$$

or equally the back-transformed Hamiltonian

$$\hat{H} \approx \sum_{ij} V_{ij} \, \mathrm{e}^{-\hat{S}} \hat{c}_i^\dagger \hat{c}_j \mathrm{e}^{\hat{S}} + \sum_I \omega_I \, \mathrm{e}^{-\hat{S}} \hat{b}_I^\dagger \hat{b}_I \mathrm{e}^{\hat{S}} - 2 \sum_{ijab} \Omega_{ijab} \mathrm{e}^{-\hat{S}} \hat{c}_i^\dagger \, \hat{c}_j \hat{c}_a^\dagger \hat{c}_b \mathrm{e}^{\hat{S}} \; . \tag{9.46}$$

As our original question was to investigate the effect the phononic system has on the exciton coupling, we will now mainly be interested in the renormalization of the V matrix. The other two terms will induce higher order electron-phonon couplings upon expansion in addition to the vibration energy and the quartic term.

Next we define the vector containing the algebra of excitonic operators $\hat{\mathbf{c}}^\dagger = \left(\hat{c}_{\text{LE1}}^\dagger, \hat{c}_{\text{LE2}}^\dagger, \hat{c}_{\text{CT1}}^\dagger, \hat{c}_{\text{CT2}}^\dagger, \hat{c}_{\text{TT}}^\dagger\right)$ which enables us to write

$$V_{ij} \, \mathrm{e}^{-\hat{S}} \hat{c}_i^\dagger \hat{c}_j \mathrm{e}^{\hat{S}} = \exp\left(-\sum_I \hat{\mathbf{c}}^\dagger \Lambda_I \hat{\mathbf{c}} \left(\hat{b}_I^\dagger - \hat{b}_I\right) \right) V_{ij} \hat{c}_i^\dagger \hat{c}_j \exp\left(\sum_I \hat{\mathbf{c}}^\dagger \Lambda_I \hat{\mathbf{c}} \left(\hat{b}_I^\dagger - \hat{b}_I\right) \right) \; , \tag{9.47}$$

where Λ is a vector of length 76, containing 5×5 matrices. The reason for this quite complicated gymnastics is, that now we can rotate into the eigenbasis of $\Lambda_I = R^\dagger D_I R$ where we checked for all values of the exciton-phonon coupling the positivity of the matrix numerically. Furthermore, the new vectors $\hat{\mathbf{f}}_I^\dagger = \hat{\mathbf{c}} R^\dagger$ get multiplied to the new densities $\hat{\mathbf{f}}_I^\dagger \hat{\mathbf{f}}_I$ whose spectrum is between zero and one, due to the Hilbert space sector we are operating in. As

---

[3] $[A, BC] = [A, B]C + B[A, C]$ and $[AB, C] = A[B, C] + [A, C]B$ tend to be extremely useful identities in all these calculations.

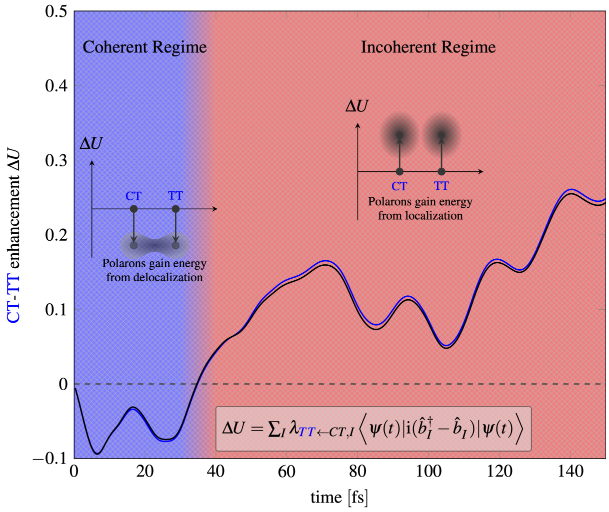

Figure 9.18: Schematic illustration of the coherence mechanism of composite exicton-phonon particles in addition to the enhancement of the CT-TT hopping.

both other elements in the term are strictly positive, the sign of the hopping elements in V is only determined by the action of the exponentials. Therefore, we expand to first order

$$V_{ij}\,\mathsf{e}^{-\hat{S}}\hat{c}_i^\dagger\hat{c}_j\mathsf{e}^{\hat{S}} = \left(1-\hat{S}+\dots\right)\hat{c}_i^\dagger\hat{c}_j\left(1+\hat{S}+\dots\right) = \hat{c}_i^\dagger\hat{c}_j - \hat{S}\hat{c}_i^\dagger\hat{c}_j + \hat{c}_i^\dagger\hat{c}_j\hat{S} + \dots \tag{9.48}$$

$$= \hat{c}_i^\dagger\hat{c}_j + \mathrm{i}\left(\sum_{abI}\Gamma_{abI}\hat{c}_a^\dagger\hat{c}_b\mathrm{i}\left(\hat{b}_I^\dagger-\hat{b}_I\right)\right)\hat{c}_i^\dagger\hat{c}_j - \mathrm{i}\hat{c}_i^\dagger\hat{c}_j\left(\sum_{abI}\Gamma_{abI}\hat{c}_a^\dagger\hat{c}_b\mathrm{i}\left(\hat{b}_I^\dagger-\hat{b}_I\right)\right) + \dots \tag{9.49}$$

$$\underset{N_{\mathrm{ex}}=1}{=} \hat{c}_i^\dagger\hat{c}_j - \mathrm{i}\sum_a\left(\hat{c}_i^\dagger\hat{c}_a\underbrace{\left(\sum_I\Gamma_{jaI}\mathrm{i}\left(\hat{b}_I^\dagger-\hat{b}_I\right)\right)}_{=\Delta\hat{U}_{ja}}\right) + \mathrm{i}\sum_a\left(\hat{c}_a^\dagger\hat{c}_j\underbrace{\left(\sum_I\Gamma_{aiI}\mathrm{i}\left(\hat{b}_I^\dagger-\hat{b}_I\right)\right)}_{\Delta\hat{U}_{ai}}\right) + \dots\,. \tag{9.50}$$

In the last line we have made use of the fact that the system is in the one exciton subspace and defined the excitonic enhancement operator $\Delta\hat{U}$ which is proportional to the momentum operator of the vibration mode $\mathrm{i}\left(\hat{b}^\dagger-\hat{b}\right)$.

By evaluation of expectation values of the enhancement with the time-evolved state $|\psi(t)\rangle$ we can estimate the effect the phonon coupling will have on the excitonic hoppings. Therefore, we have a nice interplay between an approximate analytical result and data which is easily computed from our numerics. If the sign of the enhancement is negative, the energy will be lowered upon delocalization of the effective exciton-phonon particles. Therefore, the particles tend to be in a coherent superposition. If the sign gets positive, the particles will gain energy from localization and therefore tend to remain in one electronic state. The evaluated enhancement over time for the transition of the CT to the TT level is shown in fig. 9.18. Furthermore, the other constituent of the indirect path, i.e. the transition from LE to CT is shown in fig. E.5. As we can clearly see, the coherent and the incoherent regime match with the sign of the CT-TT enhancement. Once the excitonic occupation is transferred to the intermediate charged states, it has to decay due to energetic considerations. As long as the sign of the enhancement is negative, it will preferably do so to the TT state. This enables us to propose the formation of quasi particles and their time-dependent mass as the mechanism behind the coherence time t_0 and determine it to be approximately 35 fs. Interestingly, the renormalization of the transition between LE and CT is almost constant in time and two orders of magnitude smaller than the transition from the charged molecular states.

Conclusion, Summary & Outlook

10

We came a long way during the course of this thesis. We began by explaining the difficulties of quantum many-body problems and why tensor networks are custom tailored for their treatment in 1d to simulate toy models as well as for ab-initio calculations. In order to extend the applicability to systems of higher dimension and even systems without the notion of dimensionality we introduced the concept of TTNS and implemented them in the SyTen toolkit [HLL+]. Despite being loop free, the TTNS is no longer a planar network which leads to the necessity of a special treatment for fermions. Therefore, a framework connecting the order of fermionic legs and operations on them was derived keeping automatic track of the introduced parities. Furthermore, we derived the signs introduced by the most common operators on tensor networks in order to obtain the correct pen and paper results. We found that some operations need extensive care upon implementation and set some guidelines for possible future operations whose implementation might be desired.

We extensively dealt with the question on how to map orbitals "artificially" to a network for most generic cases and explained two blackbox tools in order to do so. An algorithm to change the ordering of a pre-existing network on the fly without regeneration of all constituents was derived. Concluding the setup of our network we introduced fast ways to obtain RDMs by a bookkeeping device splitting up the individual constituents and making reuse of them as often as possible. The speedup was benchmarked to be at least two orders of magnitude in the easiest case. We also explained how to obtain oRDMs in a different basis than the one chosen for the DMRG calculation.

Leaving the field of static wavefunctions we explained the necessity for local methods and introduced the TDVP. The discussion of a generalization for TTNS was discussed and implemented in our toolkit with various sweeping patterns. The domains of use for these patterns were benchmarked. Furthermore, we implemented a real space parallel version of the TDVP speeding up calculations by simultaneously pursuing the local time-evolution of individual orbitals and implemented it in shared and distributed memory. In the course of this implementation, some changes to extend the functionality of tensor operations to GPUs were introduced by means of the CUDA library and its BLAS interface.

We extended the question for orbital order in tensor networks by introducing the notion of fermionic mode transformation, i.e. on the fly successive rotations of the single particle orbitals. This aimed at deriving a black box procedure to reduce the correlation of states during variational optimization procedures. Different possible objectives for this minimization were discussed. An elaboration why the extension to generic bases is difficult was given which lead us to a generic ansatz for the transformation matrix only being bound by requiring unitarity. Since this ansatz increased the number of free parameters in a non-convex optimization process we introduced the automatic differentiation to the tensor network to obtain numerically exact derivates. The derivation of a derivative for the matrix exponential became necessary in this course which we were able to do in a highly elegant way. Finally, we elaborated on the MPO resources growing unpleasantly in both frameworks and stated that future investigations could reactivate this method by finding ways to get this under control. Also, a benchmark for the 2d Fermi-Hubbard model was given.

As the final piece of the tensor network part we dealt with systems going beyond the BO approximation. The derivation of appropriate second quantized Hamiltonians was discussed and we gave an overview to common methods used in this field. Subsequently, we introduced a new method to restore a broken quantum symmetry in tensor networks and deal with large local Hilbert spaces simultaneously. Even though this seems custom tailored to Fermi-Bose mixtures this can even be used for other setups to restore symmetries. The mapping to an MPS was demonstrated and we discussed the issue of automatic truncation via the chosen parameters for the variational optimization. The construction of generic operators in this method was discussed as well. Concluding the theoretical considerations this led us to the application of our framework to real models.

We began by an application of our framework to the 1d Hubbard-Holstein model, one of the easiest models combining spinful electrons and lattice vibrations. The phase diagram was mapped out again highly faithfully since, even though prior investigations had found meaningful phases, they all suffered from some sort of problem. Thereby, we were able to confirm the limits in which one interaction strength dominates, and the metallic region inbetween. However, we also encountered a fascinating new behavior prior unknown which is up to date target of our scientific efforts. We checked for the role that the phonons play in this and investigated the gapless excitations above the ground state, as well as the gaps themselves.

Finally, we discussed the main goal of this thesis, i.e. simulating a large molecule ab-initio. For this two cases were chosen, first, a rather small calculation on pyrazine and second, a highly demanding first principles calculation of singlet fission (SF) in the tetracene para-dimer. Even though our focus was on the numerical control and accuracy, in the case of the pyrazine, we were still able to derive some interesting physics from it and do a thermodynamic approach. This mainly revealed classical dynamics. For the tetracene para-dimer the situation was significantly different. We initially began by introducing the reason for the current scientific interest in SF, namely, the theoretical limitation to which materials can be used for photo-absorption, the Shockley-Queisser limit, and the believe that this can be overcome by SF. This was followed by an quasi-exact coupling of five low lying diabatic modes to a high number of phononic modes and the subsequent numerically exact time-evolution. A comparison to the experimental absorption spectrum indicated the high faithfulness of our calculation. Furthermore, we clarified which phononic modes are driving the energy transfer between the systems. In an attempt to change the electronic yield after photo-absorption we started investigating the dependency of the solvent polarity as an experimentally tuneable parameter. Not only did we again find excellent agreement to experiment, but also we were able to make statements about which solvents are beneficial to our cause. As all solvents tested obtained a characteristic pattern we looked into the electronic RDM which revealed that the coherence of the diabatic states is responsible for this. Last but not least, we combined approximate analytical and numerical tools in order to explain the origin of this behavior and attributed it to quasi particle formation. These quasi particles change their delocalization behavior exactly at the characteristic time scale which could then be determined by us to high accuracy.

So far regarding what we have done, but where do we go from here? The framework derived by our tensor networks is highly powerful and enables us to extrapolate microscopic degrees of freedom to a macroscopic system for many occasions. Even though it is not a black box procedure to derive generic solutions for quantum properties of materials, there is still much to explore. We firmly believe, that we can continue to systematically investigate organic molecules in the vicinity of lattice vibrations by these tools. By tuning the experimental parameters but also by going to more realistic setups like finite temperature and larger complexes, these systematics can be extended even further. Certainly, the best case would be to describe realizable setups in which the efficiency of organic semi-conductors could be increased. We have started to describe the benefits of other tensor network topologies but there is much more to explore and maybe even a combination with other techniques can be achieved. In the course of this it might get necessary to introduce new computational models, even though, the increase of computational resources is still showing an impressive exponential growth, the resources can be taken more non-locally. Also, looking further into the direction of GPUs and into the current developements of TPUs (which we did not deal with in the course of this work at all) might be useful for this cause. Although these might seem like purely technical issues, they might be the key ingredients to obtaining the extrapolation from microscopic degrees of freedom to macroscopic systems which we originally targeted. We do share the believe, that these methods are not custom tailored but rather brute force, and there might exist solutions which are much more beautiful or elegant. But for the time being it is worth trying to obtain results in both directions, since a result in itself is not dependent on the beauty of its derivation. In conclusion, we are confident it is a highly interesting time to be involved in science and there is still substantial room for discovery.

Appendix

Mode transformation application scheme

A

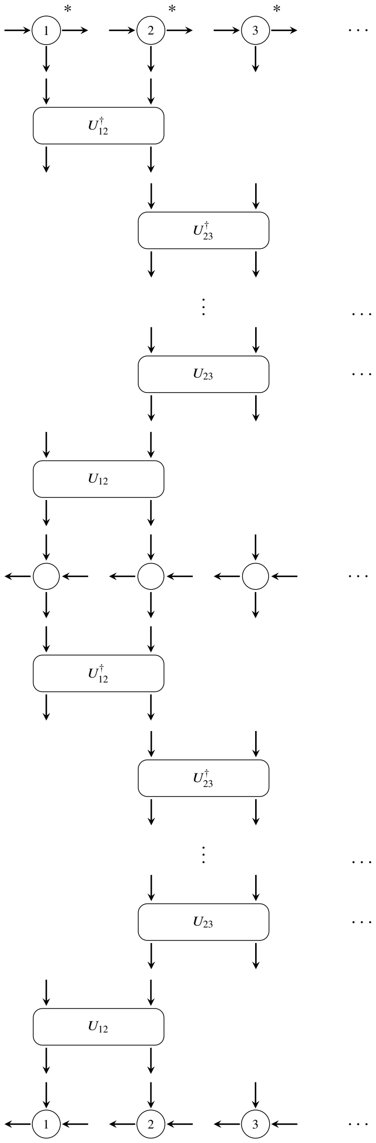

Figure A.1: Application scheme for the twosite gates in mode transformation. We subsequently apply two-site gates to the state and the operator in such a way that adjacent legs overlap. This way we introduce a global rotation in both the state and the operator.

Automatic differentiation compute graph

B

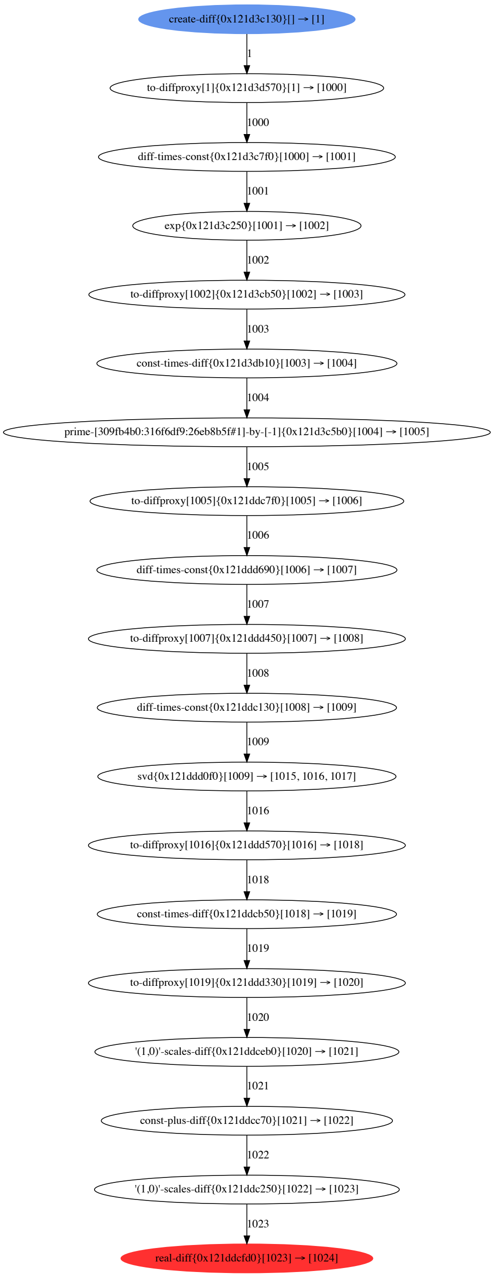

Figure B.2: Compute graph of the cost function in eq. (6.31) by the application scheme explained in section 6.2 and section 6.2.1.

Spectral densities and thermal fluctuations of the tetracene para-dimer

C

(a)

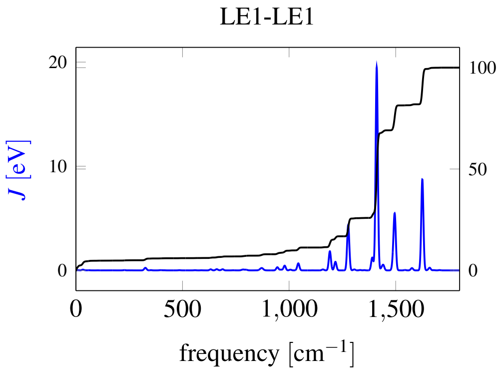

(b)

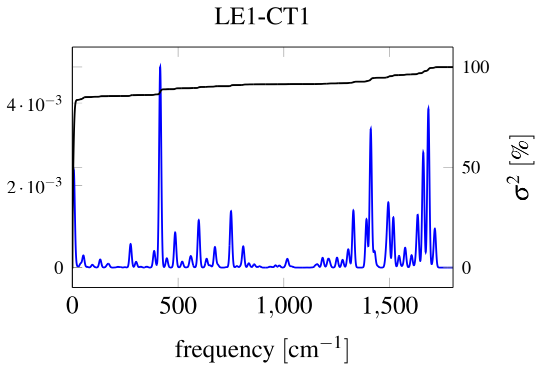

(c)

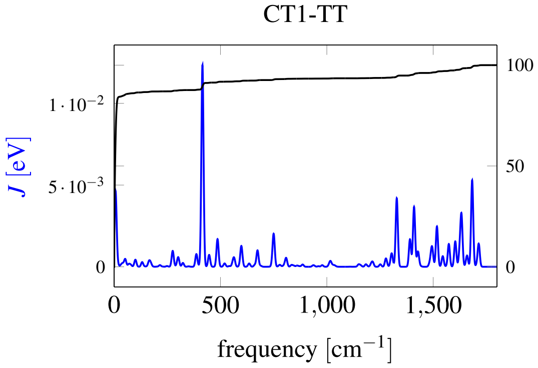

(d)

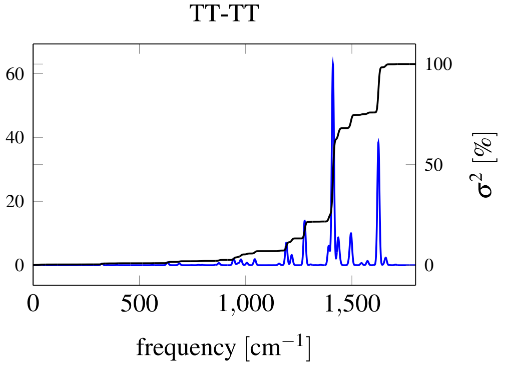

(e)

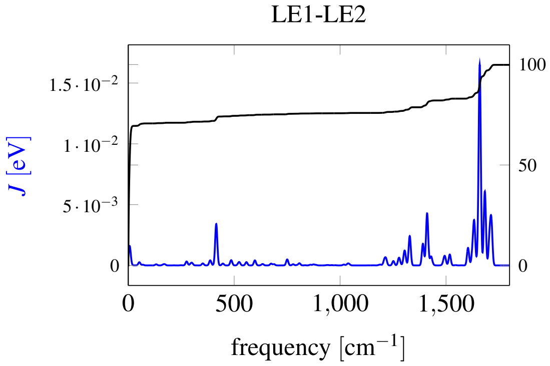

(f)

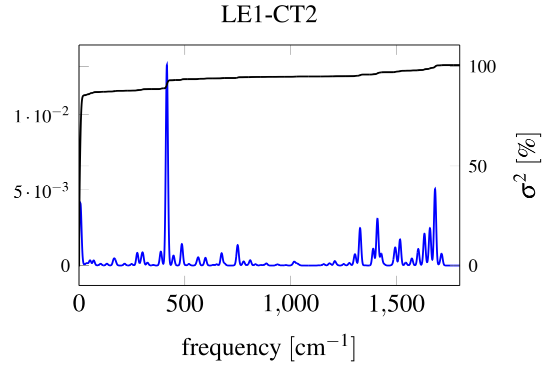

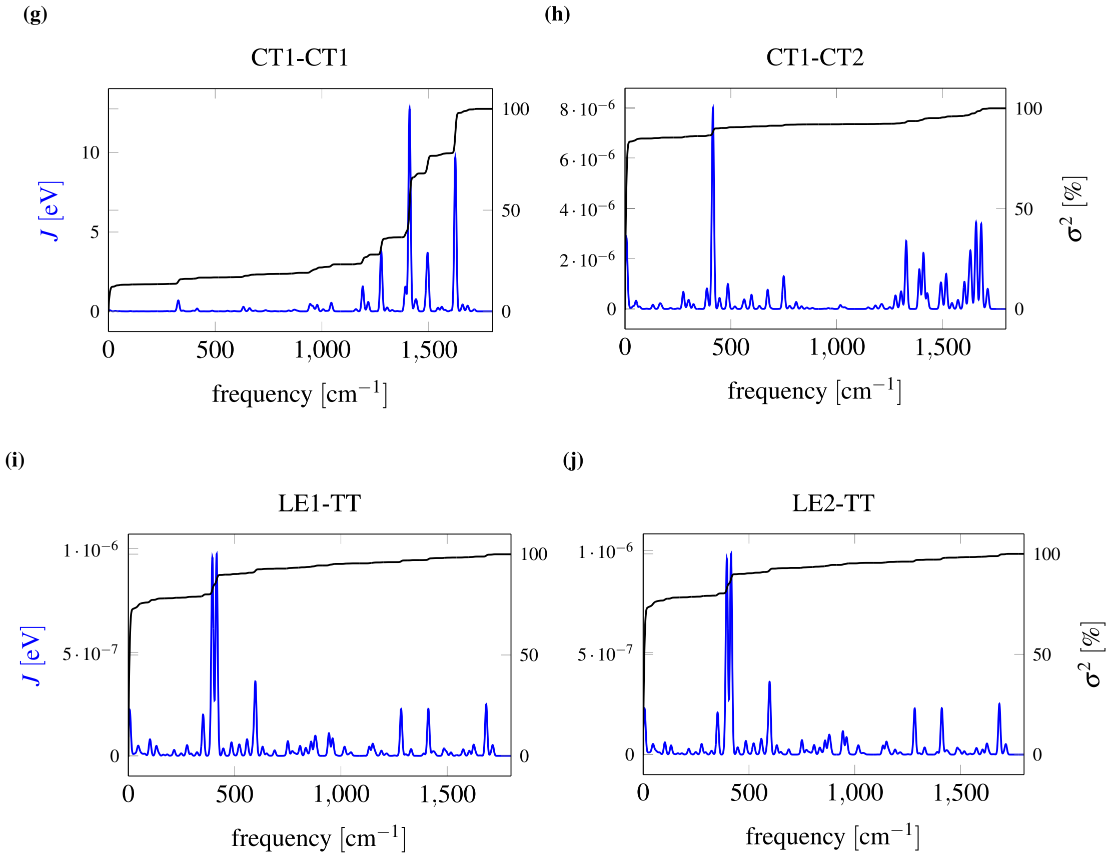

Figure C.3: Spectral densities computed for the tetracene para-dimer from eq. (9.20). The left axis shows the spectral density of the individual phononic modes for different diagonal and off-diagonal excitonic couplings. The right axis shows the relative fluctuation at room temperature to table 9.1 which indicates that the incorporation of temperature for the tetracene para-dimer is not necessary.

D

Illustration of the vibrational modes of the tetracene para-dimer

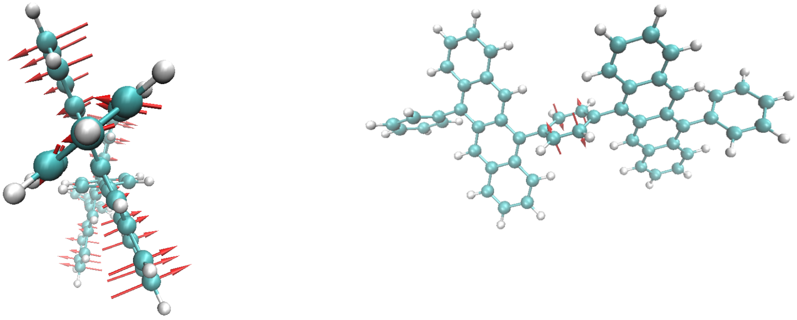

(a) Mode no. 1 (6.7 cm^{-1})

(b) Mode no. 45 (415.0 cm^{-1})

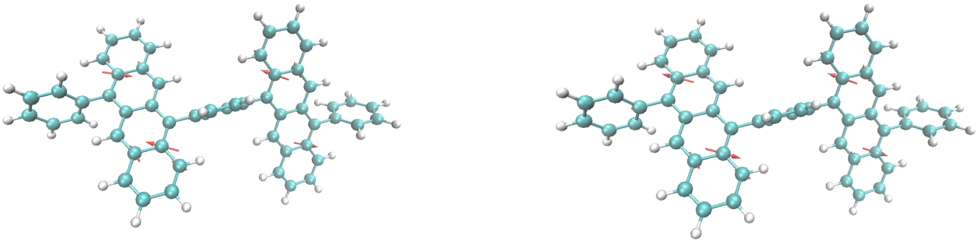

(c) Mode no. 167 (1277.0 cm^{-1})

(d) Mode no. 168 (1277.7 cm^{-1})

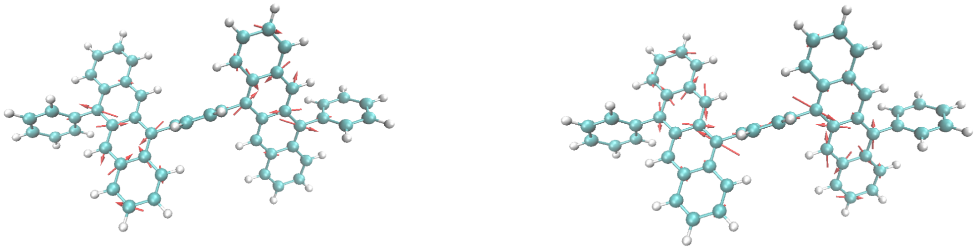

(e) Mode no. 184 (1409.6 cm^{-1})

(f) Mode no. 185 (1411.2 cm^{-1})

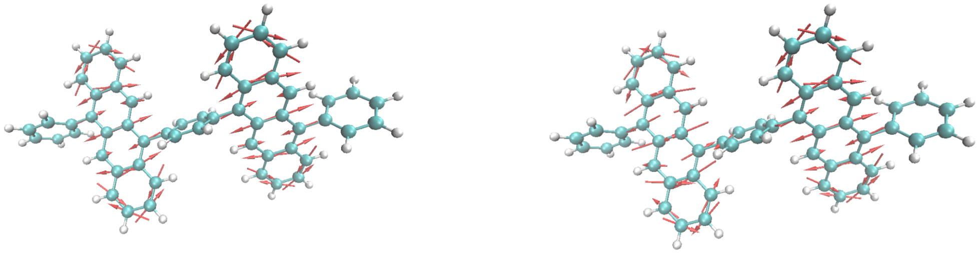

(g) Mode no. 210 (1624.9 cm^{-1})

(h) Mode no. 211 (1625.4 cm^{-1})

Figure D.4: Graphical depiction of the most import vibrational modes of the tetracene para-dimer.

Enhancement of excitonic Hamiltonian for the tetracene para-dimer

E

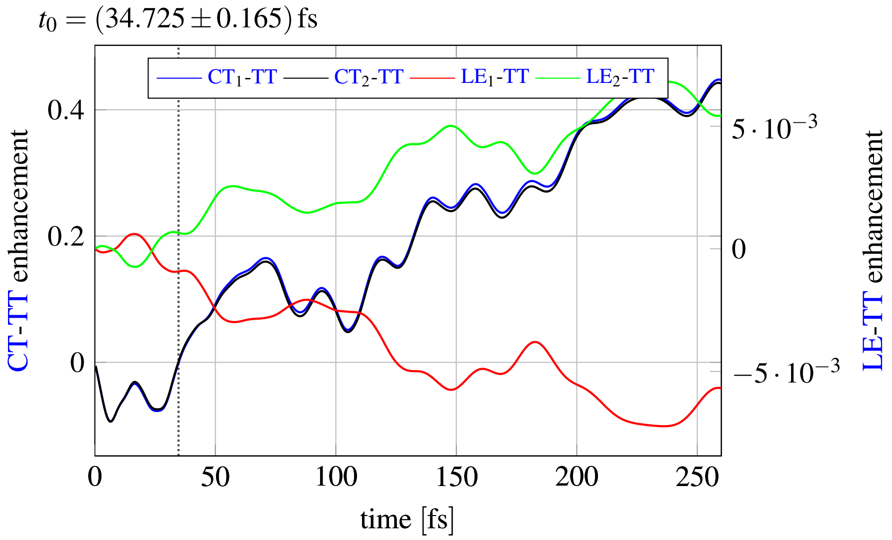

Figure E.5: Enhancement for the constituents of the indirect path, i.e. LE→CT→TT over time. The LE-CT enhancement is drawn on the right axis while the CT-TT one is one the left axis.

Symbols

$\mathcal{H}$ context dependent Hilbert space $\mathcal{H}$.

$\hat{1}$ identity matrix, $\hat{1} = \mathrm{diag}\,[1, 1, \ldots, 1]$.

$\hat{c}$ fermionic annihilation operator, $|0\rangle = \hat{c}_k\,|k\rangle$.

$\hat{b}$ bosonic annihilation operator, $|0\rangle = \hat{b}_k\,|k\rangle$.

$\hat{b}^\dagger$ bosonic creation operator, $|k\rangle = \hat{b}_k^\dagger\,|0\rangle$.

$\mathbb{C}$ complex valued vector space $\mathbb{C}$.

$\hat{c}^\dagger$ fermionic creation operator, $|k\rangle = \hat{c}_k^\dagger\,|0\rangle$.

e Euler's number, $\mathsf{e} = \lim\limits_{n\to\infty} (1 + {}^{1}\!/\!{}_{n})^n$.

i imaginary unit, $\mathsf{i}^2 = -1$.

n_{ph} Total number of truncated phonons, $0 \leq n \leq n_{\mathrm{ph}}$.

$\mathbb{R}$ real valued vector space $\mathbb{R}$.

Abbreviations

1d one-dimensional.

2d two-dimensional.

AD automatic differentiation.

AFM antiferromagnet.

BCH Baker-Campbell-Hausdorff formula.

BCS Bardeen-Cooper-Schrieffer theory.

BFGS2 Broyden-Fletcher-Goldfarb-Shanno algorithm.

BLAS Basic Linear Algebra Subprograms.

BO approximation Born-Oppenheimer approximation.

BTT binary tensor tree.

CAS-SCF complete active space self-consistent field.

CASCI complete active space configuration interaction.

CDW charge density wave.

CFT conformal field theory.

CGC Clebsch-Gordon coefficient.

CPU central processing unit.

CT charge transfer.

CUDA Compute Unified Device Architecture.

DFT density functional theory.

DMFT dynamical mean-field theory.

DMRG density matrix renormalization group.

ED exact diagonalization.

GPU graphics processing unit.

HF Hartree Fock.

HOMO highest occupied molecular orbital.

HPC high-performance computing.

irrep irreducible representation.
iSF intramolecular singlet fission.

LBO local basis optimization.
LCAO linear combination of atomic orbitals.
LE locally excited.
LUMO lowest unoccupied molecular orbital.

MCTDH multi-configurational time-dependent Hartree.
MEG multiple exciton generation.
MPI message passing interface.
MPO matrix product operator.
MPS matrix product state.

NO natural orbital.
NP-hard non-deterministic polynomial-time hard.
NRG numerical renormalization group.

open MP open multi-processing.
oRDM orbital reduced density matrix.

PEPS projected entangled pair state.
PES potential energy surface.
PP projected purification.
pRDM particle reduced density matrix.

QR QR.

RAM random-access memory.
RDM reduced density matrix.
RG renormalization group.

SA-CASSCF state averaged complete active space self consistent field.
SDW spin density wave.
SF singlet fission.
SSO single-site operator.
SVD singular value decomposition.

T3NO three-legged tree tensor network operator.
T3NS three-legged tree tensor network state.

TDVP time-dependent variational principle.

TEBD time-evolving block decimation.

tetracene para-dimer 1,4-bis(11-phenyltetracen-5-yl)benzene.

TPU tensor processing unit.

TT triplet pair.

TTNS tree tensor network state.

UHF unrestricted Hartee Fock.

UV ultraviolet.

xSF intermolecular singlet fission.

List of Figures

List of Tables

List of Algorithms

Acknowledgments

Nanos gigantum humeris insidentes — While we often highlight the contribution of previous generations of scientists we tend to forget about the people around us. Pursuing this work I often had the impression I stood on the shoulders of the people around me. Without their crucial aid, I could have never achieved this. Therefore, let me thank in particular. . .

. . . **Ulrich Schollwöck** for offering me the opportunity to do research, joining his group, always having an open ear and being an overall nice supervisor who always was in for a laugh.

. . . **Christian Ochsenfeld** for examining this thesis and being part of my committee.

. . . **Monika Aidelsburger**, **Micheal Haack**, **Torsten Enßlin** and **Otmar Biebel** for being part of my comittee.

. . . **Martin Grundner** for being a really nice colleague and becoming a good friend, working together for several years, sharing an office, a lot of fun conferences and proof reading this thesis.

. . . **Max Bramberger** for being a really nice colleague and friend, an extraordinary, yet humble physicists, working together for several years and for proof reading this thesis. And importantly, for the pen and paper game night he promised to organise at some point.

. . . **Sebastian Paeckel** for not only being the greatest supervisor anyone could wish for, but also a great colleague and friend who I already miss working with. Furthermore, for sharing my interest in history and always engaging in heated discussions.

. . . **Claudius Hubig** for all the stuff he taught me and for all the discussion we had.

. . . **Tobias Pfeffer** for teaching me countless things, most importantly being humble and a lot about how the business works, and for sharing an office with me. And for, after all, explaining me how things are supposed to be.

. . . **Nils-Oliver Linden** for being a nice colleague, teaching me a lot and always having a funny story to tell to entertain us in the office.

. . . **Adrian Kantian** for all the discussion we had, his endless patience, being a highly pleasant person and all the stuff he taught us during the genesis of various projects.

. . . **Thomas Köhler** for being a great colleague, teaching me a lot of stuff, always having an open ear and the great dinner he cooked for us in Chicago.

. . . **Tuomas Vanhalla** for sharing an office with me and the fun times and lunchbreaks we had.

. . . **Carlos Parra** for being a fun guy and friend, teaching me "un poco de español" and for introducing me to latin-american literature, which got me immediately addicted.

. . . **Örs Legeza** and **Michi Màté** for always making us feel welcome in Budapest and for all the great ideas we shared.

. . . **Roman Faber** for proof reading this thesis and giving a lot of helpful advice.

. . . **Lode Pollet** for being a really funny guy who always entertained us with good stories during coffee breaks.

. . . **Dario Hügel** and **Sebastian Schulteß** for being my original office mates, showing me around and making me feel welcome at the chair.

. . . **Lexin Ding** for being a really nice guy, who working with was a pleasure.

… **Haibo Ma**, **Zhen Luo**, **Xiaoyu Xie** and **Yihe Xu** for being nice colleagues, explaining me a lot about chemistry and the great projects we did together.

… **Felix Palm** for being a friend and a great colleague, often having good advice and for sharing my interest in bible anthropology. Furthermore, for teaching me much about Hall physics, proof reading this thesis and hopefully for more opera visits yet to come in the future.

… **Stefan Wittlinger** and **Thadeus Alcock** for being great office mates and having a lot of fun discussions.

… **Mattia Moroder** for being a really nice colleague, sharing an office with me and making a lot of good mafia jokes.

… the **IT group** of the Arnold-Sommerfeld Center and in particular **Ralph Simmler**, **Veronika Finsterwalder**, **Kalle Bamberg** and **Robert Redl** for saving me/all of us more than once with their help.

… **el Patrón** for letting me use his hacienda.

… **Andreas Swoboda**, **Ines de Vega**, **Leo Stenzel**, **Ke Liu**, **Nihal Rao**, **Julia Liebert**, **Chia-Min Chung**, **Nader Moostan**, **Henning Schlömer**, **Sreetama Das**, **Matjaz Kebric**, **Tizian Blatz**, **Lukas Homeier**, **Rajah Nutakki**, **Jonas Greitemann**, **Max Buser**, **Héloïse Albot**, **Fabian Grusdt** and **and all other members of the chair** for being great colleagues, creating a welcoming atmosphere and all the fun lunch breaks together.

… **Cordula Weber** for being a wonderful colleague, always having an open door for everyone and for saving me more than once.

… **my family** for providing me the crucial support through all these years and always being there for me. Especially, my **father** for everything he did and my sister **Sara** for proof reading this thesis twice and leaving hilariously funny comments.

… **Bianca** for so many things I can honestly not count them, among them being a caring, forgiving and selfless spouse during the last decade to whom I owe more than I could ever repay.

References in Alphabetical Order of Labels

[ABH98] Jonathan E. Atkins, Erik G. Boman, and Bruce Hendrickson. A spectral algorithm for seriation and the consecutive ones problem. *SIAM Journal on Computing*, 28(1):297–310, 1998.

[AdP06] Peter Atkins and Julio de Paula. *Physical Chemistry*. Oxford University Press, eighth edition, 2006.

[AM07] Adolfo Avella and Ferdinando Mancini. Underdoped cuprate phenomenology in the two-dimensional hubbard model within the composite operator method. *Phys. Rev. B*, 75:134518, Apr 2007.

[And72] P. W. Anderson. More is different. *Science*, 177(4047):393–396, 1972.

[And87] P. W. Anderson. The resonating valence bond state in la¡sub¿2¡/sub¿cuo¡sub¿4¡/sub¿ and superconductivity. *Science*, 235(4793):1196–1198, 1987.

[ASD15] Ethan C. Alguire, Joseph E. Subotnik, and Niels H. Damrauer. Exploring non-condon effects in a covalent tetracene dimer: How important are vibrations in determining the electronic coupling for singlet fission? *The Journal of Physical Chemistry A*, 119(2):299–311, 2015. PMID: 25522781.

[Ash68] N. W. Ashcroft. Metallic hydrogen: A high-temperature superconductor? *Phys. Rev. Lett.*, 21:1748–1749, Dec 1968.

[BA20] Daniel Bauernfeind and Markus Aichhorn. Time Dependent Variational Principle for Tree Tensor Networks. *SciPost Phys.*, 8:24, 2020.

[Bak01] H. F. Baker. Further applications of metrix notation to integration problems. *Proceedings of the London Mathematical Society*, s1-34(1):347–360, 1901.

[BC05] H. M. Bücker and G. F. Corliss. A bibliography on automatic differentiation. In H. M. Bücker, G. F. Corliss, P. D. Hovland, U. Naumann, and B. Norris, editors, *Automatic Differentiation: Applications, Theory, and Implementations*, volume 50 of *Lecture Notes in Computational Science and Engineering*, pages 321–322. Springer, New York, NY, 2005.

[BCC$^+$19] Mari Carmen Banuls, Krzysztof Cichy, J. Ignacio Cirac, Karl Jansen, and Stefan Kühn. Tensor Networks and their use for Lattice Gauge Theories. *PoS*, LATTICE2018:022, 2019.

[BCS57a] J. Bardeen, L. N. Cooper, and J. R. Schrieffer. Microscopic theory of superconductivity. *Phys. Rev.*, 106:162–164, Apr 1957.

[BCS57b] J. Bardeen, L. N. Cooper, and J. R. Schrieffer. Theory of superconductivity. *Phys. Rev.*, 108:1175–1204, Dec 1957.

[BDV$^+$15] C. Brockt, F. Dorfner, L. Vidmar, F. Heidrich-Meisner, and E. Jeckelmann. Matrix-product-state method with a dynamical local basis optimization for bosonic systems out of equilibrium. *Phys. Rev. B*, 92(24):241106, Dec 2015.

[BDZ08] Immanuel Bloch, Jean Dalibard, and Wilhelm Zwerger. Many-body physics with ultracold gases. *Rev. Mod. Phys.*, 80:885–964, Jul 2008.

[BG] Raffaele Borrelli and Maxim F. Gelin. Finite temperature quantum dynamics of complex systems: Integrating thermo-field theories and tensor-train methods. *WIREs Computational Molecular Science*, n/a(n/a):e1539.

[BG17] Raffaele Borrelli and Maxim F. Gelin. Simulation of quantum dynamics of excitonic systems at finite temperature: an efficient method based on thermo field dynamics. *Scientific Reports*, 7(1):9127, 2017.

[BHR13a] Timothy C. Berkelbach, Mark S. Hybertsen, and David R. Reichman. Microscopic theory of singlet exciton fission. i. general formulation. *J. Chem. Phys.*, 138(11):114102, 2013.

[BHR13b] Timothy C. Berkelbach, Mark S. Hybertsen, and David R. Reichman. Microscopic theory of singlet exciton fission. ii. application to pentacene dimers and the role of superexchange. *J. Chem. Phys.*, 138(11):114103, 2013.

[BHR14] Timothy C. Berkelbach, Mark S. Hybertsen, and David R. Reichman. Microscopic theory of singlet exciton fission. iii. crystalline pentacene. *The Journal of Chemical Physics*, 141(7):074705, 2014.

[BHVA$^+$14] Boye Buyens, Jutho Haegeman, Karel Van Acoleyen, Henri Verschelde, and Frank Verstraete. Matrix product states for gauge field theories. *Phys. Rev. Lett.*, 113:091601, Aug 2014.

[BK02] Sergey B. Bravyi and Alexei Yu. Kitaev. Fermionic quantum computation. *Annals of Physics*, 298(1):210–226, 2002.

[BKK18] Stefano Battaglia, Sebastian Keller, and Stefan Knecht. Efficient relativistic density-matrix renormalization group implementation in a matrix-product formulation. *Journal of Chemical Theory and Computation*, 14(5):2353–2369, 2018. PMID: 29558618.

[BKP$^+$22] Gunnar Bollmark, Thomas Köhler, Lorenzo Pizzino, Yiqi Yang, Johannes-Stephan Hofmann, Hao Shi, Shiwei Zhang, Thierry Giamarchi, and Adrian Kantian. Solving 2d and 3d lattice models of correlated fermions - combining matrix product states with mean field theory. In preparation, March 2022.

[BLMR11] G. Barcza, Ö. Legeza, K. H. Marti, and M. Reiher. Quantum-information analysis of electronic states of different molecular structures. *Phys. Rev. A*, 83:012508, Jan 2011.

[BM86] J. G. Bednorz and K. A. Müller. Possible high tc superconductivity in the ba-la-cu-o system. *Zeitschrift für Physik B Condensed Matter*, 64(2):189–193, 1986.

[BMG$^+$21] Max Bramberger, Jernej Mravlje, Martin Grundner, Ulrich Schollwöck, and Manuel Zingl. baoso$_3$: A hund's metal in the presence of strong spin-orbit coupling. *Phys. Rev. B*, 103:165133, Apr 2021.

[BMK$^+$16] Artem A. Bakulin, Sarah E. Morgan, Tom B. Kehoe, Mark W. B. Wilson, Alex W. Chin, Donatas Zigmantas, Dassia Egorova, and Akshay Rao. Real-time observation of multiexcitonic states in ultrafast singlet fission using coherent 2d electronic spectroscopy. *Nat. Chem.*, 8(1):16–23, 2016.

[BO27] M. Born and R. Oppenheimer. Zur quantentheorie der molekeln. *Annalen der Physik*, 389(20):457–484, 1927.

[BPE09] Thomas Barthel, Carlos Pineda, and Jens Eisert. Contraction of fermionic operator circuits and the simulation of strongly correlated fermions. *Phys. Rev. A*, 80:042333, Oct 2009.

[BPK74] G. Beni, P. Pincus, and J. Kanamori. Low-temperature properties of the one-dimensional polaron band. i. extreme-band-narrowing regime. *Phys. Rev. B*, 10:1896–1901, Sep 1974.

[BR19] Alberto Baiardi and Markus Reiher. Large-scale quantum dynamics with matrix product states. *Journal of Chemical Theory and Computation*, 15(6):3481–3498, 2019. PMID: 31067052.

[BR20] Alberto Baiardi and Markus Reiher. The density matrix renormalization group in chemistry and molecular physics: Recent developments and new challenges. *The Journal of Chemical Physics*, 152(4):040903, 2020.

[Bra20] Max Bramberger. Private communications. Jan 2020.

[BSOG04] Stanimir A. Bonev, Eric Schwegler, Tadashi Ogitsu, and Giulia Galli. A quantum fluid of metallic hydrogen suggested by first-principles calculations. *Nature*, 431(7009):669–672, 2004.

[BTB$^+$13] Katharina Boguslawski, Pawe l Tecmer, Gergely Barcza, Örs Legeza, and Markus Reiher. Orbital entanglement in bond-formation processes. *Journal of Chemical Theory and Computation*, 9(7):2959–2973, 2013. PMID: 26583979.

[BVV$^+$20] Jan Brandejs, Jakub Višňák, Libor Veis, Mihály Maté, Örs Legeza, and Jiří Pittner. Toward dmrg-tailored coupled cluster method in the 4c-relativistic domain. *The Journal of Chemical Physics*, 152(17):174107, 2020.

[BWHV17] Nick Bultinck, Dominic J. Williamson, Jutho Haegeman, and Frank Verstraete. Fermionic matrix product states and one-dimensional topological phases. *Phys. Rev. B*, 95:075108, Feb 2017.

[BXW$^+$15] Erik Busby, Jianlong Xia, Qin Wu, Jonathan Z. Low, Rui Song, John R. Miller, X. Y. Zhu, Luis M Campos, and Matthew Y. Sfeir. A design strategy for intramolecular singlet fission mediated by charge-transfer states in donor–acceptor organic materials. *Nat. Mater.*, 14(4):426–433, 2015.

[Cam97] J. E. Campbell. On a law of combination of operators (second paper)*. *Proceedings of the London Mathematical Society*, s1-29(1):14–32, 1897.

[Car24] Sadi Carnot. *Réflexions sur la puissance motrice du feu et sur les machines propres à développer cette puissance*. 1824.

[Cas18] David Casanova. Theoretical modeling of singlet fission. *Chem. Rev.*, 118(15):7164–7207, 2018. PMID: 29648797.

[CB84] Laurent G. Caron and Claude Bourbonnais. Two-cutoff renormalization and quantum versus classical aspects for the one-dimensional electron-phonon system. *Phys. Rev. B*, 29:4230–4241, Apr 1984.

[CBP$^+$13] Wai-Lun Chan, Timothy C. Berkelbach, Makenzie R. Provorse, Nicholas R. Monahan, John R. Tritsch, Mark S. Hybertsen, David R. Reichman, Jiali Gao, and X.-Y. Zhu. The quantum coherent mechanism for singlet fission: Experiment and theory. *Acc. Chem. Res.*, 46(6):1321–1329, 2013. PMID: 23581494.

[CC04] Pasquale Calabrese and John Cardy. Entanglement entropy and quantum field theory. *Journal of Statistical Mechanics: Theory and Experiment*, 2004(06):P06002, jun 2004.

[CC05] Pasquale Calabrese and John Cardy. Evolution of entanglement entropy in one-dimensional systems. 2005(04):P04010, apr 2005.

[CDS19] N. R. Cooper, J. Dalibard, and I. B. Spielman. Topological bands for ultracold atoms. *Rev. Mod. Phys.*, 91:015005, Mar 2019.

[CEP07] M. Cramer, J. Eisert, and M. B. Plenio. Statistics dependence of the entanglement entropy. *Phys. Rev. Lett.*, 98:220603, May 2007.

[CFP54] D. M. Chapin, C. S. Fuller, and G. L. Pearson. A new silicon p-n junction photocell for converting solar radiation into electrical power. *Journal of Applied Physics*, 25(5):676–677, 1954.

[CHH$^+$22] Dian-Teng Chen, Phillip Helms, Ashlyn R. Hale, Minseong Lee, Chenghan Li, Johnnie Gray, George Christou, Vivien S. Zapf, Garnet Kin-Lic Chan, and Hai-Ping Cheng. Using hyperoptimized tensor networks and first-principles electronic structure to simulate the experimental properties of the giant Mn84 torus. *The Journal of Physical Chemistry Letters*, 13(10):2365–2370, 2022. PMID: 35254080.

[CKG04] Garnet Kin-Lic Chan, Mihály Kállay, and Jürgen Gauss. State-of-the-art density matrix renormalization group and coupled cluster theory studies of the nitrogen binding curve. *The Journal of Chemical Physics*, 121(13):6110–6116, 2004.

[CKN$^+$16] Garnet Kin-Lic Chan, Anna Keselman, Naoki Nakatani, Zhendong Li, and Steven R. White. Matrix product operators, matrix product states, and ab initio density matrix renormalization group algorithms. *The Journal of Chemical Physics*, 145(1):014102, 2016.

[Cla50] R. Clausius. Ueber die bewegende kraft der wärme und die gesetze, welche sich daraus für die wärmelehre selbst ableiten lassen. *Annalen der Physik*, 155(4):500–524, 1850.

[Cla54] R. Clausius. Ueber eine veränderte form des zweiten hauptsatzes der mechanischen wärmetheorie. *Annalen der Physik*, 169(12):481–506, 1854.

[CLJ$^+$11] Wai-Lun Chan, Manuel Ligges, Askat Jailaubekov, Loren Kaake, Luis Miaja-Avila, and X.-Y. Zhu. Observing the multiexciton state in singlet fission and ensuing ultrafast multielectron transfer. *Science*, 334(6062):1541–1545, 2011.

[CLT$^+$13] Daniel N. Congreve, Jiye Lee, Nicholas J. Thompson, Eric Hontz, Shane R. Yost, Philip D. Reusswig, Matthias E. Bahlke, Sebastian Reineke, Troy Van Voorhis, and Marc A. Baldo. External quantum efficiency above 100% in a singlet-exciton-fission–based organic photovoltaic cell. *Science*, 340(6130):334–337, 2013.

[CM02] M. A. Cazalilla and J. B. Marston. Time-dependent density-matrix renormalization group: A systematic method for the study of quantum many-body out-of-equilibrium systems. *Phys. Rev. Lett.*, 88:256403, Jun 2002.

[COBV10] Philippe Corboz, Román Orús, Bela Bauer, and Guifré Vidal. Simulation of strongly correlated fermions in two spatial dimensions with fermionic projected entangled-pair states. *Phys. Rev. B*, 81:165104, Apr 2010.

[Coo56] Leon N. Cooper. Bound electron pairs in a degenerate fermi gas. *Phys. Rev.*, 104:1189–1190, Nov 1956.

[Coo15] James S. Cook. Mathematics stack exchange, May 2015.

[CS11] Garnet Kin-Lic Chan and Sandeep Sharma. The density matrix renormalization group in quantum chemistry. *Annual Review of Physical Chemistry*, 62(1):465–481, 2011. PMID: 21219144.

[CSYS20] Natanael C. Costa, Kazuhiro Seki, Seiji Yunoki, and Sandro Sorella. Phase diagram of the two-dimensional hubbard-holstein model. *Communications Physics*, 3(1):80, 2020.

[Dag94] Elbio Dagotto. Correlated electrons in high-temperature superconductors. *Rev. Mod. Phys.*, 66:763–840, Jul 1994.

[Deu18] Joshua M Deutsch. Eigenstate thermalization hypothesis. *Reports on Progress in Physics*, 81(8):082001, jul 2018.

[Dir29] Paul Adrien Maurice Dirac. Quantum mechanics of many-electron systems. *Proceedings of the Royal Society of London. Series A*, 123(792), 1929.

[Dir30] P. A. M. Dirac. Note on exchange phenomena in the thomas atom. *Mathematical Proceedings of the Cambridge Philosophical Society*, 26(3):376–385, 1930.

[DMD+21] Lexin Ding, Sam Mardazad, Sreetama Das, Szilárd Szalay, Ulrich Schollwöck, Zoltán Zimborás, and Christian Schilling. Concept of Orbital Entanglement and Correlation in Quantum Chemistry. *Journal of Chemical Theory and Computation*, 17(1):79–95, 2021. PMID: 33430597.

[DMDNS98] J Dukelsky, M. A Martín-Delgado, T Nishino, and G Sierra. Equivalence of the variational matrix product method and the density matrix renormalization group applied to spin chains. *Europhysics Letters (EPL)*, 43(4):457–462, aug 1998.

[DMS12] Stefan Depenbrock, Ian P. McCulloch, and Ulrich Schollwöck. Nature of the spin-liquid ground state of the $s = 1/2$ heisenberg model on the kagome lattice. *Phys. Rev. Lett.*, 109:067201, Aug 2012.

[dVSW15] Inés de Vega, Ulrich Schollwöck, and F. Alexander Wolf. How to discretize a quantum bath for real-time evolution. *Phys. Rev. B*, 92:155126, Oct 2015.

[Dys49] F. J. Dyson. The radiation theories of tomonaga, schwinger, and feynman. *Phys. Rev.*, 75:486–502, Feb 1949.

[EBJ+05] Randy J. Ellingson, Matthew C. Beard, Justin C. Johnson, Pingrong Yu, Olga I. Micic, Arthur J. Nozik, Andrew Shabaev, and Alexander L. Efros. Highly efficient multiple exciton generation in colloidal pbse and pbs quantum dots. *Nano Letters*, 5(5):865–871, 2005. PMID: 15884885.

[Eck30] Carl Eckart. The application of group theory to the quantum dynamics of monatomic systems. *Rev. Mod. Phys.*, 2:305–380, Jul 1930.

[Ein05] A. Einstein. Über einen die erzeugung und verwandlung des lichtes betreffenden heuristischen gesichtspunkt. *Annalen der Physik*, 322(6):132–148, 1905.

[ETDW03] Dassia Egorova, Michael Thoss, Wolfgang Domcke, and Haobin Wang. Modeling of ultrafast electron-transfer processes: Validity of multilevel redfield theory. *J. Chem. Phys.*, 119(5):2761–2773, 2003.

[EWN17] G. Ehlers, S. R. White, and R. M. Noack. Hybrid-space density matrix renormalization group study of the doped two-dimensional hubbard model. *Phys. Rev. B*, 95:125125, Mar 2017.

[FGL21] Gero Friesecke, Benedikt R. Graswald, and Örs Legeza. Exact matrix product state representation and convergence of a fully correlated electronic wavefunction in the infinite basis limit, 2021.

[Fie73] Miroslav Fiedler. Algebraic connectivity of graphs. *Czechoslovak Mathematical Journal*, 23(2):298–305, 1973.

[Fie89] Miroslav Fiedler. Laplacian of graphs and algebraic connectivity. *Banach Center Publications*, 25(1):57–70, 1989.

[FK90] Holger Frahm and V. E. Korepin. Critical exponents for the one-dimensional hubbard model. *Phys. Rev. B*, 42:10553–10565, Dec 1990.

[FML+19] Fabian M. Faulstich, Mihály Máté, Andre Laestadius, Mihály András Csirik, Libor Veis, Andrej Antalik, Jiří Brabec, Reinhold Schneider, Jiří Pittner, Simen Kvaal, and Örs Legeza. Numerical and theoretical aspects of the dmrg-tcc method exemplified by the nitrogen dimer. *Journal of Chemical Theory and Computation*, 15(4):2206–2220, 2019. PMID: 30802406.

[Foc30] V. Fock. „selfconsistent field“mit austausch für natrium. *Zeitschrift für Physik*, 62(11):795–805, 1930.

[Foc32] V. Fock. Konfigurationsraum und zweite quantelung. *Zeitschrift für Physik*, 75(9):622–647, 1932.

[Fre31a] J. Frenkel. On the transformation of light into heat in solids. i. *Phys. Rev.*, 37:17–44, Jan 1931.

[Fre31b] J. Frenkel. On the transformation of light into heat in solids. ii. *Phys. Rev.*, 37:1276–1294, May 1931.

[Fre34] J. Frenkel. *Wave mechanics*. Claredon Press, Oxford, 1934.

[Gau28] J. A. Gaunt. A theory of hartree's atomic fields. *Mathematical Proceedings of the Cambridge Philosophical Society*, 24(2):328–342, 1928.

[GB21] Maxim F. Gelin and Raffaele Borrelli. Simulation of nonlinear femtosecond signals at finite temperature via a thermo field dynamics-tensor train method: General theory and application to time- and frequency-resolved fluorescence of the fenna–matthews–olson complex. *Journal of Chemical Theory and Computation*, 17(7):4316–4331, 2021. PMID: 34076412.

[GHW$^+$15] J. Greitemann, S. Hesselmann, S. Wessel, F. F. Assaad, and M. Hohenadler. Finite-size effects in luther-emery phases of holstein and hubbard models. *Phys. Rev. B*, 92:245132, Dec 2015.

[Gia04] Thierry Giamarchi. *Quantum physics in one dimension*. International series of monographs on physics. Clarendon Press, Oxford, 2004.

[GKSS05] Dominique Gobert, Corinna Kollath, Ulrich Schollwöck, and Gunter Schütz. Real-time dynamics in spin-$\frac{1}{2}$ chains with adaptive time-dependent density matrix renormalization group. *Phys. Rev. E*, 71:036102, Mar 2005.

[GL21] Florian Gebhard and Örs Legeza. Tracing the mott-hubbard transition in one-dimensional hubbard models without umklapp scattering, 2021.

[Gla44] Samuel Glasstone. Quantum chemistry (eyring, henry; walter, john; kimball, george e.). *Journal of Chemical Education*, 21(8):415, 08 1944.

[Gol91] David Goldberg. What every computer scientist should know about floating-point arithmetic. *ACM Comput. Surv.*, 23(1):5–48, mar 1991.

[GP97] Alan George and Alex Pothen. An analysis of spectral envelope reduction via quadratic assignment problems. *SIAM Journal on Matrix Analysis and Applications*, 18(3):706–732, 1997.

[GPV69] N. Geacintov, M. Pope, and F. Vogel. Effect of magnetic field on the fluorescence of tetracene crystals: Exciton fission. *Phys. Rev. Lett.*, 22:593–596, Mar 1969.

[GRS$^+$17] M. Gerster, M. Rizzi, P. Silvi, M. Dalmonte, and S. Montangero. Fractional quantum hall effect in the interacting hofstadter model via tensor networks. *Phys. Rev. B*, 96:195123, Nov 2017.

[Gun97] O. Gunnarsson. Superconductivity in fullerides. *Rev. Mod. Phys.*, 69:575–606, Apr 1997.

[Gut63] Martin C. Gutzwiller. Effect of correlation on the ferromagnetism of transition metals. *Phys. Rev. Lett.*, 10:159–162, Mar 1963.

[GVW$^+$18] Klaas Gunst, Frank Verstraete, Sebastian Wouters, Örs Legeza, and Dimitri Van Neck. T3ns: Three-legged tree tensor network states. *Journal of Chemical Theory and Computation*, 14(4):2026–2033, 2018. PMID: 29481743.

[Hal95] Karen A. Hallberg. Density-matrix algorithm for the calculation of dynamical properties of low-dimensional systems. *Phys. Rev. B*, 52:R9827–R9830, Oct 1995.

[Hal15] Brian C. Hall. *Lie Groups, Lie Algebras, and Representations*. Springer, second edition, 2015.

[Har28a] D. R. Hartree. The wave mechanics of an atom with a non-coulomb central field. part i. theory and methods. *Mathematical Proceedings of the Cambridge Philosophical Society*, 24(1):89–110, 1928.

[Har28b] D. R. Hartree. The wave mechanics of an atom with a non-coulomb central field. part ii. some results and discussion. *Mathematical Proceedings of the Cambridge Philosophical Society*, 24(1):111–132, 1928.

[Har28c] D. R. Hartree. The wave mechanics of an atom with a non-coulomb central field. part iii. term values and intensities in series in optical spectra. *Mathematical Proceedings of the Cambridge Philosophical Society*, 24(3):426–437, 1928.

[Hau06] F Hausdorff. Die symbolische Exponentialformel in der Gruppentheorie. *Ber. Verh. Kgl. Saechs. Ges. Wiss. Leipzig., Math.-phys. Kl.*, 58:19–48, 1906.

[HCO$^+$11] Jutho Haegeman, J. Ignacio Cirac, Tobias J. Osborne, Iztok Pižorn, Henri Verschelde, and Frank Verstraete. Time-dependent variational principle for quantum lattices. *Phys. Rev. Lett.*, 107:070601, Aug 2011.

[Hei26] W. Heisenberg. Mehrkörperproblem und resonanz in der quantenmechanik. *Zeitschrift für Physik*, 38(6):411–426, 1926.

[HF63] J. Hubbard and Brian Hilton Flowers. Electron correlations in narrow energy bands. *Proceedings* *of the Royal Society of London. Series A. Mathematical and Physical Sciences*, 276(1365):238–257, 1963.

[HF83] Jorge E. Hirsch and Eduardo Fradkin. Phase diagram of one-dimensional electron-phonon systems. ii. the molecular-crystal model. *Phys. Rev. B*, 27:4302–4316, Apr 1983.

[HHS18] C. Hubig, J. Haegeman, and U. Schollwöck. Error estimates for extrapolations with matrix-product states. *Phys. Rev. B*, 97:045125, Jan 2018.

[Hir85] J. E. Hirsch. Two-dimensional hubbard model: Numerical simulation study. *Phys. Rev. B*, 31:4403–4419, Apr 1985.

[HK64] P. Hohenberg and W. Kohn. Inhomogeneous electron gas. *Phys. Rev.*, 136:B864–B871, Nov 1964.

[HL97] Marlis Hochbruck and Christian Lubich. On krylov subspace approximations to the matrix exponential operator. *SIAM Journal on Numerical Analysis*, 34(5):1911–1925, 1997.

[HLL$^+$] Claudius Hubig, Felix Lachenmaier, Nils-Oliver Linden, Teresa Reinhard, Leo Stenzel, Andreas Swoboda, Martin Grundner, and Sam Mardazad. The SyTen toolkit.

[HLO$^+$16] Jutho Haegeman, Christian Lubich, Ivan Oseledets, Bart Vandereycken, and Frank Verstraete. Unifying time evolution and optimization with matrix product states. *Phys. Rev. B*, 94:165116, Oct 2016.

[HM21] J.E. Hirsch and F. Marsiglio. Meissner effect in nonstandard superconductors. *Physica C: Superconductivity and its Applications*, 587:1353896, 2021.

[HMS17] C. Hubig, I. P. McCulloch, and U. Schollwöck. Generic construction of efficient matrix product operators. *Phys. Rev. B*, 95:035129, Jan 2017.

[HMSW15] C. Hubig, I. P. McCulloch, U. Schollwöck, and F. A. Wolf. Strictly single-site dmrg algorithm with subspace expansion. *Phys. Rev. B*, 91:155115, Apr 2015.

[HN06] M. C. Hanna and A. J. Nozik. Solar conversion efficiency of photovoltaic and photoelectrolysis cells with carrier multiplication absorbers. *J. Appl. Phys.*, 100(7):074510, 2006.

[Hol59] T Holstein. Studies of polaron motion: Part i. the molecular-crystal model. *Annals of Physics*, 8(3):325–342, 1959.

[HRH$^+$91] A. F. Hebard, M. J. Rosseinsky, R. C. Haddon, D. W. Murphy, S. H. Glarum, T. T. M. Palstra, A. P. Ramirez, and A. R. Kortan. Superconductivity at 18 k in potassium-doped c60. *Nature*, 350(6319):600–601, 1991.

[HSML21] Imre Hagymási, Robin Schäfer, Roderich Moessner, and David J. Luitz. Possible inversion symmetry breaking in the $s = 1/2$ pyrochlore heisenberg magnet. *Phys. Rev. Lett.*, 126:117204, Mar 2021.

[HT89] J. E. Hirsch and S. Tang. Antiferromagnetism in the two-dimensional hubbard model. *Phys. Rev. Lett.*, 62:591–594, Jan 1989.

[Hub19] Claudius Hubig. Use and implementation of autodifferentiation in tensor network methods with complex scalars, 2019.

[HvdL07] Martin Hohenadler and Wolfgang von der Linden. *Lang-Firsov Approaches to Polaron Physics: From Variational Methods to Unbiased Quantum Monte Carlo Simulations*, pages 463–502. Springer Netherlands, Dordrecht, 2007.

[IB11] Pavel Irkhin and Ivan Biaggio. Direct imaging of anisotropic exciton diffusion and triplet diffusion length in rubrene single crystals. *Phys. Rev. Lett.*, 107:017402, Jul 2011.

[Jec02] Eric Jeckelmann. Dynamical density-matrix renormalization-group method. *Phys. Rev. B*, 66:045114, Jul 2002.

[JM70] R. C. Johnson and R. E. Merrifield. Effects of magnetic fields on the mutual annihilation of triplet excitons in anthracene crystals. *Phys. Rev. B*, 1:896–902, Jan 1970.

[JNM13a] Justin C. Johnson, Arthur J. Nozik, and Josef Michl. The role of chromophore coupling in singlet fission. *Accounts of Chemical Research*, 46(6):1290–1299, 2013. PMID: 23301661.

[JNM13b] Justin C Johnson, Arthur J Nozik, and Josef Michl. The role of chromophore coupling in singlet fission. *Acc. Chem. Res*, 46(6):1290–1299, Jun 2013.

[Jon24a] J.E. Jones. On the determination of molecular fields. —II. from the equation of state of a gas. *Proceedings of the Royal Society of London. Series A, Containing Papers of a Mathematical and Physical Character*, 106(738):463–477, October 1924.

[Jon24b] J.E. Jones. On the determination of molecular fields.—i. from the variation of the viscosity of a gas with temperature. *Proceedings of the Royal Society of London. Series A, Containing Papers of a Mathematical and Physical Character*, 106(738):441–462, October 1924.

[JW28] P. Jordan and E. Wigner. Über das paulische äquivalenzverbot. *Zeitschrift für Physik*, 47(9):631–651, 1928.

[JW98] Eric Jeckelmann and Steven R. White. Density-matrix renormalization-group study of the polaron problem in the holstein model. *Phys. Rev. B*, 57:6376–6385, Mar 1998.

[Kan63] Junjiro Kanamori. Electron Correlation and Ferromagnetism of Transition Metals. *Progress of Theoretical Physics*, 30(3):275–289, 09 1963.

[KDTR15] Sebastian Keller, Michele Dolfi, Matthias Troyer, and Markus Reiher. An efficient matrix product operator representation of the quantum chemical hamiltonian. *The Journal of Chemical Physics*, 143(24):244118, 2015.

[KGV83] S. Kirkpatrick, C. D. Gelatt, and M. P. Vecchi. Optimization by simulated annealing. *Science*, 220(4598):671–680, 1983.

[KLR18] Benedikt Kloss, Yevgeny Bar Lev, and David Reichman. Time-dependent variational principle in matrix-product state manifolds: Pitfalls and potential. *Phys. Rev. B*, 97:024307, Jan 2018.

[KRU08] Micha l Karski, Carsten Raas, and Götz S. Uhrig. Single-particle dynamics in the vicinity of the mott-hubbard metal-to-insulator transition. *Phys. Rev. B*, 77:075116, Feb 2008.

[KS65] W. Kohn and L. J. Sham. Self-consistent equations including exchange and correlation effects. *Phys. Rev.*, 140:A1133–A1138, Nov 1965.

[KS17] Jamshid Moradi Kurdestany and S. Satpathy. Mott metal-insulator transition in the doped hubbard-holstein model. *Phys. Rev. B*, 96:085132, Aug 2017.

[KSP21] Thomas Köhler, Jan Stolpp, and Sebastian Paeckel. Efficient and Flexible Approach to Simulate Low-Dimensional Quantum Lattice Models with Large Local Hilbert Spaces. *SciPost Phys.*, 10:58, 2021.

[KVLE16] C. Krumnow, L. Veis, Ö. Legeza, and J. Eisert. Fermionic orbital optimization in tensor network states. *Phys. Rev. Lett.*, 117:210402, Nov 2016.

[KW99] Till D. Kühner and Steven R. White. Dynamical correlation functions using the density matrix renormalization group. *Phys. Rev. B*, 60:335–343, Jul 1999.

[KY11] Dennis D. Klug and Yansun Yao. Metallization of solid hydrogen: the challenge and possible solutions. *Phys. Chem. Chem. Phys.*, 13:16999–17006, 2011.

[LAB$^+$15] J. P. F. LeBlanc, Andrey E. Antipov, Federico Becca, Ireneusz W. Bulik, Garnet Kin-Lic Chan, Chia-Min Chung, Youjin Deng, Michel Ferrero, Thomas M. Henderson, Carlos A. Jiménez-Hoyos, E. Kozik, Xuan-Wen Liu, Andrew J. Millis, N. V. Prokof'ev, Mingpu Qin, Gustavo E. Scuseria, Hao Shi, B. V. Svistunov, Luca F. Tocchio, I. S. Tupitsyn, Steven R. White, Shiwei Zhang, Bo-Xiao Zheng, Zhenyue Zhu, and Emanuel Gull. Solutions of the two-dimensional hubbard model: Benchmarks and results from a wide range of numerical algorithms. *Phys. Rev. X*, 5:041041, Dec 2015.

[Leg21] Ö. Legeza. Private communications. Nov 2021.

[LF63] IG Lang and Yu A Firsov. Kinetic theory of semiconductors with low mobility. *Sov. Phys. JETP*, 16(5):1301, 1963.

[Lic63] William Lichten. Resonant charge exchange in atomic collisions. *Phys. Rev.*, 131:229–238, Jul 1963.

[LLWX19] Hai-Jun Liao, Jin-Guo Liu, Lei Wang, and Tao Xiang. Differentiable programming tensor networks. *Phys. Rev. X*, 9:031041, Sep 2019.

[Lof56] Joseph J. Loferski. Theoretical considerations governing the choice of the optimum semiconductor for photovoltaic solar energy conversion. *Journal of Applied Physics*, 27(7):777–784, 1956.

[LOV15] Christian Lubich, Ivan V. Oseledets, and Bart Vandereycken. Time integration of tensor trains. *SIAM Journal on Numerical Analysis*, 53(2):917–941, 2015.

[LP00] R. B. Laughlin and David Pines. The theory of everything. *Proceedings of the National Academy of Sciences*, 97(1):28–31, 2000.

[LS03] Ö. Legeza and J. Sólyom. Optimizing the density-matrix renormalization group method using quantum information entropy. *Phys. Rev. B*, 68:195116, Nov 2003.

[LS04] Ö. Legeza and J. Sólyom. Quantum data compression, quantum information generation, and the density-matrix renormalization-group method. *Phys. Rev. B*, 70:205118, Nov 2004.

[LSC17] Ch. Uma Lavanya, I. V. Sankar, and Ashok Chatterjee. Metallicity in a holstein-hubbard chain at half filling with gaussian anharmonicity. *Scientific Reports*, 7(1):3774, 2017.

[LXW03] H. G. Luo, T. Xiang, and X. Q. Wang. Comment on "time-dependent density-matrix renormalization group: A systematic method for the study of quantum many-body out-of-equilibrium systems". *Phys. Rev. Lett.*, 91:049701, Jul 2003.

[MAG69] R.E. Merrifield, P. Avakian, and R.P. Groff. Fission of singlet excitons into pairs of triplet excitons in tetracene crystals. *Chemical Physics Letters*, 3(6):386–388, 1969.

[Man08] Uwe Manthe. A multilayer multiconfigurational time-dependent hartree approach for quantum dynamics on general potential energy surfaces. *J. Chem. Phys.*, 128(16):164116, 2008.

[Man09] Uwe Manthe. Layered discrete variable representations and their application within the multiconfigurational time-dependent hartree approach. *J. Chem. Phys.*, 130(5):054109, 2009.

[Mas98] Heinrich Maschke. Ueber den arithmetischen charakter der coefficienten der substitutionen endlicher linearer substitutionsgruppen. *Mathematische Annalen*, 50(4):492–498, 1898.

[May16] Nicholas J. Mayhall. From model hamiltonians to ab initio hamiltonians and back again: Using single excitation quantum chemistry methods to find multiexciton states in singlet fission materials. *J. Chem. Theory Comput.*, 12(9):4263–4273, 2016. PMID: 27472260.

[MBN$^+$06] James E. Murphy, Matthew C. Beard, Andrew G. Norman, S. Phillip Ahrenkiel, Justin C. Johnson, Pingrong Yu, Olga I. Mićić, Randy J. Ellingson, and Arthur J. Nozik. Pbte colloidal nanocrystals: Synthesis, characterization, and multiple exciton generation. *Journal of the American Chemical Society*, 128(10):3241–3247, 2006. PMID: 16522105.

[MCBGZ19] Kiyoshi Miyata, Felisa S. Conrad-Burton, Florian L. Geyer, and X.-Y. Zhu. Triplet pair states in singlet fission. *Chem. Rev.*, 119(6):4261–4292, 2019.

[MG02] I. P McCulloch and M Gulácsi. The non-abelian density matrix renormalization group algorithm. *Europhysics Letters (EPL)*, 57(6):852–858, mar 2002.

[MGPO89] Miroslaw Malek, Mohan Guruswamy, Mihir Pandya, and Howard Owens. Serial and parallel simulated annealing and tabu search algorithms for the traveling salesman problem. *Annals of Operations Research*, 21(1):59–84, 1989.

[MGS$^+$22] Sam Mardazad, Martin Grundner, Ulrich Schollwöck, Adrian Kantian, Thomas Köhler, and Sebastian Paeckel. Emergence of bond-order wave phase in the half filled Hubbard-Holstein chain. Preliminary title, 2022.

[MH17] Adrian F. Morrison and John M. Herbert. Evidence for singlet fission driven by vibronic coherence in crystalline tetracene. *J. Phys. Chem. Lett*, 8(7):1442–1448, 2017. PMID: 28277682.

[MHR05] Gerrit Moritz, Bernd Artur Hess, and Markus Reiher. Convergence behavior of the density-matrix renormalization group algorithm for optimized orbital orderings. *The Journal of Chemical Physics*, 122(2):024107, 2005.

[MKW$^+$17] Kiyoshi Miyata, Yuki Kurashige, Kazuya Watanabe, Toshiki Sugimoto, Shota Takahashi, Shunsuke Tanaka, Jun Takeya, Takeshi Yanai, and Yoshiyasu Matsumoto. Coherent singlet fission activated by symmetry breaking. *Nat. Chem.*, 9(10):983–989, 2017.

[MMC90] H.-D. Meyer, U. Manthe, and L.S. Cederbaum. The multi-configurational time-dependent hartree approach. *Chem. Phys. Lett.*, 165(1):73–78, 1990.

[MMC92] U. Manthe, H.-D. Meyer, and L. S. Cederbaum. Wave-packet dynamics within the multiconfiguration hartree framework: General aspects and application to nocl. *J. Chem. Phys.*, 97(5):3199–3213, 1992.

[MMW$^+$16] Eric A Margulies, Claire E Miller, Yilei Wu, Lin Ma, George C Schatz, Ryan M Young, and Michael R Wasielewski. Enabling singlet fission by controlling intramolecular charge transfer in pi-stacked covalent terrylenediimide dimers. *Nat. Chem.*, 8(12):1120–1125, Dec 2016.

[MNH$^+$17] C. B. Mendl, E. A. Nowadnick, E. W. Huang, S. Johnston, B. Moritz, and T. P. Devereaux. Doping dependence of ordered phases and emergent quasiparticles in the doped hubbard-holstein model. *Phys. Rev. B*, 96:205141, Nov 2017.

[MOI20] Riccardo Mengoni, Daniele Ottaviani, and Paolino Iorio. Breaking rsa security with a low noise d-wave 2000q quantum annealer: Computational times, limitations and prospects, 2020.

[Moo65] Gordon E. Moore. Cramming more components onto integrated circuits. *Electronics*, 38(8), April 1965.

[mpi93] Mpi: A message passing interface. In *Supercomputing '93:Proceedings of the 1993 ACM/IEEE Conference on Supercomputing*, pages 878–883, 1993.

[MRR+53] Nicholas Metropolis, Arianna W. Rosenbluth, Marshall N. Rosenbluth, Augusta H. Teller, and Edward Teller. Equation of state calculations by fast computing machines. *The Journal of Chemical Physics*, 21(6):1087–1092, 1953.

[MSJ04] A. Macridin, G. A. Sawatzky, and Mark Jarrell. Two-dimensional hubbard-holstein bipolaron. *Phys. Rev. B*, 69:245111, Jun 2004.

[MST+17] Nicholas R. Monahan, Dezheng Sun, Hiroyuki Tamura, Kristopher W. Williams, Bolei Xu, Yu Zhong, Bharat Kumar, Colin Nuckolls, Avetik R. Harutyunyan, Gugang Chen, Hai-Lung Dai, David Beljonne, Yi Rao, and X. Y. Zhu. Dynamics of the triplet-pair state reveals the likely coexistence of coherent and incoherent singlet fission in crystalline hexacene. *Nat. Chem.*, 9(4):341–346, 2017.

[Muk95] S. Mukamel. *Principles of Nonlinear Optical Spectroscopy*. Oxford University Press, New York, 1995.

[Mus16] Heinz Mustroph. Potential-energy surfaces, the born–oppenheimer approximations, and the franck–condon principle: Back to the roots. *ChemPhysChem*, 17(17):2616–2629, 2016.

[MVLN10] V. Murg, F. Verstraete, Ö. Legeza, and R. M. Noack. Simulating strongly correlated quantum systems with tree tensor networks. *Phys. Rev. B*, 82:205105, Nov 2010.

[MVS+15] V. Murg, F. Verstraete, R. Schneider, P. R. Nagy, and Ö. Legeza. Tree tensor network state with variable tensor order: An efficient multireference method for strongly correlated systems. *Journal of Chemical Theory and Computation*, 11(3):1027–1036, 2015. PMID: 25844072.

[MW66] N. D. Mermin and H. Wagner. Absence of ferromagnetism or antiferromagnetism in one- or two-dimensional isotropic heisenberg models. *Phys. Rev. Lett.*, 17:1133–1136, Nov 1966.

[MWS20] Iman Mahyaeh, Jurriaan Wouters, and Dirk Schuricht. Phase diagram of the $\mathbb{Z}_3$-Fock parafermion chain with pair hopping. *SciPost Phys. Core*, 3:11, 2020.

[MXY+21] Sam Mardazad, Yihe Xu, Xuexiao Yang, Martin Grundner, Ulrich Schollwöck, Haibo Ma, and Sebastian Paeckel. Quantum dynamics simulation of intramolecular singlet fission in covalently linked tetracene dimer. *The Journal of Chemical Physics*, 155(19):194101, 2021.

[MZ15] N. Monahan and X.-Y. Zhu. Charge transfer–mediated singlet fission. *Ann. Rev. Phys. Chem.*, 66(1):601–618, 2015. PMID: 25648486.

[Nas87] K. Nasu. Many-polaron theory for superconductivity and charge-density waves in a strongly coupled electron-phonon system with quasi-two-dimensionality: An interpolation between the adiabatic limit and the inverse-adiabatic limit. *Phys. Rev. B*, 35:1748–1763, Feb 1987.

[NBL+10] A. J. Nozik, M. C. Beard, J. M. Luther, M. Law, R. J. Ellingson, and J. C. Johnson. Semiconductor quantum dots and quantum dot arrays and applications of multiple exciton generation to third-generation photovoltaic solar cells. *Chemical Reviews*, 110(11):6873–6890, 2010. PMID: 20945911.

[NC13] Naoki Nakatani and Garnet Kin-Lic Chan. Efficient tree tensor network states (ttns) for quantum chemistry: Generalizations of the density matrix renormalization group algorithm. *The Journal of Chemical Physics*, 138(13):134113, 2013.

[NLZ+10] H. Najafov, B. Lee, Q. Zhou, L. C. Feldman, and V. Podzorov. Observation of long-range exciton diffusion in highly ordered organic semiconductors. *Nat. Mater.*, 9(11):938–943, 2010.

[NM65] John A. Nelder and Roger Mead. A simplex method for function minimization. *Comput. J.*, 7:308–313, 1965.

[Ope08] OpenMP Architecture Review Board. OpenMP application program interface version 3.0, May 2008.

[OR95] Stellan Östlund and Stefan Rommer. Thermodynamic limit of density matrix renormalization. *Phys. Rev. Lett.*, 75:3537–3540, Nov 1995.

[Osb06] Tobias J. Osborne. Efficient approximation of the dynamics of one-dimensional quantum spin systems. *Phys. Rev. Lett.*, 97:157202, Oct 2006.

[PA00] L. Proville and S. Aubry. Small bipolarons in the 2-dimensional holstein-hubbard model. ii. quantum bipolarons. *The European Physical Journal B - Condensed Matter and Complex Systems*, 15(3):405–421, 2000.

[Pae20] Sebastian Paeckel. *Topological and non-equilibrium superconductivity in low-dimensional strongly correlated quantum systems*. PhD thesis, Georg-August University School of Science, 2020.

[Pau25] W. Pauli. Über den zusammenhang des abschlusses der elektronengruppen im atom mit der komplexstruktur der spektren. *Zeitschrift für Physik*, 31(1):765–783, 1925.

[PEDC05] M. B. Plenio, J. Eisert, J. Dreißig, and M. Cramer. Entropy, entanglement, and area: Analytical results for harmonic lattice systems. *Phys. Rev. Lett.*, 94:060503, Feb 2005.

[Pen71] Roger Penrose. Applications of negative dimensional tensors. *Combinatorial mathematics and its applications*, 1:221–244, 1971.

[PHCS$^+$21] G. Paleari, F. Hébert, B. Cohen-Stead, K. Barros, RT. Scalettar, and G. G. Batrouni. Quantum monte carlo study of an anharmonic holstein model. *Phys. Rev. B*, 103:195117, May 2021.

[PKM17] Sebastian Paeckel, Thomas Köhler, and Salvatore R. Manmana. Automated construction of $U(1)$-invariant matrix-product operators from graph representations. *SciPost Phys.*, 3:035, 2017.

[PKS$^+$19] Sebastian Paeckel, Thomas Köhler, Andreas Swoboda, Salvatore R. Manmana, Ulrich Schollwöck, and Claudius Hubig. Time-evolution methods for matrix-product states. *Annals of Physics*, 411:167998, 2019.

[Pla01] Max Planck. Ueber das gesetz der energieverteilung im normalspectrum. *Annalen der Physik*, 309(3):553–563, 1901.

[PM89] Janos Pipek and Paul G. Mezey. A fast intrinsic localization procedure applicable for ab initio and semiempirical linear combination of atomic orbital wave functions. *J. Chem. Phys.*, 90(9):4916–4926, 1989.

[PMB$^+$21] Felix A. Palm, Sam Mardazad, Annabelle Bohrdt, Ulrich Schollwöck, and Fabian Grusdt. Snapshot-based detection of $\frac{1}{2}$-Laughlin states: coupled chains and central charge, 2021.

[PN54] J. A. Pople and R. K. Nesbet. Self-consistent orbitals for radicals. *The Journal of Chemical Physics*, 22(3):571–572, 1954.

[POW70] M.J.D. POWELL. A new algorithm for unconstrained optimization. In J.B. Rosen, O.L. Mangasarian, and K. Ritter, editors, *Nonlinear Programming*, pages 31–65. Academic Press, 1970.

[Pri55] M. B. Prince. Silicon solar energy converters. *Journal of Applied Physics*, 26(5):534–540, 1955.

[PVR54] W. G. Pfann and W. Van Roosbroeck. Radioactive and photoelectric p-n junction power sources. *Journal of Applied Physics*, 25(11):1422–1434, 1954.

[QCS$^+$20] Mingpu Qin, Chia-Min Chung, Hao Shi, Ettore Vitali, Claudius Hubig, Ulrich Schollwöck, Steven R. White, and Shiwei Zhang. Absence of superconductivity in the pure two-dimensional hubbard model. *Phys. Rev. X*, 10:031016, Jul 2020.

[QSA$^+$21] Mingpu Qin, Thomas Schäfer, Sabine Andergassen, Philippe Corboz, and Emanuel Gull. The hubbard model: A computational perspective, 2021.

[RCT18] S. Rajagopala Reddy, Pedro B. Coto, and Michael Thoss. Intramolecular singlet fission: Insights from quantum dynamical simulations. *J. Phys. Chem. Lett*, 9(20):5979–5986, 2018.

[RCT19] S. Rajagopala Reddy, Pedro B. Coto, and Michael Thoss. Quantum dynamical simulation of intramolecular singlet fission in covalently coupled pentacene dimers. *The Journal of Chemical Physics*, 151(4):044307, 2019.

[Rec71] Ingo Rechenberg. *Evolutionsstrategie - Optimierung technischer Systeme nach Prinzipien der biologischen Evolution*. PhD thesis, 1971.

[RED65] A.G. REDFIELD. The theory of relaxation processes* *this work was started while the author was at harvard university, and was then partially supported by joint services contract n5ori-76, project order i. In John S. Waugh, editor, *Adv. Magn. Reson.*, volume 1 of *Advances in Magnetic and Optical Resonance*, pages 1–32. Academic Press, 1965.

[RNW06] Jörg Rissler, Reinhard M. Noack, and Steven R. White. Measuring orbital interaction using quantum information theory. *Chemical Physics*, 323(2):519–531, 2006.

[Roo80] Björn O. Roos. The complete active space scf method in a fock-matrix-based super-ci formulation.

International Journal of Quantum Chemistry, 18(S14):175–189, 1980.

[RTS80] Björn O. Roos, Peter R. Taylor, and Per E.M. Sigbahn. A complete active space scf method (casscf) using a density matrix formulated super-ci approach. *Chemical Physics*, 48(2):157–173, 1980.

[RWMC99] A. Raab, G. A. Worth, H.-D. Meyer, and L. S. Cederbaum. Molecular dynamics of pyrazine after excitation to the s2 electronic state using a realistic 24-mode model hamiltonian. *The Journal of Chemical Physics*, 110(2):936–946, 1999.

[S47] D R Hartree F R S. The calculation of atomic structures. *Reports on Progress in Physics*, 11(1):113–143, jan 1947.

[Sac11] Subir Sachdev. *Quantum Phase Transitions*. Cambridge University Press, 2 edition, 2011.

[SAHR81] Per E. M. Siegbahn, Jan Almlöf, Anders Heiberg, and Björn O. Roos. The complete active space scf (casscf) method in a newton–raphson formulation with application to the hno molecule. *The Journal of Chemical Physics*, 74(4):2384–2396, 1981.

[SAW$^+$19] Christoph Schnedermann, Antonios M. Alvertis, Torsten Wende, Steven Lukman, Jiaqi Feng, Florian A. Y. N. Schröder, David H. P. Turban, Jishan Wu, Nicholas D. M. Hine, Neil C. Greenham, Alex W. Chin, Akshay Rao, Philipp Kukura, and Andrew J. Musser. A molecular movie of ultrafast singlet fission. *Nature Communications*, 10(1):4207, 2019.

[SBG$^+$20] Trond Saue, Radovan Bast, André Severo Pereira Gomes, Hans Jørgen Aa. Jensen, Lucas Visscher, Ignacio Agustín Aucar, Roberto Di Remigio, Kenneth G. Dyall, Ephraim Eliav, Elke Fasshauer, Timo Fleig, Loïc Halbert, Erik Donovan Hedegård, Benjamin Helmich-Paris, Miroslav Iliaš, Christoph R. Jacob, Stefan Knecht, Jon K. Laerdahl, Marta L. Vidal, Malaya K. Nayak, Ma lgorzata Olejniczak, Jógvan Magnus Haugaard Olsen, Markus Pernpointner, Bruno Senjean, Avijit Shee, Ayaki Sunaga, and Joost N. P. van Stralen. The dirac code for relativistic molecular calculations. *The Journal of Chemical Physics*, 152(20):204104, 2020.

[SBS$^+$17] Szilárd Szalay, Gergely Barcza, Tibor Szilvási, Libor Veis, and Örs Legeza. The correlation theory of the chemical bond. *Scientific Reports*, 7(1):2237, 2017.

[SC12] Sandeep Sharma and Garnet Kin-Lic Chan. Spin-adapted density matrix renormalization group algorithms for quantum chemistry. *The Journal of Chemical Physics*, 136(12):124121, 2012.

[Sch05] U. Schollwöck. The density-matrix renormalization group. *Rev. Mod. Phys.*, 77:259–315, Apr 2005.

[Sch11] Ulrich Schollwöck. The density-matrix renormalization group in the age of matrix product states. *Annals of Physics*, 326(1):96–192, 2011. January 2011 Special Issue.

[SDV06] Y.-Y. Shi, L.-M. Duan, and G. Vidal. Classical simulation of quantum many-body systems with a tree tensor network. *Phys. Rev. A*, 74:022320, Aug 2006.

[SG88] K. Schonhammer and O. Gunnarsson. Difference between the quasiparticle and the kohn-sham-fermi surfaces. *Phys. Rev. B*, 37:3128–3129, Feb 1988.

[SGL$^+$20] Paul Secular, Nikita Gourianov, Michael Lubasch, Sergey Dolgov, Stephen R. Clark, and Dieter Jaksch. Parallel time-dependent variational principle algorithm for matrix product states. *Phys. Rev. B*, 101:235123, Jun 2020.

[SGN95] K. Schönhammer, O. Gunnarsson, and R. M. Noack. Density-functional theory on a lattice: Comparison with exact numerical results for a model with strongly correlated electrons. *Phys. Rev. B*, 52:2504–2510, Jul 1995.

[Sha48] C. E. Shannon. A mathematical theory of communication. *The Bell System Technical Journal*, 27(3):379–423, 1948.

[Sho97] Peter W. Shor. Polynomial-time algorithms for prime factorization and discrete logarithms on a quantum computer. *SIAM Journal on Computing*, 26(5):1484–1509, 1997.

[SIS$^+$15] M. Schröter, S.D. Ivanov, J. Schulze, S.P. Polyutov, Y. Yan, T. Pullerits, and O. Kühn. Exciton–vibrational coupling in the dynamics and spectroscopy of frenkel excitons in molecular aggregates. *Physics Reports*, 567:1–78, 2015. Exciton–vibrational coupling in the dynamics and spectroscopy of Frenkel excitons in molecular aggregates.

[SJS$^+$65] S. Singh, W. J. Jones, W. Siebrand, B. P. Stoicheff, and W. G. Schneider. Laser generation of excitons and fluorescence in anthracene crystals. *The Journal of Chemical Physics*, 42(1):330–342, 1965.

[SK04] R. D. Schaller and V. I. Klimov. High efficiency carrier multiplication in pbse nanocrystals: Implications for solar energy conversion. *Phys. Rev. Lett.*, 92:186601, May 2004.

[SKM$^+$21] Jan Stolpp, Thomas Köhler, Salvatore R. Manmana, Eric Jeckelmann, Fabian Heidrich-Meisner, and Sebastian Paeckel. Comparative study of state-of-the-art matrix-product-state methods for lattice models with large local hilbert spaces without u(1) symmetry. *Computer Physics Communications*, 269:108106, 2021.

[Sla28] J. C. Slater. The self consistent field and the structure of atoms. *Phys. Rev.*, 32:339–348, Sep 1928.

[Sla29] J. C. Slater. The theory of complex spectra. *Phys. Rev.*, 34:1293–1322, Nov 1929.

[Sla30] J. C. Slater. Note on hartree's method. *Phys. Rev.*, 35:210–211, Jan 1930.

[SLH$^+$21] Kewei Sun, Xiaohui Liu, Wangjun Hu, Mingtao Zhang, Guankui Long, and Yang Zhao. Singlet fission dynamics and optical spectra of pentacene and its derivatives. *Phys. Chem. Chem. Phys.*, 23:12654–12667, 2021.

[SM10] Millicent B. Smith and Josef Michl. Singlet fission. *Chem. Rev.*, 110(11):6891–6936, 2010. PMID: 21053979.

[Smi69] Felix T. Smith. Diabatic and adiabatic representations for atomic collision problems. *Phys. Rev.*, 179:111–123, Mar 1969.

[SO96] Attila Szabo and Neil S. Ostlund. *Modern Quantum Chemistry: Introduction to Advanced Electronic Structure Theory*. Dover Publications, Inc., Mineola, first edition, 1996.

[SPK05] Richard D. Schaller, Melissa A. Petruska, and Victor I. Klimov. Effect of electronic structure on carrier multiplication efficiency: Comparative study of pbse and cdse nanocrystals. *Applied Physics Letters*, 87(25):253102, 2005.

[SPV10] Sukhwinder Singh, Robert N. C. Pfeifer, and Guifre Vidal. Tensor network decompositions in the presence of a global symmetry, 2010.

[SPV11] Sukhwinder Singh, Robert N. C. Pfeifer, and Guifre Vidal. Tensor network states and algorithms in the presence of a global u(1) symmetry. *Phys. Rev. B*, 83:115125, Mar 2011.

[SQ61] William Shockley and Hans J. Queisser. Detailed balance limit of efficiency of p-n junction solar cells. *Journal of Applied Physics*, 32(3):510–519, 1961.

[SS68] C.E. Swenberg and W.T. Stacy. Bimolecular radiationless transitions in crystalline tetracene. *Chemical Physics Letters*, 2(5):327–328, 1968.

[SSPK06] Richard D. Schaller, Milan Sykora, Jeffrey M. Pietryga, and Victor I. Klimov. Seven excitons at a cost of one: Redefining the limits for conversion efficiency of photons into charge carriers. *Nano Letters*, 6(3):424–429, 2006. PMID: 16522035.

[STC19] Jon Spalding, Shan-Wen Tsai, and David K. Campbell. Critical entanglement for the half-filled extended hubbard model. *Phys. Rev. B*, 99:195445, May 2019.

[STM$^+$19] Florian A. Y. N. Schröder, David H. P. Turban, Andrew J. Musser, Nicholas D. M. Hine, and Alex W. Chin. Tensor network simulation of multi-environmental open quantum dynamics via machine learning and entanglement renormalisation. *Nature Communications*, 10(1):1062, 2019.

[Suz76a] Masuo Suzuki. Generalized trotter's formula and systematic approximants of exponential operators and inner derivations with applications to many-body problems. *Communications in Mathematical Physics*, 51(2):183–190, 1976.

[Suz76b] Masuo Suzuki. Generalized trotter's formula and systematic approximants of exponential operators and inner derivations with applications to many-body problems. *Communications in Mathematical Physics*, 51(2):183–190, 1976.

[Suz85] Masuo Suzuki. Decomposition formulas of exponential operators and lie exponentials with some applications to quantum mechanics and statistical physics. *Journal of Mathematical Physics*, 26(4):601–612, 1985.

[SV12] Sukhwinder Singh and Guifre Vidal. Tensor network states and algorithms in the presence of a global su(2) symmetry. *Phys. Rev. B*, 86:195114, Nov 2012.

[SW12] E.M. Stoudenmire and Steven R. White. Studying two-dimensional systems with the density matrix renormalization group. *Annual Review of Condensed Matter Physics*, 3(1):111–128, 2012.

[SW13] E. M. Stoudenmire and Steven R. White. Real-space parallel density matrix renormalization group. *Phys. Rev. B*, 87:155137, Apr 2013.

[SWicv+21] Thomas Schäfer, Nils Wentzell, Fedor Šimkovic, Yuan-Yao He, Cornelia Hille, Marcel Klett, Christian J. Eckhardt, Behnam Arzhang, Viktor Harkov, François-Marie Le Régent, Alfred Kirsch, Yan Wang, Aaram J. Kim, Evgeny Kozik, Evgeny A. Stepanov, Anna Kauch, Sabine Andergassen, Philipp Hansmann, Daniel Rohe, Yuri M. Vilk, James P. F. LeBlanc, Shiwei Zhang, A.-M. S. Tremblay, Michel Ferrero, Olivier Parcollet, and Antoine Georges. Tracking the footprints of spin fluctuations: A multimethod, multimessenger study of the two-dimensional hubbard model. *Phys. Rev. X*, 11:011058, Mar 2021.

[SWVC07] Norbert Schuch, Michael M. Wolf, Frank Verstraete, and J. Ignacio Cirac. Computational complexity of projected entangled pair states. *Phys. Rev. Lett.*, 98:140506, Apr 2007.

[SXC+20] Kewei Sun, Quan Xu, Lipeng Chen, Maxim F. Gelin, and Yang Zhao. Temperature effects on singlet fission dynamics mediated by a conical intersection. *The Journal of Chemical Physics*, 153(19):194106, 2020.

[TAA07] Masaki Tezuka, Ryotaro Arita, and Hideo Aoki. Phase diagram for the one-dimensional hubbard-holstein model: A density-matrix renormalization group study. *Phys. Rev. B*, 76:155114, Oct 2007.

[Tak96] Yasutami Takada. Superconductivity in the half-filled hubbard-holstein model in the antiadiabatic region. *Journal of the Physical Society of Japan*, 65(6):1544–1547, 1996.

[Tao19] Guohua Tao. Nonadiabatic simulation of singlet fission dynamics in tetracene clusters: The topology of quantum coherence in a global view. *J. Chem. Phys.*, 151(5):054308, 2019.

[TC03] Yasutami Takada and Ashok Chatterjee. Possibility of a metallic phase in the charge-density-wave–spin-density-wave crossover region in the one-dimensional hubbard-holstein model at half filling. *Phys. Rev. B*, 67:081102, Feb 2003.

[TES+91] K. Tanigaki, T. W. Ebbesen, S. Saito, J. Mizuki, J. S. Tsai, Y. Kubo, and S. Kuroshima. Superconductivity at 33 k in csxrbyc60. *Nature*, 352(6332):222–223, 1991.

[Tho52] W. Thomson. On the dynamical theory of heat, with numerical results deduced from mr joule's equivalent of a thermal unit, and m. regnault's observations on steam. *Transactions of the Royal Society of Edinburgh*, pages 261–268, 289–298, 1852.

[THRB+15a] Hiroyuki Tamura, Miquel Huix-Rotllant, Irene Burghardt, Yoann Olivier, and David Beljonne. First-principles quantum dynamics of singlet fission: Coherent versus thermally activated mechanisms governed by molecular π stacking. *Phys. Rev. Lett.*, 115:107401, Aug 2015.

[THRB+15b] Hiroyuki Tamura, Miquel Huix-Rotllant, Irene Burghardt, Yoann Olivier, and David Beljonne. First-principles quantum dynamics of singlet fission: Coherent versus thermally activated mechanisms governed by molecular π stacking. *Phys. Rev. Lett.*, 115:107401, Aug 2015.

[TLJ+13] Luca F. Tocchio, Hunpyo Lee, Harald O. Jeschke, Roser Valentí, and Claudius Gros. Mott correlated states in the underdoped two-dimensional hubbard model: Variational monte carlo versus a dynamical cluster approximation. *Phys. Rev. B*, 87:045111, Jan 2013.

[Tow16] J. Townsend. Differentiating the singular value decomposition. Online, Aug 2016.

[TR17] Roel Tempelaar and David R. Reichman. Vibronic exciton theory of singlet fission. i. linear absorption and the anatomy of the correlated triplet pair state. *J. Chem. Phys.*, 146(17):174703, 2017.

[Tro59] H. F. Trotter. On the product of semi-groups of operators. *Proc. Amer. Math. Soc. 10 (1959), 545-551*, 10:545–551, 1959.

[TUR50] A. M. TURING. I.—COMPUTING MACHINERY AND INTELLIGENCE. *Mind*, LIX(236):433–460, 10 1950.

[TVF02] S.A. Teukolsky, W.T. Vettering, and B.P. Flannery. *Numerical Recipes in C++*. Cambridge University Press, 2002.

[TW05] Matthias Troyer and Uwe-Jens Wiese. Computational complexity and fundamental limitations to fermionic quantum monte carlo simulations. *Phys. Rev. Lett.*, 94:170201, May 2005.

[Ull12] C. Ullrich. *Time-Dependent Density-Functional Theory: Concepts and Applications*. Oxford Graduate Texts. OUP Oxford, 2012.

[VAL+18] Libor Veis, Andrej Antalík, Örs Legeza, Ali Alavi, and Jiří Pittner. The intricate case of tetramethyleneethane: A full configuration interaction quantum monte carlo benchmark and multireference coupled cluster studies. *Journal of Chemical Theory and Computation*, 14(5):2439–2445, 2018. PMID: 29570291.

[VC04] F. Verstraete and J. I. Cirac. Valence-bond states for quantum computation. *Phys. Rev. A*, 70:060302, Dec 2004.

[VC06] F. Verstraete and J. I. Cirac. Matrix product states represent ground states faithfully. *Phys. Rev. B*, 73:094423, Mar 2006.

[vG01] Johann Wolfgang von Goethe. *Faust, Der Tragödie Erster Teil.* Reclam, Ditzingen, 2001.

[VGRC04] F. Verstraete, J. J. García-Ripoll, and J. I. Cirac. Matrix product density operators: Simulation of finite-temperature and dissipative systems. *Phys. Rev. Lett.*, 93:207204, Nov 2004.

[Vid03] Guifré Vidal. Efficient classical simulation of slightly entangled quantum computations. *Phys. Rev. Lett.*, 91:147902, Oct 2003.

[VT18] Tuomas I. Vanhala and Päivi Törmä. Dynamical mean-field theory study of stripe order and d-wave superconductivity in the two-dimensional hubbard model. *Phys. Rev. B*, 97:075112, Feb 2018.

[VWPGC06] F. Verstraete, M. M. Wolf, D. Perez-Garcia, and J. I. Cirac. Criticality, the area law, and the computational power of projected entangled pair states. *Phys. Rev. Lett.*, 96:220601, Jun 2006.

[Wei12] Andreas Weichselbaum. Non-abelian symmetries in tensor networks: A quantum symmetry space approach. *Annals of Physics*, 327(12):2972–3047, 2012.

[Wen64] R. E. Wengert. A simple automatic derivative evaluation program. *Commun. ACM*, 7(8):463–464, aug 1964.

[WH35] E. Wigner and H. B. Huntington. On the possibility of a metallic modification of hydrogen. *The Journal of Chemical Physics*, 3(12):764–770, 1935.

[Whi92] Steven R. White. Density matrix formulation for quantum renormalization groups. *Phys. Rev. Lett.*, 69:2863–2866, Nov 1992.

[Whi93] Steven R. White. Density-matrix algorithms for quantum renormalization groups. *Phys. Rev. B*, 48:10345–10356, Oct 1993.

[Whi96] Steven R. White. Spin gaps in a frustrated heisenberg model for cav$_4O_9$. *Phys. Rev. Lett.*, 77:3633–3636, Oct 1996.

[Wig27] E. Wigner. Einige folgerungen aus der schrödingerschen theorie für die termstrukturen. *Zeitschrift für Physik*, 43(9):624–652, 1927.

[Wil75] Kenneth G. Wilson. The renormalization group: Critical phenomena and the kondo problem. *Rev. Mod. Phys.*, 47:773–840, Oct 1975.

[WL18] Alexander Wietek and Andreas M. Läuchli. Sublattice coding algorithm and distributed memory parallelization for large-scale exact diagonalizations of quantum many-body systems. *Phys. Rev. E*, 98:033309, Sep 2018.

[WL20] Alexander Wietek and Andreas M. Läuchli. Valence bond solid and possible deconfined quantum criticality in an extended kagome lattice heisenberg antiferromagnet. *Phys. Rev. B*, 102:020411, Jul 2020.

[WLL10] Sebastian F. Walter, Lutz Lehmann, and René Lamour. Higher-order derivatives of the qr and of the real symmetric eigenvalue decomposition in forward and reverse mode algorithmic differentiation, 2010.

[WLX+21] Zhiwei Wang, Heyuan Liu, Xiaoyu Xie, Chunfeng Zhang, Rui Wang, Lan Chen, Yihe Xu, Haibo Ma, Weihai Fang, Yao Yao, Hai Sang, Xiaoyong Wang, Xiyou Li, and Min Xiao. Free-triplet generation with improved efficiency in tetracene oligomers through spatially separated triplet pair states. *Nat. Chem.*, 13(6):559–567, 2021.

[WM99] Steven R. White and Richard L. Martin. Ab initio quantum chemistry using the density matrix renormalization group. *The Journal of Chemical Physics*, 110(9):4127–4130, 1999.

[WVN14a] Sebastian Wouters and Dimitri Van Neck. The density matrix renormalization group for ab initio quantum chemistry. *The European Physical Journal D*, 68(9):272, 2014.

[WVN14b] Sebastian Wouters and Dimitri Van Neck. The density matrix renormalization group for ab initio quantum chemistry. *The European Physical Journal D*, 68(9):272, 2014.

[XLY+19] Xiaoyu Xie, Yuyang Liu, Yao Yao, Ulrich Schollwöck, Chungen Liu, and Haibo Ma. Time-dependent density matrix renormalization group quantum dynamics for realistic chemical systems. *The Journal of Chemical Physics*, 151(22):224101, 2019.

[XSBF+19] Xiaoyu Xie, Alejandro Santana-Bonilla, Weihai Fang, Chungen Liu, Alessandro Troisi, and Haibo Ma. Exciton–phonon interaction model for singlet fission in prototypical molecular crystals. *J. Chem. Theory Comput.*, 15(6):3721–3729, 2019. PMID: 30970207.

[XSF+20] Lijuan Xue, Xinyu Song, Yiwei Feng, Shibo Cheng, Gang Lu, and Yuxiang Bu. General dual-switched dynamic singlet fission channels in solvents governed jointly by chromophore structural dynamics and solvent impact: Singlet prefission energetics analyses. *J. Am. Chem. Soc.*, 142(41):17469–17479, 2020. PMID: 32927954.

[YI96] K. Yonemitsu and M. Imada. Spin-gap phase in nearly half-filled one-dimensional conductors coupled with phonons. *Phys. Rev. B*, 54:2410–2420, Jul 1996.

[YZS99] K. Yonemitsu, J. Zhong, and H.-B. Schüttler. Berry phases and pairing symmetry in holstein-hubbard polaron systems. *Phys. Rev. B*, 59:1444–1467, Jan 1999.

[ZCC+17] Bo-Xiao Zheng, Chia-Min Chung, Philippe Corboz, Georg Ehlers, Ming-Pu Qin, Reinhard M. Noack, Hao Shi, Steven R. White, Shiwei Zhang, and Garnet Kin-Lic Chan. Stripe order in the underdoped region of the two-dimensional hubbard model. *Science*, 358(6367):1155–1160, 2017.

[ZCR13] Erez Zohar, J. Ignacio Cirac, and Benni Reznik. Quantum simulations of gauge theories with ultracold atoms: Local gauge invariance from angular-momentum conservation. *Phys. Rev. A*, 88:023617, Aug 2013.

[ZJW98] Chunli Zhang, Eric Jeckelmann, and Steven R. White. Density matrix approach to local hilbert space reduction. *Phys. Rev. Lett.*, 80:2661–2664, Mar 1998.

[ZJW99] Chunli Zhang, Eric Jeckelmann, and Steven R. White. Dynamical properties of the one-dimensional holstein model. *Phys. Rev. B*, 60:14092–14104, Nov 1999.

[ZN08] Dominika Zgid and Marcel Nooijen. The density matrix renormalization group self-consistent field method: Orbital optimization with the density matrix renormalization group method in the active space. *The Journal of Chemical Physics*, 128(14):144116, 2008.

[ZR88] F. C. Zhang and T. M. Rice. Effective hamiltonian for the superconducting cu oxides. *Phys. Rev. B*, 37:3759–3761, Mar 1988.

[ZSS16] Mohamed Zaghoo, Ashkan Salamat, and Isaac F. Silvera. Evidence of a first-order phase transition to metallic hydrogen. *Phys. Rev. B*, 93:155128, Apr 2016.

[ZXJL16] Jie Zheng, Yu Xie, Shengshi Jiang, and Zhenggang Lan. Ultrafast nonadiabatic dynamics of singlet fission: Quantum dynamics with the multilayer multiconfigurational time-dependent hartree (ml-mctdh) method. *J. Phys. Chem. C*, 120(3):1375–1389, 2016.

[ZZL17] Hang Zang, Yi Zhao, and WanZhen Liang. Quantum interference in singlet fission: J- and h-aggregate behavior. *J. Phys. Chem. Lett*, 8(20):5105–5112, 2017. PMID: 28960999.

[ZZM10] Paul M. Zimmerman, Zhiyong Zhang, and Charles B. Musgrave. Singlet fission in pentacene through multi-exciton quantum states. *Nat. Chem.*, 2(8):648–652, 2010.